# Cosmic-Ray Propagation in Simulations of Cross-Helical Plasma Turbulence

Martin Simon Weidl

SIGILL. UNIVERSITAT. LUDOVIC. MAXIM.

München 2015

# Cosmic-Ray Propagation in Simulations of Cross-Helical Plasma Turbulence

Martin Simon Weidl

Dissertation
an der Fakultät für Physik
der Ludwig–Maximilians–Universität
München

vorgelegt von
Martin Simon Weidl
aus Ehingen a. d. Donau

München, den 13. Mai 2015

Erstgutachter: Prof. Dr. Harald Lesch
Zweitgutachter: Prof. Dr. Frank Jenko
Tag der mündlichen Prüfung: 9. Juli 2015

# Contents

**Zusammenfassung** **ix**

**Abstract** **x**

**1 Cosmic Rays in the Universe** **1**
- 1.1 Plasmas in astrophysics . . . . . 1
- 1.2 Astrophysical background . . . . . 3
  - 1.2.1 Supernovae . . . . . 3
  - 1.2.2 The cosmic-ray spectrum . . . . . 4
  - 1.2.3 The origin of Galactic cosmic rays . . . . . 6
  - 1.2.4 Reaching the knee . . . . . 8
- 1.3 The goal of this work . . . . . 9

**2 Basics of Magnetohydrodynamic Theory** **11**
- 2.1 Incompressible MHD equations . . . . . 12
- 2.2 Conserved quantities in ideal MHD . . . . . 15
- 2.3 Alfvén waves . . . . . 16
  - 2.3.1 Shear-Alfvén waves . . . . . 18
  - 2.3.2 Slow magnetosonic waves . . . . . 20
  - 2.3.3 Fast magnetosonic waves . . . . . 20
- 2.4 Elsasser formalism . . . . . 21
- 2.5 Theories of MHD energy spectra . . . . . 23
  - 2.5.1 Kolmogorov's scaling-invariance hypothesis . . . . . 23
  - 2.5.2 Kraichnan's scaling law . . . . . 26
  - 2.5.3 Goldreich-Sridhar theory of MHD turbulence . . . . . 27

**3 Quasilinear Theory of Velocity-Space Diffusion** **31**
- 3.1 Introduction to quasilinear theory . . . . . 32
- 3.2 Derivation of the velocity-space diffusion equation . . . . . 32
  - 3.2.1 The space-averaged Vlasov equation . . . . . 32
  - 3.2.2 Evolution of the Fourier components $\delta f$ . . . . . 34
  - 3.2.3 Evolution of the space-average $\overline{f}$ . . . . . 38
  - 3.2.4 The velocity-space diffusion equation . . . . . 40

3.3 Alfvénic turbulence models . . . . . . . . . . . . . . . . . . . . . . . . . . . 41
    3.3.1 Momentum diffusion in evolving Alfvénic turbulence . . . . . . 41
    3.3.2 The stochastic heating rate . . . . . . . . . . . . . . . . . . . . . . . 43
    3.3.3 The magnetostatic limit . . . . . . . . . . . . . . . . . . . . . . . . 46
    3.3.4 Magnetodynamic turbulence . . . . . . . . . . . . . . . . . . . . . 47

**4 Controlling Helicities in Pseudospectral MHD Simulations 51**
4.1 Numerical methods . . . . . . . . . . . . . . . . . . . . . . . . . . . . . . 52
    4.1.1 Outline of MHD equations in Turbo . . . . . . . . . . . . . . . . 52
    4.1.2 Updating the MHD fields . . . . . . . . . . . . . . . . . . . . . . . 53
    4.1.3 The cross-helical forcing scheme in detail . . . . . . . . . . . . 54
4.2 Isotropic cross-helical turbulence . . . . . . . . . . . . . . . . . . . . . . 56
    4.2.1 Initial parameters . . . . . . . . . . . . . . . . . . . . . . . . . . . . 56
    4.2.2 Reaching a steady-state configuration . . . . . . . . . . . . . . . 57
    4.2.3 Cross-helicity evolution . . . . . . . . . . . . . . . . . . . . . . . . 60
    4.2.4 Spectral analysis of the turbulent steady-states . . . . . . . . . 62
4.3 Cross-helical turbulence with order-unity mean-field . . . . . . . . . . 65
    4.3.1 Breaking the isotropy . . . . . . . . . . . . . . . . . . . . . . . . . . 65
    4.3.2 Spectral analysis . . . . . . . . . . . . . . . . . . . . . . . . . . . . . 65
    4.3.3 A closer look at the real-space field distributions . . . . . . . . 66
4.4 Cross-helical turbulence with strong magnetic mean field . . . . . . . 68
    4.4.1 Anisotropic cross-helical forcing scheme . . . . . . . . . . . . . 68
    4.4.2 Steady-state field analysis . . . . . . . . . . . . . . . . . . . . . . . 71
    4.4.3 Dispersion analysis of balanced and imbalanced turbulence . . . 72

**5 Stochastic Heating in Cross-Helical Turbulence 75**
5.1 Motivation . . . . . . . . . . . . . . . . . . . . . . . . . . . . . . . . . . . 76
5.2 Test-particle method . . . . . . . . . . . . . . . . . . . . . . . . . . . . . 77
5.3 Inclusion of Ohmic fields . . . . . . . . . . . . . . . . . . . . . . . . . . . 79
5.4 Stochastic heating in isotropic turbulence . . . . . . . . . . . . . . . . . 82
    5.4.1 Sample trajectories . . . . . . . . . . . . . . . . . . . . . . . . . . . 82
    5.4.2 Influence of cross helicity . . . . . . . . . . . . . . . . . . . . . . . 84
    5.4.3 Comparison with quasilinear predictions . . . . . . . . . . . . . 84
    5.4.4 Two-stage acceleration in static and evolving turbulence . . . . . 88
5.5 Stochastic heating in trans-Alfvénic turbulence . . . . . . . . . . . . . 90

**6 Pitch-Angle Scattering in Cross-Helical Turbulence 93**
6.1 Motivation . . . . . . . . . . . . . . . . . . . . . . . . . . . . . . . . . . . 94
6.2 Simulation parameters . . . . . . . . . . . . . . . . . . . . . . . . . . . . 95
    6.2.1 Ideal MHD . . . . . . . . . . . . . . . . . . . . . . . . . . . . . . . . 95
    6.2.2 Sub-Alfvénic turbulence . . . . . . . . . . . . . . . . . . . . . . . . 95
    6.2.3 Alfvénic test-particles . . . . . . . . . . . . . . . . . . . . . . . . . 97
    6.2.4 The pitch-angle scattering rate $\Delta_{\mu\mu}$ . . . . . . . . . . . . . . . . . 98

6.3 Dynamic turbulence . . . . . . . . . . . . . . . . . . . . . . . . . . . . . . 100
6.3.1 The magnetic moment in electrodynamic MHD . . . . . . . . . . 100
6.3.2 Results for fully electrodynamic turbulence . . . . . . . . . . . . 102
6.3.3 Results for magnetodynamic turbulence . . . . . . . . . . . . . . 105
6.4 Static turbulence . . . . . . . . . . . . . . . . . . . . . . . . . . . . . . . . 108
6.4.1 Magnetostatic turbulence . . . . . . . . . . . . . . . . . . . . . . . . 108
6.4.2 Static electromagnetic turbulence . . . . . . . . . . . . . . . . . . . 111

**7 Summary** **113**
7.1 Cross-helical forcing of incompressible turbulence . . . . . . . . . . . 113
7.2 Heating mechanisms in cross-helical turbulence . . . . . . . . . . . . . . 114
7.3 Pitch-angle scattering in imbalanced and magnetodynamic turbulence . 115
7.4 Concluding remarks . . . . . . . . . . . . . . . . . . . . . . . . . . . . . . 116

**A The Operator $\hat{P}(\mathbf{k})$** **117**

**Bibliography** **127**

**Danksagung** **128**

# Zusammenfassung

Turbulenz ist in astrophysikalischen Plasmen allgegenwärtig. Viele solche Systeme weisen eine sogenannte Kreuz-Helizität auf, also eine von Null verschiedene Korrelation zwischen Geschwindigkeits- und Magnetfeld-Fluktuationen. In einer anisotropen Magnetfeldgeometrie, z. B. im Sonnenwind oder dem interstellaren Medium, deutet die Kreuz-Helizität auf ein Ungleichgewicht zwischen Alfvén-Wellen, die sich in Richtung des gemittelten Feldes ausbreiten, und solchen, die in die Gegenrichtung propagieren, hin. Obwohl dieses Ungleichgewicht die stochastische Beschleunigung und Streuung, die geladene Teilchen in einem Plasma erfahren, dramatisch beeinflusst, wurde es in bisherigen numerischen Studien über turbulenten Teilchentransport gemeinhin außer Acht gelassen.

In dieser Arbeit nun werden rechnergestützte Simulationen von magnetohydrodynamischer Turbulenz präsentiert, in denen die Energie und die Kreuz-Helizität kontrolliert werden können, ohne jedoch kinetische oder magnetische Helizität als unerwünschte Nebenwirkung zu erzeugen. Die Stärke des mittleren Magnetfeldes bestimmt dabei die Anisotropie des Gleichgewichtszustandes. Die Simulationen erfüllen in allen Parameterbereichen die Vorhersagen, die theoretische Modelle für realistische Plasmaturbulenz treffen.

Die Diffusion kosmischer Strahlung in turbulenten Plasmen wird häufig im Rahmen der quasilinearen Theorie unter Heranziehung eines stark vereinfachten Turbulenzspektrums berechnet. Indem die Trajektorien von Testteilchen in dynamischen Turbulenzsimulationen mit Kreuz-Helizität berechnet werden, lassen sich quasilineare Ergebnisse für die Beschleunigungsrate geladener Teilchen nachprüfen. Theorie und numerische Simulation stimmen für Teilchen mit der Alfvén-Geschwindigkeit gut überein, solange resistive Effekte vernachlässigt werden können.

Weiterhin werden aus der quasilinearen Theorie berechnete Diffusionskoeffizienten mit numerisch ermittelten Streuraten für Testteilchen nach einer Gyroperiode in stark anisotropen Feldkonfigurationen verglichen, wobei der Schwerpunkt erneut beim Einfluss der Kreuz-Helizität liegt. Für alle verwendeten Werte der Kreuz-Helizität ergibt sich eine exzellente Übereinstimmung zwischen Simulationsergebnis und Vorhersage. Schließlich wird die Rolle des magnetischen Moments, einer adiabatischen Invarianten bei der Bewegung geladener Teilchen in einem Magnetfeld, für die Streuung über Zeitskalen von mehreren Gyroperioden erläutert.

# Abstract

Turbulence is a ubiquitous phenomenon in astrophysical plasmas. Most of these systems exhibit a property called cross helicity, a non-zero correlation between velocity fluctuations and magnetic-field fluctuations. In the presence of a magnetic mean-field, such as in the solar wind or in the interstellar medium, cross helicity is equivalent to an imbalance between Alfvén waves co- and counter-propagating with respect to the mean-field direction. Although this imbalance can have a dramatic influence on the heating and scattering rate of charged particles which propagate through the plasma, it is often neglected in computational studies of turbulent particle transport.

In an effort to remedy this situation, we present numerical simulations of magnetohydrodynamic turbulence in which we can control the energy and the cross helicity of the system, without injecting kinetic or magnetic helicity as an unwanted side effect. Varying the strength of a magnetic guide-field allows us to determine the degree of anisotropy that the system assumes as a steady-state configuration. Detailed analysis proves that these simulations conform to theoretical models of realistic turbulence.

The diffusion of cosmic-ray particles in turbulent plasmas is often calculated using quasilinear theory and a simplified description of the electromagnetic-field spectra. By computing the trajectories of test-particles in dynamically evolving turbulence simulations with non-zero cross helicity, we study whether such quasilinear predictions of the heating rate of charged particles are valid under realistic conditions. Theory and numerical results agree well for particles propagating at the Alfvén velocity, unless resistive effects play a dominant role.

Furthermore, strongly anisotropic field configurations are used to compare quasilinear pitch-angle diffusion coefficients with measurements of test-particle scattering after one gyroperiod. In particular, we focus on the scaling of the scattering rate with cross helicity. We observe excellent agreement in simulations of both balanced and imbalanced turbulence and explain the role of the magnetic moment, an approximate invariant of charged-particle motion, for pitch-angle scattering on timescales of several gyroperiods.

# Chapter 1

# Cosmic Rays in the Universe

> *Quantum vero ad ipsius stellae naturam attinet, quoniam ab initio, Iovis amicum lumen aemulabatur, idcirco in initio etiam suorum effectuum, laeta et prospera omnia spondere videtur, …pacemque concordiam. At quoniam, in medio, in rutilantem Martis feruorem degeneravit, …subsecuturas ingentes clades et calamitates, quales Martis virulentum sidus, mundo peculiariter influit, ut sunt bella, seditiones, captivitates et mortes principum, regnorum et urbium depopulationes, …In aere vero siccitates, flagrantes aestus, metheora ignita, atque hinc morbi pestiferi, et anhelanti veneno serpentes, atque his similia. In fine vero, ex Saturnia natura, et lucida albedine, portendit angustias, maerores, mortes, carceres, omniaque inauspicata et funesta.* [a]
>
> – *De nova et nullius aevi memoriae prius visa stella*
> (Tycho Brahe, 1573)
>
> ---
>
> [a] But regarding that star [Tycho's supernova], because at first it resembled the friendly light of Jupiter, it initially seemed to promise wealth and prosperity, …peace and harmony. Yet because it then developed the intense glow of Mars, …it fills, just like the poisonous star of Mars, the world with great calamity and wars, conflict, captivity, and the death of princes, kings, and entire cities …The air will be filled with droughts, flaming heat, burning meteors, and pestilence and venomous snakes and the like. In the end, however, it announces with its bright white color, similar to Saturn, poverty, sadness, death, incarceration, and all kinds of misfortune and decay.

## 1.1 Plasmas in astrophysics

Exhibiting a certain lack of modesty, plasma physicists often claim that 99.9 % of the matter in the universe is in the plasma state: Stars are not so much hot gas balls, as they are commonly described, but rather hot plasma balls, since their temperature is sufficiently high that all hydrogen is ionized into a mixture of protons and electrons.

In the interstellar medium (ISM) of our milky way, about one in five hydrogen atoms in the $7 \times 10^9$ solar masses of gas and dust between the stars is ionized (Draine, 2011).

As cosmologists will quickly point out, the 99.9 %-figure omits a fairly large part of the universe: Our Galaxy contains more dark matter than baryonic matter by far (summing up to $2 \times 10^{11}$ solar masses within the innermost 25 kiloparsecs, according to Kafle *et al.* (2012)), and, for the entire universe, recent observations of the cosmic microwave background by the Planck Collaboration imply that baryons amount to only 15 % of the total matter content (Planck Collaboration *et al.* , 2014). Nevertheless, the notion that a thorough understanding of the physics of plasmas is necessary in order to understand the universe loses none of its validity.

Most of the plasma is magnetized: The median of the magnetic field strength in the local ISM is estimated at around $B_{\mathrm{ISM}} \approx 6\ \mu\mathrm{G}$ (Heiles & Crutcher, 2005). Its energy density is therefore comparable to the mean thermal pressure of the interstellar plasma ($p_{\mathrm{ISM}} \approx 0.5\mathrm{eV\ cm}^{-3}$), a fact which can be expressed in terms of a 'plasma beta', $\beta = p_{\mathrm{ISM}}/[B_{\mathrm{ISM}}^2/(2\mu_0)] \sim 0.6$. Compared to typical plasmas in magnetic-confinement fusion experiments with $\beta \sim 0.05$, the interstellar magnetic field is relatively weak, almost in equipartition with the kinetic energy density!

Neither the magnetic field nor the bulk flow of the interstellar plasma are very well-ordered. Instead, both are highly turbulent, being continuously stirred by cosmic-ray winds which escape the remnants of supernovae. The energy density of these winds is, again, in rough equipartition with the magnetic fields. Of course, this equipartition is no coincidence but the result of a complicated series of feedback processes connecting all the constituents of the ISM with each other: As high-energy cosmic-ray particles diffuse across the magnetic fields, they induce turbulent motion in the bulk of the plasma, which in turn amplifies the magnetic fields. An overview of this subject can be found in Elmegreen & Scalo (2004), although the finer details of these processes are still not fully known since the complex interplay of magnetic fields, turbulence, and high-energy cosmic-ray physics represents a daunting problem for modern-day astrophysics.

The work presented in this thesis strives to further our understanding of some of these processes. As we will see, turbulence in different astrophysical plasmas is driven in different ways, but all of these stirring mechanisms lead to an asymmetry with respect to the direction of the mean magnetic field averaged over scales comparable to the system size. Since more waves propagate away from the sources providing the energy for the turbulent fluctuations than towards them, some fundamental properties of the plasma are changed compared to the symmetric or balanced case. The main goal of this thesis is to point out how these changes affect the propagation of charged particles in the plasma, such as the cosmic-ray particles mentioned above, and to demonstrate this in numerical simulations. After a realistic model of magnetohydrodynamic turbulence has been driven into states of balance or imbalance, test-particle trajectories computed concurrently with the continuously evolving turbulence are compared. We will see that the diffusion of particles in velocity-space varies significantly if the im-

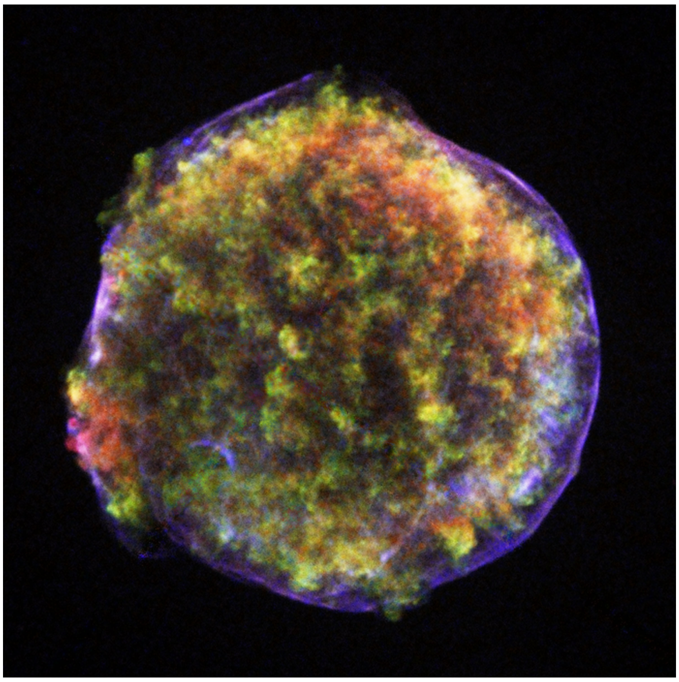

Figure 1.1: X-ray image of Tycho's supernova remnant, with pseudocolors representing 0.95–1.26 keV (red), 1.63–2.26 keV (green), and 4.1–6.1 GeV (blue). Credit: NASA/CXC/Rutgers/J.Warren & J.Hughes et al.

balanced cases are considered. Before we provide a technical discussion of how we create this imbalance in our simulations, however, a short overview of the mechanisms responsible for the asymmetry in real astrophysical plasmas is in order.

## 1.2 Astrophysical background

### 1.2.1 Supernovae

Once a star has converted almost all of its hydrogen content into radiation energy via nuclear fusion, it undergoes a dramatic evolution (*e.g.* Longair, 2011). For our Sun, this process will take $10^{10}$ years in total, about half of which have already passed. If the inert helium core generated in the course of hydrogen fusion takes up more than 10 % of the star mass, the outward radiation pressure can no longer balance self-gravitation and the core begins to contract while hydrogen fusion continues in a shell around the core. The envelope of the star expands while it turns into a red giant.

As the helium core heats up, its temperature becomes so high that helium fusion sets in and carbon and oxygen are produced. In stars with less than eight solar masses, temperatures that would allow the fusion of carbon or oxygen are never reached, since the electron degeneracy pressure prevents further contraction of the C-O core. A white dwarf is born and gradually gives off the thermal energy stored in its constituents in the form of radiation.

For an isolated white dwarf, this is the end of the story. A white dwarf that is part of a binary system, however, may accrete matter in the form of stellar winds emitted by its stellar companion. If this accretion suffices to push the total mass of the white dwarf above the Chandrasekhar limit of 1.4 solar masses, the self-gravitation is able to overcome the degeneracy pressure and the core of the dwarf contracts again. The temperature can then rise sufficiently (to about $10^9$ Kelvins) that carbon fusion commences. As the entire C-O core of the dwarf undergoes fusion in the course of a few seconds, it releases enough energy that the outer layers of the white dwarf are rapidly shed in an enormous supernova explosion. In total, the kinetic energy of such a Type Ia supernova amounts to the order of $10^{44}$ Joules.[1] The remnant of one of these massive explosions, observed almost five centuries after its explosion was reported by Tycho Brahe, is shown in figure 1.1.

Other evolutionary paths are possible for stars with heavier masses. A Type II supernova explosion, for example, occurs if the core of an extremely massive star ($M > 9M_\odot$) continues to fuse carbon, neon, oxygen, and silicon, until eventually an iron core is formed. During all of these stages, the loss of energy to neutrinos emitted in fusion processes accelerates more and more rapidly, so that the iron core finally collapses into a neutron star within a matter of seconds because of the decreasing pressure. Part of the energy released in this process (about $10^{44}$ Joules, again) accelerates the outer layers of the star outwards and thus leads to a Type II core-collapse supernova explosion.

While the type of a supernova observed today can be determined easily by analyzing the emitted spectrum, the categorization of historical supernovae is difficult. It usually relies on descriptions of the evolution of the light curve, such as the one cited at the beginning of this chapter,[2] with one notable exception: Krause *et al.* (2008) showed that the spectroscopic signature of the light echo of Tycho's supernova (SN 1572) matches the spectrum typically observed for a Type Ia supernova.

Because of their enormous energy, supernovae and their remnants are widely believed to be the source of galactic cosmic-ray particles of up to $10^{15}$ eV, about one hundred times the center-of-mass energy to which protons at the Large Hadron Collider at CERN are accelerated. Discovered by Victor Hess in August 1912 when he took a gold-leaf electroscope on several hot balloon rides (Hess, 1912), cosmic radiation (CR) remains one of the most elusive problems of astrophysics more than a century later.

### 1.2.2 The cosmic-ray spectrum

Modern-day measurements of the CR energy spectrum are obtained from calorimeters and magnetic spectrometers mounted on satellites or balloons, or from ground-based detectors which register the Cherenkov radiation produced when high-energy parti-

---

[1] Hence high-energy astrophysicists occasionally use the unit 'f.o.e.', or ten to the fifty-one ergs (the equivalent of $10^{44}$ Joules in cgs units) to describe the energy output of a supernova.

[2] To be fair, a large part of Tycho Brahe's report is significantly more quantitative and scientific than the cited excerpt.

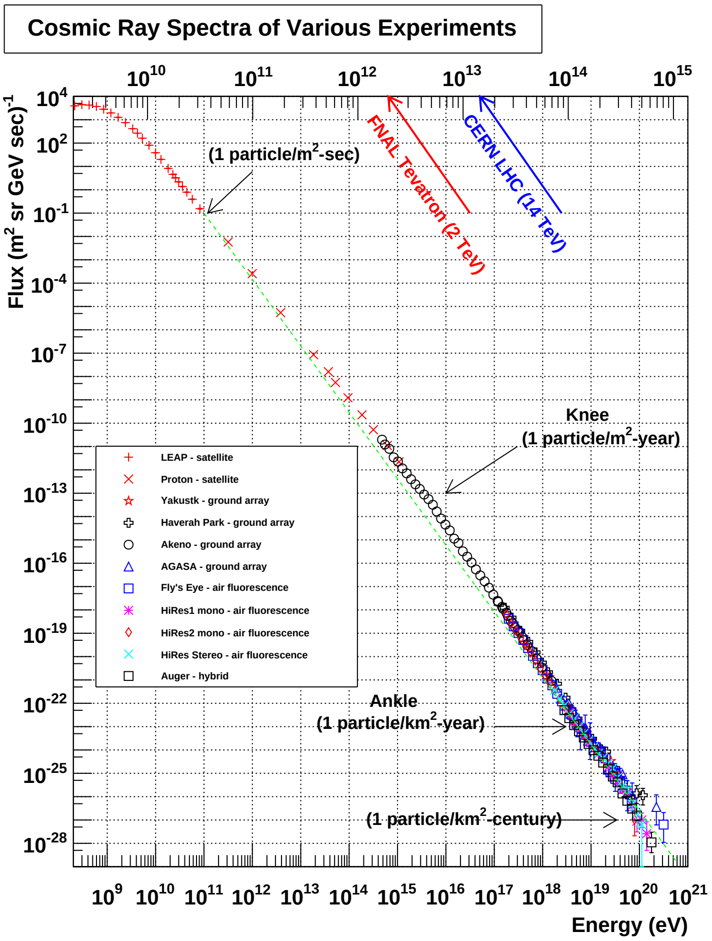

Figure 1.2: The cosmic-ray primary energy spectrum (lower abscissa) including the ‘cosmic-ray knee’ (the spectral break at about $10^{15.5}$ eV) and the ‘ankle’ ($10^{18.5}$ eV). On the upper abscissa, the center-of-mass energy of protons achieved at Fermilab’s Tevatron and CERN’s LHC is compared to the equivalent lab-frame energy for CR protons (lower abscissa). Credit: William Hanlon. Used with permission

cles hit the upper layers of our atmosphere (Stanev, 2011). The spectrum is depicted in figure 1.2 and exhibits several interesting features: While the CR flux scales as $E^{-2.7}$ in the interval from about 10 GeV to several PeV, after this so-called ‘cosmic-ray knee’ (at $\sim 10^{15.5}$ eV) the spectrum then steepens to about $E^{-3.0}$ for approximately three decades. It appears to flatten for about another decade up to about 30 EeV, only to drop off quickly afterwards.

This rapid flux decrease at $10^{19.5}$ eV was first explained by Greisen (1966) and Zatsepin & Kuz’min (1966) as a result of the strong blueshift of the cosmic microwave background (CMB) in the frame of high-energy protons. If the energy of the blueshifted CMB photon is about 340 MeV (for a proton energy of $\sim 10^{20}$ eV), the cross-section of the $\Delta^+$ resonance reaches its maximum of 0.5 millibarn or $5 \times 10^{35}$ cm$^2$:

$$\begin{aligned} p+\gamma &\longrightarrow \Delta^+ \longrightarrow & p+\pi^0, \\ p+\gamma &\longrightarrow \Delta^+ \longrightarrow & n+\pi. \end{aligned}$$

This resonance produces a pion and reduces the proton energy by about 20 %. Since the energy loss distance for this and other photoproduction processes is only about 13 megaparsecs, GZK predicted that no proton above this threshold energy of $10^{20}$ eV should be ever observed farther than about 50 megaparsecs from its origin. Indeed, this GZK suppression is clearly visible in figure 1.2, as both of the two large air shower detectors (HiRES and the Pierre Auger Observatory) have detected a sharp steepening of the spectrum above $5 \times 10^{19}$ eV (Berezinsky, 2013).

The other major feature of the CR spectrum, the knee at about $3 \times 10^{15}$ eV, is generally believed to mark the transition from CR particles originating within our Galaxy to particles with an extragalactic source. As mentioned earlier, the former part of the CR population is presumably accelerated in supernova remnants (SNR), as $\gamma$-radiation emitted, for instance, by the supernova remnant RX J1713.7-3946 indicates the presence of ultrarelativistic particles with an energy of at least 100 TeV (HESS Collaboration *et al.* , 2004).

### 1.2.3 The origin of Galactic cosmic rays

It was Fermi (1949) who first proposed that CR particles can be stochastically accelerated when they are scattered off irregularities in the Galactic magnetic field. If the scatter events are considered as elastic collisions, CR particles gain energy in the observer's frame if the collision is head-on. Fermi's original suggestion was that the magnetic turbulence in molecular clouds would be sufficient to result in the observed CR spectrum. While this hypothesis satisfactorily explained why the spectrum exhibits a power-law (but not the spectral exponent), the energy gain would be too slow if the magnetic mirrors that serve as scattering sites were moving isotropically in the galaxy as they do in molecular clouds: The acceleration rate only scales as $(V/c)^2$, where $V$ is the velocity of the magnetic mirror, whence this theory has become widely known as second-order Fermi acceleration.

A dramatic improvement in the efficiency of the acceleration occurs if the scattering sites are moving predominantly opposite to the CR particle, such that head-on collisions become more probable. In this scenario Fermi acceleration is akin to a particle bouncing back and forth between two solid walls moving towards each other, and the rate of energy gain becomes linearly proportional to $(V/c)$. Situations favoring this first-order Fermi acceleration process are common in the vicinity of traveling shock fronts: In their rest frame, the interstellar gas both upstream and downstream of the shock is flowing towards the shock front (Bell, 1978). High-energy particles escaping the downstream region of the shocks around expanding SNRs can thus undergo diffusive shock acceleration (DSA), as some of them are reflected back by the upstream

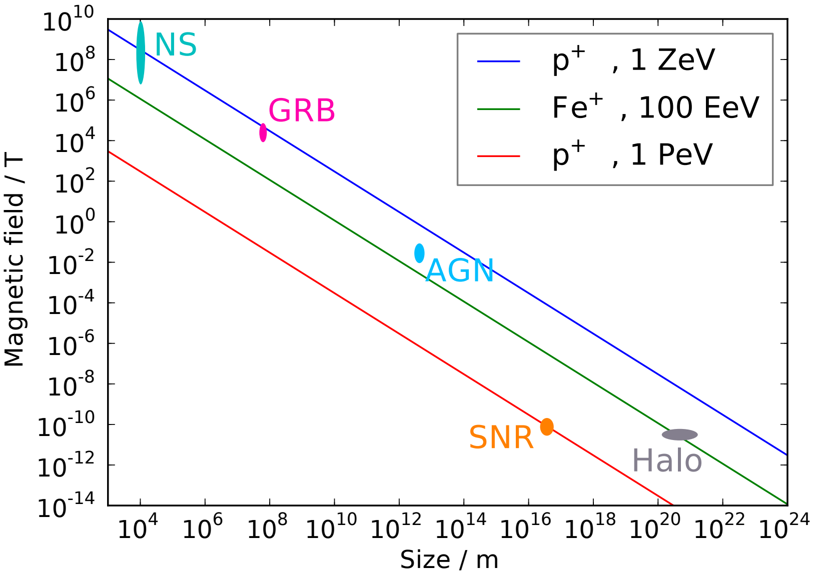

Figure 1.3: Hillas plot for protons and iron nuclei at various energies, including the location on the plot of supernova remnants, the Galactic Halo, active galactic nuclei, gamma-ray bursts, and neutron stars. After Hillas (1984)

turbulence only to be reflected again in the downstream region. Assuming the particles are isotropized stochastically on both sides of the shock front and have a small but non-zero chance of escaping towards the upstream without being reflected, one finds that the energy spectrum of the escaping CR particles follows a power-law $E^{-2}$ (Longair, 2011). The remaining difference to the observed exponent $-2.7$ is likely due to the spatial diffusion through the ISM until a cosmic-ray particle can be detected on Earth (Schlickeiser, 2002).

That supernovae are almost the only known candidates for accelerating protons to PeV energies within the Galaxy can be deduced from the following considerations: If a particle with charge $Ze$ and mass $m$ is to be accelerated to an energy $E$ within any astrophysical object by DSA, the size $L$ of that object should be large enough to contain the gyroradius of the particle at that energy, $r_g \sim (E/c)/(ZeB)$. Here $B$ is the typical magnetic field strength that can be expected at the acceleration site. Rephrasing that statement as a condition for the properties of the candidate object, $B$ and $L$, we obtain

$$BL > \frac{E}{Zec}.$$

Drawing several objects from high-energy astrophysics into a $L-B$ diagram, as first done by Hillas (1984), one can easily rule out objects which lie below the line $(E/Zec)/L$ for a given particle type and energy (figure 1.3). While protons cannot be accelerated to energies above the knee in SNRs, knee-energies are just attainable according to this criterion.

### 1.2.4 Reaching the knee

A more stringent limit was posited by Lagage & Cesarsky (1983), who noted that the most efficient part of the DSA process only lasts about 1000 years. After this time span, the mass swept up by the shock becomes comparable to the mass originally ejected by the supernova, and the shock front decelerates as it enters the blast-wave or Sedov-Taylor (ST) stage of its evolution (Taylor, 1950; Sedov, 1958). Tycho's SNR is presumably undergoing this transition currently (Morlino & Caprioli, 2012). If one assumes that the magnetic field upstream of the shock is comparable to the background field in the ISM ($\sim \mu$G), the maximum energy which a CR proton can gain before the acceleration efficiency decreases in the ST stage is limited to about $10^{14}$ eV using otherwise optimistic assumptions. In more realistic calculations, this estimate is decreased even further by another order of magnitude (Lagage & Cesarsky, 1983).

The conclusion one can draw from this LG limit is that either SNRs are, in fact, not the sites of CR acceleration up to the knee, or that the upstream magnetic field strength is higher than in the ISM. X-ray measurements of Tycho's SNR, for example, show that just downstream of the shock the magnetic field can reach several hundred microgauss (Völk *et al.* , 2005), which would translate to an upstream field at least ten times stronger than the ISM background field (shock compression amplifies the magnetic field by about 3.3 as it passes to the downstream region (Morlino & Caprioli, 2012)). Since the energy distribution in a SNR shock front is far from thermodynamic equilibrium, there are several instabilities that possibly could be responsible for the excess intensity of the upstream field:

- **Bell's non-resonant hybrid instability:** The current of escaping CR particles far upstream of the shock front induces a return current in the ISM plasma, which is able to strongly amplify the background magnetic field (Bell, 2004). This mechanism initially leads to significantly faster growth than other instabilities. It is still unclear whether the excited wavelengths are large enough to scatter high-energy CR particles sufficiently fast that efficient DSA is possible, but in the analytically tractable linear phase of the instability this is definitely not the case.

- **Drury's pressure-gradient instability:** Small inhomogeneities in the background plasma density are amplified when the shock front approaches. Since the number density of CR particles immediately upstream of the shock is larger than at a greater distance due to the CR confinement, a gradient in the CR pressure perpendicular to the shock front exists which can cause a quick growth of the inhomogeneities, amplifying the magnetic field even more strongly (Drury & Falle, 1986).

- **Cosmic-ray streaming instability:** The scattering of a beam of super-Alfvénic CR particles streaming along a magnetic mean-field in a plasma induces the growth of shear-Alfvén waves propagating in the streaming direction, while the CRs are decelerated to about the Alfvén velocity (Kulsrud & Pearce, 1969; Skilling,

> 1975). (A detailed description of shear-Alfvén waves can be found in chapter 2.) However, this **resonant Alfvén instability**, as it is also called, saturates already at low turbulence amplitudes.

It is still subject of active debate whether the magnetic field amplification (MFA) provided by each process (or, even more likely, a combination of all three processes) is sufficient to explain the acceleration of protons up to the PeV region of the CR spectrum. This is due to the strongly nonlinear nature of the problem: Escaping CR particles drive the instabilities and cause magnetic field growth, which in turn scatters the CR particles faster, decreases their upstream density, and thus reduces the growth rate of the instability. A stronger scattering, however, means that CR particles are accelerated more efficiently since the time between two 'bounces' in the DSA process is shortened, and might potentially favor the MFA process again. Moreover, the length scales involved span a wide range, from the width of the shock front (about 0.1 parsecs) to the gyroradius of the particles undergoing DSA (roughly $10^{10}$ meters). It is not even certain how the DSA process is initiated, since a highly superthermal CR population is required so that it can create the MFA needed to scatter and confine it, posing the so-called 'injection problem' (Longair, 2011).

## 1.3 The goal of this work

An investigation of how charged particles are heated and scattered in turbulent plasmas can therefore not provide a final answer to this difficult problem, but it can add pieces to the puzzle, which may allow us to get closer to the full picture. The cosmic-ray streaming instability leads to a particularly interesting turbulence configuration, in which more waves propagate parallel to the escaping CR current than opposite to it (*e.g.* Schlickeiser & Shalchi, 2008), while a significant portion of the CR population is decelerated to the Alfvén velocity. The same effect also occurs in the solar wind, where waves predominantly travel outwards if one is close to the Sun, but reach a balance between outward and inward propagation at greater distances (Marsch & Tu, 1990). The question of how this balance or imbalance affects the transport of charged particles is the central theme of this work.

A basic outline of the more technical aspects of magnetohydrodynamics, given in chapter 2, will lay the groundwork for understanding the simulations we present. Chapter 3 contains a derivation of the theoretically expected heating and scattering rates in imbalanced turbulence. In chapter 4, we explain the numerical methods we employ and provide a careful analysis of imbalanced-turbulence simulations. These electromagnetic-field configurations are then used in chapter 5 to investigate the propagation and heating of charged particles in imbalanced turbulence and to compare our numerical results for different parameters with the theoretical predictions derived in chapter 3. The scattering of charged particles in the same turbulent fields will be the focus of chapter 6, and a detailed comparison with the analytical results will be performed again. A final summary of our result can be found in chapter 7, where we discuss how the work presented here may be continued in the future.

# Chapter 2

# Basics of Magnetohydrodynamic Theory

> *Si hubiera estado presente en la Creación, habría dado algunas indicaciones útiles para el mejor ordenamiento del Universo.* [a]
>
> – Attributed to Alfonso X El Astrólogo (1221–1284)

---

[a] If I had been there during the Creation, I could have given some useful advice for a better ordering of the Universe.

## Chapter Summary

- The behavior of shear fluctuations in plasmas on large scales, both in time and space, is well described by incompressible magnetohydrodynamics.
- Without dissipation or external forcing, magnetohydrodynamics conserves not only energy but also cross helicity, *i.e.* the correlation of fluctuations of the bulk velocity and of the magnetic field.
- Incompressible plasmas in a strong magnetic field allow the propagation of shear-Alfvén waves both along and opposite to the field.
- Cross helicity measures the dominance of one Alfvén-wave population over the other.
- The spectrum of turbulent fluctuations can be shown to follow a power-law in hydrodynamics and - with some modifications - in magnetohydrodynamics.

In this chapter we will present the basic equations of incompressible magnetohydrodynamics as we will use them throughout the remainder of this work.

## 2.1 Incompressible MHD equations

Magnetohydrodynamic theory (MHD) describes a plasma as a quasi-neutral fluid composed of only one particle species, without accounting separately for electrons and ions. ‘Quasi-neutral’ in this context implies that, at least on the length scales of interest, the number densities of electrons and ions ($n_e$ and $n_i$) are approximately equal everywhere in the system. This assumption entails that the MHD description of a plasma is limited to fluctuations with wavelengths significantly larger than the Debye length $\lambda_D = (\epsilon_0 T/e^2 n_e)^{1/2}$ or the mean-free path $\lambda_{\mathrm{mfp}}$ of both ions and electrons.

The quasi-neutrality condition allows us to introduce a single mass density distribution $\rho(\mathbf{x}, t) = m_i n_i$ since the electron mass $m_e$ is negligible compared to the ion mass $m_i$. Throughout this thesis, the coordinates in space and time are denoted by $\mathbf{x}$ and $t$, respectively. We assume that no particle sources exist. Then the conservation of mass implies that the change of mass in a volume element $V$ must be matched by the mass flow through the surface of the volume $S$, or

$$\partial_t \int_V \rho \, d^3x + \int_S (\rho \mathbf{u}) \cdot d^2\mathbf{S} = 0. \tag{2.1}$$

where $\mathbf{u}(\mathbf{x}, t)$ is the bulk velocity of the plasma. Replacing the surface integral by a volume integral over the divergence of $\rho\mathbf{u}$, we obtain the continuity equation known from Eulerian hydrodynamics:

$$\partial_t \rho + (\mathbf{u} \cdot \nabla)\rho + \rho(\nabla \cdot \mathbf{u}) = 0. \tag{2.2}$$

In an incompressible medium, the mass density is uniformly constant in time and space, hence the application of the chain rule yields

$$\frac{d}{dt}\rho(\mathbf{x}, t) = \partial_t \rho(\mathbf{x}, t) + (\mathbf{u} \cdot \nabla)\rho(\mathbf{x}, t) \equiv 0, \tag{2.3}$$

We can compare this condition with equation (2.2) to find that any incompressible medium can be characterized as having zero divergence of the velocity field, $\nabla \cdot \mathbf{u} \equiv 0$. The symmetry of this condition with the similar condition on the magnetic field ($\nabla \cdot \mathbf{B} \equiv 0$) is one of the main reasons that studying turbulence in incompressible media is so convenient.

Likewise, the momentum equation is entirely analogous to the momentum equation of hydrodynamics,

$$\frac{d}{dt}(\rho \mathbf{u}) = \mathbf{f} - \nabla p + \nu \nabla^2 \mathbf{u}, \tag{2.4}$$

where $\mathbf{f}$ is the density of forces acting on the medium and $p$ is the thermal pressure, while $\nu$ is the kinematic viscosity responsible for dissipation. In magnetohydrodynamics, the forcing density is given by the Lorentz force $\mathbf{j} \times \mathbf{B}$ if no external driving is applied, where $\mathbf{j}$ is the density of the electrical current and $\mathbf{B}$ is the magnetic field.

Assuming an incompressible plasma ($d\rho/dt \equiv 0$) again, we obtain:

$$\rho\left[\partial_t \mathbf{u} + (\mathbf{u}\cdot\nabla)\,\mathbf{u}\right] = \mathbf{j}\times\mathbf{B} - \nabla p - \nu\nabla^2\mathbf{u}. \tag{2.5}$$

The magnetic field $\mathbf{B}$ must, of course, be divergence-free according to Maxwell's laws,

$$\nabla\cdot\mathbf{B} \equiv 0, \tag{2.6}$$

and is otherwise determined from initial conditions and then evolves as expressed by Faraday's law:

$$\partial_t \mathbf{B} = -\nabla\times\mathbf{E}, \tag{2.7}$$

with $\mathbf{E}$ denoting the electric field as derived from a generalized Ohm's law. Several forms of this law exist for more complex fluid models than simple MHD (see Goedbloed & Poedts, 2004), treating ions and electrons separately in order to describe wave modes which are not included in standard magnetohydrodynamics (*e.g.* Cramer, 2001; Goedbloed & Poedts, 2004; Freidberg, 2014). One of these forms, which allows us to detail the approximations one has to make in order to arrive at the resistive-MHD model which we will focus on, reads (Belmont *et al.* , 2014):

$$\mathbf{E} = -\mathbf{u}_e\times\mathbf{B} + \eta\mathbf{j} - \frac{1}{n_e e}\left(\rho_e\frac{du_e}{dt} + \nabla\cdot\mathbb{P}_e\right), \tag{2.8}$$

where $n_e$, $\mathbf{u}_e$, and $\mathbb{P}_e$ are the number density, the velocity, and the (possibly anisotropic) pressure tensor of the electron gas, while $\eta$ is the magnetic diffusivity.

The last term on the right-hand side is usually neglected in magnetohydrodynamics, and we can justify this with the following scaling arguments: If we estimate the thermal pressure of the electrons as $p_e \sim n_e m_e u_e^2$, the size of the electron pressure-tensor gradient compares to the $\mathbf{u}_e\times\mathbf{B}$-term as

$$\frac{p_e/(Ln_e e)}{u_e B} \sim \frac{n_e m_e u_e^2}{Ln_e e u_e B} \sim \frac{r_e}{L} \ll 1, \tag{2.9}$$

assuming a typical gradient length-scale $L$ that is much larger than the electron gyroradius $r_e = u_e/\Omega_e$, where $\Omega_e = eB/m_e$ is the electron Larmor frequency in a magnetic field of typical intensity $B$.

We have thus not only assumed that the electron pressure tensor is isotropic. We have completely ignored the dependency of the pressure term on any microscopic event, such as particle collisions, and simply postulated that a Maxwellian equilibrium distribution of the particle velocities is *somehow* achieved. Although this may appear to be a drastic ad-hoc assumption, Freidberg (2014) points out that many results for equilibrium configurations of plasmas are independent of the specific model used for the evolution of the pressure tensor, explaining why MHD is often successful even when these validity conditions are actually violated.

If, on the other hand, the electron velocity changes at a typical plasma oscillation frequency $\omega$ that is much slower than $\Omega_e$, the other term in the parentheses compares to $\mathbf{u}_e \times \mathbf{B}$ as

$$\frac{\rho_e \omega u_e/(n_e e)}{u_e B} \sim \frac{\omega}{\Omega_e} \ll 1, \tag{2.10}$$

A third approximation consists in assuming the electrical current is sufficiently small compared to the ion velocity, $j = en_e|\mathbf{u}_i - \mathbf{u}_e| \ll en_e u_i$, that one can take the electron velocity as equal to the bulk velocity of the ions and let $\mathbf{u}_i \sim \mathbf{u}_e \equiv \mathbf{u}$.

The electric field can then simply be written as

$$\mathbf{E} = -\mathbf{u} \times \mathbf{B} + \eta \mathbf{j} = -\mathbf{u} \times \mathbf{B} + \frac{\eta}{\mu_0} \nabla \times \mathbf{B}, \tag{2.11}$$

where the current density is simply the curl of the magnetic field, $\mathbf{j} = \nabla \times \mathbf{B}/\mu_0$, from Ampère's law. We will refer to the first term on the right-hand side as the motional electric field, and to the second term as the Ohmic electric field. Maxwell's displacement current term, the time derivative of the electric field that also appears in Ampère's law, is neglected since it is only important for relativistic particle velocities, a regime in which standard MHD is no longer applicable. Hence we assume that the plasma bulk speed remains small compared to the speed of light, $u \ll c$.

In summary, the necessary assumptions for the validity of incompressible resistive MHD are:

- that density fluctuations can be neglected compared to the average mass density,
- that the typical length scales of fluctuations in the plasma far exceed the electron gyroradius, the Debye length, and the mean-free path for particle collisions,
- that their time scales are long compared to the electron gyroperiod,
- that the electric current is small so that no distinction between ion and electron velocity need be made,
- that the bulk speed of the plasma is non-relativistic.

As long as all of these approximations are valid, the evolution of the magnetic field can be written as

$$\partial_t \mathbf{B} = \nabla \times (\mathbf{u} \times \mathbf{B} - \eta \mathbf{j}), \tag{2.12}$$

closing the system of equations.

## 2.2 Conserved quantities in ideal MHD

We define the kinetic energy density[1] $\mathcal{E}_{\text{kin}}$ and the magnetic energy density $\mathcal{E}_{\text{mag}}$ as integrals over the entire system volume $V$:

$$\mathcal{E}_{\text{kin}} = \frac{1}{2}\int_V \frac{d^3x}{V}\,\mathbf{u}(\mathbf{x})^2, \tag{2.13}$$

$$\mathcal{E}_{\text{mag}} = \frac{1}{2}\int_V \frac{d^3x}{V\mu_0\rho}\,\mathbf{B}(\mathbf{x})^2. \tag{2.14}$$

After a straightforward calculation using the defining equations of resistive MHD, (2.5) and (2.12), the evolution of both energies can be expressed as follows:

$$\begin{aligned}\frac{d}{dt}\mathcal{E}_{\text{kin}} &= \mathbf{u}\cdot\frac{d}{dt}\int_V \frac{d^3x}{V}\,\mathbf{u}(\mathbf{x}) \\ &= -\nu\int_V \frac{d^3x}{V}\,[\nabla\times\mathbf{u}(\mathbf{x})]^2, \qquad (2.15)\\ \frac{d}{dt}\mathcal{E}_{\text{mag}} &= \mathbf{B}\cdot\frac{d}{dt}\int_V \frac{d^3x}{V\rho\mu_0}\,\mathbf{B}(\mathbf{x}) \\ &= -\eta\int_V \frac{d^3x}{V\rho\mu_0}\,[\nabla\times\mathbf{B}(\mathbf{x})]^2. \qquad (2.16)\end{aligned}$$

In other words, if both dissipative coefficients vanish, $\nu = \eta = 0$, the total energy of the MHD system is conserved. This variant of the MHD equations is usually called ideal magnetohydrodynamics. Only if either coefficient is non-zero or both are, energy is depleted from the system via viscous friction (in case of $\nu > 0$) or Ohmic heating (in case of $\eta > 0$).

These considerations do not apply, of course, if an external forcing mechanism supplies the system with a constant energy input, such as a piston stirring the fluid or irregularly spaced supernova explosions adding turbulent energy to the interstellar medium. In these cases a steady-state on macroscopic scales is still possible if the energy input rate is matched by dissipation on small length scales via either friction or Ohmic heating. As we are about to see later in this chapter, such a steady-state assumption is necessary in order to predict the distribution of turbulent energy between different length scales of the system.

In the absence of external forces and dissipation, however, the total energy is not the only invariant of ideal MHD. It is possible to show that the magnetic helicity,[2] defined as the scalar product of the magnetic vector potential **A** and the magnetic field $\mathbf{B} = \nabla \times \mathbf{A}$,

---

[1] Since we assume an incompressible medium with a constant mass density $\rho$, we leave it out of the definition of the kinetic energy and instead normalize the magnetic energy by $\rho$. Although the term 'energy' is then not completely accurate anymore, referring to a quantity with dimensions of $u^2$, this is a common shorthand in the theory of incompressible turbulence and rarely leads to confusion.

[2] The kinetic helicity, defined as $\mathcal{H}_{\text{kin}} = \int d^3x\,\mathbf{u}\cdot(\nabla\times\mathbf{u})/V$, is only an invariant of ideal hydrodynamics, *i.e.* if the fluid is actually neutral and not only quasi-neutral so that no magnetic field exists.

$$\mathcal{H}_{\mathrm{mag}} = \int_V \frac{d^3x}{V}\, \mathbf{A}(\mathbf{x}) \cdot \mathbf{B}(\mathbf{x}), \tag{2.17}$$

is also conserved as long as one can safely ignore the effects of external forcing or small-scale dissipation. Heuristically speaking, $\mathcal{H}_{\mathrm{mag}}$ shows whether the magnetic field is dominated by right-handed waves[3] (in which case $\mathcal{H}_{\mathrm{mag}} > 0$), left-handed waves ($\mathcal{H}_{\mathrm{mag}} < 0$), or whether both polarizations are equally common ($\mathcal{H}_{\mathrm{mag}} = 0$). Another ideal invariant is the cross helicity, defined as the scalar product of the velocity field and the magnetic field,

$$\mathcal{K} = \int_V \frac{d^3x}{V}\, \mathbf{u}(\mathbf{x}) \cdot \mathbf{B}(\mathbf{x}), \tag{2.18}$$

which measures the winding of the magnetic fieldlines around the velocity fieldlines instead of the vector potential.

Indeed, after taking the time derivatives of the scalar products and inserting the electric field in the Weyl gauge such that $\mathbf{E} = -\partial_t \mathbf{A}$, one obtains for the time evolution of the helicities:

$$\frac{d}{dt}\mathcal{H}_{\mathrm{mag}} = -2 \int_V \frac{d^3x}{V\mu_0}\, \eta \mathbf{j} \cdot \mathbf{B}, \tag{2.19}$$

$$\frac{d}{dt}\mathcal{K} = -\int_V \frac{d^3x}{V\mu_0}\, (\eta + \nu) \sum_{i,j} \mathbf{j} \cdot (\nabla \times \mathbf{u}). \tag{2.20}$$

As explained in the previous chapter, the cross helicity $\mathcal{K}$, or rather the normalized cross helicity $\sigma_c = \mathcal{K}/\mathcal{E}$, can vary dramatically in realistic turbulence settings such as SNR shock fronts or the solar wind, changing the nature of wave-particle interactions in such media. Since we have just shown both $\mathcal{K}$ and $\mathcal{E}$ to be ideally invariant, these variations must be caused by non-ideal processes, such as the excitation of Alfvén waves by cosmic-ray particles (Kulsrud & Pearce, 1969) or energy dissipation due to velocity shear (Roberts *et al.* , 1992). Before we can study wave-particle interactions as a function of cross helicity, we need to understand the connection between Alfvénic turbulence and cross helicity.

## 2.3 Alfvén waves

Now that we have established the basic equations of magnetohydrodynamics, we can proceed with a linear perturbation analysis around the following equilibrium configuration: We assume that not only the mass density $\rho_0$ but also the thermal pressure

---

[3] 'Right-handed', in this case, means that the magnetic fieldlines are winded clockwise around fieldlines of the vector potential, so that the sense of rotation of the magnetic field around **A** is given by the right-hand rule.

$p_0$ is initially constant everywhere, let a constant magnetic field with intensity $B_0$ act along the positive $z$ direction and assume that the equilibrium velocity field vanishes. In this case, we can introduce perturbations of all fields such that

$$\begin{aligned}\mathbf{u}(\mathbf{x}) &= \delta\mathbf{u}(\mathbf{x}),\\ \mathbf{B}(\mathbf{x}) &= B_0\hat{\mathbf{z}} + \delta\mathbf{B}(\mathbf{x}),\\ \mathbf{j}(\mathbf{x}) &= \nabla\times\delta\mathbf{B}(\mathbf{x}),\\ \rho(\mathbf{x}) &= \rho_0 + \delta\rho(\mathbf{x}),\\ p(\mathbf{x}) &= p_0 + \delta p(\mathbf{x}),\end{aligned}$$

where we allow for a deviation from the incompressibility condition in form of a small (first-order) fluctuation in the plasma density $\delta\rho(\mathbf{x})$. The relation between pressure and density for such a small deviation is best described by the adiabatic condition with the adiabatic coefficient $\gamma$,

$$\frac{dp}{d\rho} = \gamma\frac{p}{\rho}. \tag{2.21}$$

Applying this first-order perturbation to the MHD momentum equation, we find

$$\rho_0\partial_t\delta\mathbf{u}(\mathbf{x},t) = -\nabla\delta p(\mathbf{x},t) + [\nabla\times\delta\mathbf{B}(\mathbf{x},t)]\times B_0\hat{\mathbf{z}} + \nu\nabla^2\delta\mathbf{u}(\mathbf{x},t). \tag{2.22}$$

We will ignore the dissipative term in the following and focus on the propagation of waves in ideal MHD instead. In order to simplify the analysis, we transform the previous equation into Fourier space by assuming that all perturbations are of the form $\delta\mathbf{u}(\mathbf{x},t) = \delta\mathbf{u}\exp(\imath\mathbf{k}\mathbf{x} - \imath\omega t)$ *et cetera*, and obtain:

$$-\omega\rho_0\delta\mathbf{u} = -\mathbf{k}\delta p + [\mathbf{k}\times\delta\mathbf{B}]\times B_0\hat{\mathbf{z}}. \tag{2.23}$$

Performing the same operations with the evolution equation (2.12) for the magnetic field and setting $\eta = 0$ again yields

$$-\omega\delta\mathbf{B} = -\mathbf{k}\times(\delta\mathbf{u}\times B_0\hat{\mathbf{z}}). \tag{2.24}$$

After inserting this expression for $\delta\mathbf{B}$ in the linearized ideal MHD momentum equation, we can apply the 'BAC-CAB' rule to simplify the resulting quintuple vector product, and obtain

$$\begin{aligned}\omega^2\rho_0\delta\mathbf{u} &= \omega\mathbf{k}\delta p + \{\mathbf{k}\times[-\mathbf{k}\times(\delta\mathbf{u}\times\mathbf{B_0})]\}\times\mathbf{B_0}\\ &= [\mathbf{B_0}\times(\mathbf{k}\times\mathbf{B_0}) + \gamma p_0\mathbf{k}](\mathbf{k}\cdot\delta\mathbf{u}) - (\mathbf{k}\cdot\mathbf{B_0})(\mathbf{k}\times\delta\mathbf{u})\times\mathbf{B_0},\end{aligned} \tag{2.25}$$

where we have employed the continuity equation (2.2) to replace the pressure gradient:

$$\begin{aligned}\omega\mathbf{k}\delta p &= \omega\mathbf{k}\left(\gamma\frac{p_0}{\rho_0}\delta\rho\right)\\ &= \imath\gamma\frac{p_0}{\rho_0}\mathbf{k}\underbrace{(-\imath\omega\delta\rho)}_{\partial_t\delta\rho(\mathbf{x},t)}\\ &= \imath\gamma\frac{p_0}{\rho_0}\mathbf{k}(-\imath\mathbf{k}\cdot\rho_0\delta\mathbf{u})\\ &= \gamma p_0(\mathbf{k}\cdot\delta\mathbf{u})\mathbf{k}.\end{aligned} \tag{2.26}$$

The $z$-axis is already defined as the direction in which the magnetic equilibrium field $\mathbf{B_0}$ is pointing. Hence we are free to define the $x$ direction to be perpendicular to both $\mathbf{B_0}$ and the wave vector $\mathbf{k}$, so that the latter can be decomposed into

$$\mathbf{k} = k_\perp\hat{\mathbf{y}} + k_\parallel\hat{\mathbf{z}}. \tag{2.27}$$

This decomposition allows us to write the dispersion relation (2.25) in form of a matrix equation:

$$\begin{pmatrix} \omega^2 - k_\parallel^2 v_A^2 & 0 & 0 \\ 0 & \omega^2 - k_\perp^2 v_s^2 - k^2 v_A^2 & -k_\perp k_\parallel v_s^2 \\ 0 & -k_\perp k_\parallel v_s^2 & \omega^2 - k_\parallel^2 v_s^2 \end{pmatrix} \cdot \begin{pmatrix} \delta u_x \\ \delta u_y \\ \delta u_z \end{pmatrix} = \mathbf{0}, \tag{2.28}$$

where we have made use of the Alfvén velocity $v_A$ and the sound velocity $v_s$, which are defined as

$$v_A = \frac{B_0}{\sqrt{\rho_0\mu_0}}, \tag{2.29}$$

$$v_s = \sqrt{\gamma\frac{p_0}{\rho_0}}. \tag{2.30}$$

### 2.3.1 Shear-Alfvén waves

The most straightforward solution of the matrix dispersion relation consists in setting the upper left matrix entry equal to zero,

$$\omega^2 - v_A^2 k_\parallel^2 \equiv 0, \tag{2.31}$$

and limiting the velocity oscillations to the $x$ direction so that the bottom two entries of the matrix product in the dispersion relation are identically zero:

$$\delta u_y \equiv \delta u_z \equiv 0. \tag{2.32}$$

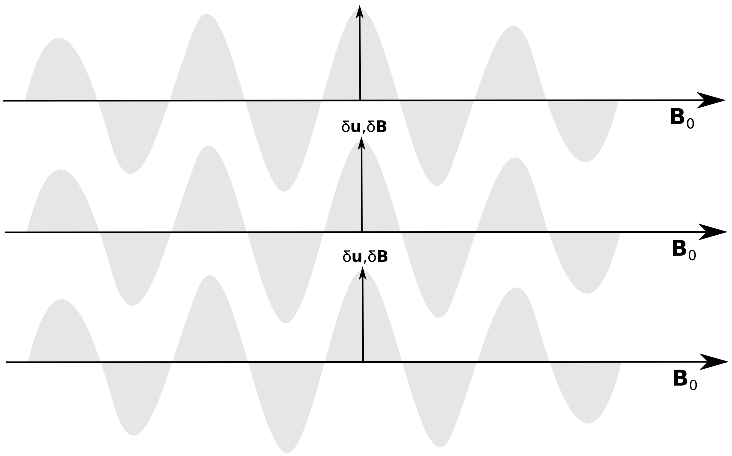

Figure 2.1: Sketch of shear-Alfvén waves propagating along a magnetic mean-field $\mathbf{B_0}$ in analogy to a plucked string

Since the velocity oscillations ($\delta\mathbf{u} \parallel \hat{\mathbf{x}}$) are perpendicular to both the equilibrium magnetic field ($\mathbf{B_0} \parallel \hat{\mathbf{z}}$) and the wave vector ($\mathbf{k} \perp \hat{\mathbf{x}}$), we obtain the purely transverse shear-Alfvén wave. As is obvious from equation (2.26), the density stays uniformly constant if the velocity field oscillates perpendicularly to the direction of propagation. The fact that the sound speed does not appear in the dispersion relation also indicates that the shear-Alfvén mode represents an incompressible oscillation of the plasma – hence it is this mode that our investigation of cosmic-ray diffusion in incompressible turbulence will focus on in later chapters.

A useful analogy allows us to view the magnetic field lines in the plasma as strings of a musical instrument, and to consider shear-Alfvén waves as oscillations traveling along the plucked strings (figure 2.1). In fact, the fluctuations of the magnetic field are parallel (or antiparallel) and proportional to the velocity oscillations:

$$\delta\mathbf{B}(\mathbf{x},t) = \pm\sqrt{\mu_0\rho_0}\,\delta\mathbf{u}(\mathbf{x},t), \tag{2.33}$$

a property which is closely related to Alfvén's famous flux-freezing theorem (Alfvén, 1942), stating that in an ideal, incompressible plasma, magnetic field lines behave as if they were physically attached to the fluid medium,

$$\int_{S(t)} \mathbf{B}(\mathbf{x},t)\cdot d^2\mathbf{S} = \text{const} \tag{2.34}$$

if the surface $S(t)$ is evolved according to the MHD momentum equation (2.5).

Both the group and the phase velocity are equal to the Alfvén velocity, as can easily be gleaned from the dispersion relation

$$\omega = \pm v_A k_{\|}. \tag{2.35}$$

Thus shear-Alfvén waves are entirely non-dispersive. They are directed either along the direction of the equilibrium magnetic field or opposite to it.

### 2.3.2 Slow magnetosonic waves

If we admit compressional modes as well and relax the condition $\delta u_y = \delta u_z = 0$, the dispersion relation allows for two additional solutions. Setting the determinant of the lower right $2 \times 2$ matrix in equation (2.28) equal to zero, we obtain the condition:

$$\omega^2 = \frac{k^2}{2}\left[(v_A^2 + v_s^2) \pm \sqrt{(v_A^2 + v_s^2) - 4v_A^2 v_s^2 \frac{k_\|^2}{k^2}}\right]. \tag{2.36}$$

Upon taking the minus sign, we get the dispersion relation for the slow magnetosonic wave,

$$\omega = \pm\frac{k}{\sqrt{2}}\sqrt{(v_A^2 + v_s^2) - \sqrt{(v_A^2 + v_s^2) - 4v_A^2 v_s^2 \frac{k_\|^2}{k^2}}}. \tag{2.37}$$

In the limit of perpendicular propagation ($k_\| \to 0$), its oscillation frequency vanishes ($\omega \to 0$) as the slow wave becomes a simple translation of the equilibrium condition without any force acting to restore the previous configuration.

If we let the slow wave propagate parallel to the magnetic mean-field ($k_\|^2 \to k^2$), its dispersion relation merges with the regular sound wave in a strongly magnetized plasma (*i.e.* $\omega = \pm v_s k$ if $v_A \gg v_s$), and with the shear-Alfvén wave in a weakly magnetized plasma ($\omega = \pm v_A k$ if $v_A \ll v_s$).

### 2.3.3 Fast magnetosonic waves

On the other hand, taking the plus sign in equation (2.36) yields the dispersion relation for the fast magnetosonic wave,

$$\omega = \pm\frac{k}{\sqrt{2}}\sqrt{(v_A^2 + v_s^2) + \sqrt{(v_A^2 + v_s^2) - 4v_A^2 v_s^2 \frac{k_\|^2}{k^2}}}, \tag{2.38}$$

which behaves opposite to the slow wave in the limit of parallel propagation: It merges with the regular sound wave in a weakly magnetized plasma and with the shear-Alfvén wave in a strongly magnetized plasma.

For perpendicular propagation ($k_\| \to 0$), the solution of the dispersion relation is purely longitudinal, given by $\delta\mathbf{u} \parallel \mathbf{k} \perp \mathbf{B_0}$. The plasma density and the magnetic-field density oscillate in phase with each other perpendicularly to the mean-field, yielding the strongest restoring force and hence the fastest wave velocity.

The dispersion relations of all three Alfvénic modes are shown in figure 2.2 for a ratio of Alfvén and sound speed $v_A/v_s = 1.25$, similar to what one may expect in

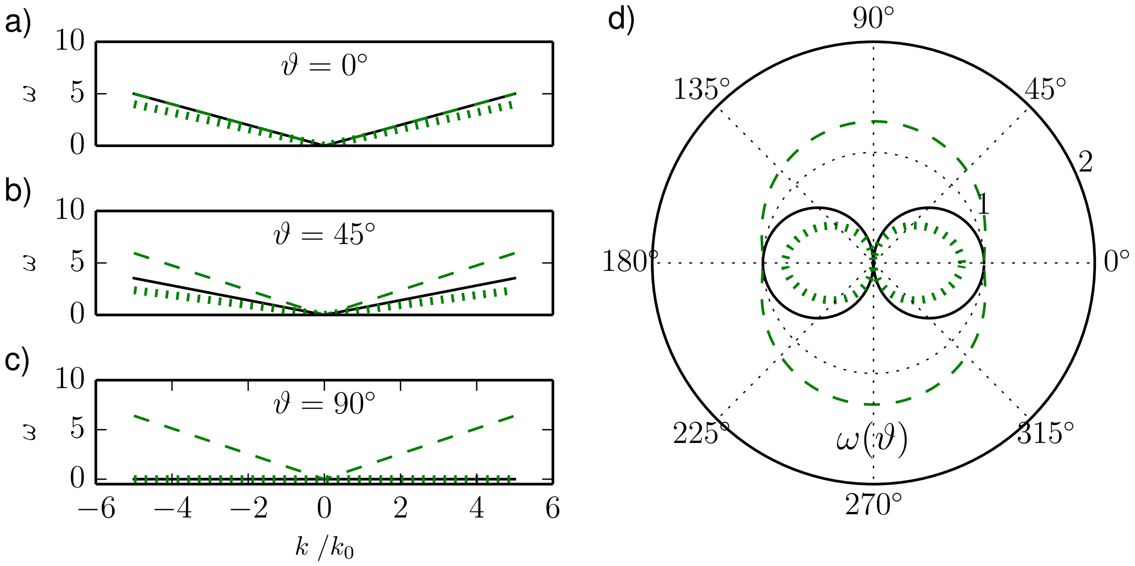

Figure 2.2: Dispersion relation of the shear-Alfvén wave (black solid line) and the slow (green dotted) and fast (green dashed) magnetosonic wave for different propagation directions with respect to the magnetic field, with $\omega$ in units of $v_A k_0$ and $v_A/v_s = 5/4$. (*a*) Propagation parallel to the magnetic field. (*b*) Propagation at an angle of 45° with respect to the magnetic-field direction. (*c*) Propagation perpendicular to the magnetic field. (*d*) Angular dependency of the wave frequency $\omega$ as a function of the angle with respect to the magnetic mean-field $\mathbf{B_0}$ for $k = k_0$

the neutral interstellar medium if one takes a magnetic mean-field of $B_0 \sim 3\ \mu$G and $n_i\ T \sim 2,000$ K cm$^{-3}$.

We will now show how the constant phase velocity of the shear-Alfvén wave connects it to the cross helicity $\mathcal{K}$.

## 2.4 Elsasser formalism

Since the magnetic field component of shear-Alfvén waves is related to their velocity fluctuations via equation (2.33), we can use this simple relation and introduce two new fields, the Elsasser fields,[4] as linear superpositions of magnetic and velocity fields (Elsasser, 1950):

$$\mathbf{z}^+(\mathbf{x},t) = \mathbf{u}(\mathbf{x},t) + \frac{1}{\sqrt{\rho_0\mu_0}}\mathbf{B}(\mathbf{x},t), \qquad (2.39)$$

---

[4] Walter Maurice Elsasser (b. 1904 in Mannheim, d. 1991 in Baltimore, MD), who introduced this formalism in 1950 and would later become one of the founders of geodynamo theory, never spelled his last name with an umlaut, not even before he emigrated to the US in 1936. Since the last name of several astronomers, astrophysicists, and of asteroid (4385) is Elsässer , the expression 'Elsässer variables' is used frequently but erroneously in the literature.

$$\mathbf{z}^-(\mathbf{x},t) = \mathbf{u}(\mathbf{x},t) - \frac{1}{\sqrt{\rho_0\mu_0}}\mathbf{B}(\mathbf{x},t). \tag{2.40}$$

In terms of these Elsasser variables, the equations of incompressible magnetohydrodynamics can be written in a completely symmetric fashion:

$$\partial_t\mathbf{z}^+ = -\mathbf{z}^- \cdot \nabla\mathbf{z}^+ - \nabla P + \frac{\nu+\eta}{2}\nabla^2\mathbf{z}^+ + \frac{\nu-\eta}{2}\nabla^2\mathbf{z}^-, \tag{2.41}$$

$$\partial_t\mathbf{z}^- = -\mathbf{z}^+ \cdot \nabla\mathbf{z}^- - \nabla P + \frac{\nu+\eta}{2}\nabla^2\mathbf{z}^- + \frac{\nu-\eta}{2}\nabla^2\mathbf{z}^+, \tag{2.42}$$

where the total pressure $P = p + B^2/2\mu_0$ combines both the thermal pressure $p$ and the magnetic pressure $B^2/2\mu_0$. Note that in ideal MHD, or generally if $\eta = \nu$, the nonlinear terms vanish if either $\mathbf{z}^+$ or $\mathbf{z}^-$ are zero.

The main advantage which one gains by writing the MHD equations in this manner becomes even more apparent if first-order perturbations $\delta\mathbf{u}$ and $\delta\mathbf{B}$ are reintroduced. Neglecting the dissipative terms, the linearized equations then reduce to two simple wave equations,

$$\partial_t\mathbf{z}^+ = +\frac{\mathbf{B_0}}{\sqrt{\rho_0\mu_0}} \cdot \nabla z^+, \tag{2.43}$$

$$\partial_t\mathbf{z}^- = -\frac{\mathbf{B_0}}{\sqrt{\rho_0\mu_0}} \cdot \nabla z^-, \tag{2.44}$$

the obvious solutions to which can be obtained by the traveling-wave ansatz $\mathbf{z}^+(\mathbf{x} + \mathbf{B_0}t/(\mu_0\rho_0)^{1/2})$ and $\mathbf{z}^-(\mathbf{x} - \mathbf{B_0}t/(\mu_0\rho_0)^{1/2})$, respectively. In other words, if a strong equilibrium magnetic field $\mathbf{B_0}$ is present, the positive Elsasser field $\mathbf{z}^+$ can be viewed as describing shear-Alfvén wave fluctuations propagating opposite to the equilibrium magnetic field with both phase and group velocity equal to the Alfvén velocity. Simultaneously, the negative Elsasser field $\mathbf{z}^-$ corresponds to shear-Alfvén waves traveling along the magnetic field $\mathbf{B_0}$ at the Alfvén speed.

Since we have seen that the nonlinear terms require both $\mathbf{z}^+ \neq 0$ and $\mathbf{z}^- \neq 0$, they can only generate turbulent interactions if both types of Alfvén waves are present. If the initial conditions in a plasma can be described by shear-Alfvén waves propagating in only one direction with respect to the mean-field, no other wave modes will appear as time progresses and turbulence will not start to develop.

In order to compare the amount of energy propagating in the two directions along and opposite to $\mathbf{B_0}$, it is common to introduce the Elsasser energies:

$$\mathcal{E}^+ = \frac{1}{4}\int_V \frac{d^3x}{V}\left[\delta\mathbf{u}(\mathbf{x}) + \frac{\delta\mathbf{B}(\mathbf{x})}{\sqrt{\mu_0\rho_0}}\right]^2, \tag{2.45}$$

$$\mathcal{E}^- = \frac{1}{4}\int_V \frac{d^3x}{V}\left[\delta\mathbf{u}(\mathbf{x}) - \frac{\delta\mathbf{B}(\mathbf{x})}{\sqrt{\mu_0\rho_0}}\right]^2, \tag{2.46}$$

which allows writing the total energy of the MHD system (normalized by the density) as a sum of the mean-field energy and the two Elsasser energies:

$$\begin{aligned}\mathcal{E} &= \mathcal{E}_{\text{kin}} + \mathcal{E}_{\text{mag}} \\ &= \int_V \frac{d^3x}{V} \left[ \frac{\delta\mathbf{u}(\mathbf{x})^2}{2} + \frac{(\mathbf{B_0} + \delta\mathbf{B}(\mathbf{x}))^2}{2\mu_0\rho_0} \right] \\ &= \int_V \frac{d^3x}{V} \frac{\mathbf{B_0}^2}{2\mu_0\rho_0} + \mathcal{E}^+ + \mathcal{E}^-. \end{aligned} \tag{2.47}$$

Similarly the cross helicity of the system can be expressed as the difference of the Elsasser energies:

$$\mathcal{K} = \int_V \frac{d^3x}{V} \delta\mathbf{u} \cdot \delta\mathbf{B} = \int_V \frac{d^3x}{V} \left[ \frac{(\delta\mathbf{u} + \delta\mathbf{B})^2 - (\delta\mathbf{u} - \delta\mathbf{B})^2}{4} \right] = \mathcal{E}^+ - \mathcal{E}^-. \tag{2.48}$$

Hence we obtain the important result that positive cross helicity in incompressible MHD implies the dominance of shear-Alfvén waves propagating opposite to $\mathbf{B_0}$, while a negative cross helicity implies that the turbulence exhibits an abundance of co-propagating waves. On the other hand, if $\mathcal{K} = 0$ holds, neither wave-type dominates and the turbulence is balanced overall.

## 2.5 Theories of MHD energy spectra

As the previous section has shown, Alfvén waves are an important conceptual framework and can be of immense help when we try to approach magnetohydrodynamic turbulence analytically. This is one of the main reasons why turbulence is often considered in spectral space instead of real space: After a Fourier transformation of the magnetohydrodynamic equations, it becomes manifest that without the nonlinear terms energy would be 'trapped' in the wave mode it is injected into and, instead of developing into turbulence, an Alfvén wave would simply travel along the equilibrium magnetic field undisturbed.

### 2.5.1 Kolmogorov's scaling-invariance hypothesis

With the nonlinear terms in place, however, the energy in the scale at which it is injected can 'cascade' to other scales, as the nonlinear terms allow for communication between different modes and therefore different length scales. Phenomenologically speaking, increasing the free energy of a system will lead to formation of eddies and vortices on a macroscopic scale, but these eddies will break up into smaller whirls, which can then again dissolve into even smaller vortices. The first systematic description of this transfer of turbulent energy from large scales to microscopic lengths was

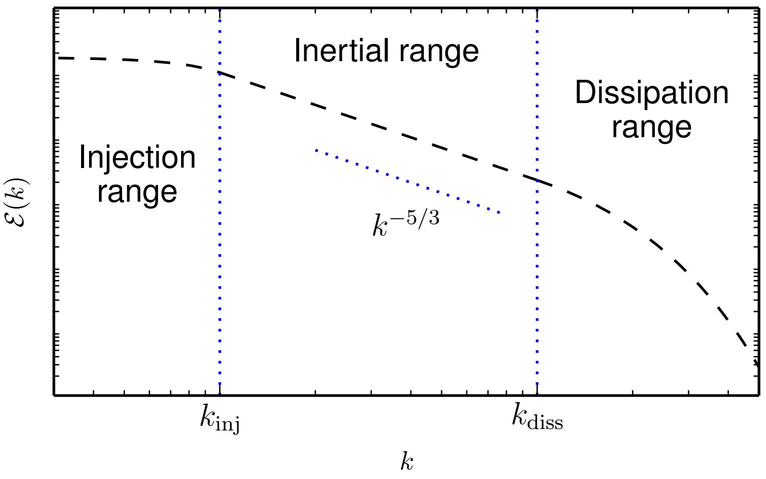

Figure 2.3: Sketch of an energy spectrum according to Kolmogorov's scale-invariance hypothesis: The spectrum follows a $k^{-5/3}$-law in the inertial range between the injection wavenumber $k_{\text{inj}}$ and the dissipation wavenumber $k_{\text{diss}}$ and then drops off sharply in the dissipation range ($k > k_{\text{diss}}$)

given by Richardson (1922), hence this particular way of viewing turbulence as a cascade from small $k$ to larger $k$ is sometimes termed "Richardson's cascade".

In his heuristic derivation of the energy distribution between different length scales under equilibrium conditions, Kolmogorov (1991 (originally 1941)) assumed that the rate at which energy is transported from large to small length scales is constant over a certain range of wavelengths. This 'inertial scale' begins at the typical length scale at which energy is injected and extends down towards the scale at which energy is dissipated from the system via friction (figure 2.3). The crucial insight of Kolmogorov was that the cascading process inside the inertial range is independent of both the details of the forcing on larger scales and the details of the viscous dissipation on smaller scales. Without this 'locality of turbulence', the energy rate would necessarily vary within the inertial range.

Kolmogorov's reasoning was as follows: If the typical magnitude of velocity fluctuations on the length scale $\lambda$ is $v_\lambda$, then it is reasonable to assume that the time scale $\tau_\lambda$ on which this perturbation in the velocity field will trickle down to smaller scales is of order

$$\tau_\lambda \sim \lambda / v_\lambda, \tag{2.49}$$

since these are the only characteristic scales present in the problem.

Kolmogorov's central hypothesis is based on the scale-invariance of the energy cascade over the entire extent of the inertial range. In other words, the rate at which energy is transported from large scales to small scales is independent of the length scale. Since energy is proportional to the square of the velocity, Kolmogorov's hypothesis can be phrased as

$$\varepsilon \sim \frac{v_\lambda^2}{\tau_\lambda} \sim \frac{v_\lambda^3}{\lambda} \sim \text{const} \tag{2.50}$$

or equivalently $v_\lambda^3 \sim \varepsilon\lambda$.

We define the energy spectrum $\mathcal{E}(k)$ such that $\mathcal{E}(k)\,dk$ is the energy contained in the wavenumber interval $[k, k+dk)$,

$$\mathcal{E}(k) = \frac{1}{2}\left|\int d^3k\ \mathbf{u}(\mathbf{x}) e^{\imath\mathbf{k}\cdot\mathbf{x}}\right|^2 . \tag{2.51}$$

If we argue that the wavenumber $k$ corresponds to a length-scale $\lambda \sim k^{-1}$, then dimensional reasoning implies the following relation in three-dimensional space:

$$v_\lambda^2 \sim \int \mathcal{E}(k)\,dk, \tag{2.52}$$

so that we can derive, at least heuristically, using equation (2.50),

$$\mathcal{E}(k) \sim v_\lambda^2 k^{-1} \sim (\varepsilon\lambda)^{2/3}\lambda \sim \varepsilon^{2/3}\lambda^{5/3}, \tag{2.53}$$

or expressed as Kolmogorov's famous −5/3-law in terms of the wavenumber $k$:

$$\mathcal{E}(k) \sim C_K \varepsilon^{2/3} k^{-5/3}. \tag{2.54}$$

Experimental and numerical investigations have yielded for Kolmogorov's constant the value $C_K \approx 1.6$ (Sreenivasan, 1995; Gotoh & Fukayama, 2001).

Kolmogorov's theory is striking because of its remarkable conceptual simplicity: Its only real argument is the assumption that the energy cascade rate $\varepsilon$ is scale-invariant in the inertial range of the spectrum. As was shown much later, the shape of velocity increments in developed turbulence deviates from what Kolmogorov's 1941 theory predicts due to the spatial variation of energy dissipation (*e.g.* Davidson, 2004), and a theory that would consistently describe this deviation is still one of the main goals of hydrodynamic theory. But this 'scaling anomaly' notwithstanding, Kolmogorov's achievement was to predict a spectral slope that is observed in a wide variety of turbulent systems, ranging from magnetic-field fluctuations in the solar wind to turbulent flows in wind channels on earth (Grant *et al.* , 1962; Coleman, 1968; Saddoughi & Veeravalli, 1994; Podesta *et al.* , 2007).

If the kinematic viscosity $\nu$ is known for a particular system, it is also possible to determine the approximate length scale at which the energy cascade ends and turbulent energy is not transported to smaller scales anymore, but instead converted into viscous heating. The kinematic viscosity has the units of a diffusion coefficient, length squared divided by time, while the energy cascade rate $\varepsilon$ has units of velocity squared divided by time, so dimensional arguments yield the following relation for Kolmogorov's dissipation length $\ell_K$:

$$\ell_K \sim \left(\frac{\nu^3}{\varepsilon}\right)^{1/4} . \tag{2.55}$$

### 2.5.2 Kraichnan's scaling law

Kolmogorov's analysis is valid as long as there is no universal velocity-scale describing the propagation of waves, which is generally true in hydrodynamics without an external magnetic field. If such a magnetic mean field $\mathbf{B_0}$ permeates a magnetohydrodynamic system, however, an additional characteristic velocity is introduced, the Alfvén velocity $v_A$.

Furthermore, the transport of energy is now limited to the exchange of energy between co- and counter-propagating waves, as only the nonlinear terms which involve both $z^+$ and $z^-$ in equations (2.41) and (2.42) enable the cascading process towards smaller length scales – a linear evolution equation would not transfer energy from one scale to another. The period of time over which oppositely directed Alfvén waves interact must be shorter than in Kolmogorov's hypothesis. In the previous subsection, we assumed that the scale of velocity fluctuations and the wave velocity are comparable; thus we overestimated the interaction time of two communicating wave modes by a factor of $v_A/z_\lambda$, where $z_\lambda$ is the perturbation of an Elsasser variable caused by a traveling Alfvén-wave package. Since the exchange of energy between two Alfvén waves will not be a coherent process and rather resemble a diffusive random walk in the energy content of each wave mode, we must square this factor to obtain the time $T_\lambda$ until energy comparable to the amount in Kolmogorov's analysis has cascaded to smaller scales in magnetohydrodynamics. We obtain

$$T_\lambda \sim \frac{\lambda}{v_A}\left(\frac{v_A}{z_\lambda}\right)^2 \sim \frac{\lambda v_A}{z_\lambda^2}, \tag{2.56}$$

where $\lambda/v_A$ corresponds to the interaction time assumed by Kolmogorov for merely hydrodynamic turbulence.

If we otherwise proceed as in Kolmogorov's analysis, the energy cascade rate becomes

$$\varepsilon \sim \frac{z_\lambda^2}{T_\lambda} \sim \frac{z_\lambda^4}{\lambda v_A}, \tag{2.57}$$

and assuming that this rate is independent of the length scale $\lambda$, we find for the energy spectrum $\mathcal{E}(k)$:

$$\mathcal{E}(k) \sim z_\lambda^2 k^{-1} \sim (\varepsilon \lambda v_A)^{1/2} k^{-1} \sim C_{IK} \varepsilon^{1/2} v_A^{1/2} k^{-3/2}, \tag{2.58}$$

which is the famous −3/2-law discovered by Iroshnikov (1964) and Kraichnan (1965). Although this analysis is significantly more sophisticated than Kolmogorov's reasoning with dimensional arguments, the difference between the scaling laws $k^{-5/3}$ and $k^{-3/2}$ is extremely difficult to resolve in experiments or numerical simulations. An analysis of solar-wind data by Podesta *et al.* (2007) partially reconciled proponents of both theories and found that the spectrum of velocity fluctuations followed Kraichnan's scaling while the spectrum of magnetic-field perturbations exhibited a Kolmogorov-like scaling.

The situation is complicated further by the fact that the interaction time $T_\lambda$ may be different for co- and counter-propagating waves. In imbalanced turbulence, characterized by non-zero cross helicity or more energy in Alfvén waves traveling in one direction than in the opposite direction, the energy spectra for the positive and negative Elsasser energies will in general exhibit different spectral slopes, as discovered by Grappin *et al.* (1983). Their analysis revealed that the Elsasser spectra can be written as

$$\mathcal{E}^{\pm}(k) \sim \nu v_A \ell_K^{-m_\pm} k^{-m_\pm}, \tag{2.59}$$

where the spectral indices $m_\pm$ fulfill the relation

$$m_+ + m_- = 3, \tag{2.60}$$

so that the Iroshnikov-Kraichnan solution can be considered a special case corresponding to balanced turbulence with $m_+ = m_- = 3/2$.

### 2.5.3 Goldreich-Sridhar theory of MHD turbulence

The analysis above implicitly assumed resonant three-wave interactions: two oppositely directed Alfvén waves of wavenumbers $k_1$ and $k_2$ transfer energy to a mode with $k_3 = k_1 - k_2$. As Goldreich and Sridhar showed in their seminal papers (Sridhar & Goldreich, 1994; Goldreich & Sridhar, 1995), however, this assumption becomes completely invalid in strongly Alfvénic turbulence, in which the velocity fluctuations are of order $z_\lambda \sim v_A \lambda_\perp / \lambda_\parallel$, where $\lambda_\perp$ and $\lambda_\parallel$ are the correlation length scales of the turbulence perpendicular and parallel to the magnetic mean-field.

The reason the three-wave assumption must break down is that the Alfvénic dispersion relation

$$\omega(k) = \pm v_A k_\parallel \tag{2.61}$$

does not allow for both the resonance condition in wavenumber space and frequency space to be fulfilled simultaneously unless one of the participating wavenumber is zero: The system

$$\mathbf{k}_1 + \mathbf{k}_2 = \mathbf{k}_3, \qquad |\omega(k_1)| + |\omega(k_2)| = |\omega(k_3)|, \tag{2.62}$$

only has a solution if either $k_{1,\parallel} = 0$ or $k_{2,\parallel} = 0$. Hence no cascade to smaller length scales along the mean field is possible through three-wave interactions.

Goldreich and Sridhar argued that resonant four-wave interactions are a possible alternative mechanism for distributing energy among modes with different parallel wavenumbers, but that these are naturally far less efficient than the three-wave interactions assumed by Iroshnikov and Kraichnan. Whereas the latter introduced the increased interaction time scale $T_\lambda$ in their three-wave analysis, as outlined above, Goldreich and Sridhar instead proposed that, in weakly Alfvénic turbulence, the relevant interaction time scale for resonant four-wave cascading is of the order

$$T'_\lambda = \frac{1}{k_\| v_A} \times \left( \frac{k_\| v_A}{k_\perp z_\lambda} \right)^4. \tag{2.63}$$

Demanding that the energy cascade rate be independent of the length scale $\lambda$,

$$\varepsilon \sim \frac{z_\lambda^2}{T'_\lambda} \sim \frac{z_\lambda^6 k_\perp^4}{k_\|^3 v_A^3} \sim \text{const}, \tag{2.64}$$

we obtain for the scaling of the fluctuations of the Elsasser variables:

$$z_\lambda \sim \varepsilon^{1/6} k_\perp^{-2/3} k_\|^{1/2} v_A^{1/2}. \tag{2.65}$$

This finally allows us to write the Goldreich-Sridhar spectrum of anisotropic magnetohydrodynamic turbulence as

$$\mathcal{E}(k_\perp, k_\|) \sim z_\lambda^2 k_\perp^{-2} \sim \varepsilon^{1/3} v_A k_\perp^{-10/3}, \tag{2.66}$$

where the anisotropic spectrum $\mathcal{E}(k_\perp, k_\|)$ is defined such that

$$z_\lambda^2 \sim \iiint \mathcal{E}(k_\perp, k_\|)\, d^2 k_\perp \, dk_\|. \tag{2.67}$$

These arguments are only strictly valid for perpendicular velocity fluctuations small enough for the turbulence to be called weakly Alfvénic, such that

$$z_\lambda \lesssim v_A \lambda_\perp / \lambda_\|. \tag{2.68}$$

This inequality can be derived from the condition that the eddy-turnover time $T_\lambda$ be approximately equal to the nonlinear interaction time $T'_\lambda$. If fluctuations are so small that $z_\lambda \ll v_A \lambda_\perp / \lambda_\|$ ('weak turbulence'), the energy contained in them is transferred to smaller parallel scales via the four-wave interaction process. Since the transport to smaller perpendicular wavenumbers can occur in three-wave processes, $\lambda_\perp$ will decrease faster than $\lambda_\|$ until the inequality (2.68) becomes an approximate equality, which was termed the 'critical balance' condition by Goldreich and Sridhar.

If, on the other hand, the turbulence is strong such that the inequality (2.68) is violated, the weak-turbulence theory described above is no longer applicable, as explicitly stressed by Goldreich and Sridhar in their original paper, and a more elaborate theory of strong turbulence is required. For this case, Goldreich & Sridhar (1995) showed that the generation of shear-Alfvén waves contributes to the transport of energy to smaller length scales along the magnetic field, reducing $\lambda_\|$ and hence increasing the right-hand side of inequality (2.68) until, again, it becomes an approximate equality. The important conclusion is that both weak and strong magnetohydrodynamic turbulence will converge towards a state in which critical balance approximately holds.

At the transition from weak to strong turbulence, we can identify the correlation scales with the inverse wavenumbers such that $k_\perp \sim \lambda_\perp^{-1}$ and $k_\| \sim \lambda_\|^{-1}$. In this case, the condition (2.64) that the energy cascade rate be constant in the inertial range becomes, using critical balance,

$$\varepsilon \sim \frac{z_\lambda^6 k_\perp^4}{k_\|^3 v_A^3} \sim \frac{v_A^6 k_\|^3}{k_\perp^2} \sim \text{const}, \tag{2.69}$$

which allows us to derive the relation between the parallel and the perpendicular wavenumber:

$$k_\perp \sim \varepsilon^{-1/2} v_A^3 k_\|^{3/2}. \tag{2.70}$$

Hence the regime in which the Goldreich-Sridhar spectrum can be expected in the perpendicular direction (as Goldreich and Sridhar called it, the inertial range of the four-wave energy cascade) is dependent on the parallel length scale over which the turbulence is measured. This peculiarity of the Goldreich-Sridhar theory is often interpreted as a spectral anisotropy that becomes more pronounced on shorter length scales.

Inserting this relation between $k_\perp$ and $k_\|$ into equation (2.66), we find for the scaling of the spectrum perpendicular to the mean-field

$$\begin{aligned}\int \mathcal{E}(k_\perp)\, d^2k_\perp\, dk_\| &\sim \int dk_\perp \times (\varepsilon^{1/3} v_A k_\perp^{-10/3})\, (\varepsilon^{1/3} v_A^{-2} k_\perp^{2/3})\, k_\perp \\ &\sim \int dk_\perp\ \varepsilon^{2/3}\ v_A^{-1}\ k_\perp^{-5/3},\end{aligned} \tag{2.71}$$

and for the spectrum parallel to the mean-field[5]

$$\begin{aligned}\int \mathcal{E}(k_\perp)\, d^2k_\perp\, dk_\| &\sim \int dk_\| \times (\varepsilon^{1/3} v_A k_\perp^{-10/3})\, \left(\varepsilon^{-1/2} v_A^3 k_\|^{3/2}\right)^2 \\ &\sim \int dk_\|\ \varepsilon\ v_A^{-3}\ k_\|^{-2}.\end{aligned} \tag{2.72}$$

Particularly noteworthy about these results is that, according to equation (2.71), the perpendicular spectrum in Goldreich-Sridhar theory exhibits the same scaling exponent as the isotropic energy spectrum derived by Kolmogorov.

* * *

The subject of MHD turbulence becomes particularly involved when scaling exponents for the spectra of turbulent fluctuations are to be predicted. After this concise overview of the analytical theory of MHD scaling laws, we will make extremely simple assumptions regarding the MHD energy spectra in the next section. This will allow us to derive the diffusion coefficients of cosmic-ray particles in magnetohydrodynamic turbulence as functions of the cross helicity. In subsequent chapters, we will compare these coefficients with simulations of more realistic MHD turbulence, similar to (yet even more realistic than) the models introduced above.

---

[5] Biskamp (2003) gives a scaling of $k_\|^{-5/2}$ after inserting the critical-balance condition into (2.71). However, he neglects to transform the infinitesimal $dk_\perp$ as well.

# Chapter 3

# Quasilinear Theory of Velocity-Space Diffusion

*O polish'd perturbation! golden care!*

– *Henry IV* (William Shakespeare, 1597)

**Chapter Summary**

- Quasilinear theory expands the equations of motion in a strong magnetic mean-field to second order in field perturbations. Therefore it requires knowledge of the power spectrum of the fields.
- If the distribution of charged particles in a plasma deviates only little from an isotropic distribution, analytical predictions of the heating rate and the pitch-angle diffusion rate can be obtained.
- Assuming the absence of electric fields or wave propagation simplifies the results significantly.

After the brief presentation of elements of magnetohydrodynamic theory related to cross helicity contained in the previous chapter, our focus shifts to the kinetic theory of test-particle diffusion. We will derive the diffusion coefficients of cosmic-ray transport in simple analytical models, and then compare these in later chapters with transport coefficients obtained in realistic numerical MHD simulations.

## 3.1 Introduction to quasilinear theory

The groundwork for the quasilinear theory (QLT) of cosmic-ray diffusion was laid by Jokipii (1966), who first derived the diffusion coefficients for parallel and perpendicular transport in the magnetic turbulence of the interstellar medium. His work focused on high-energy cosmic-ray particles, with a velocity so much faster than that of the Alfvén waves described in the previous chapter that the evolution of the turbulence and the influence of the electric fields can be neglected. Moreover, the power-law slab spectrum (equation (3.60) below), which has almost become a conventional assumption in QLT ('Standard QLT' according to Shalchi (2009)), was originally used in Jokipii's seminal article. We will cite his result at the end of this chapter, but the derivation of quasilinear diffusion coefficients we present here will be more general and include both effects, as in Kennel & Engelmann (1966); Tverskoĭ (1967); Gendrin (1968); Kulsrud & Pearce (1969); Lee (1982); Schlickeiser (1989). Although we will limit our considerations to non-relativistic particles, the extension to the relativistic regime is straightforward (Lerche, 1968).

The quasilinear theory for the diffusion of charged particles in electromagnetic turbulence is in essence a perturbation analysis: The turbulent fields are modeled as small deviations from a constant and homogeneous magnetic mean field $\mathbf{B_0}$, along which the $z$ axis is conventionally defined. The average electrostatic field is taken as zero since the conductivity of the plasma in which the charged particles propagate is assumed too high. Relating the electric and the magnetic turbulent fields via Faraday's law, one can expand the equations of motion up to second order in these field deviations. This method allows a fairly accurate prediction of the scattering of charged particles in both position and momentum space, under the condition that the turbulent perturbations are sufficiently small compared to the magnetic mean field.

## 3.2 Derivation of the velocity-space diffusion equation

### 3.2.1 The space-averaged Vlasov equation

Our derivation of the quasilinear theory of velocity-space diffusion, which will follow along the lines of Kennel & Engelmann (1966) and Schlickeiser (1989), begins with the Vlasov equation for the evolution of the phase-space density $F(\mathbf{x}, \mathbf{v}, t)$ of charged particles in electromagnetic fields (Vlasov, 1938):

$$\frac{\partial F}{\partial t} + \mathbf{v} \cdot \nabla_{\mathbf{x}} F + \frac{q}{m} \left[ \mathbf{E}(\mathbf{x}, t) + \mathbf{v} \times \mathbf{B}(\mathbf{x}, t) \right] \cdot \nabla_{\mathbf{v}} F = 0. \tag{3.1}$$

Here $q/m$ is the charge-to-mass ratio, $\mathbf{x}$ and $\mathbf{v}$ are the position and velocity at which the phase-space density $F$ is taken, and $\mathbf{E}$ and $\mathbf{B}$ are the electric and magnetic field, respectively. A rigorous derivation of this equation would take up too much space to be included in this chapter, but for a detailed description of the individual steps leading to equation (3.1) the reader shall be referred to monographies on the kinetic theory of gases (*e.g.* Liboff, 2003). As becomes clear in such a formal derivation of the Vlasov equation, **E** and **B** actually refer to the mean-field values of the electromagnetic fields: One assumes that the phase-space density $F$ is smooth enough to obtain the macroscopic mean-fields **E** and **B** without knowledge of small-scale density fluctuations or, in mathematical terms, that the statistical ensemble average $\langle \mathbf{E}F\rangle$ is identical to $\langle \mathbf{E}\rangle\langle F\rangle$.

Our primary goal in this chapter is obtaining a description of the evolution of the charged-particle distribution in velocity space: the rate at which turbulent interactions change the direction of the particle momentum relative to the mean-field direction , and the rate at which the norm of the particle momentum varies because of heating by turbulent electromagnetic fields. To this end, we will mainly be concerned with finding the time evolution of the velocity-space density $\overline{f}(\mathbf{v},t)$. This time dependence is obtained from averaging the phase-space density $F$ over the volume $V$ in which the charged-particle gas is contained,

$$\overline{f}(\mathbf{v},t) = \frac{1}{V}\int_V d^3x\, F(\mathbf{x},\mathbf{v},t). \tag{3.2}$$

We will describe deviations from this average density in terms of the Fourier components of $F$,

$$\delta f(\mathbf{k},\mathbf{v},t) = \int_V d^3\mathbf{x}\, \left[F(\mathbf{x},\mathbf{v},t) - \overline{f}(\mathbf{v},t)\right] e^{-\imath\mathbf{k}\cdot\mathbf{x}}. \tag{3.3}$$

This procedure amounts to transforming the particle position represented by the coordinate **x** to Fourier space (represented by **k**). The second argument of the phase-space density, the particle velocity **v**, remains as is since it appears explicitly (twice) as a coefficient in the Vlasov equation.

Using this decomposition, the Vlasov equation can be transformed into Fourier space as well by subtracting from equation (3.1) its own space average. The Vlasov equation simplifies immensely after being averaged over position space since $\overline{f}$ vanishes at infinity. After multiplying by $\exp(-\imath\mathbf{k}\cdot\mathbf{x})$ and integrating over position space, we get:

$$\begin{aligned}\frac{\partial}{\partial t}\delta f(\mathbf{k},\mathbf{v},t) &+ \mathbf{v}\cdot\imath\mathbf{k}\delta f(\mathbf{k},\mathbf{v},t)\\ &\underbrace{+\frac{q}{m}\int d^3x\,\left[\mathbf{E}(\mathbf{x},t)+\mathbf{v}\times\mathbf{B}(\mathbf{x},t)\right]\cdot\nabla_{\mathbf{v}}F(\mathbf{x},\mathbf{v},t)\,e^{-\imath\mathbf{k}\cdot\mathbf{x}}}_{\mathcal{I}(\mathbf{k})} = 0.\end{aligned} \tag{3.4}$$

The remaining integral $\mathcal{I}(\mathbf{k})$, which constitutes the third term on the left-hand side, may then be split into a term involving only $\overline{f}$, a term involving the constant magnetic mean field $\mathbf{B_0}$, and a convolution of the Fourier-transformed fields and $\delta f$:

$$\begin{aligned}\mathcal{I}(\mathbf{k}) = \frac{q}{m} \times \Bigg\{ & \Big[\tilde{\mathbf{E}}(\mathbf{k},t) + \mathbf{v} \times \tilde{\mathbf{B}}(\mathbf{k},t)\Big] \cdot \nabla_{\mathbf{v}} \overline{f} \\ & + (\mathbf{v} \times \mathbf{B_0}) \cdot \nabla_{\mathbf{v}} \delta f \\ & + \frac{1}{2} \int \frac{d^3k'}{(2\pi)^3} \Big[\tilde{\mathbf{E}}(\mathbf{k}-\mathbf{k}',t) + \mathbf{v} \times \tilde{\mathbf{B}}(\mathbf{k}-\mathbf{k}',t)\Big] \cdot \nabla_{\mathbf{v}} \delta f(\mathbf{k}',\mathbf{v},t) \\ & + \frac{1}{2} \int \frac{d^3k'}{(2\pi)^3} \Big[\tilde{\mathbf{E}}(\mathbf{k}',t) + \mathbf{v} \times \tilde{\mathbf{B}}(\mathbf{k}',t)\Big] \cdot \nabla_{\mathbf{v}} \delta f(\mathbf{k}-\mathbf{k}',\mathbf{v},t) \Bigg\}. \end{aligned} \tag{3.5}$$

However, we will neglect the convolution terms in the bottom two lines of the above expression in the spirit of a linear perturbation analysis: Since both terms involve the product of turbulent fields with deviations from the average phase-space density, we can treat them as second-order terms and ignore them in the remainder of this analysis.

### 3.2.2 Evolution of the Fourier components $\delta f$

As we have already performed a Fourier transformation of the position domain of the phase-space density, it is advantageous to treat the electromagnetic fields in a similar fashion. The Fourier-transformed fields $\tilde{\mathbf{E}}$ and $\tilde{\mathbf{B}}$ are defined as

$$\tilde{\mathbf{E}}(\mathbf{k},t) = \int d^3\mathbf{x}\; \mathbf{E}(\mathbf{x},t)\, e^{-\imath \mathbf{k}\cdot\mathbf{x}}, \tag{3.6}$$

$$\tilde{\mathbf{B}}(\mathbf{k},t) = \int d^3\mathbf{x}\; \mathbf{B}(\mathbf{x},t)\, e^{-\imath \mathbf{k}\cdot\mathbf{x}}. \tag{3.7}$$

If we again let the $z$ direction be the direction along which the magnetic mean field points, it is useful to decompose the electric field into components reflecting left-hand and right-hand circular polarization with respect to this direction:

$$E_R(\mathbf{k}) = \frac{\tilde{E}_x(\mathbf{k}) - \imath \tilde{E}_y(\mathbf{k})}{\sqrt{2}}, \qquad E_L(\mathbf{k}) = \frac{\tilde{E}_x(\mathbf{k}) + \imath \tilde{E}_y(\mathbf{k})}{\sqrt{2}}, \qquad E_{||}(\mathbf{k}) = \tilde{E}_z(\mathbf{k}), \tag{3.8}$$

and define an analogous decomposition into $B_R, B_L$, and $B_{||}$ for the magnetic field:

$$B_R(\mathbf{k}) = \frac{\tilde{B}_x(\mathbf{k}) - \imath \tilde{B}_y(\mathbf{k})}{\sqrt{2}}, \qquad B_L(\mathbf{k}) = \frac{\tilde{B}_x(\mathbf{k}) + \imath \tilde{B}_y(\mathbf{k})}{\sqrt{2}}, \qquad B_{||}(\mathbf{k}) = \tilde{B}_z(\mathbf{k}). \tag{3.9}$$

Introducing the azimuthal angle $\psi$ at which the wave vector $\mathbf{k}$ is oriented with respect to the positive $x$-axis, we can write

$$k_x = k_\perp \cos\psi, \qquad k_y = k_\perp \sin\psi, \qquad k_z = k_{||}. \tag{3.10}$$

We now employ a similar definition for the angle $\phi$ subtended by the perpendicular component of the velocity vector $v_\perp$ and the positive $x$-axis,

$$v_x = v_\perp \cos\phi, \qquad v_y = v_\perp \sin\phi, \qquad v_z = v_\parallel. \tag{3.11}$$

In order to simplify the Vlasov equation even more, we can make use of Faraday's law and express the magnetic field in terms of the electric field and the wave frequency $\omega_{\mathbf{k}}$,

$$\tilde{\mathbf{B}}(\mathbf{k}) = \frac{\mathbf{k}}{\omega_{\mathbf{k}}} \times \tilde{\mathbf{E}}(\mathbf{k}), \tag{3.12}$$

where the electric field is expressed in terms of its left- and right-handed circularly polarized components,

$$\tilde{\mathbf{E}} = \left( \frac{E_R + E_L}{\sqrt{2}}; \quad \imath\frac{E_R - E_L}{\sqrt{2}}; \quad E_\parallel \right). \tag{3.13}$$

It is now possible to transform the term in $\mathcal{I}(\mathbf{k})$ that is linear in the fields (*i.e.* the one proportional to $\nabla_{\mathbf{v}}\overline{f}$) to cylindrical coordinates as well and integrate the term involving $\mathbf{B_0}$ by parts:

$$\begin{aligned}
\mathcal{I}(\mathbf{k}) \;=\;& \frac{q}{m}\left[\tilde{\mathbf{E}}(\mathbf{k}) + \mathbf{v} \times \left(\frac{\mathbf{k}}{\omega_{\mathbf{k}}} \times \tilde{\mathbf{E}}(\mathbf{k})\right)\right] \cdot \nabla_{\mathbf{v}}\overline{f} + \frac{q}{m}(\mathbf{v} \times \mathbf{B_0}) \cdot \nabla_{\mathbf{v}}\delta f = \\
=\;& +\frac{q}{m} e^{\imath(\phi-\psi)} \left[ \frac{E_R e^{\imath\psi}}{\sqrt{2}} \left(\hat{\Lambda} + \imath\frac{\omega_{\mathbf{k}} - k_\parallel v_\parallel}{\omega_{\mathbf{k}} v_\perp}\partial_\phi\right) + \frac{k_\perp E_\parallel}{2\omega_{\mathbf{k}}}\left(\hat{H} + \imath\frac{v_\parallel}{v_\perp}\partial_\phi\right)\right]\overline{f} \\
& +\frac{q}{m} e^{-\imath(\phi-\psi)} \left[ \frac{E_L e^{-\imath\psi}}{\sqrt{2}} \left(\hat{\Lambda} - \imath\frac{\omega_{\mathbf{k}} - k_\parallel v_\parallel}{\omega_{\mathbf{k}} v_\perp}\partial_\phi\right) + \frac{k_\perp E_\parallel}{2\omega_{\mathbf{k}}}\left(\hat{H} - \imath\frac{v_\parallel}{v_\perp}\partial_\phi\right)\right]\overline{f} \\
& +\frac{q}{m}\left[\imath\frac{k_\perp}{\omega_{\mathbf{k}}}\left(\frac{E_L e^{-\imath\phi} - E_R e^{\imath\phi}}{\sqrt{2}}\right)\partial_\phi + E_\parallel\frac{\partial}{\partial v_\parallel}\right]\overline{f} \\
& +\frac{q}{m} B_0 \partial_\phi \delta f \\
& + \mathcal{O}(\delta f^2),
\end{aligned} \tag{3.14}$$

where we again choose to neglect terms of higher than first order in the perturbation from the average phase-space density, as our analysis assumes this deviation to be small. In the above expression we have used hats to indicate symbols which denote differential operators. The two operators $\hat{\Lambda}$ and $\hat{H}$ are defined as

$$\hat{\Lambda}(\mathbf{k}) = \left(1 - \frac{k_\parallel v_\parallel}{\omega_{\mathbf{k}}}\right)\frac{\partial}{\partial v_\perp} + \frac{k_\parallel v_\parallel}{\omega_{\mathbf{k}}}\frac{\partial}{\partial v_\parallel}, \tag{3.15}$$

$$\hat{H} = v_\parallel \frac{\partial}{\partial v_\perp} - v_\perp \frac{\partial}{\partial v_\parallel}. \tag{3.16}$$

Going back to equation (3.4), we perform a Fourier transformation in time, which corresponds to replacing the time derivative by $\partial_t = -\imath\omega_{\mathbf{k}}$, and use cylindrical coordinates to obtain:

$$-\imath\omega_{\mathbf{k}}\delta f + \imath k_\perp v_\perp(\cos\phi\cos\psi + \sin\phi\sin\psi)\,\delta f + \imath k_\| v_\| \delta f = -\mathcal{I}(\mathbf{k}), \tag{3.17}$$

or, if one moves the term in $\mathcal{I}(\mathbf{k})$ that only involves $\mathbf{B_0}$ to the left-hand side,

$$\hat{L}(\mathbf{k})\delta f(\mathbf{k},\mathbf{v},t) = \hat{P}(\mathbf{k})\overline{f}(\mathbf{v},t), \tag{3.18}$$

where the differential operators $\hat{P}(\mathbf{k})$ and $\hat{L}(\mathbf{k})$ have been introduced to abbreviate two rather lengthy terms:

$$\begin{aligned}
\hat{P}(\mathbf{k}) = &-\frac{q}{m}\left[\tilde{\mathbf{E}}(\mathbf{k}) + \mathbf{v}\times\left(\frac{\mathbf{k}}{\omega_{\mathbf{k}}}\times\tilde{\mathbf{E}}(\mathbf{k})\right)\right]\cdot\nabla_{\mathbf{v}} &(3.19)\\
= &-\frac{q}{m}e^{\imath(\phi-\psi)}\left[\frac{E_R e^{\imath\psi}}{\sqrt{2}}\left(\hat{\Lambda} + \imath\frac{\omega_{\mathbf{k}} - k_\| v_\|}{\omega_{\mathbf{k}} v_\perp}\partial_\phi\right) + \frac{k_\perp E_\|}{2\omega_{\mathbf{k}}}\left(\hat{H} + \imath\frac{v_\|}{v_\perp}\partial_\phi\right)\right]\\
&-\frac{q}{m}e^{-\imath(\phi-\psi)}\left[\frac{E_L e^{-\imath\psi}}{\sqrt{2}}\left(\hat{\Lambda} - \imath\frac{\omega_{\mathbf{k}} - k_\| v_\|}{\omega_{\mathbf{k}} v_\perp}\partial_\phi\right) + \frac{k_\perp E_\|}{2\omega_{\mathbf{k}}}\left(\hat{H} - \imath\frac{v_\|}{v_\perp}\partial_\phi\right)\right]\\
&-\frac{q}{m}\left[\imath\frac{k_\perp}{\omega_{\mathbf{k}}}\left(\frac{E_L e^{-\imath\phi} - E_R e^{\imath\phi}}{\sqrt{2}}\right)\partial_\phi + E_\|\frac{\partial}{\partial v_\|}\right]; &(3.20)\\
\hat{L}(\mathbf{k}) = &-\imath\left[\omega_{\mathbf{k}} - k_\| v_\| - k_\perp v_\perp\cos(\phi-\psi)\right] - \Omega_0\partial_\phi\\
= &-\Omega_0\exp\left(\frac{-\imath\left[(\omega_{\mathbf{k}} - k_\| v_\|)\phi - k_\perp v_\perp\sin(\phi-\psi)\right]}{\Omega_0}\right)\\
&\times\frac{\partial}{\partial\phi}\quad\exp\left(\frac{\imath\left[(\omega_{\mathbf{k}} - k_\| v_\|)\phi - k_\perp v_\perp\sin(\phi-\psi)\right]}{\Omega_0}\right). &(3.21)
\end{aligned}$$

Here we have introduced the gyrofrequency $\Omega_0 = qB_0/m$ of a charged particle with charge-to-mass ratio $q/m$ in the mean field. While it is straightforward to see how the operator $\hat{L}$ arises, deriving the polarization tensor $\hat{P}(\mathbf{k})$ is a little more tedious. The interested reader may refer to Appendix A for the technical details.

With $\hat{L}$ written as in equation (3.21), inverting it becomes a trivial task:[1]

$$\begin{aligned}
\hat{L}(\mathbf{k})^{-1} = &-\Omega_0^{-1}\exp\left(\frac{-\imath\left[\omega_{\mathbf{k}}\phi - k_\| v_\|\phi - k_\perp v_\perp\sin(\phi-\psi)\right]}{\Omega_0}\right)\\
&\times\int^{\phi} d\phi'\exp\left(\frac{\imath\left[\omega_{\mathbf{k}}\phi' - k_\| v_\|\phi' - k_\perp v_\perp\sin(\phi'-\psi)\right]}{\Omega_0}\right)
\end{aligned}$$

---

[1] Here $\int^x dx'\exp(\ldots)$ denotes the antiderivative with respect to $d/dx$, a short-hand notation we use in order to avoid dividing by a term that we will later let go to zero.

$$= -\Omega_0^{-1} \sum_{\ell,n} J_n\left(\frac{k_\perp v_\perp}{\Omega_0}\right) J_\ell\left(\frac{k_\perp v_\perp}{\Omega_0}\right) \exp\left(\imath(n-\ell)\psi - \frac{\imath(\omega_{\mathbf{k}} - k_\parallel v_\parallel - \ell\Omega_0)\phi}{\Omega_0}\right)$$
$$\times \int^{\phi} d\phi' \exp\left(\frac{\imath(\omega_{\mathbf{k}} - k_\parallel v_\parallel - n\Omega_0)\phi'}{\Omega_0}\right), \tag{3.22}$$

after the twofold application of a definition of the first-order Bessel function $J_n$,

$$\exp\left(\frac{\imath k_\perp v_\perp}{\Omega_0} \sin\alpha\right) = \sum_{n=-\infty}^{\infty} J_n\left(\frac{k_\perp v_\perp}{\Omega_0}\right) e^{\imath n\alpha}. \tag{3.23}$$

The next assumption we have to make is the gyrotropy of the fields, that is their symmetry around the magnetic mean-field direction. If this condition is fulfilled, the averaged phase-space density $\overline{f}$ will depend only weakly on the azimuthal direction of the particle velocity since every value of the azimuthal angle $\phi$ is equivalent from the point of view of a diffusing particle. Hence $\overline{f}$ can be split into a $\phi$-averaged part $\mathfrak{f}$, which depends only on the two velocity components perpendicular and parallel to the $z$ direction, $v_\perp$ and $v_\parallel$, and another part $\delta\mathfrak{f}$ with a weak dependence on $\phi$:

$$\mathfrak{f}(v_\perp, v_\parallel, t) = \int_0^{2\pi} \frac{d\phi}{2\pi} \overline{f}(\mathbf{v}, t), \tag{3.24}$$
$$\delta\mathfrak{f}(\mathbf{v}, t) = \overline{f}(\mathbf{v}, t) - \mathfrak{f}(v_\perp, v_\parallel, t). \tag{3.25}$$

In line with our assumption of gyrotropic turbulence we assume that $\delta\mathfrak{f}$ can be neglected in the first-order approximation of our analysis. Thus we replace $\overline{f}$ by $\mathfrak{f}$ in equation (3.18) and can set all derivatives with respect to $\phi$ to zero, simplifying matters significantly:

$$\begin{aligned}
\delta f(\mathbf{k}, \mathbf{v}, t) &= \hat{L}(\mathbf{k})^{-1} \hat{P}(\mathbf{k}) \overline{f}(\mathbf{v}, t) \\
&= -\frac{q}{m} \sum_{\ell,n=-\infty}^{\infty} \frac{J_n J_\ell}{\Omega_0} \exp\left[i(n-\ell)\psi - \frac{\imath}{\Omega_0}(\omega_{\mathbf{k}} - k_\parallel v_\parallel - \ell\Omega_0)\phi\right] \\
&\quad \times \int^{\phi} d\phi' \exp\left[\frac{\imath}{\Omega_0}(\omega_{\mathbf{k}} - k_\parallel v_\parallel - n\Omega_0)\phi'\right] \\
&\quad \times \left\{ e^{\imath(\phi-\psi)} \left[\frac{E_R(\mathbf{k}) e^{\imath\psi}}{\sqrt{2}} \hat{\Lambda}(\mathbf{k}) + \frac{k_\perp E_\parallel(\mathbf{k})}{2\omega_{\mathbf{k}}} \hat{H}(\mathbf{k})\right] \right. \\
&\quad + e^{-\imath(\phi-\psi)} \left[\frac{E_L(\mathbf{k}) e^{-\imath\psi}}{\sqrt{2}} \hat{\Lambda}(\mathbf{k}) + \frac{k_\perp E_\parallel(\mathbf{k})}{2\omega_{\mathbf{k}}} \hat{H}(\mathbf{k})\right] \\
&\quad \left. + E_\parallel(\mathbf{k}) \frac{\partial}{\partial v_\parallel} \right\} \overline{f}(\mathbf{v}, t)
\end{aligned}$$

$$
\begin{aligned}
&= -\frac{q}{m}\sum_{\ell,n=-\infty}^{\infty}\frac{J_\ell}{\Omega_0}\exp\left[i(n-\ell)\psi - \frac{\imath}{\Omega_0}(\omega_{\mathbf{k}} - k_\| v_\| - \ell\Omega_0)\phi\right] \\
&\quad \times \int^{\phi}\exp\left[\frac{\imath}{\Omega_0}(\omega_{\mathbf{k}} - k_\| v_\| - n\Omega_0)\phi'\right]d\psi' \\
&\quad \times \left[E_\perp(\mathbf{k},n)\hat{\Lambda}(\mathbf{k}) + E_\|(\mathbf{k})\left(\frac{k_\perp}{\omega_{\mathbf{k}}}\hat{H} + \frac{\partial}{\partial v_\|}\right)\right]\overline{f}(\mathbf{v},t),
\end{aligned}
\tag{3.26}
$$

where we have omitted the argument of the Bessel functions $J_{\ell,n}(k_\perp v_\perp/\Omega_0)$ and defined

$$
E_\perp(\mathbf{k},n) = \frac{E_R(\mathbf{k})}{\sqrt{2}}e^{\imath\psi}\,J_{n+1}\left(\frac{k_\perp v_\perp}{\Omega_0}\right) + \frac{E_L(\mathbf{k})}{\sqrt{2}}e^{-\imath\psi}\,J_{n-1}\left(\frac{k_\perp v_\perp}{\Omega_0}\right). \tag{3.27}
$$

The indices of the Bessel functions in $E_\perp$ are shifted by one due to the complex phases $e^{\pm\imath(\phi-\psi)}$ in equation (3.26). By applying definition (3.23), we can absorb these phase terms in the exponential factor on the left-hand side of that definition and then change the index over which the sum is taken from $\ell$ to $n = \ell \pm 1$.

### 3.2.3 Evolution of the space-average $\overline{f}$

Now that we have obtained a solution for the Fourier components $\delta f$ of $F$, we continue with our original task of describing the evolution of the space-averaged phase-space density $\overline{f}$. To this end we rewrite the space-averaged Vlasov equation, which we have already used to derive equation (3.4), in terms of the differential operator $\hat{P}$:

$$
\begin{aligned}
0 =& \partial_t\overline{f} + \frac{q}{m}\int\frac{d^3x}{V}\left[\mathbf{E}(\mathbf{x},t) + \mathbf{v}\times\mathbf{B}(\mathbf{x},t)\right]\cdot\nabla_{\mathbf{v}}F \\
=& \partial_t\overline{f} + \frac{q}{m}\int\frac{d^3x}{V}\left\langle\mathbf{v}\times\mathbf{B_0} + \left\{\int\frac{d^3k}{(2\pi)^3}\left[\tilde{\mathbf{E}}(-\mathbf{k},t) + \mathbf{v}\times\tilde{\mathbf{B}}(-\mathbf{k},t)\right]e^{-\imath\mathbf{k}\cdot\mathbf{x}}\right\}\right. \\
&\left.\cdot\nabla_{\mathbf{v}}\left[\overline{f} + \int\frac{d^3k'}{(2\pi)^3}\delta f(\mathbf{k}',\mathbf{v},t)e^{\imath\mathbf{k}'\cdot\mathbf{x}}\right]\right\rangle \\
=& \partial_t\overline{f} - \frac{q}{m}B_0\partial_\phi\overline{f} + \left\{\frac{q}{m}\int\frac{d^3k}{V(2\pi)^3}\left[\tilde{\mathbf{E}}(-\mathbf{k},t) + \mathbf{v}\times\tilde{\mathbf{B}}(-\mathbf{k},t)\right]\cdot\nabla_{\mathbf{v}}\delta f(\mathbf{k},\mathbf{v},t)\right\} \\
=& \partial_t\overline{f} - \Omega_0\partial_\phi\overline{f} - \int\frac{d^3k}{V(2\pi)^3}\hat{P}(-\mathbf{k})\delta f(\mathbf{k},\mathbf{v},t).
\end{aligned}
\tag{3.28}
$$

As noted above, our analysis is based on deviations from a gyrotropic phase-space distribution being negligibly small. Hence we can integrate the space-averaged Vlasov equation above over the azimuthal angle $\phi$ in velocity space and insert the Fourier components $\delta f$ written as in equation (3.26), which finally yields for the gyro-averaged velocity-space distribution $\mathfrak{f}$:

$$\begin{aligned}
\partial_t \mathfrak{f} =& \int_0^{2\pi} \frac{d\phi}{2\pi} \int \frac{d^3k}{V(2\pi)^3} \hat{P}(-\mathbf{k}) \hat{L}^{-1} \hat{P}(\mathbf{k}) \overline{f} \\
=& \int_0^{2\pi} \frac{d\phi}{2\pi} \int \frac{d^3k}{V(2\pi)^3} \times \\
& \Bigg\{ -\frac{q}{m} e^{\imath(\phi-\psi)} \left[ \frac{E_R e^{\imath\psi}}{\sqrt{2}} \left( \hat{\Lambda}(\mathbf{k}) + \imath \frac{\omega_{\mathbf{k}} - k_{\|} v_{\|}}{\omega_{\mathbf{k}} v_{\perp}} \partial_\phi \right) + \frac{k_{\perp} E_{\|}}{2\omega_{\mathbf{k}}} \left( \hat{H}(\mathbf{k}) + \imath \frac{v_{\|}}{v_{\perp}} \partial_\phi \right) \right]^* \\
& - \frac{q}{m} e^{-\imath(\phi-\psi)} \left[ \frac{E_L e^{-\imath\psi}}{\sqrt{2}} \left( \hat{\Lambda}(\mathbf{k}) - \imath \frac{\omega_{\mathbf{k}} - k_{\|} v_{\|}}{\omega_{\mathbf{k}} v_{\perp}} \partial_\phi \right) + \frac{k_{\perp} E_{\|}}{2\omega_{\mathbf{k}}} \left( \hat{H}(\mathbf{k}) - \imath \frac{v_{\|}}{v_{\perp}} \partial_\phi \right) \right]^* \\
& - \frac{q}{m} \left[ \imath \frac{k_{\perp}}{\omega_{\mathbf{k}}} \left( \frac{E_L e^{-\imath\phi} - E_R e^{\imath\phi}}{\sqrt{2}} \right) \partial_\phi + E_{\|} \frac{\partial}{\partial v_{\|}} \right]^* \Bigg\} \times \hat{L}^{-1}(\mathbf{k}) \hat{P}(\mathbf{k}) \overline{f}. \qquad (3.29)
\end{aligned}$$

Here we have used the fact that $\hat{P}(-\mathbf{k})$ is the complex conjugate of $\hat{P}(\mathbf{k})$, as can be easily verified by inverting the sign of $\mathbf{k}$ in the definition of $\hat{P}$, equation (3.20). We denote the complex conjugate of $z$ by $z^*$.

If we allow for a small imaginary part of $\omega_{\mathbf{k}} = \overline{\omega}_{\mathbf{k}} + i\epsilon$, corresponding to a small growth or decay rate of the mode $\mathbf{k}$, and then take the limit of $\epsilon \to 0$, we can apply the Sochocki-Plemelj theorem (see Stix, 1992) to write the integral over the $\phi$-dependent part of $\hat{L}^{-1}(\mathbf{k})$ (the two exponentials in (3.22)) as follows:

$$\begin{aligned}
\lim_{\epsilon\to 0} \int_0^{2\pi} \frac{d\phi}{2\pi} e^{-\imath(\overline{\omega}_{\mathbf{k}} + \imath\epsilon - k_{\|} v_{\|} - m\Omega_0)\phi/\Omega_0} \int^{\phi} d\phi' e^{\imath(\overline{\omega}_{\mathbf{k}} + \imath\epsilon - k_{\|} v_{\|} - n\Omega_0)\phi'/\Omega_0} = \\
= \lim_{\epsilon\to 0} \int_0^{2\pi} \frac{d\phi}{2\pi} e^{-\imath(\overline{\omega}_{\mathbf{k}} + \imath\epsilon - k_{\|} v_{\|} - m\Omega_0)\phi/\Omega_0} \frac{e^{\imath(\overline{\omega}_{\mathbf{k}} + \imath\epsilon - k_{\|} v_{\|} - n\Omega_0)\phi/\Omega_0}}{\imath(\overline{\omega}_{\mathbf{k}} + \imath\epsilon - k_{\|} v_{\|} - n\Omega_0)/\Omega_0} \\
= \Omega_0 \, \delta_{m,n} \times \left[ \mathcal{P}\left( \frac{1}{\overline{\omega}_{\mathbf{k}} - k_{\|} v_{\|} - n\Omega_0} \right) - \pi\imath \, \delta(\overline{\omega}_{\mathbf{k}} - k_{\|} v_{\|} - n\Omega_0) \right], \qquad (3.30)
\end{aligned}$$

and thus arrive at (the principal parts $\mathcal{P}$ of $+k_{\|}$ and $-k_{\|}$ cancel each other out):

$$\begin{aligned}
\partial_t \mathfrak{f} =& \frac{q^2}{m^2} \int \frac{d^3k}{V(2\pi)^3} \\
& \times \sum_{n=-\infty}^{\infty} \left\{ E_{\perp}(\mathbf{k},n) \left[ \hat{\Lambda}(\mathbf{k}) + \frac{\omega_{\mathbf{k}} - k_{\|} v_{\|}}{\omega_{\mathbf{k}} v_{\perp}} \right] + E_{\|}(\mathbf{k}) J_n \left[ \frac{\partial}{\partial v_{\|}} + \frac{n\Omega_0}{\omega_{\mathbf{k}} v_{\perp}} \hat{H}(\mathbf{k}) \right] \right\}^* \\
& \times \pi\Omega_0 \delta(\omega_{\mathbf{k}} - k_{\|} v_{\|} - n\Omega_0) \left\{ E_{\perp}(\mathbf{k},n) \hat{\Lambda}(\mathbf{k}) + E_{\|}(\mathbf{k}) J_n \left[ \frac{\partial}{\partial v_{\|}} + \frac{n\Omega_0}{\omega_{\mathbf{k}} v_{\perp}} \hat{H}(\mathbf{k}) \right] \right\} \overline{f}. \qquad (3.31)
\end{aligned}$$

For stable wave modes (with $\epsilon = 0$), equation (3.18) can only be solved for $\delta f(\mathbf{k}, \mathbf{v}, t)$ if the resonance condition $\omega_{\mathbf{k}} = k_{\|} v_{\|} + n\Omega_0$ can be fulfilled for a (positive or negative) integer value of $n$. In other words, the wave affects the trajectory of a cosmic-ray particle only if the wave frequency in a reference frame co-moving with the particle along the magnetic mean-field is an integer multiple of the gyrofrequency – or if the wave frequency vanishes in this co-moving frame altogether (if resonance occurs for $n = 0$). The latter case is known as Landau resonance, in analogy with Landau damping describing the absorption of plasma-wave energy by resonant charged particles (see Landau (1946) or any basic plasma physics textbook).

An electromagnetic wave propagating parallel to the magnetic mean-field has no perpendicular electric field since $\mathbf{E} = \mathbf{k}\times\mathbf{B} = 0$. However, if an electrostatic oscillation is excited in the plasma, it will produce parallel electric fields that are able to coherently accelerate or decelerate a charged particle along the magnetic mean-field, since the oscillation appears as a static electric field in the frame of the particle.

On the other hand, if $n \neq 0$ the wave-particle interaction is known as gyroresonance or cyclotron resonance. In this case the perpendicular electric field of the wave will primarily scatter the angle of the particle velocity with respect to the magnetic mean-field.

### 3.2.4 The velocity-space diffusion equation

In summary, and assuming again gyrotropy such that $\overline{f}$ on the right-hand side of equation (3.31) can be replaced by the gyro-averaged velocity-space density $\mathfrak{f}$, we can write our result symbolically as an integral over a Dirac functional (*e.g.* Kennel & Engelmann, 1966; Schlickeiser, 1989),

$$\partial_t \mathfrak{f} = 2\pi \frac{q^2}{m^2} \int \frac{d^3k}{V(2\pi)^3} \sum_{n=-\infty}^{\infty} v_\perp^{-1} \hat{\Lambda}(\mathbf{k}) v_\perp \langle W^* W\rangle(\mathbf{k}, n) \hat{\Lambda}(\mathbf{k}) \delta(\omega_\mathbf{k} - k_\parallel v_\parallel - n\Omega_0) \mathfrak{f}, \tag{3.32}$$

where the terms in square brackets have been transformed as follows, anticipating the resonance condition $n\Omega_0 = \omega_\mathbf{k} - k_\parallel v_\parallel$:

$$\left[\hat{\Lambda}(\mathbf{k}) + \frac{\omega_\mathbf{k} - k_\parallel v_\parallel}{\omega_\mathbf{k} v_\perp}\right] = v_\perp^{-1} \hat{\Lambda}(\mathbf{k}) v_\perp, \tag{3.33}$$

and

$$\left[\frac{\partial}{\partial v_\parallel} + \frac{n\Omega_0}{\omega_\mathbf{k} v_\perp} \hat{H}(\mathbf{k})\right] = \frac{\partial}{\partial v_\parallel} + \frac{\omega_\mathbf{k} - k_\parallel v_\parallel}{\omega_\mathbf{k}} \left(v_\parallel \frac{\partial}{\partial v_\perp} - v_\perp \frac{\partial}{\partial v_\parallel}\right) = \frac{v_\parallel}{v_\perp} \hat{\Lambda}(\mathbf{k}). \tag{3.34}$$

Both transformations are straightforward to derive by inserting the definitions (3.15) and (3.16). We have introduced the polarization tensor $\langle W^* W\rangle$, defined as

$$\langle W^* W\rangle(\mathbf{k}, n) = \left[E_\perp(\mathbf{k}, n) + \frac{v_\parallel}{v_\perp} J_n E_\parallel(\mathbf{k})\right]^* \left[E_\perp(\mathbf{k}, n) + \frac{v_\parallel}{v_\perp} J_n E_\parallel(\mathbf{k})\right]. \tag{3.35}$$

One last change of coordinates is useful before we can become more specific as to which type of waves interacts with the phase-space distribution: In order to see more easily how strongly the particles are deflected by the turbulence they propagate in, we introduce the angle between the particle velocity and the magnetic mean-field in the form of the pitch-angle cosine $\mu = v_{\|}/(v_{\perp}^2 + v_{\|}^2)$. Written in terms of $\mu$ and $v$, the differential operator $\hat{\Lambda}$ becomes

$$\begin{aligned}\hat{\Lambda}(\mathbf{k}) &= \left(1 - \frac{k_{\|}v_{\|}}{\omega_{\mathbf{k}}}\right)\sqrt{1-\mu^2}\left(\frac{\partial}{\partial v} - \frac{\mu}{v}\frac{\partial}{\partial \mu}\right) + \frac{k_{\|}v_{\|}}{\omega_{\mathbf{k}}}\left(\frac{v_{\|}}{v}\frac{\partial}{\partial v} + \frac{v_{\perp}^2}{p^3}\frac{\partial}{\partial \mu}\right) \\ &= \begin{cases} \sqrt{1-\mu^2}\left(\frac{\partial}{\partial v} + \frac{1-\mu^2}{v}\frac{\partial}{\partial \mu}\right), & \text{for}\, n = 0, \\ \left(1 - \frac{k_{\|}v_{\|}}{\omega_{\mathbf{k}}}\right)\sqrt{1-\mu^2}\left[\left(1 + \frac{\mu v k_{\|}}{n\Omega_0}\right)\frac{\partial}{\partial v} + \left(\frac{(1-\mu^2)k_{\|}v}{n\Omega_0} - \mu\right)v^{-1}\frac{\partial}{\partial \mu}\right], & \text{for}\, n \neq 0. \end{cases}\end{aligned} \tag{3.36}$$

while equation (3.32) itself maintains its form in pitch-angle coordinates.

## 3.3 Alfvénic turbulence models

### 3.3.1 Momentum diffusion in evolving Alfvénic turbulence

Our investigation involves the interaction of cosmic-ray particles with shear-Alfvén waves, which are defined by the very simple dispersion relation

$$\omega_{\mathbf{k}} = -\beta v_A k_{\|}, \quad \beta = \pm 1, \tag{3.37}$$

with the Alfvén speed defined as $v_A^2 = B_0^2/(\mu_0 \rho)$, as in subsection 2.3.1. The sign of $\beta$ distinguishes Alfvén waves propagating in the direction of the mean magnetic field ($\beta = -1$) from waves propagating in the opposite direction ($\beta = 1$). We have adopted the same sign convention for co- and counter-propagating waves as in the previous chapter on magnetohydrodynamics, hence the minus sign in the dispersion relation.

Employing the Alfvén-wave dispersion relation, we can express $k_{\|}$ in terms of the Alfvén speed,

$$k_{\|} = \frac{n\Omega_0}{\frac{\omega_{\mathbf{k}}}{k_{\|}} - v_{\|}} = \frac{n\Omega_0}{-\beta v_A - \mu v},$$

and simplify $\hat{\Lambda}$ (for $n \neq 0$) by bringing it into the form

$$\begin{aligned}\hat{\Lambda}(\mathbf{k}) =& \frac{k_{\|}}{\omega_{\mathbf{k}}}(-\beta v_A - \mu v)\sqrt{1-\mu^2}\left\{\left(1 + \frac{\mu v}{-\beta v_A - \mu v}\right)\frac{\partial}{\partial v}\right. \\ &\left. + \left[(1-\mu^2)v(-\beta v_A - \mu v)^{-1} - \mu\right]v^{-1}\frac{\partial}{\partial \mu}\right\} \\ =& \frac{k_{\|}}{\omega_{\mathbf{k}}}\sqrt{1-\mu^2}\left[-\beta v_A \frac{\partial}{\partial v} + (v + \beta \mu v_A)v^{-1}\frac{\partial}{\partial \mu}\right].\end{aligned} \tag{3.38}$$

Assuming we deal with incompressible Alfvénic turbulence, made up only of shear-Alfvén waves propagating either in the direction of the magnetic mean-field or opposite to it can exist, we let $k_\perp = 0$, $k = k_\parallel$, and consequently $E_\parallel = 0$. As explained above, Landau resonance (for $n = 0$) can only occur if the electric field has a parallel component, so we can limit our analysis to gyroresonant interactions with $n \neq 0$. Furthermore we assume that the spectral power of the wave turbulence can be neatly divided into the energy of waves propagating in either direction, similar to the Elsasser energies $\mathcal{E}^\pm$ introduced in the previous chapter. Hence the magnetic turbulence can be modeled as the superposition of a component due to co-propagating waves, $B^-_{L,R}$, and Alfvén waves propagating in the negative $z$-direction, $B^+_{L,R}$. Under these conditions the integral over $\langle W^* W\rangle(\mathbf{k}, n)$ can be written in terms of the longitudinal power spectrum of the magnetic field,

$$\int dk_\parallel \, P^\beta_{L,R}(k_\parallel) = \int \frac{d^3k}{V} \langle B^\beta_{L,R}(\mathbf{k})^* B^\beta_{L,R}(\mathbf{k})\rangle(\mathbf{k}, n). \tag{3.39}$$

This gives, after converting the electric field back to the magnetic field with Faraday's induction equation,

$$\begin{aligned}\int \frac{d^3k}{V}\langle W^* W\rangle(\mathbf{k}, n) &= \int \frac{d^3k}{V}\frac{1}{4}\left(\langle E_R(\mathbf{k})^* E_R(\mathbf{k})\rangle \delta_{n,-1} + \langle E_L(\mathbf{k})^* E_L(\mathbf{k})\rangle \delta_{n,+1}\right) \\ &= \int dk_\parallel \, \frac{\omega^2_{\mathbf{k}_\parallel}}{4k^2_\parallel} \sum_{\beta=\pm1} \left(P^\beta_R(k_\parallel)\delta_{n,-1} + P^\beta_L(k_\parallel)\delta_{n,+1}\right).\end{aligned} \tag{3.40}$$

Combining equations (3.32), (3.38), and (3.40), the diffusion equation reads

$$\begin{aligned}\partial_t \mathfrak{f} =& \frac{\pi q^2}{2m^2} \sum_{\beta=\pm1} \left[\left(1 + \frac{\beta\mu v_A}{v}\right)\partial_\mu - \beta v_A \partial_v\right] \frac{v}{|\mu v + \beta v_A|}(1-\mu^2) \\ &\times \left(P^\beta_R(k_\parallel)\delta_{n,-1} + P^\beta_L(k_\parallel)\delta_{n,+1}\right)\left[\left(1 + \frac{\beta\mu v_A}{v}\right)\partial_\mu - \beta v_A \partial_v\right]\mathfrak{f},\end{aligned} \tag{3.41}$$

or, to put it more concisely

$$\partial_t \mathfrak{f} = \left(\partial_\mu D_{\mu\mu}\partial_\mu + \partial_\mu D_{\mu p}\partial_p + p^{-2}\partial_p p^2 D_{\mu p}\partial_\mu + p^{-2}\partial_p(p^2 D_{pp}\partial_p)\right)\mathfrak{f}, \tag{3.42}$$

if we switch from velocity-space to momentum-space, $p = mv$, and introduce the following diffusion coefficients:

$$D_{\mu\mu} = \sum_{\beta=\pm1} \frac{\pi\Omega_0^2}{2}(1-\mu^2)\frac{(1+\beta\mu v_A/v)^2}{|\mu v + \beta v_A|}\,\frac{P^\beta_L[-\Omega_0/(\mu v + \beta v_A)] + P^\beta_R[+\Omega_0/(\mu v + \beta v_A)]}{B_0^2}, \tag{3.43}$$

$$D_{\mu p} = -\sum_{\beta=\pm 1} \frac{\pi\Omega_0^2}{2} \beta m v_A (1-\mu^2) \frac{1+\beta\mu v_A/v}{|\mu v+\beta v_A|}\, \frac{P_L^\beta[-\Omega_0/(\mu v+\beta v_A)] + P_R^\beta[+\Omega_0/(\mu v+\beta v_A)]}{B_0^2}, \tag{3.44}$$

$$D_{pp} = \sum_{\beta=\pm 1} \frac{\pi\Omega_0^2}{2} m^2 v_A^2 \frac{1-\mu^2}{|\mu v+\beta v_A|}\, \frac{P_L^\beta[-\Omega_0/(\mu v+\beta v_A)] + P_R^\beta[+\Omega_0/(\mu v+\beta v_A)]}{B_0^2}. \tag{3.45}$$

Equation (3.42) constitutes the first important result for our later investigation, the Fokker-Planck equation for the velocity-space diffusion of charged particles in Alfvénic turbulence. We will compare the pitch-angle diffusion coefficient $D_{\mu\mu}$ predicted by this equation with the short-term behavior that we observe in test-particle simulations in chapter 6. To determine the rate of stochastic heating, which we will investigate for isotropic pitch-angle distributions in chapter 5, we first need to average over the pitch-angle.

### 3.3.2 The stochastic heating rate

In strong turbulence one expects that all particle populations will be isotropized quickly with a typical scattering time $\tau \ll k_{\mathrm{min}}^{-1} v_A^{-1}$, and, averaging over (yet) another degree of freedom, we introduce a pitch-angle-averaged momentum distribution $G(p,t)$, which only depends on the norm of $\mathbf{p}$, and a deviation $g(\mu,v,t)$:

$$G(p,t) = \int_{-1}^{+1} d\mu\, \mathfrak{f}(\mu,v,t), \tag{3.46}$$

$$g(\mu,p,t) = \mathfrak{f}(\mu,v,t) - G(p,t). \tag{3.47}$$

Integrating the diffusion equation (3.42) over $\mu$ yields

$$\begin{aligned} \frac{1}{2}\frac{\partial G}{\partial t} &= \left[ D_{\mu\mu}\partial_\mu g + \frac{1}{2} D_{\mu p}\partial_p G + D_{\mu p}\partial_p g \right]_{\mu=-1}^{\mu=+1} \\ &\quad + \frac{1}{2p^2}\partial_p p^2 \left( \int_{-1}^{+1} d\mu\, D_{\mu p}\partial_\mu g + \frac{1}{2}\int_{-1}^{+1} d\mu\, D_{pp}\partial_p G + \int_{-1}^{+1} d\mu\, D_{pp}\partial_p g \right), \end{aligned} \tag{3.48}$$

where the terms evaluated at $\mu = \pm 1$ vanish since all diffusion coefficients include the factor $(1-\mu^2)$, giving 0 for parallel and antiparallel particle propagation.

Subtracting the averaged equation from the diffusion equation, we obtain

$$\begin{aligned} \partial_\mu \left( D_{\mu\mu}\partial_\mu g + \frac{1}{2} D_{\mu p}\partial_p G + D_{\mu p}\partial_p g \right) &= -\partial_t g + p^{-2}\partial_p p^2 \left[ \left( D_{\mu p}\partial_\mu g - \frac{1}{2}\int_{-1}^{+1} d\mu\, D_{\mu p}\partial_\mu g \right) \right. \\ &\quad \left. + \frac{1}{2}\left( D_{pp} - \frac{1}{2}\int_{-1}^{+1} d\mu\, D_{pp} \right)\partial_p G + \left( D_{pp}\partial_p g - \frac{1}{2}\int_{-1}^{+1} d\mu\, D_{pp}\partial_p g \right) \right]. \end{aligned} \tag{3.49}$$

This equation can be simplified drastically if we assume that the deviation $g$ from an isotropic pitch-angle distribution is of order of the small scattering time $\tau$, while the pitch-angle diffusion coefficient $D_{\mu\mu}$ is of order $\tau^{-1}$. Moreover, we will assume that the particles travel at speeds much greater than the Alfvén speed and introduce the smallness parameter $\gamma = v_A/v$ such that $D_{\mu p} \in \mathcal{O}(\gamma)$ and $D_{pp} \in \mathcal{O}(\gamma^2)$. After neglecting all terms that are at least second-order in either $\gamma$ or $\tau$, the diffusion-convection equation simplifies to

$$\partial_\mu \left( D_{\mu\mu} \partial_\mu g + \frac{1}{2} D_{\mu p} \partial_p G \right) = 0. \tag{3.50}$$

Using the fact that $D_{\mu\mu}(\pm 1) = D_{\mu p}(\pm 1) = 0$, we conclude that the above expression must vanish for all values of $\mu$:

$$D_{\mu\mu} \partial_\mu g + \frac{1}{2} D_{\mu p} \partial_p G = 0. \tag{3.51}$$

Another integration over $\mu$ from $-1$ to $+1$ yields the final solution for $g$ in dependence of $G$, which we can then insert into equation (3.48):

$$g(\mu, p, t) = -\frac{1}{2} \int_\mu^{+1} d\mu' \, \frac{D_{\mu p}(\mu')}{D_{\mu\mu}(\mu')} \partial_p G, \tag{3.52}$$

where this time the constant of integration is determined by the condition that $g$, the deviation of $\overline{f}$ from its own pitch-angle average $G$, must vanish when integrated over all possible values of $\mu$ from $-1$ to $+1$:

$$\int_{-1}^{+1} d\mu \, g(\mu, p, t) = 0. \tag{3.53}$$

Had we bothered to include in our derivation a $z$-dependency of the phase-space density and thus explicitly considered inhomogeneities in $G$ along the mean magnetic field, we would have found two additional terms that can lead to local deviations in the pitch-angle distribution (*cf.* Schlickeiser, 1989): One term is proportional to the derivative of $G$ along the mean-field direction $z$ and represents the simple observation that density gradients in position space will lead to an inhomogeneous pitch-angle distribution while the density is isotropizing.

The second term is proportional to the gradient of $G$ in momentum space, as it might result, for instance, from a relative velocity between the source of cosmic-ray particles and the observer. Hence this term is the origin of the Compton-Getting effect, which predicts that observations measure an anisotropic distribution of high-energy cosmic-ray sources merely due to to the movement of the Milky Way (Compton & Getting, 1935). To this date, however, this anisotropy has not been actually measured.

In order to obtain the final form of the cosmic-ray transport equation, we insert equation (3.52) into equation (3.48), neglecting terms of second or higher order in $\gamma$ or

$\tau$ as before, and obtain

$$\begin{aligned}\partial_t G(p,t) &= p^{-2}\partial_p\left(p^2\int_{-1}^{+1} d\mu\, D_{\mu p}\partial_\mu g + \frac{p^2}{2}\int_{-1}^{+1} d\mu\, D_{pp}\partial_p G\right)\\ &= p^{-2}\partial_p\left(\frac{p^2}{2}\int_{-1}^{+1} d\mu\, D_{pp}\partial_p G - \frac{p^2}{2}\int_{-1}^{+1} d\mu\, \frac{D_{\mu p}^2}{D_{\mu\mu}}\partial_p G\right)\end{aligned} \tag{3.54}$$

or more concisely:

$$\partial_t G(p,t) = p^{-2}\frac{\partial}{\partial p}\left[p^2\mathcal{D}_{pp}\frac{\partial}{\partial p}G(p,t)\right], \tag{3.55}$$

where we have defined the new momentum-diffusion coefficient $\mathcal{D}_{pp}$, which corresponds to the rate of stochastic heating:

$$\mathcal{D}_{pp} = \frac{1}{2}\int_{-1}^{+1} d\mu\left(D_{pp} - \frac{D_{\mu p}^2}{D_{\mu\mu}}\right). \tag{3.56}$$

Following Dung & Schlickeiser (1990), we now define the parameter $r$ as the ratio of energy of the co-propagating Alfvén waves and the total wave energy for each polarization:

$$r_{L,R} = \frac{P_{L,R}^-}{P_{L,R}^+ + P_{L,R}^-}. \tag{3.57}$$

Since we do not investigate the effect of magnetic helicity in this work, we will make no distinction between left-and right-handed polarization and assume for simplicity that the same ratio describes both polarizations, $r = r_L = r_R$. This allows us, moreover, to define a cross-helicity parameter $\sigma_c$ similar to the definition in terms of the Elsasser energies in the previous chapter:

$$\sigma_c = 2r - 1. \tag{3.58}$$

As a comparison with equation (3.57) reveals, $\sigma_c = +1$ characterizes Alfvénic turbulence in which only Alfvén waves propagating opposite to the magnetic mean field are present, while $\sigma_c = -1$ corresponds to a wave population with only co-propagating waves.

Under the assumption of zero magnetic helicity, it is possible to write the diffusion coefficients in terms of $\sigma_c$. Before doing so, however, we must decide which form of the spectrum we assume for $P$. As we have already shown in the previous chapter, one expects a power-law spectrum of the form $P(k) \propto k^{-s}$ from theoretical considerations. We impose the additional condition that all wave vectors are either parallel or antiparallel to the $z$ direction, a constraint that leads to what is usually called slab turbulence. This picture is obviously in perfect agreement with the shear-Alfvén wave model we have introduced earlier. Introducing the two spectral indices $s^+$ and $s^-$ and a lower cut-off of the spectrum at the wavenumber $k_{\mathrm{min}}$, the spectrum can be written as

$$P^{\pm}(k_z)\,dk_z = P_0^{\pm}\left(\frac{k_z}{k_{\mathrm{min}}}\right)^{-s^{\pm}} dk_z. \tag{3.59}$$

Assuming that the ratio of energies in both Alfvén-wave populations as expressed via the parameter $r$ is constant across the entire spectrum, we can introduce another parameter $P_0 = P^+ + P^-$ reflecting the combined spectral power of both Alfvén-wave populations such that

$$P_0^{\pm} = P_0 \times \frac{1 \pm \sigma_c}{2}. \tag{3.60}$$

This allows us to write the velocity-space diffusion coefficients as a function of the cross-helicity parameter $\sigma_c$ and the two spectral exponents $s^{\pm}$:

$$D_{\mu\mu} = \frac{\pi}{4}\,(1-\mu^2)P_0 \sum_{\beta=\pm 1} \Omega_0^{2-s^{\beta}}\,\frac{1+\beta\sigma_c}{B_0^2}\,(s^{\beta}-1)\,k_{\mathrm{min}}^{s^{\beta}-1}\,v^{s^{\beta}-1}\,(1+\beta\mu\gamma)^2\,|\mu+\beta\gamma|^{s^{\beta}-1}, \tag{3.61}$$

$$\begin{aligned} D_{\mu p} = &-\frac{\pi}{4}\,m v_A\,(1-\mu^2)P_0 \\ &\times \sum_{\beta=\pm 1} \beta\Omega_0^{2-s^{\beta}}\,\frac{1+\beta\sigma_c}{B_0^2}\,(s^{\beta}-1)\,k_{\mathrm{min}}^{s^{\beta}-1}\,v^{s^{\beta}-1}\,(1+\beta\mu\gamma)\,|\mu+\beta\gamma|^{s^{\beta}-1}, \end{aligned} \tag{3.62}$$

$$\begin{aligned} D_{pp} = &\frac{\pi}{4}\,m^2 v_A^2\,(1-\mu^2)P_0 \\ &\times \sum_{\beta=\pm 1} \Omega_0^{2-s^{\beta}}\,\frac{1+\beta\sigma_c}{B_0^2}\,(s^{\beta}-1)\,k_{\mathrm{min}}^{s^{\beta}-1}\,v^{s^{\beta}-1}\,|\mu+\beta\gamma|^{s^{\beta}-1}. \end{aligned} \tag{3.63}$$

These coefficients give predictions of cosmic-ray diffusion in imbalanced turbulence, as discussed in chapter 2, although under extremely simplified assumptions about the spectrum of both co- and counter-propagating Alfvén-wave energies (equation (3.60)).

### 3.3.3 The magnetostatic limit

Jokipii (1966) originally derived the magnetostatic limit of these diffusion coefficients, as we explained at the beginning of this chapter. High-energy cosmic-ray particles in the interstellar medium have a kinetic energy that exceeds their rest mass by far, with energies ranging from 1 GeV to several hundred TeV for galactic cosmic rays alone. In this case the velocity $v$ of the charged particles is approximately equal to the speed of light and the Alfvén velocity $v_A$ becomes negligibly small compared to $v$. Heuristically speaking, we can assume that the turbulent magnetic fields of the interstellar medium are fixed in time and neglect the effect of traveling waves since cosmic-ray particles pass through the turbulence much faster than the waves.

In this limit ($v_A \to 0$), the diffusion coefficients of the Fokker-Planck equation become:

$$
\begin{aligned}
D_{\mu\mu} &= \frac{\pi\Omega_0^2}{2}(1-\mu^2)\,\frac{1}{|\mu v|}\,\frac{P_L[-\Omega_0/(\mu v)] + P_R[+\Omega_0/(\mu v)]}{B_0^2}, && (3.64)\\
D_{\mu p} &= 0, && (3.65)\\
D_{pp} &= 0, && (3.66)
\end{aligned}
$$

and consequently

$$\mathcal{D}_{pp} = 0. \tag{3.67}$$

Obviously the cosmic-ray momentum is a constant in the fast-particle limit since both $D_{\mu p}$ and $D_{pp}$ disappear. Only the pitch-angle diffusion coefficient $D_{\mu\mu}$ remains since even relativistic cosmic-ray particles gyrate around magnetic field lines and can hence be deflected by perturbations of the magnetic field.

### 3.3.4 Magnetodynamic turbulence

In quasilinear models it can sometimes be convenient to retain the time dependence of the magnetic fields while the electric fields are ignored, although no physical scenario can be given in which this approximation would be justified. In this case, the Lorentz force acts perpendicularly to the particle velocity and the total energy of the particle must be conserved:

$$\frac{\partial}{\partial t}E = m\mathbf{v}\cdot[\mathbf{B}(\mathbf{x},t)\times\mathbf{v}] = 0. \tag{3.68}$$

In this case the norm of the momentum of a particle must also be constant, and it follows that we can set $D_{\mu p} = D_{pp} = 0$ right away as no diffusion in momentum space can occur and all terms in $\partial_p$ must vanish. Deriving the new form of $D_{\mu\mu}^{(\mathrm{md})}$ requires more subtlety; the new form of the integral $\mathcal{I}(\mathbf{k})$ becomes

$$
\begin{aligned}
\mathcal{I}^{(\mathrm{md})}(\mathbf{k}) =& \frac{q}{m}e^{\imath(\phi-\psi)}\left[\frac{E_R e^{\imath\psi}}{\sqrt{2}}\left(\hat{\Lambda} - \frac{\partial}{\partial v_\perp} - \imath\frac{k_\parallel v_\parallel}{\omega_{\mathbf{k}} v_\perp}\partial_\phi\right) + \frac{k_\perp E_\parallel}{2\omega_{\mathbf{k}}}\left(\hat{H} + \imath\frac{v_\parallel}{v_\perp}\partial_\phi\right)\right]\overline{f} && (3.69)\\
&+ \frac{q}{m}e^{-\imath(\phi-\psi)}\left[\frac{E_L e^{-\imath\psi}}{\sqrt{2}}\left(\hat{\Lambda} - \frac{\partial}{\partial v_\perp} + \imath\frac{k_\parallel v_\parallel}{\omega_{\mathbf{k}} v_\perp}\partial_\phi\right) + \frac{k_\perp E_\parallel}{2\omega_{\mathbf{k}}}\left(\hat{H} - \imath\frac{v_\parallel}{v_\perp}\partial_\phi\right)\right]\overline{f} && (3.70)\\
&+ \frac{q}{m}B_0\partial_\phi\delta f && (3.71)\\
&+ \mathcal{O}(\delta f^2). && (3.72)
\end{aligned}
$$

The remaining derivation proceeds completely analogously to the electrodynamic case described so far. The final result $D_{\mu\mu}^{(\mathrm{md})}$ for the pitch-angle diffusion coefficient in

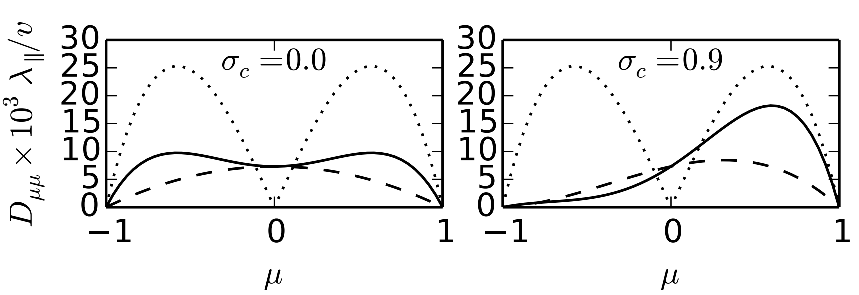

Figure 3.1: Shapes of the pitch-angle diffusion coefficient $D_{\mu\mu}$ according to quasilinear theory for Alfvén-speed particles ($v = v_A$) in magnetostatic turbulence (dotted), magnetodynamic turbulence (dashed), and fully electrodynamic MHD turbulence (solid lines) with amplitude $\delta B/B_0 = 0.1$ and Kolmogorov-like spectra $s^+ = s^- = 5/3$ for normalized cross helicities $\sigma_c = 0.0$ and $\sigma_c = 0.9$. ($\lambda_\| = 2\pi/k_{\min}$)

this 'magnetodynamic' turbulence model is (*cf.* Shalchi *et al.* , 2009):

$$D_{\mu\mu}^{(\mathrm{md})} = \sum_{\beta=\pm1} \frac{\pi\Omega_0^2}{4}(1-\mu^2)\frac{1}{|\mu v + \beta v_A|}\frac{P_L^\beta[-\Omega_0/(\mu v + \beta v_A)] + P_R^\beta[+\Omega_0/(\mu v + \beta v_A)]}{B_0^2}. \quad (3.73)$$

A comparison with equation (3.62) yields that the result is almost identical with the electrodynamic pitch-angle diffusion coefficient, apart from the missing factor $(1-\mu\beta v_A)^2$ in the numerator.

---

We have derived the form of the pitch-angle diffusion coefficient $D_{\mu\mu}$ predicted by quasilinear theory, for fully electrodynamic turbulence and two more abstract scenarios: magnetodynamic and magnetostatic turbulence, where the heating of test-particles due to the motional electric field is neglected. Although we had to use highly simplified shapes for the power spectra of the turbulence, we were able to give relatively straightforward expressions for the rate of particle scattering as a function of cross helicity, or the degree of imbalance.

The dependence of these rates on the pitch-angle cosine $\mu$ is compared in figure 3.1 for balanced and strongly cross-helical turbulence. While the graphs of all three scenarios exhibit a perfect symmetry with respect to the $\mu = 0$-axis in the balanced case, the asymmetry of co- and counter-propagating Alfvén waves in the imbalanced case results in a strongly asymmetric shape of the $\mu$-$D_{\mu\mu}$-plot for electrodynamic and magnetodynamic turbulence. However, since both Alfvén-wave types are indistinguishable in a frozen snapshot of the turbulent magnetic field, this asymmetry disappears in magnetostatic imbalanced turbulence.

The momentum-diffusion coefficient $\mathcal{D}_{pp}$ disappears if the electric fields are ignored, so we will compare our simulation results only to the electrodynamic result given in equation (3.55). We will show that the general dependence on the cross helicity $\sigma_c$ in our MHD simulations is predicted accurately by quasilinear theory, even though it is also derived using a simplified shape of the power spectrum. The next chapter discusses the methodology of these simulations, with an emphasis on the difference between the simple theoretical power spectrum and the more realistic spectrum which our numerical study uses.

# Chapter 4

# Controlling Helicities in Pseudospectral MHD Simulations

*As explorer of the earth*
*and adventurer of the stars I know that*
*I should've known. Now the sorrow spectrum*
*grows and the world will stay unsaved.*
*I know that I should've seen.*

– *Darkday* (Edge of Sanity, 1992)

**Chapter Summary**

- We solve the pseudospectral equations for incompressible MHD using the TURBO code.
- A special cross-helical forcing scheme allows the continuous injection of both energy and cross helicity by correlated driving of the velocity and magnetic field.
- Steady-state turbulent fields with an arbitrary amount of cross helicity can be constructed for an isotropic configuration or a weak homogeneous external magnetic field.
- The spectra of the fields in the inertial range agree well with the predictions by Iroshnikov & Kraichnan and Goldreich & Sridhar presented in chapter 2.
- More anisotropic turbulence with a stronger magnetic mean-field can be generated if the forcing scheme is adapted accordingly.

Our goal in later chapters will be to compare the diffusion coefficients derived in the previous chapter with charged-particle transport in realistic three-dimensional magnetohydrodynamic turbulence with non-zero cross helicity. In this chapter, the method by which we obtain cross-helical turbulence is explained and MHD field configurations are analyzed.

Some of the content presented here has been presented at the Cosmic-Rays in the Interstellar Medium workshop (Weidl *et al.* , 2014).

## 4.1 Numerical methods

### 4.1.1 Outline of MHD equations in TURBO

We use the pseudospectral MHD code TURBO (see Teaca *et al.* , 2009), which solves the equations of resistive incompressible MHD on a cubic grid with periodic boundaries. These equations have been reviewed in chapter 2. As the mass density $\rho$ remains constant in incompressible media, the momentum equation (2.5) becomes

$$\rho\left[\partial_t \mathbf{u} + (\mathbf{u}\cdot\nabla)\mathbf{u}\right] = \mathbf{j}\times\mathbf{B} + \nu\rho\,\nabla^2\mathbf{u} - \nabla p, \tag{4.1}$$

Using Alfvénic units, the magnetic field strength can be expressed in units of velocity, with $\mathbf{b} = \mathbf{B}/\sqrt{\mu_0\rho}$. Decomposing $\mathbf{b}$ into a magnetic mean-field $\mathbf{B_0}$ that is constant and a fluctuating component $\delta\mathbf{b}$, we can express the Lorentz force term as

$$\begin{aligned}\mathbf{j}\times(\mathbf{B_0}+\delta\mathbf{b}) &= -(\mathbf{B_0}+\delta\mathbf{b})\times(\nabla\times\delta\mathbf{b})\\ &= [(\mathbf{B_0}+\delta\mathbf{b})\cdot\nabla]\delta\mathbf{b} - \nabla\frac{\mathbf{b}^2}{2}\end{aligned} \tag{4.2}$$

and obtain

$$\partial_t\mathbf{u} = -(\mathbf{u}\cdot\nabla)\mathbf{u} + [(\mathbf{B_0}+\delta\mathbf{b})\cdot\nabla]\delta\mathbf{b} + \nu\,\nabla^2\mathbf{u} - \nabla\tilde{p}, \tag{4.3}$$

where the normalized pressure $\tilde{p} = p/\rho + \mathbf{b}^2/2$ composed of both thermal and magnetic pressure was introduced.

Analogously rewriting Faraday's law, which relates the magnetic field to the motional electric field, as

$$\begin{aligned}-\nabla\times\mathbf{e}_{\mathrm{mot}} &= \nabla\times[(\mathbf{u}\times(\mathbf{B_0}+\delta\mathbf{b})]\\ &= [(\mathbf{B_0}+\delta\mathbf{b})\cdot\nabla]\mathbf{u} - (\mathbf{u}\cdot\nabla)\delta\mathbf{b},\end{aligned} \tag{4.4}$$

we can write the evolution equation for $\delta\mathbf{b}$ in a fashion that is symmetric to the momentum equation:

$$\partial_t\delta\mathbf{b} = -(\mathbf{u}\cdot\nabla)\delta\mathbf{b} + [(\mathbf{B_0}+\delta\mathbf{b})\cdot\nabla]\mathbf{u} + \eta\,\nabla^2\delta\mathbf{b}. \tag{4.5}$$

Splitting both equations into linear and nonlinear terms and introducing external forcing terms $\mathbf{f}_u$ and $\mathbf{f}_b$ on the right-hand sides yields

$$\partial_t\mathbf{u} = [-(\mathbf{u}\cdot\nabla)\mathbf{u} + (\delta\mathbf{b}\cdot\nabla)\delta\mathbf{b}] + \Big[(\mathbf{B_0}\cdot\nabla)\delta\mathbf{b} + \nu\,\nabla^2\mathbf{u}\Big] + [\nabla\tilde{p}] + [\mathbf{f}_u], \tag{4.6}$$

$$\partial_t \delta\mathbf{b} = [-(\mathbf{u}\cdot\nabla)\delta\mathbf{b} + (\delta\mathbf{b}\cdot\nabla)\mathbf{u}] + \Big[(\mathbf{B_0}\cdot\nabla)\mathbf{u} + \eta\ \nabla^2\delta\mathbf{b}\Big] \qquad + [\mathbf{f}_b]. \tag{4.7}$$

Turbo, as a pseudospectral code, evolves the set of turbulent fields $\mathbf{u}, \delta\mathbf{b}$ by separately computing the nonlinear terms in real space, the linear terms in spectral space, and the pressure term via the incompressibility condition. More explicitly, after the fields have been updated by only the nonlinear terms at the beginning of a time step, they are Fourier transformed into spectral representations $\tilde{\mathbf{u}}(\mathbf{k}), \tilde{\mathbf{b}}(\mathbf{k})$,

$$\tilde{\mathbf{u}}(\mathbf{k}) = \sqrt{\frac{1}{2\pi\ V}} \int_V d^3x\ \mathbf{u}(\mathbf{x})\ e^{\imath\mathbf{k}\cdot\mathbf{x}}, \tag{4.8}$$

$$\tilde{\mathbf{b}}(\mathbf{k}) = \sqrt{\frac{1}{2\pi\ V}} \int_V d^3x\ \mathbf{b}(\mathbf{x})\ e^{\imath\mathbf{k}\cdot\mathbf{x}}, \tag{4.9}$$

in order to compute the linear terms in the updating procedure, as described below.

### 4.1.2 Updating the MHD fields

After applying an upper cut-off to the spectrum in order to prevent a spill-over from unresolved wavelengths into the result of the nonlinear step (2/3-dealiasing, Orszag (1971)), the Fourier-space fields are updated by the linear terms:

$$\partial_t \tilde{\mathbf{u}} = \Big[\imath(\mathbf{B_0}\cdot\mathbf{k})\tilde{\mathbf{b}} - \nu\ k^2\tilde{\mathbf{u}}\Big], \tag{4.10}$$

$$\partial_t \tilde{\mathbf{b}} = \Big[\imath(\mathbf{B_0}\cdot\mathbf{k})\tilde{\mathbf{u}} - \eta\ k^2\tilde{\mathbf{b}}\Big]. \tag{4.11}$$

Next the divergence-free condition on $\mathbf{u}$ and $\mathbf{b}$ is enforced by subtracting the divergence from the Fourier-space fields:

$$\tilde{\mathbf{u}} \mapsto \tilde{\mathbf{u}} - \mathbf{k}\frac{\mathbf{k}\cdot\tilde{\mathbf{u}}}{k^2}\Delta t, \tag{4.12}$$

$$\tilde{\mathbf{b}} \mapsto \tilde{\mathbf{b}} - \mathbf{k}\frac{\mathbf{k}\cdot\tilde{\mathbf{b}}}{k^2}\Delta t. \tag{4.13}$$

This procedure corresponds to a projection of each mode onto the plane orthogonal to each wave vector $\mathbf{k}$. We can easily see that this operation takes care of the pressure-gradient term as well by taking the divergence of equation (4.3):

$$\partial_t(\nabla\cdot\mathbf{u}) = 0 = \nabla\cdot[-(\mathbf{u}\cdot\nabla)\mathbf{u} + (\delta\mathbf{b}\cdot\nabla)\delta\mathbf{b}] + \nabla^2\tilde{p}, \tag{4.14}$$

where we used $\nabla\cdot\mathbf{u} \equiv \nabla\cdot\delta\mathbf{b} \equiv 0$ and moreover assumed a divergence-free forcing scheme such that $\nabla\cdot\mathbf{f}_u \equiv \nabla\cdot\mathbf{f}_b \equiv 0$. In Fourier-space this equation can easily be inverted to find an expression for $\tilde{p}$:

$$\mathcal{F}[\tilde{p}] = -\frac{k_\alpha k_\beta}{k^2}(\tilde{\mathbf{u}}\circledast\tilde{\mathbf{u}} - \tilde{\mathbf{b}}\circledast\tilde{\mathbf{b}})_{\alpha\beta}, \tag{4.15}$$

where we have introduced the convolution operator $\circledast$ for the Fourier transform of the nonlinear operators,

$$(\tilde{\mathbf{u}} \circledast \tilde{\mathbf{u}})_{\alpha\beta} = \int d^3k' u_\alpha(\mathbf{k}') u_\beta(\mathbf{k}-\mathbf{k}'). \tag{4.16}$$

Fourier-transforming the original momentum-evolution equation, one can show that it may as well be written as

$$\partial_t \tilde{u}_\alpha = \left(\delta_{\alpha\beta} - \frac{k_\alpha k_\beta}{k^2}\right) \imath k_\gamma (\tilde{\mathbf{u}} \circledast \tilde{\mathbf{u}} - \tilde{\mathbf{b}} \circledast \tilde{\mathbf{b}})_{\beta\gamma} - \imath k_\beta B_{0,\beta} \tilde{b}_\alpha - \nu k^2 \tilde{u}_\alpha + f_{u,\alpha}. \tag{4.17}$$

Essentially, as the term in parentheses implies, the pressure-gradient term in Fourier space serves to project the nonlinear term of the momentum-evolution equation onto the plane perpendicular to the wave vector $\mathbf{k}$. Our numerical scheme simply splits off this projection into another stage of the evolution algorithm. Thus we can neglect the pressure in our calculations provided that we perform the divergence-subtraction after every time step.

Finally the forcing terms $\tilde{\mathbf{f}}_u$ and $\tilde{\mathbf{f}}_b$ are applied, as will be described below:

$$\tilde{\mathbf{u}} \mapsto \tilde{\mathbf{u}} + \tilde{\mathbf{f}}_u \Delta t, \tag{4.18}$$

$$\tilde{\mathbf{b}} \mapsto \tilde{\mathbf{b}} + \tilde{\mathbf{f}}_b \Delta t. \tag{4.19}$$

This entire procedure is embedded in a third-order Runge-Kutta integrator. Conservation of bulk momentum and magnetic mean-field are guaranteed by the pseudospectral method, which only updates modes with $\mathbf{k} \neq 0$. If Turbo is run parallelized among several processing units, the real-space field arrays are distributed into slices along the $z$ direction while the Fourier-space field arrays are split along $y$. Since most calculations are local within the respective space, communication between processing units is mainly due to the Fast-Fourier transformation and back-transformation and the collection of diagnostic information.

### 4.1.3 The cross-helical forcing scheme in detail

The forcing scheme we use, which was first introduced by Teaca (2010), decomposes the Fourier-transformed fields $\tilde{\mathbf{u}}(\mathbf{k})$ and $\tilde{\mathbf{b}}(\mathbf{k})$ into eigenmodes $\mathbf{h}_{R/L}$ of the curl operator for each individual wave number $\mathbf{k}$,

$$\mathbf{h}_R(\mathbf{k}) = \hat{\mathbf{i}} \times \hat{\mathbf{k}} + \imath\, \hat{\mathbf{i}}, \tag{4.20}$$

$$\mathbf{h}_L(\mathbf{k}) = \hat{\mathbf{i}} \times \hat{\mathbf{k}} - \imath\, \hat{\mathbf{i}}, \tag{4.21}$$

with $\hat{\mathbf{i}}$ an arbitrary unit vector linearly independent of $\hat{\mathbf{k}} = \mathbf{k}/|\mathbf{k}|$. It is easily proven that both $\mathbf{h}_R$ and $\mathbf{h}_L$ are eigenvectors of the curl operator in Fourier space, $\imath\mathbf{k}\times\cdot$:

$$\begin{aligned}\imath\mathbf{k}\times\left[\hat{\mathbf{i}}\times\hat{\mathbf{k}}\pm\imath\hat{\mathbf{i}}\right] &= \imath\left[k\hat{\mathbf{i}}-\hat{\mathbf{k}}(\hat{\mathbf{i}}\cdot\mathbf{k})\pm\imath\,\mathbf{k}\times\mathbf{i}\right]\\ &= \pm k\left(\hat{\mathbf{i}}\times\hat{\mathbf{k}}\pm\imath\,\hat{\mathbf{i}}\right),\end{aligned} \tag{4.22}$$

where the upper sign refers to the right-handed eigenvector $\mathbf{h}_R$ and the lower sign to $\mathbf{h}_L$.

Since both $\tilde{\mathbf{u}}$ and $\tilde{\mathbf{b}}$ are Fourier transforms of divergence-free fields (hence $\mathbf{k}\cdot\tilde{\mathbf{u}}\equiv\mathbf{k}\cdot\tilde{\mathbf{b}}\equiv 0$), they are elements of the vector space spanned by $\mathbf{h}_R(\mathbf{k})$ and $\mathbf{h}_L(\mathbf{k})$ at each point in spectral space:

$$\tilde{\mathbf{u}}(\mathbf{k}) = \tilde{u}_R(\mathbf{k})\mathbf{h}_R(\mathbf{k}) + \tilde{u}_L(\mathbf{k})\mathbf{h}_L(\mathbf{k}), \tag{4.23}$$

$$\tilde{\mathbf{b}}(\mathbf{k}) = \tilde{b}_R(\mathbf{k})\mathbf{h}_R(\mathbf{k}) + \tilde{b}_L(\mathbf{k})\mathbf{h}_L(\mathbf{k}). \tag{4.24}$$

As our goal is a forcing algorithm that injects energy and cross helicity into the turbulent MHD fields, we define the corresponding injection rates $\epsilon_{\text{inj}}$ and $\sigma_{\text{inj}}$ via the Fourier-transformed forcing terms $\tilde{\mathbf{f}}_u$ and $\tilde{\mathbf{f}}_b$:

$$\epsilon_{\text{inj}} = \underbrace{\left\langle\tilde{\mathbf{f}}_u\cdot\tilde{\mathbf{u}}^*\right\rangle}_{\epsilon^u} + \underbrace{\left\langle\tilde{\mathbf{f}}_b\cdot\tilde{\mathbf{b}}^*\right\rangle}_{\epsilon^b}, \tag{4.25}$$

$$\sigma_{\text{inj}} = \frac{\left\langle\tilde{\mathbf{f}}_u\cdot\tilde{\mathbf{b}}^*\right\rangle + \left\langle\tilde{\mathbf{f}}_b\cdot\tilde{\mathbf{u}}^*\right\rangle}{\epsilon_{\text{inj}}}, \tag{4.26}$$

with $\epsilon^u$ and $\epsilon^b$ expressing the rates at which energy is added to the velocity field and the magnetic field, respectively.

Expressing the forcing terms in the helical-decomposition form, we introduce the coefficients $\upsilon^{u/b}_{R/L}(\mathbf{k})$ and $\beta^{u/b}_{R/L}(\mathbf{k})$ via

$$\tilde{\mathbf{f}}_u(\mathbf{k}) = \left[\upsilon^u_R(\mathbf{k})\tilde{u}_R(\mathbf{k}) + \beta^u_R(\mathbf{k})\tilde{b}_R(\mathbf{k})\right]\mathbf{h}_R(\mathbf{k}) + \left[\upsilon^u_L(\mathbf{k})\tilde{u}_L(\mathbf{k}) + \beta^u_L(\mathbf{k})\tilde{b}_L(\mathbf{k})\right]\mathbf{h}_L(\mathbf{k}), \tag{4.27}$$

$$\tilde{\mathbf{f}}_b(\mathbf{k}) = \left[\upsilon^b_R(\mathbf{k})\tilde{u}_R(\mathbf{k}) + \beta^b_R(\mathbf{k})\tilde{b}_R(\mathbf{k})\right]\mathbf{h}_R(\mathbf{k}) + \left[\upsilon^b_L(\mathbf{k})\tilde{u}_L(\mathbf{k}) + \beta^b_L(\mathbf{k})\tilde{b}_L(\mathbf{k})\right]\mathbf{h}_L(\mathbf{k}). \tag{4.28}$$

Non-zero kinetic and magnetic helicity express a dominance of right-handed waves over left-handed waves or vice versa (see chapter 2), so neither helicity will be driven by a forcing mechanism which ensures that the magnitudes of either handedness are approximately equal. Hence we demand that the coefficients of $\mathbf{h}_R$ and $\mathbf{h}_L$ are equal everywhere in $\mathbf{k}$-space. Inserting the forcing term definitions (4.28) into (4.26) and solving for the coefficients, we then obtain after some tedious algebra:

$$\upsilon^u_{R/L}(\mathbf{k}) = \frac{\epsilon^u(\mathbf{k})}{2}\left(\sigma\frac{C^*_{R/L}(\mathbf{k})}{D^*_{R/L}(\mathbf{k})} - 2\frac{E^b_{R/L}(\mathbf{k})}{D^*_{R/L}(\mathbf{k})}\right), \tag{4.29}$$

$$\beta^u_{R/L}(\mathbf{k}) = \frac{\epsilon^u(\mathbf{k})}{2}\left(\frac{C^*_{R/L}(\mathbf{k})}{D^*_{R/L}(\mathbf{k})} - 2\sigma\frac{E^u_{R/L}(\mathbf{k})}{D^*_{R/L}(\mathbf{k})}\right), \tag{4.30}$$

$$\upsilon^b_{R/L}(\mathbf{k}) = \frac{\epsilon^b(\mathbf{k})}{2}\left(\frac{C_{R/L}(\mathbf{k})}{D_{R/L}(\mathbf{k})} - 2\sigma\frac{E^b_{R/L}(\mathbf{k})}{D_{R/L}(\mathbf{k})}\right), \tag{4.31}$$

$$\beta^b_{R/L}(\mathbf{k}) = \frac{\epsilon^b(\mathbf{k})}{2}\left(\sigma\frac{C_{R/L}(\mathbf{k})}{D_{R/L}(\mathbf{k})} - 2\frac{E^u_{R/L}(\mathbf{k})}{D_{R/L}(\mathbf{k})}\right), \tag{4.32}$$

with the following abbreviations:

$$E^u_{R/L}(\mathbf{k}) = \frac{1}{2}\left|\tilde{u}_{R/L}(\mathbf{k})\right|^2, \tag{4.33}$$

$$E^b_{R/L}(\mathbf{k}) = \frac{1}{2}\left|\tilde{b}_{R/L}(\mathbf{k})\right|^2, \tag{4.34}$$

$$C_{R/L}(\mathbf{k}) = \tilde{u}_{R/L}(\mathbf{k}) \cdot \tilde{b}^*_{R/L}(\mathbf{k}), \tag{4.35}$$

$$D_{R/L}(\mathbf{k}) = C_{R/L}(\mathbf{k}) - 4E^u_{R/L}(\mathbf{k})\, E^b_{R/L}(\mathbf{k}). \tag{4.36}$$

The energy and cross-helicity injection is distributed evenly among a discrete number $N_f$ of wave modes in the pseudospectral implementation, in such a manner that $\epsilon^{u/b}(\mathbf{k}) = \epsilon^{u/b}/N_f$ if $\mathbf{k}$ is one of the forced modes. At the end of each Runge-Kutta step, the spectral representations of velocity and magnetic field are updated according to (4.19), with the conservation of $\nabla \cdot \mathbf{u} \equiv 0$ and $\nabla \cdot \mathbf{b} \equiv 0$ being guaranteed by the helical decomposition scheme as the force is orthogonal to the mode on which it acts by definition (both $\mathbf{h}_R$ and $\mathbf{h}_L$ are orthogonal to $\mathbf{k}$).

In the following we present and analyze simulations driven by this algorithm.

## 4.2 Isotropic cross-helical turbulence

### 4.2.1 Initial parameters

We start with an isotropic field configuration (so no magnetic mean field is applied, $\mathbf{B_0} = 0$) on a cubic grid with periodic boundary conditions and 512 grid cells in each direction. Since the side lengths of the cube in real space are set to $2\pi$, the modes that can be resolved by the simulation are the ones with integer wavenumbers, $(k_x, k_y, k_z) \in \{1, \ldots, 512\}^3$. Taking into account the aliasing effect introduced by the nonlinear terms (Orszag, 1971), the maximum wavenumber which can be resolved in each direction is actually reduced to $k_{\max} = 512/3 \approx 170$.

The initial fields are constructed by choosing three random phases $\theta_1, \theta_2, \varphi$ for each of the modes and then assigning to each point on the grid the complex vector

$$\tilde{\mathbf{u}}(k) = \mathcal{A}(k) \times \begin{pmatrix} (-ak_y k + bk_x k_z)/(k_\perp k) \\ (+ak_x k + bk_y k_z)/(k_\perp k) \\ -bk_\perp/k \end{pmatrix}, \tag{4.37}$$

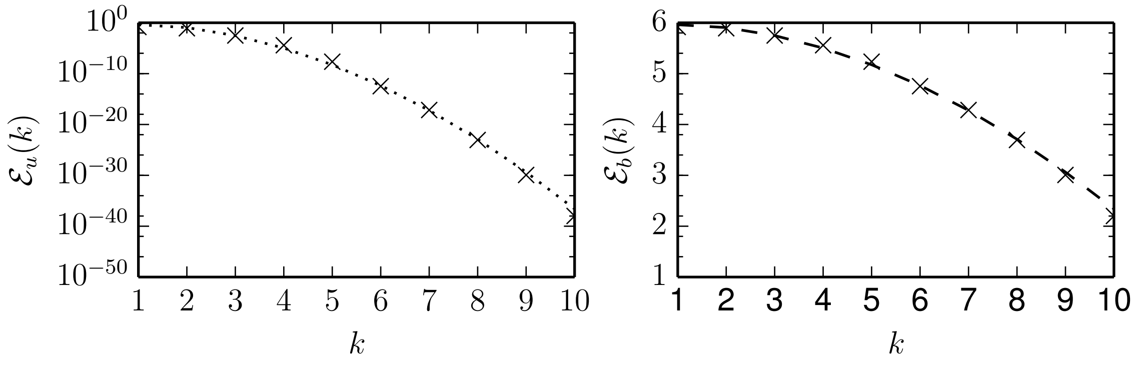

Figure 4.1: Initial spectra of the energy in the velocity field, $\mathcal{E}_u(k) \propto |\tilde{u}(k)|^2$ (left), and in the magnetic field (right), $\mathcal{E}_b(k) \propto |\tilde{b}(k)|^2$, in arbitrary units, with the function $\mathcal{A}(\mathbf{k})$ plotted as dashed line

with $k_\perp^2 = k_x^2 + k_y^2$ and the complex coefficients

$$a = e^{\imath\theta_1} \cos\varphi, \tag{4.38}$$

$$b = e^{\imath\theta_2} \sin\varphi. \tag{4.39}$$

The same algorithm is used to construct the initial magnetic field perturbation, and since the complex phases are chosen independently of each other, the correlation between the velocity and the magnetic field, and hence the cross helicity, is zero. Moreover, it is trivial to confirm that this random vector field is by construction divergence-free ($\mathbf{k} \cdot \tilde{\mathbf{u}} \equiv 0$), has zero helicity ($(\mathbf{k} \times \tilde{\mathbf{u}}) \cdot \tilde{\mathbf{u}} \equiv 0$), and that its norm is determined by the function $\mathcal{A}(k)$:

$$|\tilde{\mathbf{u}}(\mathbf{k})|^2 = |\mathcal{A}(\mathbf{k})|^2. \tag{4.40}$$

In all of our simulations we start with Gaussian potentials for the velocity and magnetic fields, yielding for the function $\mathcal{A}(\mathbf{k})$:

$$\mathcal{A}(\mathbf{k}) = A \times |\mathbf{k}| \, \exp\left( -\frac{|\mathbf{k}|^2}{2\sigma_k^2} \right). \tag{4.41}$$

In order to ensure that the spectrum is a decreasing function of $k$ over the entire spectral range, we choose a narrow Gaussian with $\sigma_k = 1.5$. The initial spectral energy distribution of the velocity field and the magnetic field are shown in figure 4.1 for the $k$-interval over which the spectrum is initialized.

### 4.2.2 Reaching a steady-state configuration

We apply our cross-helical forcing scheme with energy injection rates $\epsilon^u = \epsilon^b = 0.05$. An initial steady-state configuration is obtained by running the simulation at zero cross-helicity injection until kinetic and magnetic energy fluctuate by less than ten percent. Subsequently we use these balanced steady-state fields as initial condition for four separate runs.

The cross-helicity injection rate which we set in these runs varies from $\sigma = 0.0$ to $\sigma = 0.8$, as our goal is to obtain turbulence configurations with different degrees of cross helicity. The viscosity $\nu$ and resistivity $\eta$ are chosen to be equal to 0.00066, sufficiently large that Kolmogorov's dissipation length is resolved by the grid:

$$k_{\max} \times \ell_K = \frac{512}{3} \times \left( \frac{\nu^3}{\epsilon_u + \epsilon_b} \right)^{1/4} \approx 1.25. \tag{4.42}$$

In this isotropic setup, the forced modes are arranged in a spherical shell $2.5 < (k_x^2 + k_y^2 + k_z^2)^{1/2} < 3.5$ around the origin of spectral space. The total energy injection rate $\epsilon = \epsilon^u + \epsilon^b = 0.1$ is thus distributed over $N_f = 19$ different modes. By forcing modes at low wavenumbers, we allow the injected energy and cross helicity to cascade towards larger wavenumbers and assume a steady-state configuration which is, at least on smaller length scales corresponding to $k > 5$, generated by the self-organizing turbulence rather than our forcing mechanism.

The evolution of energy and energy dissipation for each $\sigma$ is shown in figure (4.2). Clearly the initial configuration is already in a steady state for $\sigma = 0$, and the fluctuation of the total energy is negligibly small. On the other hand, applying a non-zero cross-helicity injection rate results in a short period of energy growth, until the system again settles into a steady state. This is especially visible in the strongly cross-helical run with $\sigma = 0.8$ (red line), in which the energy dissipation drops sharply within the first 50 Alfvén times, only to return to its steady-state value $\mathcal{D}_{\text{tot}} \approx \epsilon_{\text{inj}}$ afterwards. At this value the energy injected at large length scales is compensated for by viscous dissipation on small scales and the total energy of the system stays constant.

In comparing the time evolution of the different runs, we have normalized time by the specific Alfvén time of each run, $t_A = L_{\text{int}}/v_A$. $L_{\text{int}}$ is the integral length scale or correlation scale of each turbulent field configuration, defined via (Pope, 2000),

$$L_{\text{int}}^2 = \sum_{i=1}^{3} \left( \int d^3k \frac{\pi}{2} \frac{\tilde{b}_i(\mathbf{k}) \tilde{b}_i^*(\mathbf{k})}{E_b} \delta(k_i) \right)^2, \tag{4.43}$$

whereas the Alfvén velocity is simply the root-mean-square value of the magnetic field in Alfvénic units, $v_A = \langle b^2 \rangle^{1/2}$.

Plots of the distribution of the velocity and magnetic field intensity in real space are presented for sample steady-state configurations in figure 4.3. Examining the distribution of energy between the kinetic and magnetic energy more closely, we plot the Alfvén ratio $r_A = \langle u^2 \rangle / \langle b^2 \rangle$ in figure 4.4. Although in each run a quasi-steady value of $r_A$ is eventually attained, this value depends strongly on the choice of $\sigma$: The higher the level of cross-helicity injection is set, the larger the kinetic energy grows relative to the magnetic energy of the system, although the magnetic energy dominates in each of

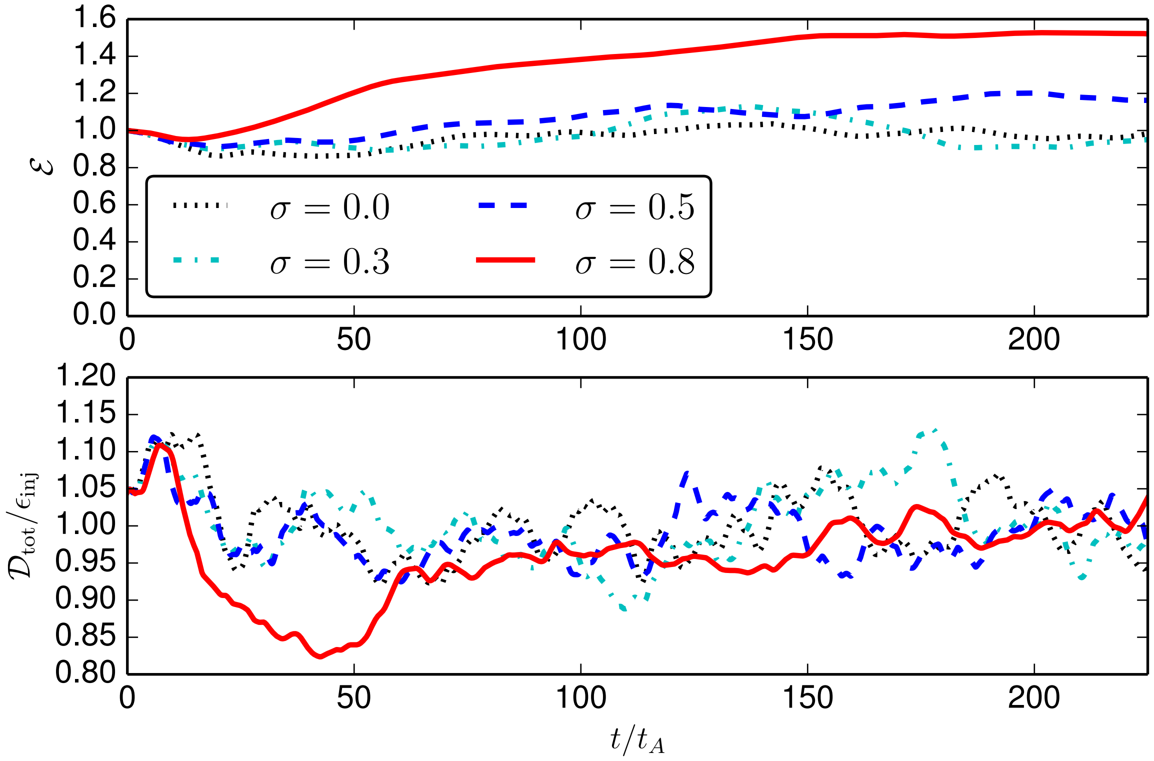

Figure 4.2: Evolution of total energy $\mathcal{E} = \langle \mathbf{u}^2 + \mathbf{b}^2 \rangle/2$, normalized to its value at $t = 0$, and energy dissipation relative to energy injection rate, $\mathcal{D}/\epsilon$, for isotropic MHD runs with four different cross-helicity injection rates: $\sigma = 0.0$ (black, dotted), $\sigma = 0.3$ (cyan, dash-dotted), $\sigma = 0.5$ (blue, dashed), and $\sigma = 0.8$ (red, solid)

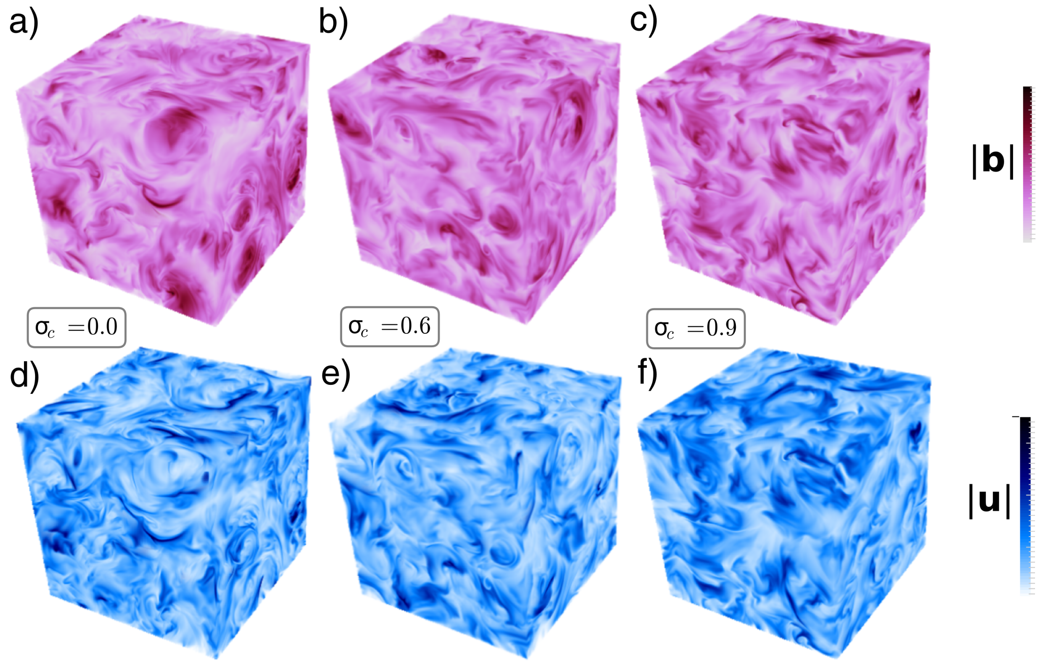

Figure 4.3: Spatial distribution of magnetic (top row) and velocity (bottom row) field intensity in isotropic MHD turbulence with normalized cross-helicity values (*a*,*d*) $\sigma_c = \mathcal{K}/\mathcal{E} = 0.0$, (*b*,*e*) $\sigma_c = 0.6$, (c,f) $\sigma_c = 0.9$

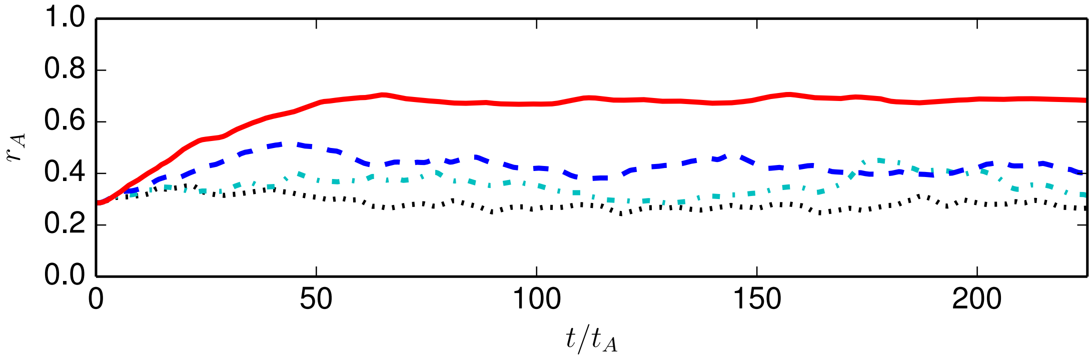

Figure 4.4: Evolution of the Alfvén ratio $r_A = \langle \mathbf{u}^2 \rangle / \langle \mathbf{b}^2 \rangle$ for different cross-helicity injection rates (color scheme as in previous figure)

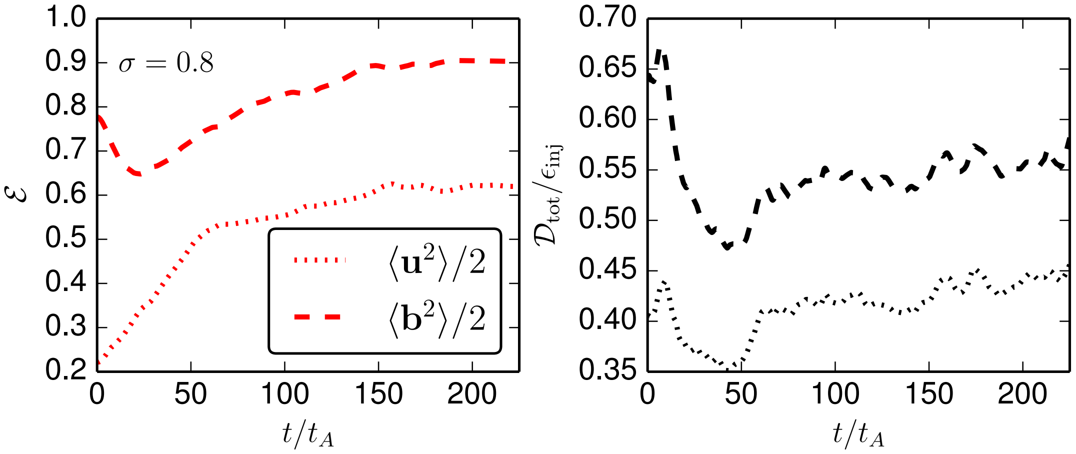

Figure 4.5: Left: evolution of the magnetic energy (dashed) and the kinetic energy (dotted) for strong cross-helicity injection $\sigma = 0.8$, normalized to the total energy at $t = 0$. Right: evolution of the magnetic (dashed) and kinetic (dotted) dissipation rate for the same run

the runs.

Once more the case with the highest cross-helicity injection rate exhibits a very dynamic behavior during the first 50 Alfvén times, in which the energy injected into the system is mainly deposited in the velocity field (figure 4.5) whereas the magnetic energy even decreases for a short period of about twenty Alfvén times. This observation interestingly agrees with solar-wind measurements, in which the fast wind is marked by both higher cross helicity and a larger Alfvén ratio than the slow solar wind (Marsch & Tu, 1990).

### 4.2.3 Cross-helicity evolution

We now take a closer look at the quantity we are most interested in, the normalized cross helicity $\sigma_c = \mathcal{K}/\mathcal{E}$. Its growth in the forced MHD simulations is initially propor-

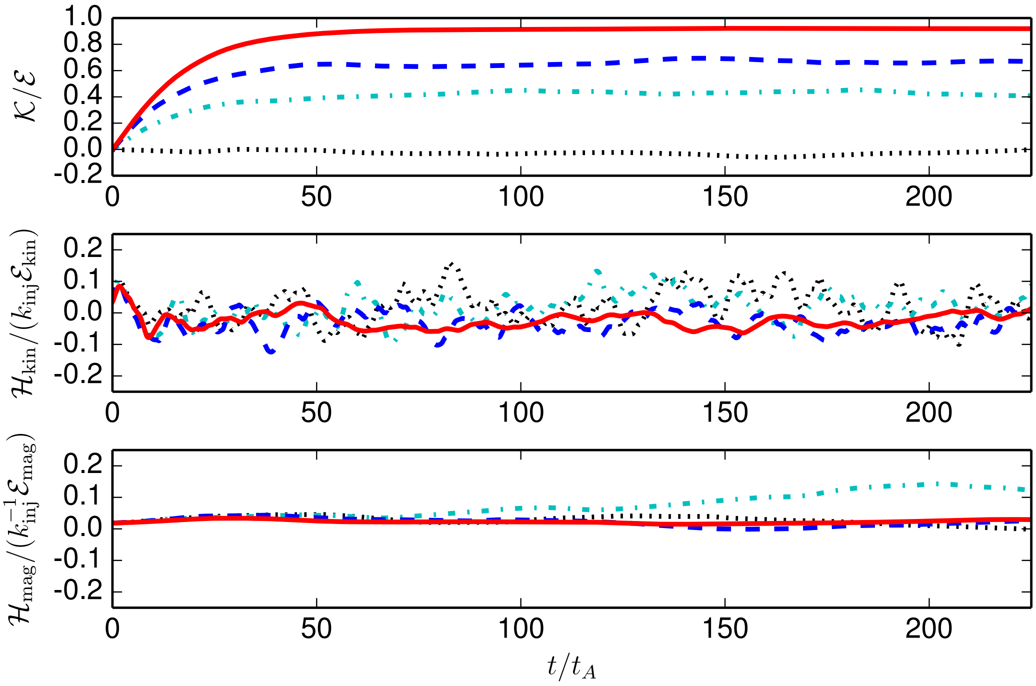

Figure 4.6: Evolution of the normalized cross helicity $\sigma_c = \mathcal{K}/\mathcal{E}$, the normalized kinetic helicity $\mathcal{H}_{\rm kin} = k_{\rm inj}\mathcal{E}_{\rm kin}$, and the normalized magnetic helicity $\mathcal{H}_{\rm mag} = \mathcal{E}_{\rm mag}/k_{\rm inj}$ for different cross-helicity injection rates (color scheme as in previous figure)

tional to the value of $\sigma$ chosen, as shown in figure (4.6), before a steady-state of the normalized cross helicity is eventually reached. In this latter regime, cross-helicity fluctuations are remarkably small, indicating that the system is in complete equilibrium.

There is a clear correlation between the value of $\sigma$ and the steady-state value of $\mathcal{K}/\mathcal{E}$, as one might expect. However, the injection rate of cross helicity is not necessarily identical to the normalized cross helicity $\mathcal{K}/\mathcal{E}$ of the steady state. Instead the equilibrium value is slightly higher than $\sigma$ as the cross helicity cascades from the injection scales to smaller length scales, allowing for non-zero cross-helicity values in a wider spectral range than only the injection range, in which the forcing scheme enforces the chosen value of $\sigma$.

In order to visualize the cascade of cross helicity from larger to smaller scales, we depict in figure 4.7 the evolution of the spectral cross-helicity $C(\mathbf{k}) = \mathrm{Re}(C_R(\mathbf{k}) + C_L(\mathbf{k}))$ from the initial configuration with $\mathcal{K}/\mathcal{E} = 0$ to the steady-state with $\mathcal{K}/\mathcal{E} \approx 0.9$, which can be achieved with a cross-helicity injection rate $\sigma = 0.8$. The graph of $C(k)$ exhibits a visible 'hump' around the injection interval $2.5 < k < 3.5$ shortly after the cross-helicity injection has begun ($t = 2t_A$). It later converges towards a smooth steady-state slope of $C(k) \propto k^{-2}$ as time progresses and cross helicity is also transported to smaller scales by a mechanism similar to the energy-cascade.

Meanwhile, the cross-helical forcing we employ ensures that the magnetic and kinetic helicities remain negligibly small throughout all simulations (figure 4.6) as the

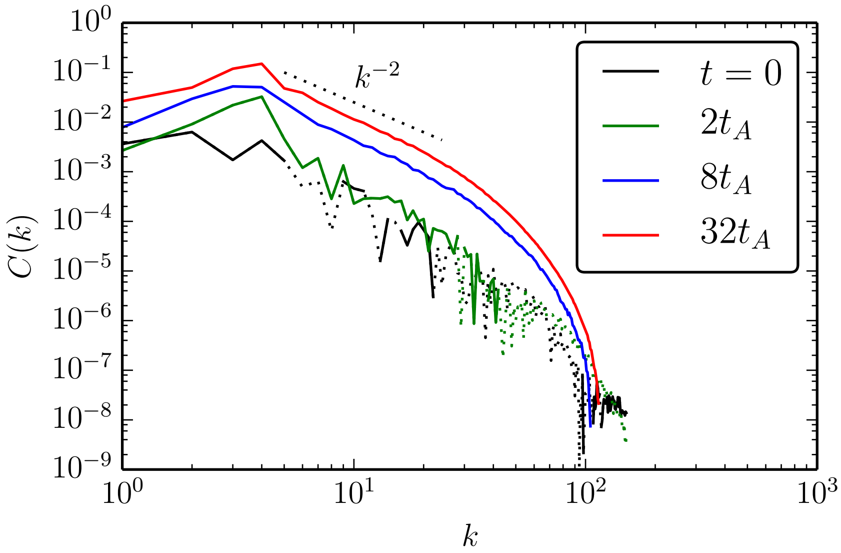

Figure 4.7: Evolution of the spectral cross-helicity function $C(\mathbf{k})$ during the injection of cross helicity into a balanced steady-state configuration (with initially $\mathcal{K}/\mathcal{E} \approx 0$) at an injection rate $\sigma = 0.8$. The initial spectrum is drawn in black with the absolute values of negative values shown as dotted lines. Also shown are the graphs of $C(\mathbf{k})$ after 2, 8, and 32 Alfvén times

energy injection into modes of left-handed and right-handed modes is equal in every single time step. Our experiments with other forcing schemes have shown a tendency to develop significant magnetic or kinetic helicity (or even both) as an unwanted side effect of cross helicity injection. In particular we have tested how our cross-helical-forcing mechanism fares compared to Elsasser forcing. This relatively simple scheme injects cross helicity into a pseudospectral simulation by forcing the Elsasser variables $\tilde{\mathbf{z}}^{\pm} = \tilde{\mathbf{u}} \pm \tilde{\mathbf{b}}$ in a given region of spectral space, without any regard for the other helicities. However, we have found that Elsasser forcing often increases the values of $\mathcal{H}_{\text{kin}}$ or $\mathcal{H}_{\text{mag}}$ uncontrollably (see figure 4.8), especially if the chosen value of cross-helicity injection is large, as in figures 4.8b,d). Since this property of Elsasser forcing is obviously detrimental to our goal of comparing the propagation of test-particles in simulations with a theory of turbulence with zero magnetic helicity, we have decided to favor the cross-helical-forcing scheme.

### 4.2.4 Spectral analysis of the turbulent steady-states

The spectra of both velocity and magnetic fields in our simulations match Kraichnan's characteristic spectral index of −3/2 well. Evidence for this statement is shown in figure 4.9, which compares the spectra of the ($\sigma = 0.0$)-steady-state with the strongly cross-helical case. In both plots the expected slope is compensated by multiplying the spectra by $k^{3/2}$, resulting in a clearly visible inertial range ($3 < k < 20$) where the lines are almost parallel to the $k$-axis, although this regime visibly extends even further

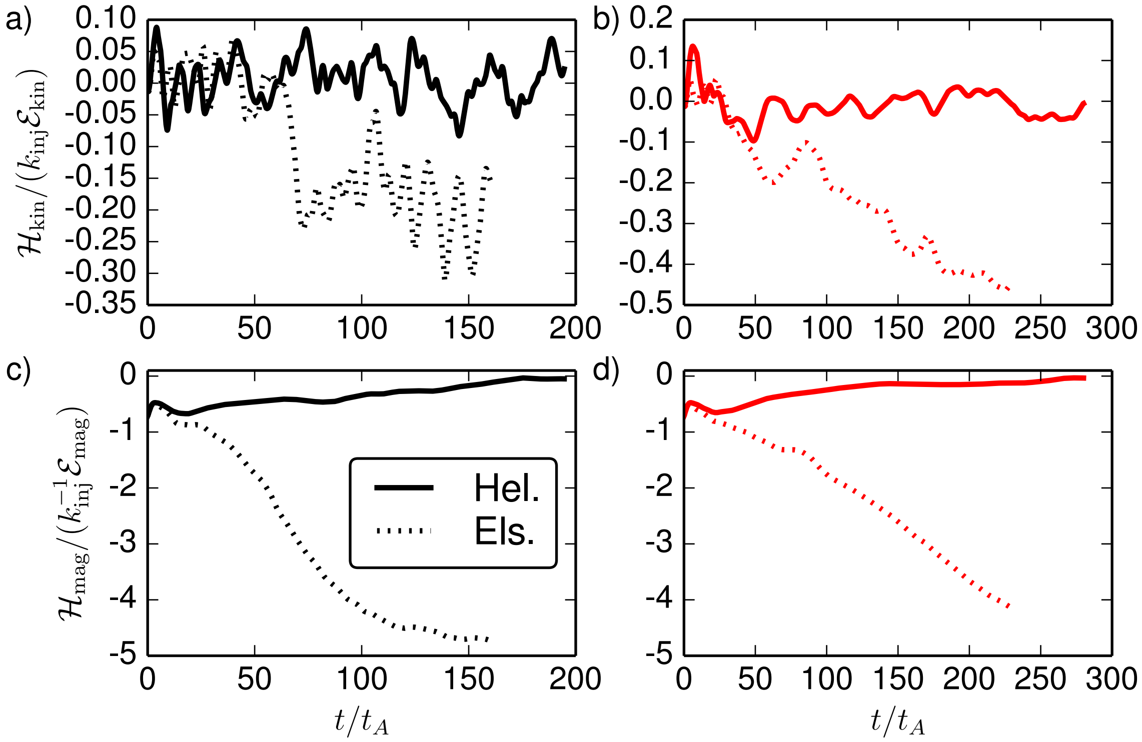

Figure 4.8: Evolution of kinetic helicity $\mathcal{H}_{\rm kin}$ and magnetic helicity $\mathcal{H}_{\rm mag}$ for cross-helical (solid lines) and Elsasser (dashed lines) forcing schemes and different cross-helicity injection rates. (*a*) Kinetic-helicity evolution at $\sigma = 0$. (*b*) Kinetic-helicity evolution with $\sigma = 0.8$. (*c*) Magnetic-helicity evolution with $\sigma = 0$. (*d*) Magnetic-helicity evolution with $\sigma = 0.8$

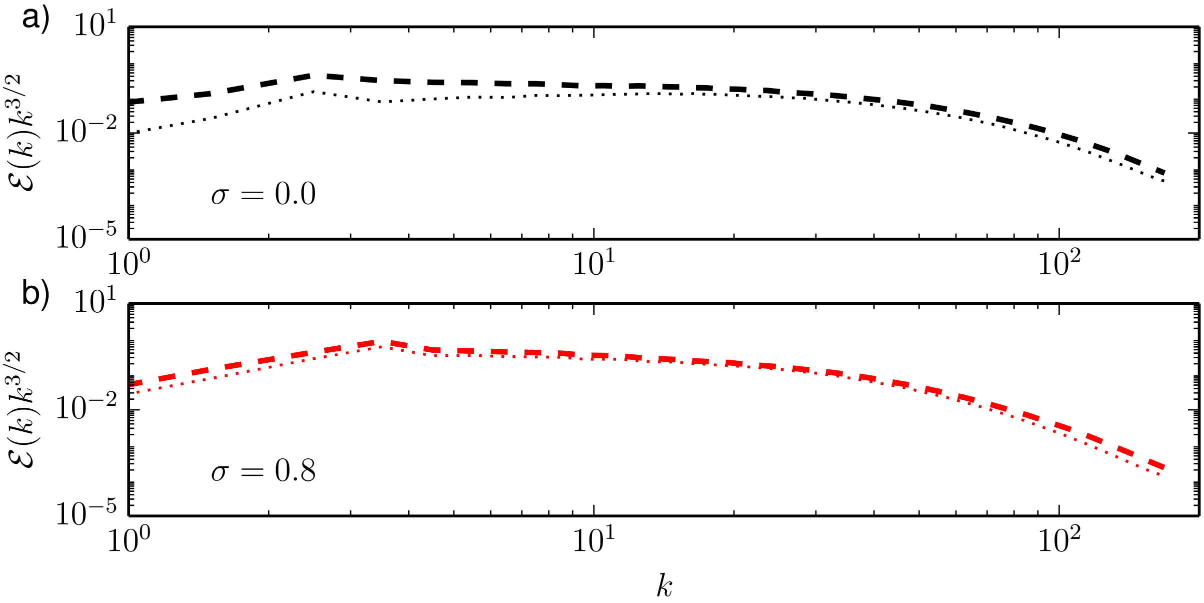

Figure 4.9: Isotropic spectra of the kinetic (dotted) and magnetic (dashed) energy for (*a*) $\sigma = 0.0$ and (*b*) $\sigma = 0.8$

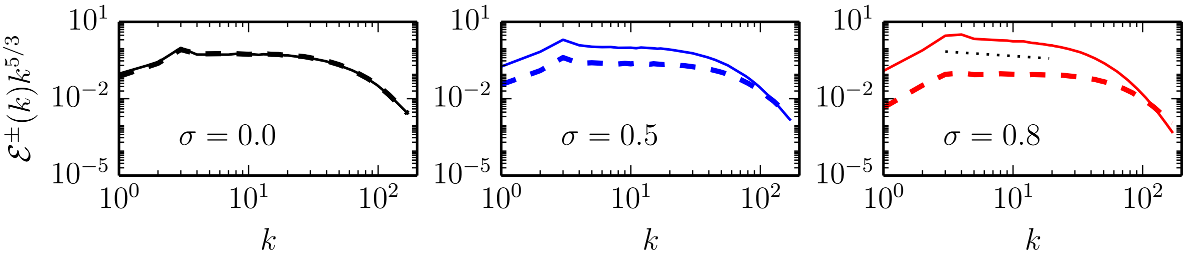

Figure 4.10: Isotropic spectra of the positive (thin solid lines) and negative (thick dashed lines) Elsasser energies, $\mathcal{E}^{\pm}(k) = |\tilde{\mathbf{u}}(k) \pm \tilde{\mathbf{b}}(k)|^2/4$. The dashed line indicates a scaling of $k^{-2}$

towards high-$k$ values in the zero cross-helicity case. To the left, a small peak at $k \approx 3$ marks the wavenumber interval in which the forcing mechanism supplies energy to the system at a constant rate.

The effect of cross-helicity injection becomes patently obvious in plots of the steady-state Elsasser spectra at various values for the injection rate $\sigma$, as figure 4.10 confirms. Here we show the spectral distribution of the Elsasser energies $\mathcal{E}^{\pm}(k) = |\tilde{\mathbf{u}}(k) \pm \tilde{\mathbf{b}}(k)|^2/4$, which have already been connected to Alfvén waves propagating along and opposite to a strong homogeneous magnetic mean-field in chapter 2. While this interpretation is difficult to uphold in the absence of a mean-field, it is easy to see from the definition of $\mathcal{E}^+$ and $\mathcal{E}^-$ that a positive correlation of velocity and magnetic field coincides with a dominance of the positive Elsasser energy and vice versa.

In all three runs depicted here, the negative Elsasser spectrum agrees well with a scaling according to Kolmogorov's $k^{-5/3}$-prediction, since the dashed lines in all plots are approximately horizontal. However, the scaling of the positive Elsasser energy deviates from this simple prediction increasingly and becomes steeper as the cross helicity grows, resembling rather $k^{-2}$ in the run with $\sigma = 0.8$ (the dotted line in figure 4.10). This deviation seems to confirm the modified-scaling hypothesis in cross-helical turbulence already suggested by Grappin *et al.* (1983), briefly outlined in subsection 2.5.2. In light of the constant scaling of the negative Elsasser energy, we tend towards agreeing with the explanation of this phenomenon proposed by Perez & Boldyrev (2010): Due to a ‘pinning’ effect at the dissipation scale, where both $\tilde{\mathbf{u}}$ and $\tilde{\mathbf{b}}$ become negligibly small, the spectra of both Elsasser energies are comparable at large wavenumbers. Since one of the Elsasser energies must have a higher value overall if the cross helicity is non-zero, however, the wavenumber-scalings of both spectra must differ at the upper end of the inertial range. At lower $k$-values, on the other hand, the scalings will be comparable again, in agreement with figure 4.10.

## 4.3 Cross-helical turbulence with order-unity mean-field

### 4.3.1 Breaking the isotropy

Although completely isotropic MHD turbulence is not uncommon in space on large scales, turbulent fields usually arrange themselves in a configuration for which a non-zero mean component of the magnetic field can be found if one averages over length scales smaller than the entire system size. The most well-known cause of this tendency towards self-organization of magnetic fields is the galactic dynamo effect (Parker, 1971; Vallee, 1991), which is for example suspected of causing the magnetic spiral observed in the Milky Way (Vallée, 2008). The presence of a magnetic mean-field will align the propagation of Alfvén waves along this mean-field and has an important effect on the dynamics of cross-helical turbulence.

In order to investigate the details of this phenomenon, we now compare the isotropic fields generated in the previous section with turbulent runs in which a magnetic mean-field $\mathbf{B_0}$ has been applied along the $z$-axis. The exact procedure involves first creating an isotropic set of MHD fields in a balanced steady-state with $\sigma_c = 0.0$, as in the previous section, and then applying an external constant magnetic field $\mathbf{B_0}$ while the turbulence is being driven into a new, anisotropic quasi-equilibrium. Finally the cross-helical-forcing mechanism is used to inject cross helicity into the system at four different rates, similar to the isotropic cases. If the mean-field strength is chosen to be 'trans-Alfvénic', *i.e.* comparable to the turbulence amplitude ($\mathbf{B_0}^2 \sim \langle \delta \mathbf{b}^2 \rangle$), the isotropic forcing mechanism described above can be used without any further adaptation.

The energy of the modes which are driven by the forcing scheme is redistributed quickly by the nonlinear terms, in such a way that the turbulence reaches an anisotropic steady-state configuration. In this case, the correlation length along the mean-field direction is larger than in the perpendicular directions, serving as a clear indication of the anisotropy of the new equilibrium configuration.

The application of a magnetic mean field while energy is being injected at a constant rate results in a small increase of the steady-state value of $\langle \delta \mathbf{b}^2 \rangle$. This is hardly surprising, as the ongoing formation of coherent structures along the mean-field direction reduces the level of viscous and magnetic dissipation occurring in fields with strong shear. The upshot of this new equilibrium state with higher turbulent magnetic energy is that some re-adjustment of $\mathbf{B_0}$ is required to maintain a trans-Alfvénic steady state as shown in figure 4.11. Note that in the bottom plot of that figure both the cross helicity $\mathcal{K} = \langle \mathbf{u} \cdot \delta \mathbf{b} \rangle$ and the normalization coefficient $\mathcal{E} = \langle u^2 + \delta \mathbf{b}^2 \rangle$ do not include the external-mean-field contribution to the total energy, only the contribution of the turbulent magnetic field.

### 4.3.2 Spectral analysis

Similarly to the isotropic cases, the balanced steady state with an order-unity mean field exhibits equipartition between positive and negative Elsasser energies $\mathcal{E}^{\pm}$. This

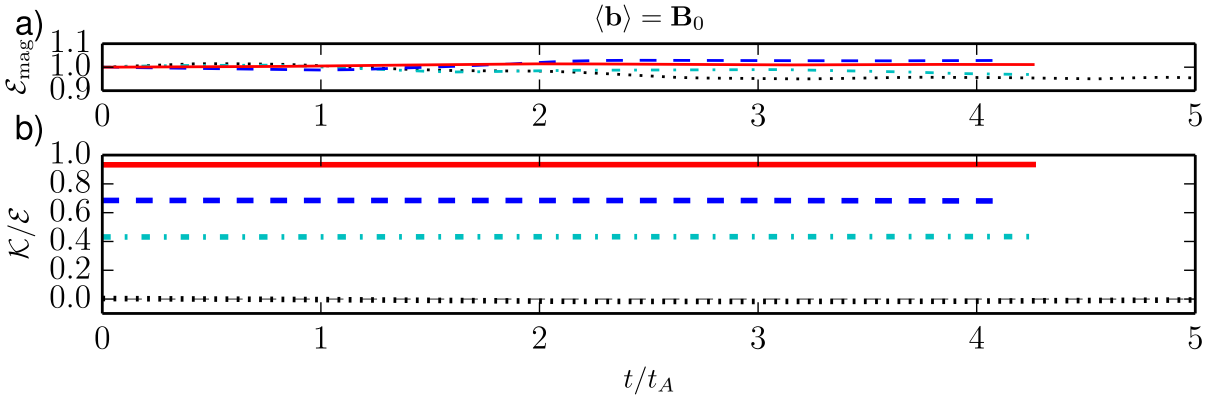

Figure 4.11: Evolution of ($a$) magnetic energy $\mathcal{E}_{\rm mag} = \delta \mathbf{b}^2/2$, normalized to its value at $t = 0$, and ($b$) normalized cross helicity $\sigma_c = \mathcal{K}/\mathcal{E}$ for runs with a trans-Alfvénic magnetic mean-field, for different cross-helicity injection rates: $\sigma_{\rm inj} = 0.0$ (black, dotted), $\sigma_{\rm inj} = 0.3$ (cyan, dash-dotted), $\sigma_{\rm inj} = 0.5$ (blue, dashed), and $\sigma_{\rm inj} = 0.8$ (red, solid)

equipartition is apparent in the left-hand column of figure 4.12, which shows the Elsasser spectra taken either perpendicular to the magnetic mean-field (top row) or parallel to it (bottom row). Both imbalanced cases with a positive cross helicity show a dominance of $\mathcal{E}^+$ over $\mathcal{E}^-$ in the steady-state configuration, which becomes more pronounced at higher cross-helicity injection rates.

The spectral slopes of the Elsasser energies in the balanced case are close to their expected values in a steady state, with a scaling parallel to the mean-field direction that goes approximately as $\mathcal{E}(k_z) \propto k_z^{-2}$. This exponent is in agreement with the theory of anisotropic turbulence put forward by Goldreich & Sridhar (1995), as explained in subsection 2.5.3. The scaling in the perpendicular direction could be regarded as either again confirming the Goldreich-Sridhar theory, if one interprets the scaling to follow a $k_\perp^{-5/3}$-law in the inertial range, or as being in support of Kraichnan's prediction, $\mathcal{E}(k_\perp) \propto k_\perp^{-3/2}$. We make no claim of being able to decide which hypothesis is true from our results, as the inertial range of our $512^3$ run is too small to definitively distinguish between both scalings.

In the strongly cross-helical cases, the slopes of positive and negative Elsasser energies differ again, with the dominant positive Elsasser energy exhibiting a faster decrease with both the perpendicular and the parallel wave number. The scaling of the negative Elsasser energy remains similar to the one found in the steady-state configuration of the run with zero cross helicity.

### 4.3.3 A closer look at the real-space field distributions

Having examined the spectra of the turbulent fields in such great detail, we can now move on to a qualitative analysis of the real-space configurations. Snapshots of the norm of the velocity and the magnetic fields in the steady-states are shown in figure 4.13. A careful look at this figure in juxtaposition to plots of isotropic turbulence

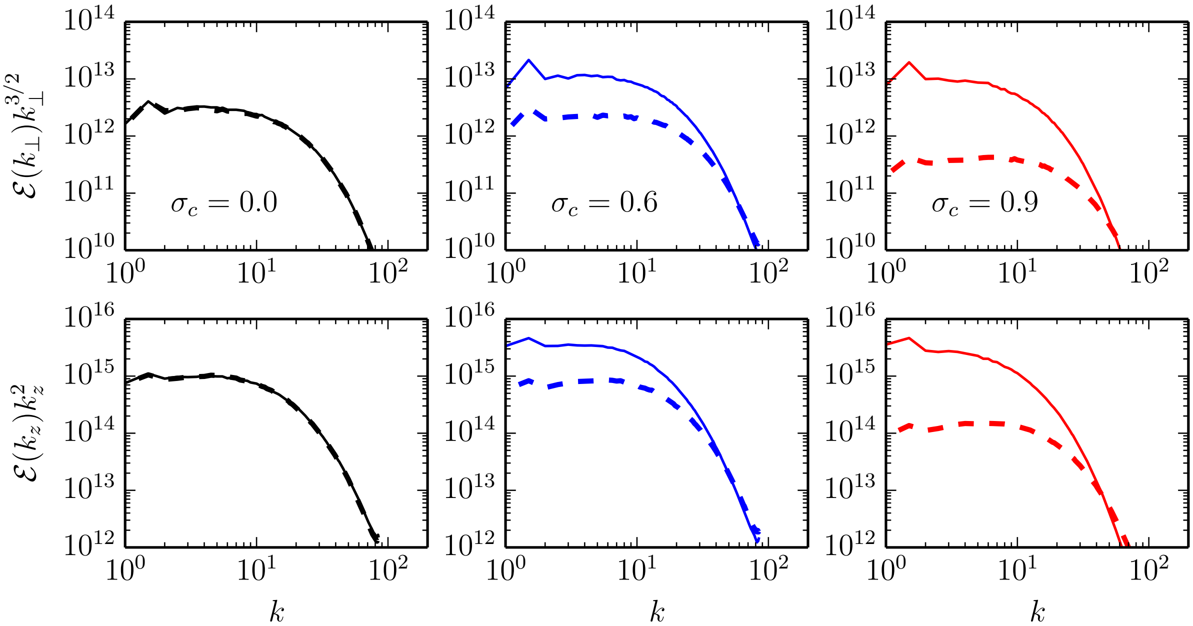

Figure 4.12: Spectra of positive (thin solid) and negative (thick dashed) Elsasser energies, $\mathcal{E}^{\pm}(k) = [\tilde{\mathbf{u}}(k) \pm \tilde{\mathbf{b}}(k)]^2/4$ in MHD turbulence with an order-unity mean-field. Shown are the spectra perpendicular to the mean-field (top row) and parallel to it (bottom row) for three different values of the normalized cross helicity

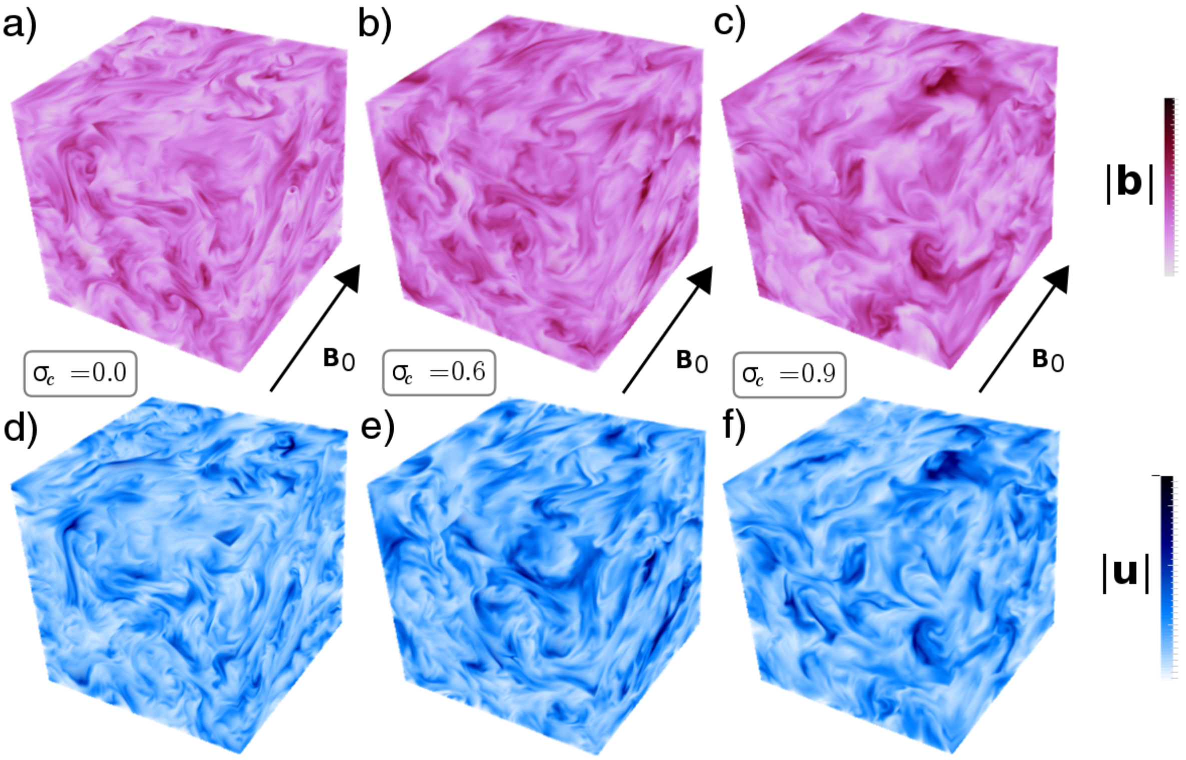

Figure 4.13: Spatial distribution of magnetic (top row) and velocity (bottom row) field intensity in MHD turbulence with an order-unity mean-field $\mathbf{B_0}$ directed as indicated by the arrows, with normalized cross-helicity values (*a*,*d*) $\sigma_c = 0.0$, (*b*,*e*) $\sigma_c = 0.6$, (c,f) $\sigma_c = 0.9$

in figure 4.3 confirms that a magnetic mean-field $\mathbf{B}_0^2 \sim \delta\mathbf{b}^2$ along the $z$ axis introduces a small level of anisotropy in its direction, while the turbulent fields remain isotropic in the perpendicular $x$-$y$ plane.

The difference between cases with different cross helicity is equally apparent if one examines the plots thoroughly: Although even in the balanced cases ($\sigma_c \sim 0.0$) regions in which the magnetic field attains its peak often also exhibit high velocity values, the correlation between both fields is visibly more pronounced in the strongly cross-helical runs. Besides this increased correlation, which follows naturally from the definition of cross helicity, the different mean-field cases do not exhibit any obvious qualitative difference: Both the typical extent of coherent structures and the variation of the field amplitudes appear remarkably similar in all runs.

The role of cross helicity becomes more obvious in a quantitative analysis of the alignment of velocity and magnetic field, $\cos[\angle(\mathbf{u},\mathbf{b})]$ (figure 4.14). The cross-helical cases exhibit a positive level of alignment by definition, whereas the balanced cases contain regions of positive and negative alignment in equal measure. As observed in other simulations of balanced turbulence (Matthaeus *et al.* , 2008), the alignment histograms of both $\sigma_c = 0.0$ runs, isotropic and order-unity mean-field, are peaked at the extremal values $\cos[\angle(\mathbf{u},\mathbf{b})] = \pm 1$. These peaks are less pronounced in the presence of a magnetic mean field, however, since the freedom of the magnetic field to align itself with the velocity field is constrained by the homogeneous mean field.

On the other hand, when one considers only the fluctuations in the magnetic field, $\delta\mathbf{b} = \mathbf{b} - \mathbf{B}_0$, the alignment histograms of even the cross-helical mean-field runs are barely distinguishable from the isotropic runs without a mean-field for comparable values of $\sigma_c$. Naturally the shape of the histogram becomes more skewed towards positive alignment values as the cross helicity increases, reflecting the larger correlation between velocity and magnetic field. This skewness is reduced if one uses an alignment definition that measures the angle between $\mathbf{u}$ and the total magnetic field $\mathbf{B_0} + \delta\mathbf{b}$ ($\cos\angle(\mathbf{u},\mathbf{b})$, dashed line in figure 4.14h). This is because in some regions the velocity field is directed in the negative $z$-direction, opposite to $\mathbf{B}_0$, and this region will contribute to the negative-alignment half of the $\cos\angle(\mathbf{u},\mathbf{b})$-histogram even if the magnetic fluctuation $\delta\mathbf{b}$ also has a negative $z$-component at that point, and is hence positively aligned with the velocity fluctuation.

## 4.4 Cross-helical turbulence with strong magnetic mean field

### 4.4.1 Anisotropic cross-helical forcing scheme

The emergence or application of a strong magnetic mean-field $|\mathbf{B_0}| \gg |\delta\mathbf{b}|$ in one direction will not only lead to an increase in the speed at which waves propagate along that direction, but as a consequence turbulent structures will be preferentially elongated along the mean-field. Applying a strong mean-field $\mathbf{B_0}^2 \sim 100\langle\delta\mathbf{b}^2\rangle$ to an isotropically

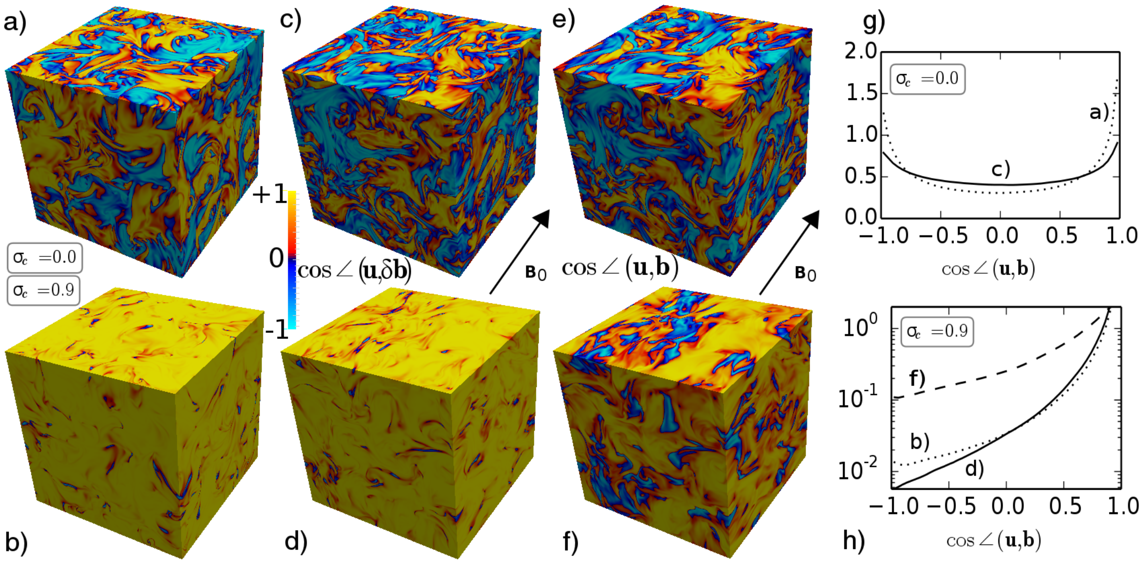

Figure 4.14: Alignment of velocity and magnetic fields in balanced (top row) and strongly cross-helical (bottom row) turbulence. (*a*,*b*) $\cos\angle(\mathbf{u},\mathbf{b})$ for zero-mean-field. (*c*,*d*) $\cos\angle(\mathbf{u},\delta\mathbf{b})$ for order-unity mean-field. (*e*,*f*) $\cos\angle(\mathbf{u},\mathbf{b})$ for order-unity mean-field. (*g*,*h*) Histograms of distributions of $\cos\angle(\mathbf{u},\mathbf{b})$ in zero-mean-field (dotted), and of $\cos\angle(\mathbf{u},\mathbf{b})$ (solid) and $\cos\angle(\mathbf{u},\delta\mathbf{b})$ (dashed) in order-unity mean-field

driven turbulence simulation has therefore proved to result in extremely volatile helicity values. Instead, the forcing algorithm needs to anticipate the field anisotropy by injecting energy in an anisotropic ellipsoidal shell in spectral space.

Consequently, in order to obtain ‘sub-Alfvénic’ turbulence with a mean-field this strong, we force modes with a wave vector $\mathbf{k}$ that fulfills $2.5 < (k_x^2 + k_y^2 + 10^2 k_z^2)^{1/2} < 3.5$, while simultaneously decreasing the resolution in the $z$ direction by a factor of 10. Computationally speaking, the forcing scheme injects energy and cross helicity at the same array positions as before. Since we maintain a cubic grid with size of $512^3$ cells for the numerical solution of the MHD equations, our sub-Alfvénic runs therefore simulate turbulence in an anisotropic domain with a physical size of $2\pi \times 2\pi \times 20\pi$. Accordingly we derive a perpendicular and parallel correlation length from the wavenumbers of the forced modes: $\lambda_\perp = 2\pi/3$ and $\lambda_{||} = 20\pi/3$, respectively.

Since we use isotropic viscosity and diffusivity coefficients, energy dissipation remains an essentially isotropic process, while the physical size of the numerical domain is anisotropic. Kolmogorov’s dissipation length therefore corresponds to fewer grid cells in the direction along the mean-field than perpendicular to it, and resolving it with the same accuracy in both directions is impossible. Although this numerical artifact causes numerical instabilities at more extreme anisotropies, the parallel resolution is still sufficient to resolve the dissipation length at a guide field strength $|\mathbf{B_0}| \sim 10|\delta\mathbf{b}|$ ($\ell_K$ corresponds to 1.25 grid cells) and a stable steady state is eventually reached for each run.

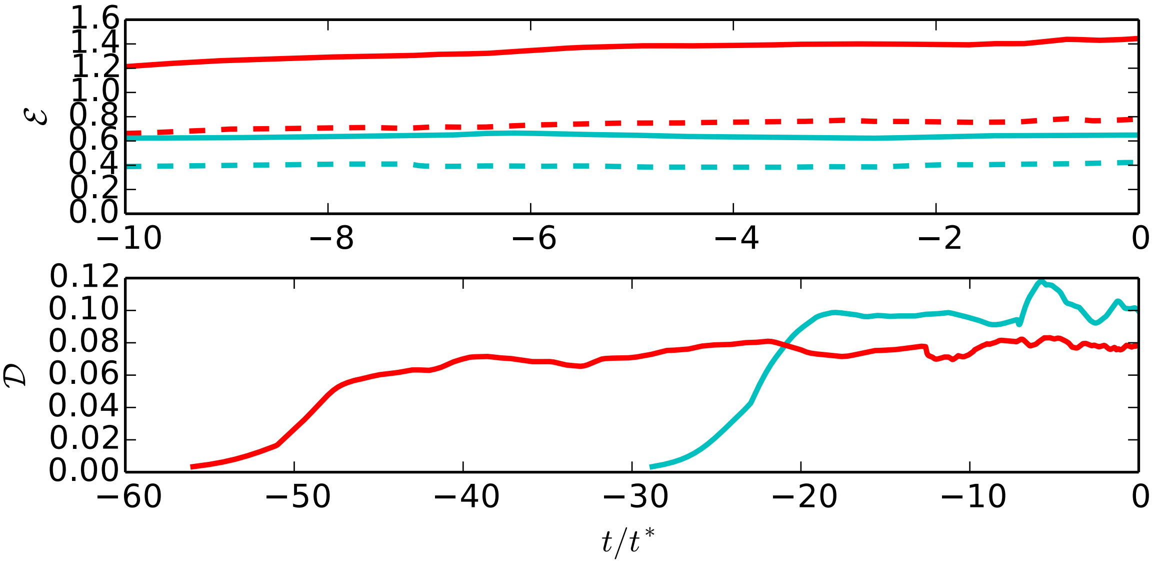

Figure 4.15: Top: evolution of the magnetic energy (dashed) and total energy (solid line) for $\sigma_c = 0.0$ (cyan) and $\sigma_c = 0.9$ (red) in sub-Alfvénic turbulence with ${\mathbf{B_0}}^2 \sim 100\langle\delta\mathbf{b}^2\rangle$. Bottom: evolution of the energy dissipation rate (colors as in top panel)

---

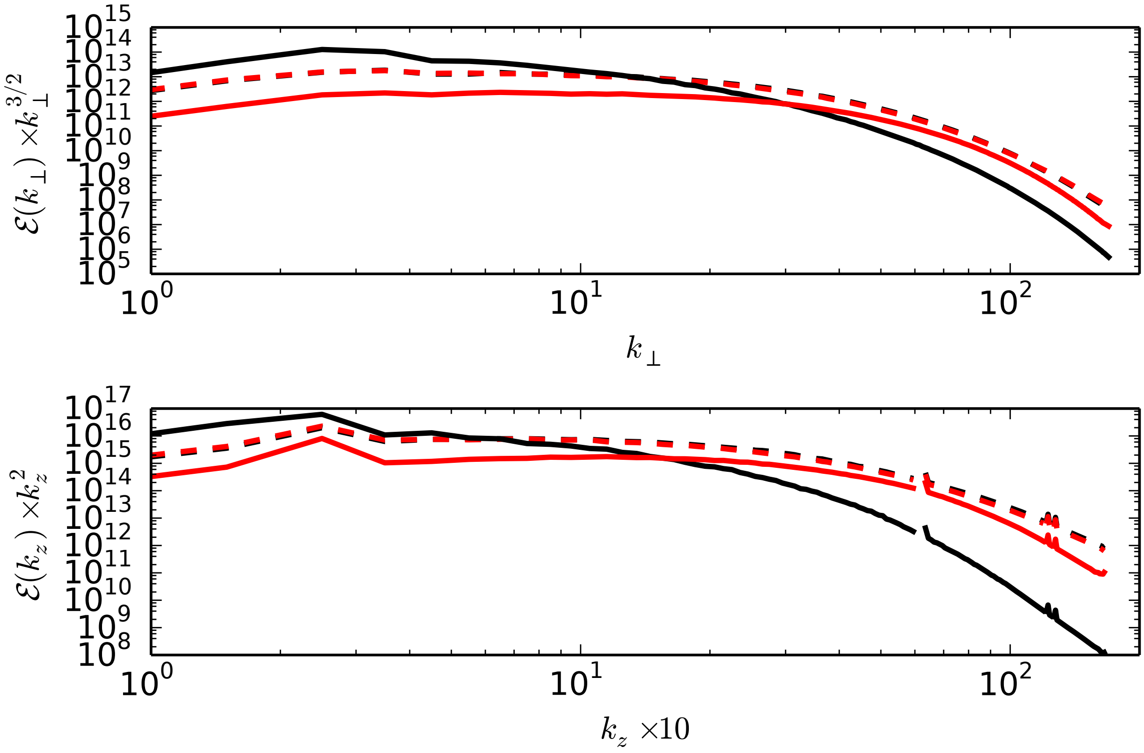

Figure 4.16: Steady-state spectra of positive (black) and negative (red) Elsasser energies, $\mathcal{E}^\pm = (\tilde{\mathbf{u}} \pm \tilde{\mathbf{b}})^2/4$, for balanced ($\sigma_c = 0.0$, dashed lines) and strongly imbalanced ($\sigma_c = 0.9$, solid lines) cases with a strong magnetic mean-field ${\mathbf{B_0}}^2 \sim 100\langle\delta\mathbf{b}^2\rangle$. (*a*) Spectrum perpendicular to $\mathbf{B_0}$. (*b*) Parallel spectrum

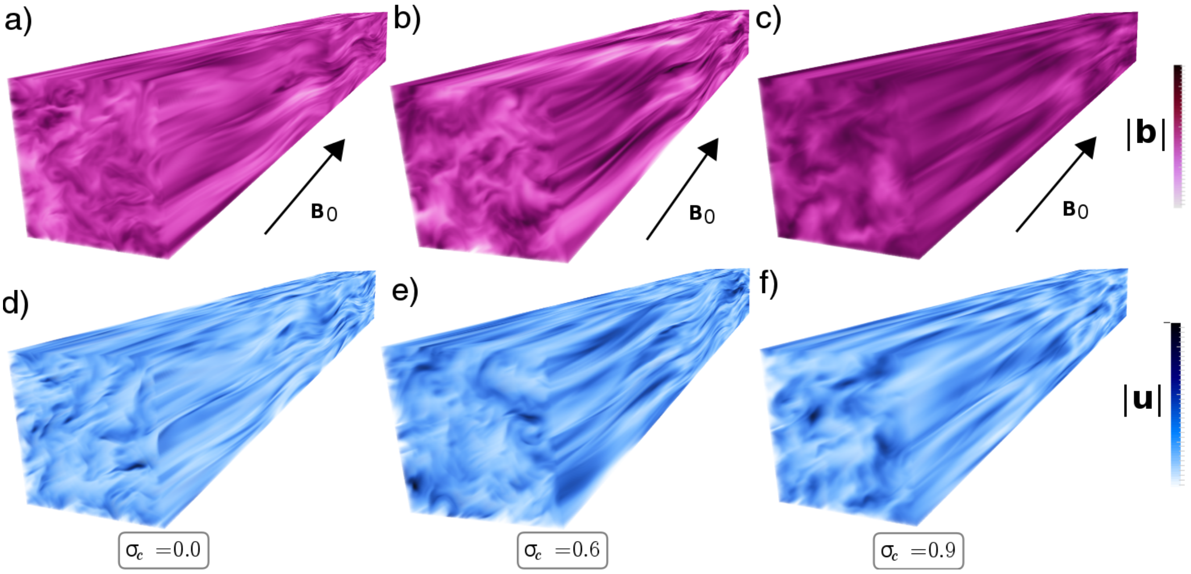

Figure 4.17: Spatial distribution of magnetic (top row) and velocity (bottom row) field intensity with magnetic mean-field $\mathbf{B_0} = 100\langle\delta\mathbf{b}^2\rangle^{1/2}$ in turbulence with normalized cross-helicity values of (*a*,*d*) $\sigma_c = 0.0$, (*b*,*e*) $\sigma_c = 0.6$, (*c*,*f*) $\sigma_c = 0.9$

### 4.4.2 Steady-state field analysis

The evolution of the magnetic energy, the total energy, and their dissipation for zero cross-helicity injection and strong cross-helicity injection ($\sigma = 0.8$) are compared in figure 4.15. Figure 4.16 provides comparisons of the spectra of the Elsasser energies parallel and perpendicular to the mean-field direction. As is particularly apparent in the latter graph, the Elsasser energy with the same sign as the total cross helicity dominates over the opposite Elsasser energy, while both Elsasser energies are in equipartition in the balanced case.

The spectra in the direction parallel to the mean field show a similar dominance of the Elsasser energy with the same sign as the cross-helicity (figure 4.16). As analytical predictions and recent numerical investigations have shown (Beresnyak, 2014), one expects a scaling $\mathcal{E} \propto k_z^{-2}$, and indeed this scaling fits our simulations well in the balanced case. As before, the spectral indices of the positive and negative Elsasser energies differ slightly in the cross-helical cases (Grappin *et al.* , 1983).

The alignment of velocity and magnetic field structures along the magnetic mean field is extremely apparent in sample snapshots of the steady-state field configurations (figure 4.17). Both fields also appear more correlated with each other in a run with a high cross-helicity injection rate of $\sigma_c = 0.9$.

The imbalance of the cross-helical cases is also obvious in plots of the spatial distribution of the cosine between the velocity field and the magnetic field $\mathbf{b} = \mathbf{B_0} + \delta\mathbf{b}$. The zero-cross-helicity case exhibits positive and negative values of $\cos\angle(\mathbf{u},\mathbf{b})$ in approximately equal proportion (figure 4.18a,b). For the strongly cross-helical case with $\sigma_c = 0.9$, the velocity field shows a similarly weak correlation with the total magnetic

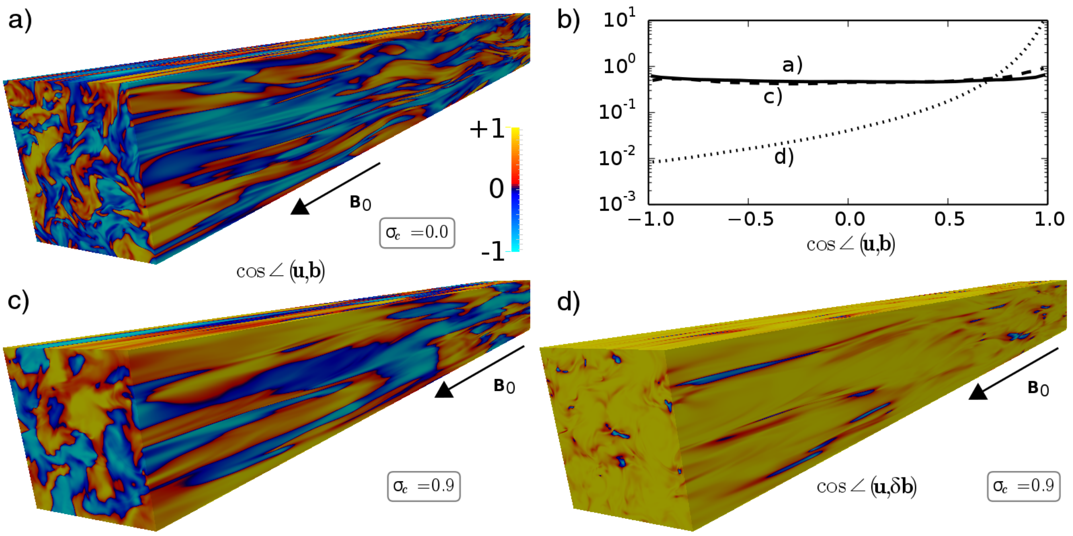

Figure 4.18: (*a*) Alignment of velocity and magnetic fields, cos $\angle(\mathbf{u}, \mathbf{b})$, in balanced turbulence. (*b*) Histograms of alignment in steady-state balanced turbulence (line a), alignment of velocity and total magnetic field (line c) and of velocity and magnetic fluctuations (line d) in strongly cross-helical turbulence. (*c*) Alignment distribution of cos $\angle(\mathbf{u}, \mathbf{b})$ in strongly cross-helical turbulence ($\sigma_c = 0.9$). (*d*) Distribution of cos $\angle(\mathbf{u}, \delta\mathbf{b})$ in the same snapshot of strongly cross-helical turbulence

field (figure 4.18c). (However, note the small changes in the slope of the histogram curve in subplot 4.18b at the extremal values cos $\angle(\mathbf{u}, \mathbf{b}) = \pm 1$.) Positive values dominate if the alignment cos $\angle(\mathbf{u}, \delta\mathbf{b})$ between the velocity field and only the fluctuations of the magnetic field is considered (figure 4.18d). A similar plot of cos $\angle(\mathbf{u}, \delta\mathbf{b})$ for the balanced case is not depicted since it varies only negligibly from the total-field alignment (figure 4.18a).

Due to the almost identical distribution of the alignment of $\mathbf{u}$ and $(\mathbf{B_0} + \delta\mathbf{b})$ in balanced and cross-helical turbulence, both cases exhibit a similar level of isotropy in the motional electric field along the mean-field direction (figure 4.19), with the global average $\langle e_z \rangle = 0.000458\langle|\mathbf{e}|\rangle$ in the balanced case and $\langle e_z \rangle = -0.000034\langle|\mathbf{e}|\rangle$ in the strongly cross-helical case. The distribution of $e_z$ is thus symmetric around $e_z = 0$ with an approximately exponential drop-off in both directions (Breech *et al.* , 2003).

### 4.4.3 Dispersion analysis of balanced and imbalanced turbulence

However, asymmetry in another sense can be demonstrated: We analyzed spectra of the magnetic field, Fourier-transformed in space and time (figure 4.20). To minimize the influence of non-ideal effects, we evolved the fields without any forcing or dissipation. Most of the energy can be found in modes which fulfill the dispersion relation of shear-Alfvén waves, $\omega = v_A k_z$. This is clear evidence of Alfvén waves traveling along and opposite to the mean-field direction, confirming that the evolution of the MHD

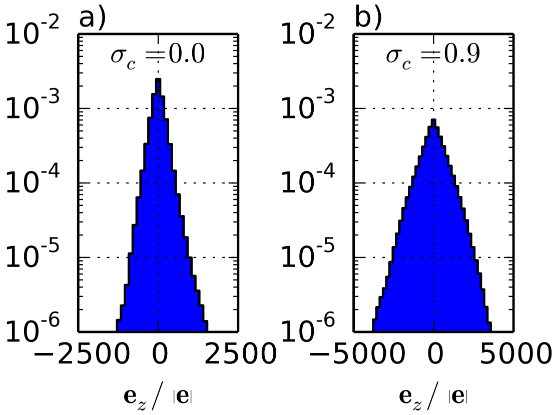

Figure 4.19: Histograms of the parallel component of the electric field for snapshots of (*a*) balanced turbulence, (*b*) strongly cross-helical turbulence

turbulence is mainly shaped by propagating shear-Alfvén waves. The large amount of energy at low parallel wavenumbers $k_z \sim 0$, visible as vertical stripes in the plots, is due to the parallel steady-state spectrum (*cf.* figure 4.16).

The $x$-shaped dispersion plot of the balanced case is symmetric with respect to the $k_z = 0$ line, indicating that the waves propagating parallel and antiparallel to the mean field are equally energetic. In the strongly cross-helical case, there is more energy in the modes along $\omega = +v_A k_z$ than in the modes with the oppositely directed phase velocity along $\omega = -v_A k_z$, particularly at larger $k_z$.

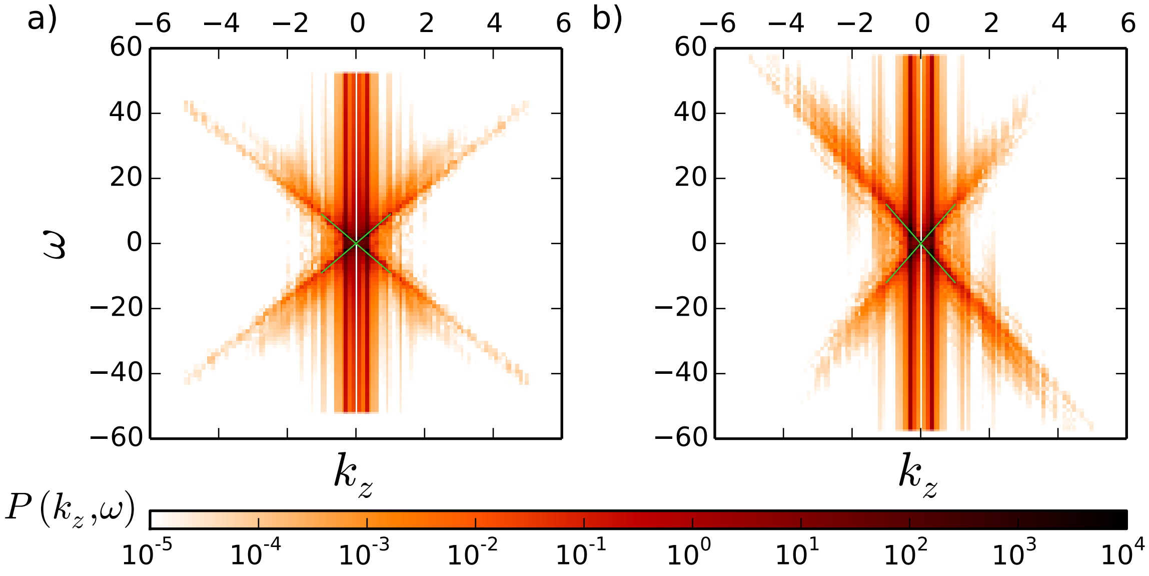

Figure 4.20: Power spectra $P(k_z, \omega)$ of (*a*) balanced ($\sigma_c = 0.0$) and (*b*) strongly cross-helical ($\sigma_c = 0.9$) MHD turbulence, with the phase velocity $\omega / k_z = \pm v_A$ drawn in as light green crosses

Thus our cross-helical forcing algorithm facilitates not only control over the correlation between velocity and magnetic field. The cross-helical turbulence in our simulations also matches the description of Alfvénic turbulence given in chapter 2, while exhibiting negligible kinetic or magnetic helicity.

On one hand, the numerical solution of the MHD equations includes nonlinear interactions realistically. Isotropic and trans-Alfvénic turbulence is therefore simulated more accurately than if we were to artificially impose the same simple slab-spectrum that we used for analytic modeling in chapter 3. On the other hand, we have shown that the inertial range of our $512^3$ runs is wide enough that the power-law indices of the spectra can be measured. This allows us to compare trajectories computed in realistic MHD turbulence with quasilinear predictions of charged-particle heating in the next chapter.

# Chapter 5

# Stochastic Heating in Cross-Helical Turbulence

*Above the sky at the top of the world,*
*Closer than we ever thought we could be . . .*
*On the rise, energized*
*Breathing in gradually and rising to the source*
*Breathing out steadily and capturing the force*

– *On The Rise* (Samael, 2007)

**Chapter Summary**

- Quasilinear theory describes the stochastic acceleration of charged particles in MHD turbulence as diffusion in momentum space.
- The stochastic acceleration by the motional electric force on large length scales is complemented by Ohmic heating due to the Ohmic electric field on small length scales.
- Ohmic heating is effective if particles with a small gyroradius are trapped in current filaments, with a transverse extent similar to the dissipation scale in our simulation.
- Whereas Ohmic heating is independent of the cross helicity of the turbulence, the stochastic heating by the motional electric field decreases as the cross helicity becomes larger.
- The scaling of the momentum-diffusion rate with both the normalized cross helicity and the gyroradius agrees with quasilinear predictions for large gyroradii.

We now turn to test-particle simulations performed in the field configurations which were generated as described in the previous chapter. Parts of this chapter have been published in Physical Review E (Teaca *et al.* , 2014).

## 5.1 Motivation

The previous chapter contained an explanation of how electromagnetic-field configurations of incompressible magnetohydrodynamic turbulence with zero or non-zero cross helicity can be created. The helical-forcing mechanism which we have employed guarantees that kinetic and magnetic helicity remain negligibly small, both for isotropic turbulence and for strongly anisotropic turbulence with a magnetic mean-field.

Using the turbulent fields of these cross-helical MHD runs, we will expound our investigation of the heating and stochastic acceleration of charged particles with velocities comparable to the Alfvén velocity $v_A$ in this chapter. This analysis will enable us to compare predictions of the heating rate of cosmic-ray particles in cross-helical turbulence, as obtained from quasilinear theory in chapter 3, with realistic simulations of test-particle heating in fully-evolving three-dimensional incompressible MHD turbulence.

The heating and scattering of charged particles in turbulent fields obtained in MHD simulations has already been studied before by other authors. For example, Ambrosiano *et al.* (1988) used test-particles in static snapshots of a reconnecting current sheet to study the heating of charged particles, and found a strong dependence on the gyroradius. More recently, the advancing computational power available to researchers has made the simultaneous evolution of test-particle trajectories and MHD fields possible. Lehe *et al.* (2009) and Lynn *et al.* (2011) used this method to investigate the agreement of realistic particle heating with quasilinear theory, observing that wave-particle interactions are not sharply resonant at the frequencies predicted by QLT; instead, the bandwidth of resonant frequencies is significantly broadened. No previous study that we know about has focused on the role of cross helicity, however.

Although the velocity of cosmic-ray particles usually exceeds the Alfvén velocity in the interstellar medium, where typically $v_A \sim 10{,}000\ \mathrm{m\ s^{-1}}$, the effect of cross-helical turbulence on the propagation of Alfvén-speed particles is especially evident. The importance of this particular velocity regime lies in the fact that small turbulent fluctuations of the magnetic field will propagate along the mean magnetic field at the local Alfvén velocity. This applies even if the system is isotropic on large scales and the magnetic mean-field exists only when one averages the magnetic field over a small sub-volume of the entire simulation domain.

As we emphasized in our explication of quasilinear theory in chapter 3, the effect of turbulent fluctuations on the trajectory of charged particles is greatest if the wave and the propagating particle are in resonance with each other. Expressed via the argument of the Dirac functional which appears in the derivation of QLT, this means that the wave-particle interaction deflects or heats the cosmic-ray particle most efficiently if:

$$\omega_{\mathbf{k}} - v_{\|} k_{\|} - n\Omega_0 = 0, \tag{5.1}$$

where $\omega_{\mathbf{k}}$ and $k_{\|}$ are the wave frequency of the turbulent fluctuation and the wave vector component parallel to the local magnetic mean field, respectively. The particle velocity along the mean field is denoted by $v_{\|}$, while $\Omega_0$ is its gyrofrequency in the local magnetic field. The greater the absolute value of the integer index $n$ is in this resonance condition, the less efficient the resonant interaction becomes. Thus it follows that the maximum efficiency of the interaction is achieved if

$$v_{\|} \sim \frac{\omega_{\mathbf{k}}}{k_{\|}} = v_A, \tag{5.2}$$

where we have assumed that the dominant type of turbulent fluctuations follows the dispersion relation of shear-Alfvén waves.

Note that if condition (5.2) holds exactly, such that $n = 0$ (Landau resonance), the energy transfer between particles and waves is strongest, but only if an electric-field component parallel to the magnetic mean-field exists (*e.g.* Stix, 1992; Somov, 2006). This is not the case in incompressible turbulence, in which the only possible Alfvénic wave type is the shear-Alfvén mode with no parallel electric field (see chapter 2), and the wave-particle interaction are dominated by the gyroresonant modes with $n \neq 0$. Hence, the rate at which charged particles in Alfvénic turbulence diffuse in position-space as well as in velocity-space is greatest if the velocity of the particles is comparable, but not equal to the locally measured Alfvén velocity.

## 5.2 Test-particle method

Thus, in order to quantify the diffusion rate in momentum-space numerically, we investigate the propagation of Alfvénic ($v \sim v_A$) charged particles in MHD turbulence. To this end, we inject test particles into several Turbo simulations, which were initialized with the helical-forcing procedure that was detailed in the previous chapter. The test-particle injection takes place only after energy and cross-helicity of each run have settled into a steady-state (as shown for example in figure 4.11), so both quantities can be assumed to stay constant for the entire duration of the test-particle propagation.

In the test-particle approach, this means that the back-reaction which the scattered charged particles may have on the electromagnetic fields is not accounted for; only the influence of the fields on the particles is included in these simulations. This is not a deficiency in terms of self-consistency, however, if the charge density of the test-particle population in our simulations is low enough. Assuming this density is sufficiently small, the feedback of the scattered test-particle trajectories on the turbulence can be taken as negligible. To quantify this condition, we demand that the current produced by the charged test-particles with charge density $\rho_{CR}$ is much smaller than the one produced by the MHD fluid, or

$$\rho_{CR} \ll \frac{B}{\mu_0 \, \ell \, v_A}, \tag{5.3}$$

where $B$ is a typical value of the magnetic field strength (in physical units) and $\ell$ corresponds to a typical gradient-length scale of the magnetic field.

First we begin by analyzing charged-particle acceleration by propagating 50,000 test-particles through each turbulent setup. The Lorentz force we use to calculate the particle trajectories includes an electric-field term derived from both the Ohmic electric field $\mathbf{e}_{\text{ohm}} = \eta \nabla \times \mathbf{b}$, with $\eta$ the magnetic diffusivity of the plasma and $\mathbf{b}$ the total magnetic field in Alfvén units (defined in chapter 2), and the motional electric field $\mathbf{e}_{\text{mot}} = -\mathbf{u} \times \mathbf{b}$:

$$\begin{aligned}\frac{d}{dt}\mathbf{x} &= \mathbf{v}, \\ \frac{d}{dt}\mathbf{v} &= \alpha\left(\mathbf{e}_{\text{ohm}} + \mathbf{e}_{\text{mot}} + \mathbf{v} \times \mathbf{b}\right) \\ &= \alpha\left[\eta \nabla \times \mathbf{b} - \mathbf{u} \times \mathbf{b} + \mathbf{v} \times \mathbf{b}\right]. \end{aligned} \tag{5.4}$$

Here $\alpha$ is the charge-to-mass ratio of the particles, the mass of which we set to be unity for convenience. In this case $r_g(0) = v_\perp/(\alpha v_A)$ is the initial gyroradius of a particle with a velocity component $v_\perp$ perpendicular to the local magnetic field, if the intensity of the field corresponds to the root-mean-square value of the volume-averaged magnetic field. Since this coincides with our definition of the Alfvén velocity, the intensity of the local magnetic field can then be written as $|\mathbf{b}| = v_A$ in the Alfvénic units which Turbo makes use of.

As we have justified above with our goal of obtaining the maximum efficiency of the resonant interaction, all test-particles are injected with an initial velocity equal to the Alfvén velocity, $|\mathbf{v}(0)| = v_A$. The initial direction of this velocity as well as the initial position of the particles in the simulation domain are chosen at random with uniform probability densities.

We treat the charge-to-mass ratio $\alpha$ of the test-particles as a parameter distinguishing five different test-particle ensembles because this is the parameter allowing us to control the initial gyroradius of the test-particles, all of which start with the same velocity $v_A$. Expressed in terms of Kolmogorov's dissipation length $\ell_K$ (defined in chapter 2), the gyroradius at the time of the test-particle injection takes the values $r_g(0)/\ell_K \in \{0.1, 0.3, 1.0, 3.0, 10.0\}$.

Since the acceleration we study occurs over several Alfvén times, we evolve the test-particle trajectories in parallel with the MHD fields to simulate realistic interactions with propagating Alfvén waves. Although this additional computational effort slows down the calculation of the diffusion coefficients considerably, it is necessary for an accurate simulation of the wave-particle interaction in this Alfvénic-velocity regime.

On the other hand, the scattering of cosmic-ray particles traveling at relativistic velocities through imbalanced turbulence has previously been investigated by Beresnyak *et al.* (2011). In their publication, the relativistic equations of motions (without the Ohmic force) were employed to propagate test-particles through static snapshots of magnetohydrodynamic turbulence with various degrees of imbalance. Since the electric fields in those simulations were too small to result in a significant amount of particle heating over the entire time for which the trajectories were simulated, the energy gain of the test-particles was negligibly small. The authors concluded that, for relativistic particles, stochastic acceleration can be neglected independently of how strongly imbalanced the MHD turbulence is.

Returning to our numerical scheme, equation (5.4) is solved numerically by applying an implicit fourth-order Runge-Kutta solver with an adaptive determination of the time step. Thus we ensure that the numerical step-size of the RK4 solver is sufficiently small to resolve the gyration of a test-particle, even if the intensity of the local magnetic field, which determines the actual gyrofrequency of a particle together with its charge-to-mass ratio, is several times the root-mean-square field intensity.

## 5.3 Inclusion of Ohmic fields

As we are particularly interested in analyzing the interplay of the Ohmic fields at small length scales with the motional electric fields at larger scales, we continue including the dissipation terms in the computation of the MHD fields while the test-particle trajectories are being evolved. We thus ensure that the force on the test-particles is consistent with the MHD equations, since the inclusion of the Ohmic force $\mathbf{e}_{\mathrm{ohm}} = \eta\nabla \times \mathbf{b}$ on the particles implies a non-zero magnetic diffusivity $\eta$. Due to our desire to maintain a steady-state during the test-particle calculation, the energy dissipated at small scales continues being resupplied via the energy and cross-helicity injection scheme described in chapter 4.

The reason underlying our interest in the Ohmic field is that these fields are strongest in thin, dynamically evolving current filaments where $\nabla \times \mathbf{b} = \mathbf{e}_{\mathrm{ohm}}/\eta$ attains a sharp local maximum intensity (*cf.* figure 5.1). Unlike in similar MHD simulations dedicated solely to the investigation of reconnection-acceleration phenomena (*e.g.* Matthaeus *et al.* , 1984; Ambrosiano *et al.* , 1988; Onofri *et al.* , 2006; Kowal *et al.* , 2011), these structures arise spontaneously during the evolution of the electromagnetic fields. We do not seed them by choosing an initial shape of the magnetic field that would favor their formation. Comparing normalized histograms of the Ohmic electric fields with histograms of Gaussian distributions with the same standard deviations (as in figure 5.2), we find that the Ohmic field is strongly intermittent and exhibits an abundance of data with high absolute value, visible in the histogram plots in the form of extremely heavy tails.

Due to the highly intermittent nature of these filaments, a description in terms of a spectral energy density, as required for a quasilinear description of particle diffusion, is necessarily flawed. The information about the complex phases of the Fourier components, which would be necessary to reconstruct the intermittency of the fields, cannot be deduced from the power spectra of the magnetic field. Our aim is therefore to compare the heating effect which Ohmic fields in current filaments provide in numerical simulations with the heating rate due to the motional fields, which are considered in quasilinear diffusion theory.

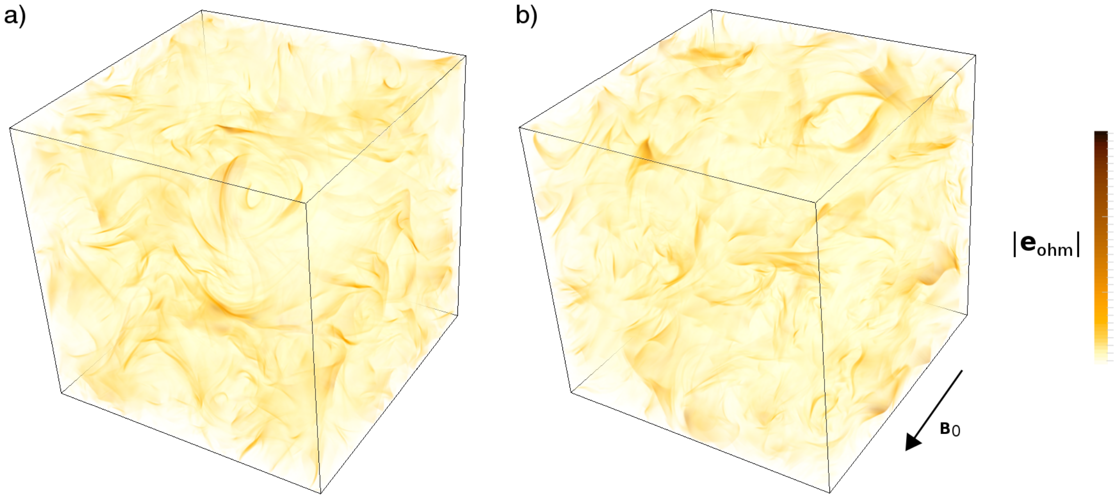

Figure 5.1: Spatial distribution of the Ohmic electric field $\mathbf{e}_{\mathrm{ohm}} = \eta \nabla \times \mathbf{b}$ in (*a*) isotropic MHD turbulence and (*b*) turbulence with an order-unity mean-field (for both cases $\sigma_c = 0.0$)

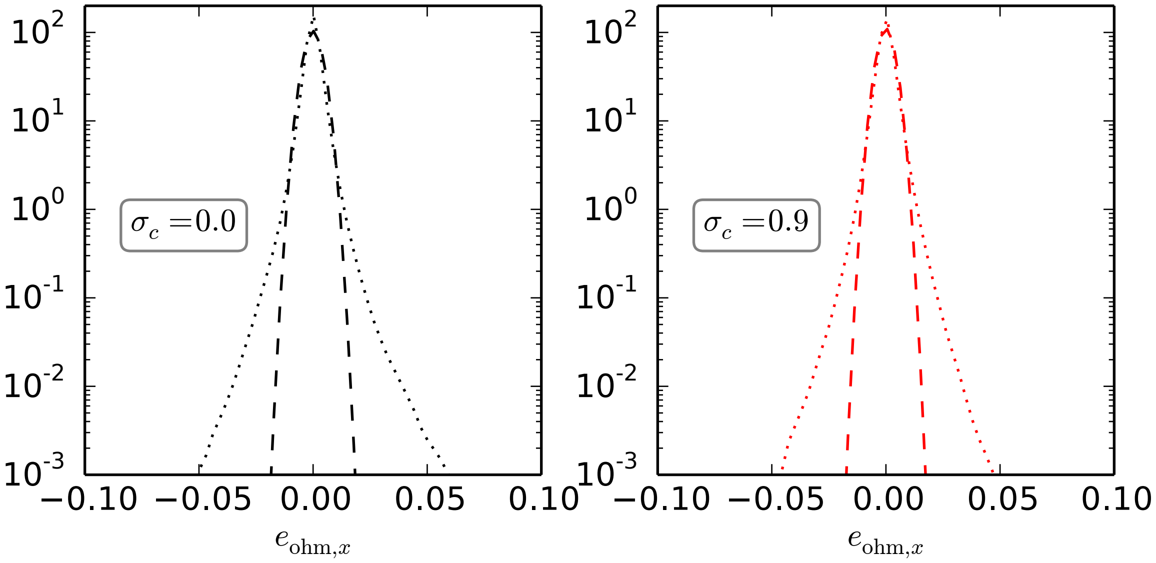

Figure 5.2: Histograms of the $x$-component of the Ohmic electric field (dotted lines) in isotropic MHD turbulence with (*a*) $\sigma_c = 0.0$ and (*b*) $\sigma_c = 0.9$. The dashed lines mark centralized Gaussian distributions with the same standard deviation as the $e_{\mathrm{ohm},z}$-histograms

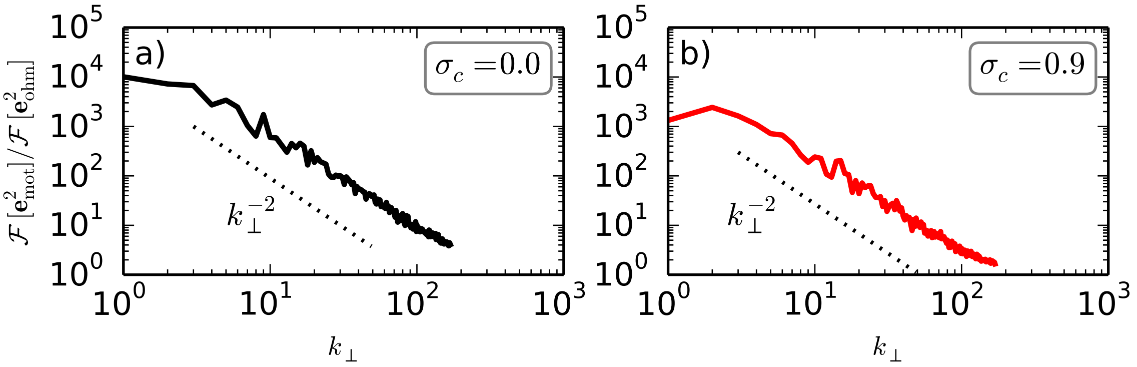

Figure 5.3: Ratio of motional and Ohmic power spectra perpendicular to the mean field direction for steady-state snapshots with normalized cross helicity (*a*) $\sigma_c = 0.0$ and (*b*) $\sigma_c = 0.9$

This goal is also the motivation for normalizing the particle gyroradius by Kolmogorov's dissipation length $\ell_K$, which constitutes a good approximation of the typical transverse extent of current filaments observed in MHD simulations (*e.g.* Dmitruk *et al.* , 2004). Trajectories of particles with a gyroradius much larger than $\ell_K$ will only be accelerated in current filaments for short periods of time while the particles cross the filament. Smaller gyroradii will cause particles to be trapped within current filaments, where they will be accelerated along them for longer times.

The increasing relative importance of Ohmic electric fields at smaller length scales, compared to the motional electric field, is easily seen in plots of the power spectra of each field type. The ratio of the motional-field over the Ohmic-field power spectrum for MHD turbulence with an order-unity magnetic mean field is drawn in figure 5.3. The motional-field spectrum drops much faster with increasing wave number than the Ohmic-field spectrum over the inertial range, resulting in the decrease of the shown ratio as one goes to larger $k_\perp$. Hence the relative heating contribution of $\mathbf{e}_{\mathrm{ohm}}$ becomes more significant at smaller gyroradii. Although the power of the Ohmic fields remains below the motional-field power across the spectrum (as the depicted ratio remains larger than unity throughout the inertial range), the high intermittency of the Ohmic electric field (see figure 5.1) still leads to a much faster acceleration at smaller gyroradii than at large gyroradii.

Figure 5.3 also already hints at a subtle yet crucial difference between balanced (zero cross-helicity) and cross-helical turbulence: Although the power spectra for the Ohmic electric field are almost indistinguishable for both balanced and strongly cross-helical turbulence, the ratio of motional to Ohmic-field power is lower in the latter case, implying that the motional field is weaker overall. Although this difference may appear insignificant from the figure, it will become important as we investigate the rate of stochastic heating.

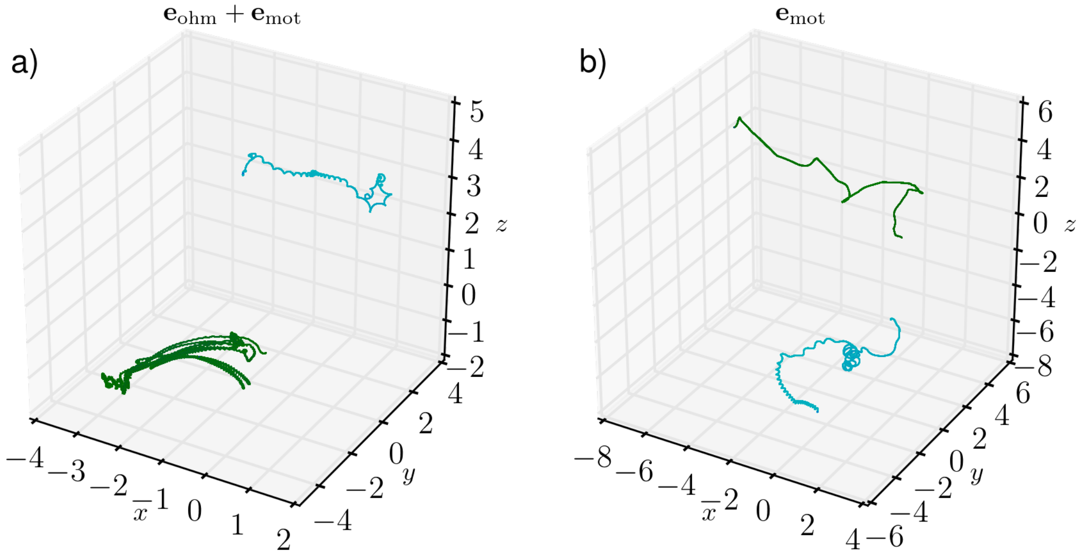

Figure 5.4: Sample test-particle trajectories for initial velocity $v(0) = v_A$ and initial gyroradius $r_g(0) = 0.3\ell_K$ (green) and $r_g(0) = 10\ell_K$ (cyan) for propagation (*a*) with and (*b*) without the Ohmic electric field $\mathbf{e}_{\rm ohm}$ for $0 < t < 30t_A$

## 5.4 Stochastic heating in isotropic turbulence

### 5.4.1 Sample trajectories

Plots of sample test-particle trajectories provide further evidence for this interpretation (figure 5.4): Particles with smaller gyroradii are quickly trapped in current filaments, where they experience a drastic change in particle energy because of the Ohmic electric field. An example of this is shown as the green trajectory in figure 5.4a with several oscillations back and forth along a current filament. Meanwhile larger-gyroradii particles perform a random walk through large parts of the simulation domain without being captured and continuously accelerated by current-filament structures (the cyan trajectory in the same plot).

If test-particles are not subjected to the Ohmic field but only the motional electric field, the difference between large and small gyroradii becomes less obvious. Both test-particles in figure 5.4b simply trace the magnetic fieldlines on which they start, without being trapped by regions with a strong local current density. Without the contribution of the Ohmic heating, however, the energy gain is greatly reduced: For example, the kinetic energy of the test-particle with $r_g(0) = 0.3\ell_K$ in figure 5.4b increases by a factor of 3.6 over the 30 Alfvén times depicted because of stochastic heating. The Ohmic field included in the calculation of the trajectory of a particle with the same charge-to-mass ratio in figure 5.4a, on the other hand, accelerates this particle to 130 times its initial energy during the same period of time.

Figure 5.5 shows both the trajectory of a test-particle trapped in several current-filament structures because of its small initial gyroradius ($r_g(0) = 0.1\ell_K$) and the spa-

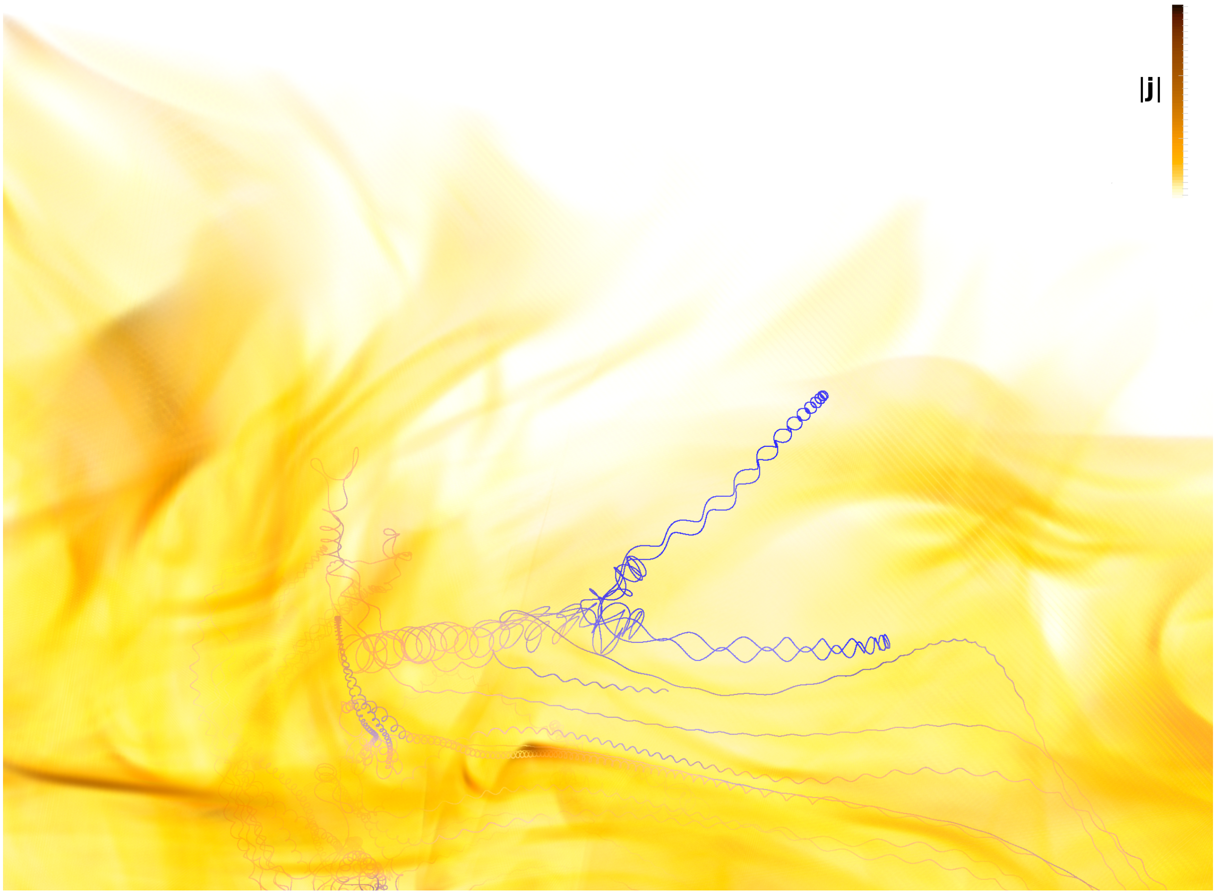

Figure 5.5: Trajectory (blue) of a test-particle with initial gyroradius $r_g(0) = 0.1\ell_K$ and initial velocity $v(0) = v_A$ in isotropic MHD turbulence with zero cross helicity. Additionally, the spatial distribution of the electric-current density $|\mathbf{j}|$ is superposed in orange

tial distribution of the current density. The two pieces of the trajectory in the center of the image are clear examples of how trapping works in detail: The component of the particle velocity along the magnetic field is reduced and eventually inverted by the extremely strong Ohmic field. During this entire process, which looks as if the particle were reflected, the gyroradius of the trajectory stays approximately constant.[1] Along the bottom of the same figure the alignment of the test-particle trajectory with filaments of strong electric current is clearly visible, while the left-hand side of the picture shows the extremely random motion of the test-particle in a region with very strong turbulence.

---

[1] As a sidenote, we remark that the magnetic turbulence in all simulations presented in this chapter is too strong for adiabatic invariance to hold – in other words, the magnetic moment $M_{\mathrm{mag}} = mv_\perp^2/(2B)$ is not conserved, not even approximately, in contrast to the runs in sub-Alfvénic turbulence which we will discuss in chapter 6. Hence the reflection shown in figure 5.5 cannot be attributed to a simple magnetic-mirror effect, in which the gyroradius of the trajectory would strongly decrease as the particle approaches the reflection point.

The main effect of non-zero cross helicity on the electric fields is a reduction of the strength of the motional field $\mathbf{e}_{\mathrm{mot}}$, as we previously mentioned in the context of figure 5.3. The Ohmic-field intensity, on the other hand, is barely affected by increasing the cross helicity. We thus infer that the alignment of the magnetic field with the velocity field does not change the relative abundance of current-filament-like structures in the simulation domain.

### 5.4.2 Influence of cross helicity

The histograms (figure 5.6) of the kinetic-energy distribution $E = v^2/2$ (the mass of all particles is taken to be unity) provide clear and unambiguous evidence that the test-particle populations gain energy over the simulation time. Although a very small proportion of the test-particles is actually decelerated to energies less than the initial $E(0) = v_A^2/2$, both the mean energy (marked with vertical lines in the plots) and the peak energy (red circles) of the ensembles increase as time progresses.

We now focus on the effect of cross helicity, starting with our results in isotropic MHD simulations without an external magnetic mean-field. Comparing the stochastic-acceleration rate of different turbulence configurations on test-particle ensembles with the same normalized charge, we have found that the most efficient acceleration is obtained in balanced turbulence with zero cross helicity ($\sigma_c = 0.0$). As shown in figure 5.6, the acceleration proceeds at a similar rate in weakly cross-helical turbulence ($\sigma_c = 0.3$), but the energization is significantly slower in configurations with strong cross-helicity ($\sigma_c = 0.9$): Both the peak and the mean of the kinetic energy of each population increase at smaller rates the higher the level of cross helicity is.

Qualitatively speaking, of course, this diminished stochastic acceleration in cross-helical turbulence is what one expects: The averaged norm of $\mathbf{e}_{\mathrm{mot}}$, the cross product of magnetic and velocity field, is smaller if both fields are aligned in turbulence with higher absolute cross helicity. With a smaller average value of the electric field, the rate of stochastic acceleration of charged particles will also be reduced.

### 5.4.3 Comparison with quasilinear predictions

A more quantitative measure of the acceleration rate can be obtained by calculating the momentum diffusion coefficient

$$\mathcal{D}_{pp} = \frac{\left\langle [\mathbf{v}(\Delta t) - \mathbf{v}(0)]^2 \right\rangle}{2\Delta t}, \tag{5.5}$$

for each test-particle ensemble in our simulations, where $\Delta t$ is a time period during which the evolution of the averaged velocity-norm can be called diffusive, such that $\mathcal{D}_{pp}$ as defined above can be assigned a constant value.

How important it is that this time period be chosen carefully is evident from figure 5.7, which shows the evolution of the mean-square-displacement of the momen-

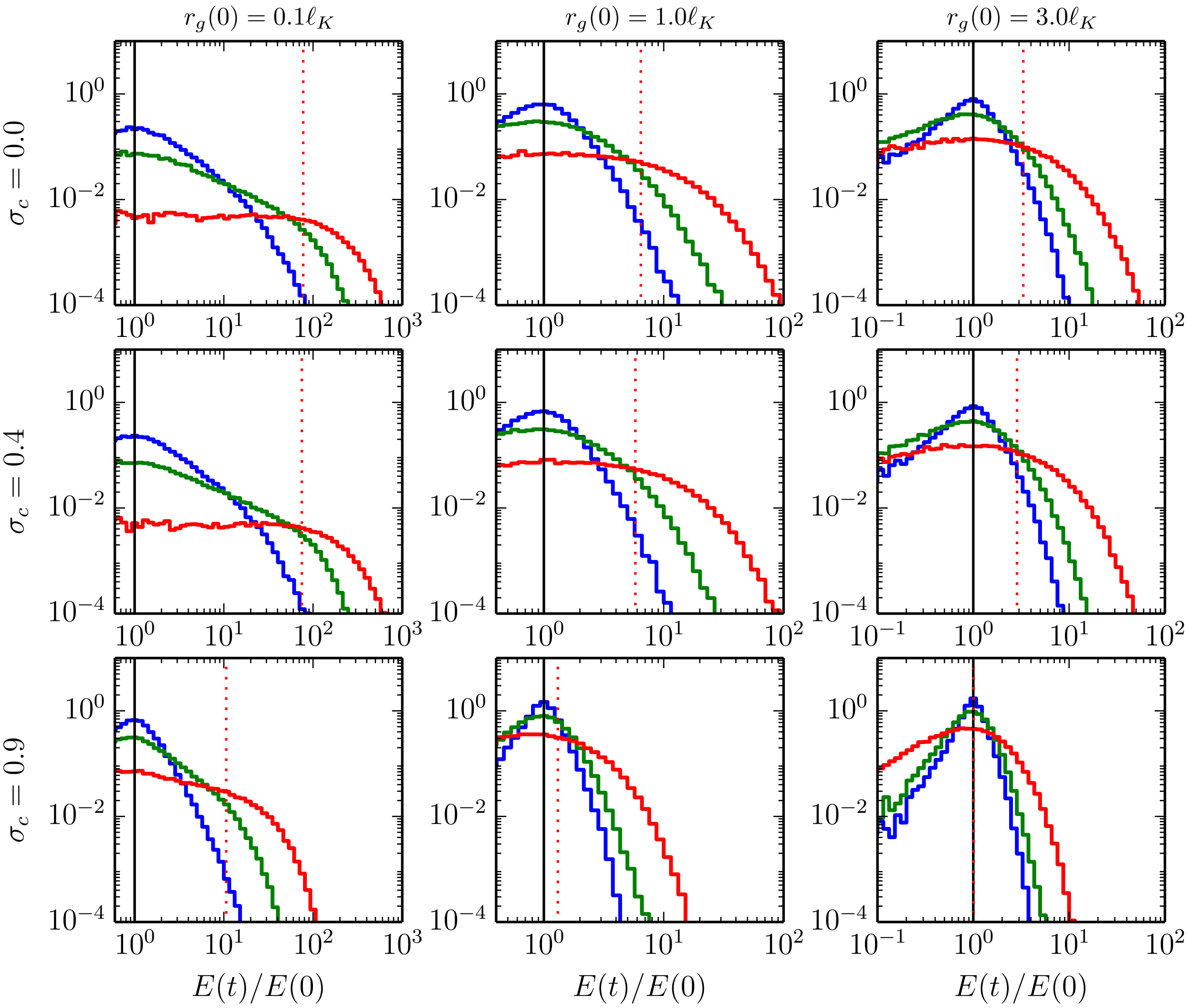

Figure 5.6: Energy histograms of test-particle simulations with $r_g(0) = 0.1\ell_K, 1.0\ell_K$, and ß.$0\ell_K$ (from left to right column) for isotropic MHD turbulence with cross-helicity values of $\sigma_c = 0.0, 0.4$, and 0.9 (from top to bottom row) at different multiples of the Alfvén time $t/t_A = 0$ (black), $t/t_A = 1$ (blue), $t/t_A = 5$ (green), and $t/t_A = 25$ (red)

tum vectors of several test-particle ensembles. At the beginning of the simulation, this evolution is dominated by particles starting out in regions with a very strong and locally uniform electric field. The acceleration of these particles will initially be ballistic, such that the numerator of $\mathcal{D}_{pp}$ in definition (3.62) will grow as $\Delta t^2$, as evidenced by the sharp increase of the mean-square-displacement in all cases shown. Only after propagating for a couple of Alfvén times has every test-particle population sampled a large enough range of electric-field values that the slopes of the graphs remain constant, indicating that the particle motion in momentum-space has become diffusive. The time periods which we have selected to determine the values of $\mathcal{D}_{pp}$ of each test-particle ensemble are marked by the dashed lines in figure 5.7.

The prediction for $\mathcal{D}_{pp}$ found using quasilinear theory in equation (3.62) accounts for the possibility of different values of the energies and spectral exponents for the populations of co- and counter-propagating Alfvén-waves. In order to simplify that equation, we will follow the suggestion of Dung & Schlickeiser (1990) and assume the identity of both spectral exponents, $s^+ = s^- = s$. At least in the large-$k$ part of the inertial range, close to the dissipation range, this assumption is well-justified even for all of the cross-helical runs because of the pinning effect mentioned in chapter 4, or the convergence of the positive and negative Elsasser-energy spectra for $k \longrightarrow 2\pi/\ell_K$. Using this assumption, $\mathcal{D}_{pp}$ in equation (3.62) can be written as (Dung & Schlickeiser, 1990):

$$\mathcal{D}_{pp} = m^2 v_A^2 \, v \, \frac{\delta B^2}{B_0^2} \, \frac{\pi(s-1)}{s(s+2)} \, k_{\min}^{1-s} \times r_g^{-s+2} \, (1 - \sigma_c^2). \tag{5.6}$$

In order to visualize how well this scaling is matched by our test-particle simulations, we have renormalized the values of the numerically determined momentum-diffusion coefficients by the cross-helicity scaling $(1 - \sigma_c^2)$ before plotting them in figure 5.8 as a function of the initial gyroradius. Note that the initial gyroradius is inversely proportional to the charge-to-mass ratio in our setup with constant initial velocity and energy; therefore it is not surprising that populations with a larger initial gyroradius correspond to smaller values of $\mathcal{D}_{pp}$.

For gyroradii larger than the dissipation length, the rescaled momentum-diffusion coefficients of ensembles with the same charge-to-mass ratio take almost the same value for all cross helicities. Referring to the plot in figure 5.8, this conclusion can

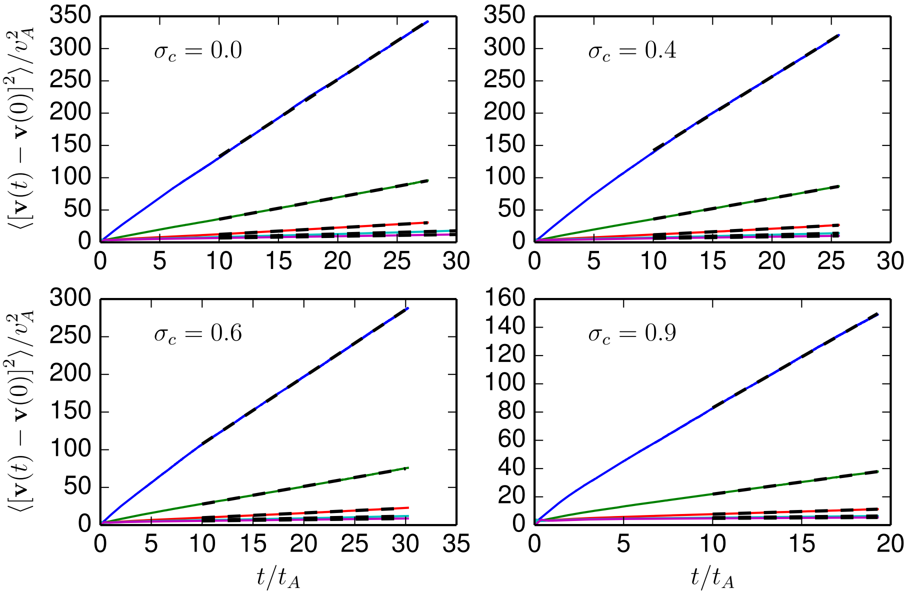

Figure 5.7: Evolution of mean-square displacement in velocity-space for test-particle populations with different initial gyroradii (blue: $r_g(0) = 0.1\ell_K$; green: $r_g(0) = 0.3\ell_K$; red: $r_g(0) = 1.0\ell_K$; cyan: $r_g(0) = 3.0\ell_K$; purple: $r_g(0) = 10.0\ell_K$) in turbulence with various values of the normalized cross-helicity $\sigma_c$

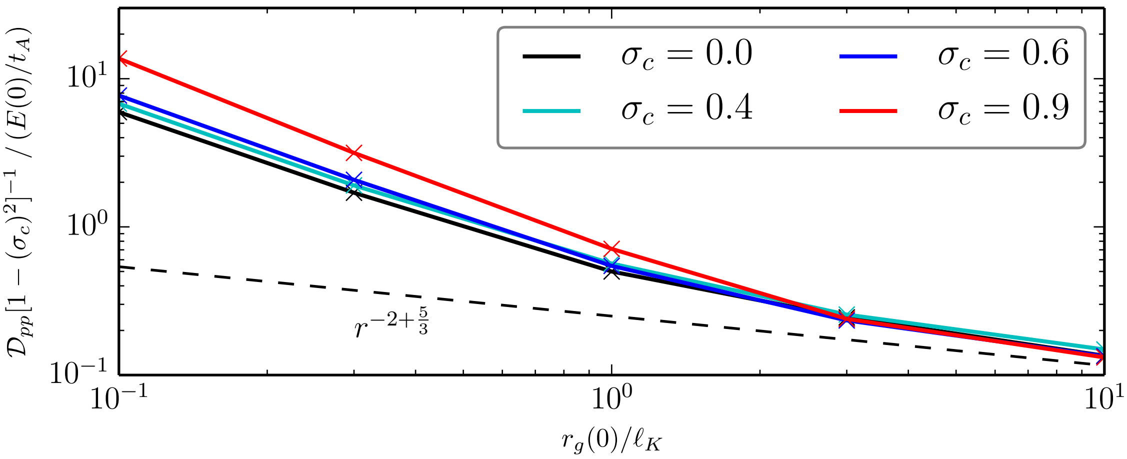

Figure 5.8: Normalized momentum-diffusion coefficient $\mathcal{D}_{pp}/(1-{\sigma_c}^2)$, numerically determined as detailed in the text, as a function of the initial test-particle gyroradius for diffusive propagation in isotropic MHD turbulence with four different values of the normalized cross helicity

be drawn from the four graphs coinciding at $r_g(0) \gtrsim 3\ell_K$. Hence we find that the rather simple $(1-{\sigma_c}^2)$ scaling of $\mathcal{D}_{pp}$ predicted by quasilinear diffusion theory for a slab-turbulence model is sufficiently robust to remain valid in realistic MHD turbulence with three-dimensional spectra. This result is particularly impressive if one remembers the complex shapes of the Elsasser and magnetic-field spectra in our runs, which deviate significantly from the simplistic assumptions of QLT, especially in the case of the positive Elsasser energy (cf. chapter 4 for a more detailed analysis of the spectra).

It is in this large-gyroradius regime that the scaling of the momentum-diffusion coefficient as a function of the initial gyroradius $r_g(0)$ also matches the QLT prediction $\mathcal{D}_{pp} \sim r_g^{2-s}$ to a far greater degree than for charge-to-mass ratios corresponding to $r_g(0) < \ell_K$. A line which represents the scaling of $\mathcal{D}_{pp}$ in an idealized turbulence configuration with Kolmogorov scaling exponent of $s = 5/3$ is included in figure 5.8 as a visual guideline.

For gyroradii comparable to or below the dissipation length, however, the matching of the rescaled momentum diffusion coefficients for different cross helicities becomes worse. We attribute this effect to a dominance of Ohmic heating by $\mathbf{e}_{\mathrm{ohm}}$, the mean amplitude of which is independent of $\sigma_c$. This constituent of the electric field will be the most effective accelerating mechanism for test-particles so strongly magnetized that their trajectories do not sample a significant amount of fluctuations of the electric field in one gyroperiod. The stochastic heating due to the motional electric field is far less important for these particles: Over the course of a gyroperiod, the velocity of the particle perpendicular to the magnetic field will be alternately aligned with $\mathbf{e}_{\mathrm{mot}}$ and directed opposite to it; hence acceleration and subsequent deceleration will approximately cancel each other out. The same fundamental difference in the acceleration of small- and large-gyroradius cosmic-ray particles has also been observed in other simulations that used snapshots of magnetohydrodynamic turbulence (Ambrosiano *et al.* , 1988; Dmitruk *et al.* , 2004; Dalena *et al.* , 2014), although the authors of those studies paid no attention to the level of cross helicity in their field configurations.

### 5.4.4 Two-stage acceleration in static and evolving turbulence

We would like to point out that it constitutes an important difference whether the test-particles are being propagated through static snapshots of electrodynamic fields or through dynamically evolving turbulence. The probability of a test-particle with sufficiently small gyroradius becoming trapped and repeatedly accelerated in a region with a current-filament-like structure is greatly enhanced if the turbulence is static. However, after the particles have gained enough energy to escape any current filament because of their increased gyroradius, the efficiency of their acceleration is dramatically reduced since unidirectional heating via the Ohmic electric field is no longer possible. The contribution of stochastic heating via the motional electric field is almost negligible. Apparently $\mathbf{e}_{\mathrm{mot}}$ requires dynamic evolution in order to become an efficient accelerator. This observation is reminiscent of Fermi-II acceleration, which is only efficient if the turbulent fluctuations scattering cosmic-ray particles are colliding with these particles head-on, as explained in chapter 1. If the fluctuations are immobile, as is the case in static-turbulence runs, the efficiency of stochastic heating becomes almost imperceptibly small. The onset of saturation of the test-particles' mean energy in a static snapshot of strongly cross-helical turbulence is displayed in figure 5.9 for three different charge-to-mass ratios, and compared to the evolution if the turbulence is allowed to evolve dynamically. After an initial rapid acceleration in the static cases, the heating rate of particles with enough energy to escape the filaments quickly decreases (dash-dotted lines). This allows the kinetic energy of test-particles in the evolving runs (solid lines) to quickly catch up as their acceleration rate remains constant (compare figure 5.7).

Two analogous time regimes can be defined for the dynamic-turbulence evolution of the mean energy if, instead of the total energy, only the squared norm of the velocity component parallel to the local magnetic field is considered. Plots of the evolution of this 'parallel energy' in isotropic MHD turbulence (figure 5.10) clarify this two-stage acceleration process further:

- Initially, when the gyroradius of the test-particles is smaller than the typical width of a current filament, the electric-field components perpendicular to the local magnetic field are unable to accelerate a charged particle coherently, and the net change of the norm of the perpendicular momentum will amount to zero. Instead, as shown by the steep increase of the parallel energy in figure 5.10, a charged particle will undergo coherent acceleration along or opposite to the magnetic-field direction until they are able to escape the structure in which they have started, analogously to the test-particles in the static-turbulence runs described above.

- After the particles in the dynamic-turbulence runs have escaped, however, they are still continuously accelerated, as shown in figure 5.9. Yet now this acceleration, mainly via the motional electric field, is no longer necessarily aligned with the direction of the local magnetic field direction because of the large gyroradius of the particles. In fact, the distinction between parallel and perpendicular energy has become meaningless in this regime since the turbulent fields are isotropic on these scales, and the perpendicular-energy components increase at the same rate as the parallel component. Eventually, equipartition between all directions is achieved. In figure 5.10, this last stage is marked by the convergence of $\langle v_\parallel^2 \rangle$ to the isotropic limit $\langle v^2/3 \rangle$.

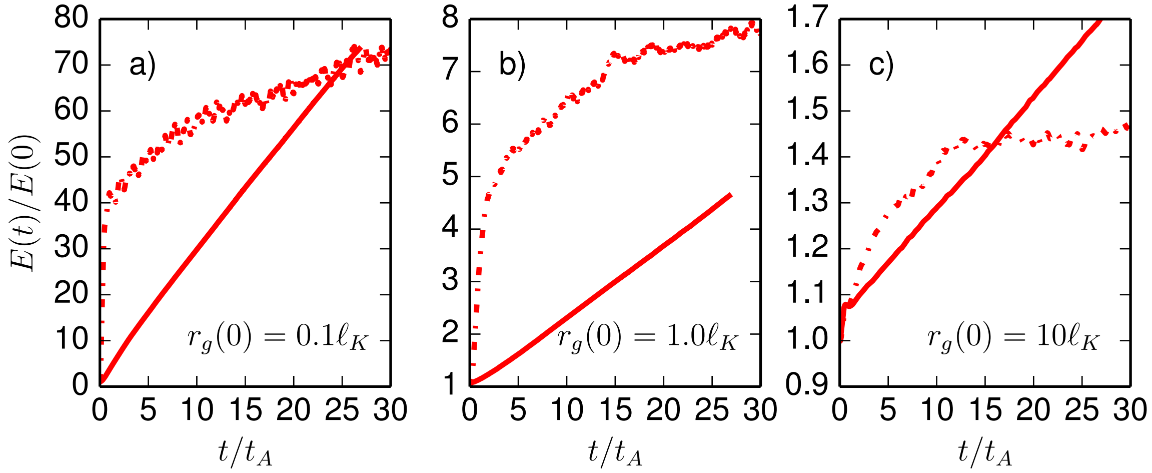

Figure 5.9: Mean energy of test-particle ensembles as a function of time, in a static snapshot of MHD turbulence (dashed lines) and dynamically evolving turbulence (solid lines). (*a*) Initial gyroradius $r_g(0) = 0.1\ell_K$. (*b*) $r_g(0) = \ell_K$. (*c*) $r_g(0) = 10\ell_K$.

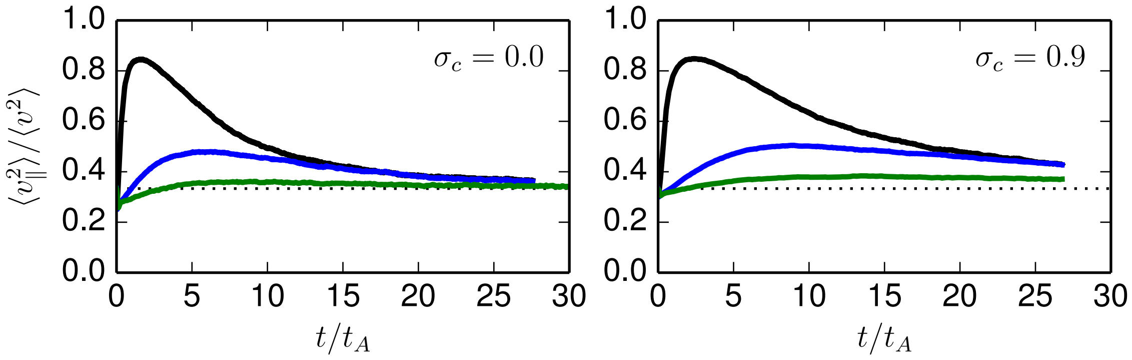

Figure 5.10: Parallel energy normalized to the total energy as a function of time for different initial gyroradii (black: $r_g(0) = 0.1\ell_K$; blue: $r_g(0) = 1.0\ell_K$; green: $r_g(0) = 3.0\ell_K$) in balanced isotropic turbulence (left) and strongly cross-helical isotropic turbulence (right)

## 5.5 Stochastic heating in trans-Alfvénic turbulence

The quasilinear derivation of the momentum-diffusion coefficient $\mathcal{D}_{pp}$ in chapter 3 was based on the expansion of the Vlasov-Maxwell equations around a strong magnetic mean-field along the $z$ direction. However, the scaling of $\mathcal{D}_{pp}$ with both the normalized cross helicity $\sigma_c$ and, at least in the non-Ohmic regime, the initial gyroradius $r_g(0)$, in figure 5.8 matches the QLT predictions even in the absence of a large-scale mean-field. Even stochastic heating in isotropic MHD turbulence can be described by quasilinear diffusion theory!

Despite this surprising success of the quasilinear approach, the factor $(\delta B/B_0)^2$ in equation (5.6) means that the absolute numerical value of $\mathcal{D}_{pp}$ cannot be compared between theory and simulation – the quasilinear expression diverges in the limit $|\mathbf{B_0}| \to 0$. We have therefore also run test-particles in our MHD-field configurations of trans-Alfvénic turbulence, with a weak magnetic mean-field $\mathbf{B_0} \sim \langle \delta \mathbf{b}^2 \rangle^{1/2}$. Although this intensity of $\mathbf{B_0}$ is hardly strong enough to provide rigorous justification to the perturbation ansatz of quasilinear theory, one would expect that at least the same scaling relations which hold even for isotropic turbulence apply in trans-Alfvénic turbulence, as well.

Indeed, the coincidence of all four graphs in figure 5.11 for gyroradii larger than $\ell_K$ confirms that the momentum-diffusion coefficient is proportional to $(1-\sigma_c^2)$ in imbalanced (in the sense that $\sigma \neq 0$), weakly Alfvénic turbulence, too. Despite the alignment of the turbulent structures along $\mathbf{B_0}$, the main effect of non-zero cross helicity remains a reduction of the average intensity of the motional electric field and hence of the rate of stochastic acceleration. For charged particles with a gyroradius small enough to be coherently accelerated in current filaments, Ohmic fields represent the primary source of heating, exactly as in isotropic turbulence; thus the curves in figure 5.11 deviate from each other more strongly for $r_g(0) < \ell_K$.

The application of a weak mean-field affects the evolution of the parallel-energy ratio $\langle v_\parallel^2 \rangle / \langle v^2 \rangle$ only to a small degree. Figure 5.12 shows the same initial increase and eventual decrease of this ratio that we have already explained in the context of figure 5.10.

A subtle difference with respect to the isotropic case can be observed for large gyroradii nonetheless: The slope of the graph of the normalized momentum-diffusion coefficient for $r_g(0) \gtrsim 3.0\ell_K$ is noticeably flatter if a weak mean-field is applied (compare figures 5.8 and 5.11). The dashed line drawn in the graph of the trans-Alfvénic case corresponds to the scaling one would expect for $s = 3/2$ and is steeper than in the isotropic case, but this is the value one expects for the scaling of the perpendicular spectrum according to Kraichnan's theory, $\mathcal{E}(k_\perp) \propto k_\perp^{-3/2}$. The slab spectrum used to derive equation (5.6) actually corresponds more closely to the parallel spectrum, which exhibits a scaling of approximately $\mathcal{E}(k_\parallel) \propto k_\parallel^{-2}$, as shown in chapter 4. This scaling exponent, also predicted by Goldreich-Sridhar theory (equation (2.72)), implies that the normalized momentum-diffusion coefficient becomes independent of the gyroradius

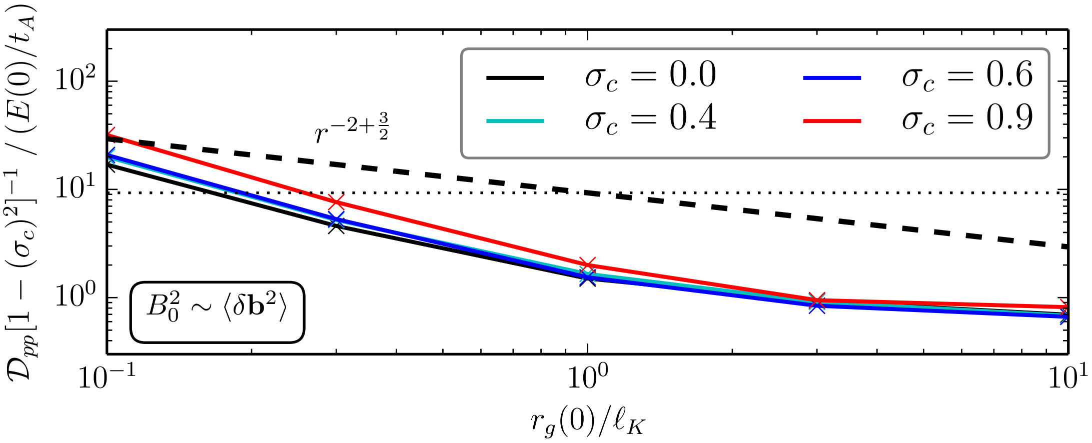

Figure 5.11: Normalized momentum-diffusion coefficient $\mathcal{D}_{pp}/(1-\sigma_c{}^2)$ as a function of the initial test-particle gyroradius for diffusive propagation in trans-Alfvénic MHD turbulence ($\mathbf{B_0} \sim \langle \delta \mathbf{b}^2 \rangle^{1/2}$) with four different values of the normalized cross helicity. The dashed and dotted lines indicate the scaling one would expect from equation (5.6) for $s = 3/2$ and $s = 2$, respectively

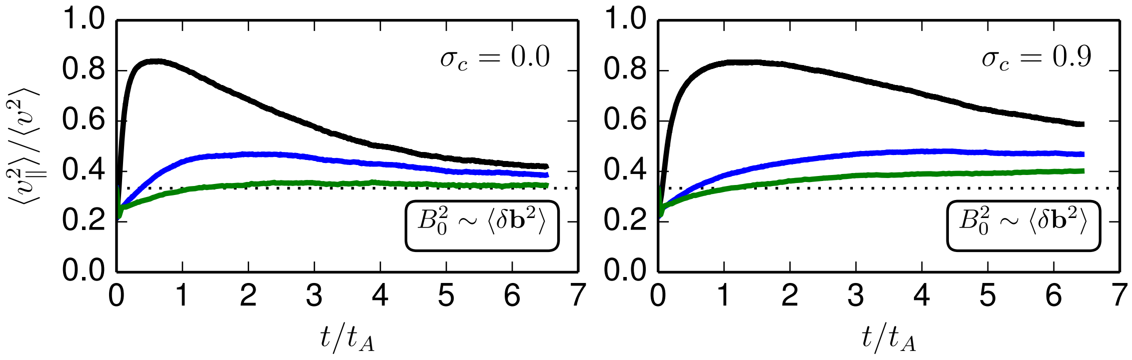

Figure 5.12: Parallel energy normalized to the total energy as a function of time for different initial gyroradii (black: $r_g(0) = 0.1\ell_K$; blue: $r_g(0) = 1.0\ell_K$; green: $r_g(0) = 3.0\ell_K$) in balanced trans-Alfvénic turbulence (left) and strongly cross-helical trans-Alfvénic turbulence (right) with $\mathbf{B_0} \sim \langle \delta \mathbf{b}^2 \rangle^{1/2}$

(dotted line in figure 5.11) if only the contribution of the motional electric field is considered (since $\mathcal{D}_{pp} \propto r^{-2+s}$). In this sense the flat slope of the graph 5.11 at large $r_g(0)$ indicates that the spectrum of turbulent fluctuations parallel to the mean-field matters far more for stochastic heating than the perpendicular spectrum, which partially explains the success of a simple slab-turbulence model even for realistically evolving three-dimensional MHD turbulence.

This insight about the general applicability of the slab-turbulence model concludes our chapter on the effect of cross-helical MHD turbulence on the stochastic heating of cosmic-ray particles. As we already showed in chapter 3, stochastic heating can be interpreted as the change of the norm of the momentum due to diffusion in velocity-space. In this chapter, we proved that the heating of charged particles, as quantified by the momentum-diffusion coefficient $\mathcal{D}_{pp}$, in realistic cross-helical turbulence can be explained by quasilinear diffusion theory, if the gyroradius of the particles is so large that they can escape spontaneously forming current filaments. Given enough time, this situation is reached even by particles with an initially small gyroradius because of the two-stage acceleration process described above: Although particles are being accelerated parallel to the local magnetic field by the Ohmic field, they can escape the current filaments since their perpendicular velocity also increases as a result of turbulent pitch-angle scattering – the subject of the next chapter.

# Chapter 6

# Pitch-Angle Scattering in Cross-Helical Turbulence

> *Wie verbinden sich Nichts und All? Im Kreise, der sich drehend fortbewegt, im Rad, das rollt. Ich bin an das Rad geschmiedet, das Rad des Schicksalswagens, den die Sonnenrosse durch die Äonen mit sich reißen.* [a]
>
> – *Der Kreidekreis* (Klabund, 1925)

---

[a] How are Void and Space connected? In the circle that turns and advances, in the wheel that rolls. I am forged to the wheel, the wheel of Destiny's cart, pulled away through the aeons by the steeds of the Sun.

**Chapter Summary**

- QLT diffusion coefficients are reliable predictors of the pitch-angle scattering of Alfvénic and slightly super-Alfénic particles in balanced and imbalanced sub-Alfvénic turbulence, at least for a few gyroperiods.
- In imbalanced turbulence, the pitch-angles of particles which propagate in the same direction as the dominant Alfvén-wave population are initially scattered less effectively than counter-propagating particles.
- On longer timescales, the adiabatic invariance of particle ensembles with a small gyroradius compared to the parallel correlation length limits the spread of the pitch-angle distribution.
- Coherent interactions with propagating Alfvén waves make prolonged pitch-angle diffusion possible, but the scattering asymmetry will be the opposite of what quasilinear theory, which neglects the Landau resonance, predicts.

After examining the heating rate and thus the momentum diffusion coefficient of particles in the previous chapter, we continue in this chapter with an analysis of the pitch-angle scattering in realistic magnetohydrodynamic turbulence. We will focus on the scattering of test-particles in sub-Alfvénic turbulence ($\mathbf{B_0}^2 \sim 100\langle \delta \mathbf{b}^2 \rangle$) with different degrees of cross helicity over short time scales. Details of how these turbulent field configurations are constructed have already been explained in chapter 4, while we refer the reader to the previous chapter for a description of the numerical implementation of the test-particle integrator.

An article containing the main results of this chapter has been submitted to the Astrophysical Journal (Weidl *et al.* , 2015).

## 6.1 Motivation

The rate at which charged particles are scattered by MHD turbulence determines the accuracy to which we can pinpoint the origin of high-energy cosmic-ray particles (see chapter 1). The cosmic-ray literature dealing with this subject is therefore extensive, starting with the seminal papers about QLT referenced in chapter 3 (*e.g.* Jokipii, 1966; Kennel & Engelmann, 1966; Schlickeiser, 1989). Recent contributions of note have either consisted in extensions of QLT to nonlinear diffusion theories (see Shalchi, 2009) or comparisons with numerical simulations (*e.g.* Qin *et al.* , 2002; Qin & Shalchi, 2009; Tautz *et al.* , 2013).

These simulations were based on a magnetostatic field configuration: Assuming that the velocity of the propagating particles exceeds the Alfvén speed by far, and that their energy is too large to be affected by stochastic heating, test-particle trajectories are computed in static snapshots of MHD fields, using only the magnetic part of the Lorentz equation without considering the electric acceleration. In most cases, these fields were constructed analytically, by summing up a large number of modes with a given spectrum, usually a Kolmogorov-like slab spectrum, like the one we used in chapter 3.

If magnetic spectra of static turbulence are prescribed like that, cross helicity is irrelevant since neither the direction of propagation of the waves nor the structure of the velocity field matters. Therefore numerical investigations of pitch-angle scattering have usually ignored cross helicity altogether. A notable exception is again given by Beresnyak *et al.* (2011), who determined an averaged pitch-angle diffusion coefficient from test-particle simulations in snapshots of balanced and imbalanced trans-Alfvénic turbulence and failed to notice any significant influence of the cross helicity.

As our simulation setup allows us to perform test-particle simulations in fully electrodynamic turbulence, we are able to include several effects for which cross helicity is extremely important. Before we discuss the results of these runs, however, the parameters to be used in those simulations need to be considered.

## 6.2 Simulation parameters

### 6.2.1 Ideal MHD

Unlike the simulations presented in the previous chapter, most runs in this chapter use a generalized Ohm's law that neglects the Ohmic electric field when we compute the test-particle trajectories, which corresponds to setting the magnetic diffusivity to $\eta \equiv 0$. Thus only the motional electric field is active:

$$\mathbf{e} = -\mathbf{u} \times \mathbf{b}.$$

In order to ensure that the local electric field lies in the plane perpendicular to the local magnetic field up to machine accuracy, we compensate for numerical errors introduced by the interpolation of $\mathbf{u}$ and $\mathbf{b}$ (see chapter 4) and explicitly project $\mathbf{e}$ onto this plane. In other runs, we will ignore even the motional electric fields and study the scattering due to only the magnetic field, juxtaposing the scattering properties of both mechanisms.

The addition of Ohmic fields added an interesting secondary heating mechanism in the previous chapter, but it would be counterproductive for our present objective: A comparison of pitch-angle scattering in imbalanced turbulence with analytical results requires that the Lorentz force be as close as possible to the ideal-MHD assumptions which were used in the QLT derivation of chapter 3, where no Ohmic field was considered. The inclusion of the Ohmic field in our simulations would affect the measured pitch-angle scattering rates and must hence be avoided to facilitate a fair comparison of those rates with QLT. However, the difference between runs with and without the Ohmic field is not too great. Since we want to maximize the effect of the motional electric field in this chapter, we are limited in our choice of parameters and set the gyroradii of the test-particles well within the inertial range of the turbulence, where Ohmic heating is negligible.

In order to stay as consistent as possible within the limits of a test-particle approach, we must set the magnetic diffusivity in the MHD equations to zero as well. Therefore we choose a non-dissipative setup with $\eta \equiv \nu \equiv 0$, also getting rid of the viscous-damping term, and switch off the external forcing before test-particles are injected, such that $\epsilon_{\mathrm{inj}} \equiv 0$. In short, we simulate the conditions of ideal magnetohydrodynamics, exactly as we assumed in the derivation of the quasilinear diffusion coefficients.

### 6.2.2 Sub-Alfvénic turbulence

The turbulent magnetic fields $\delta\mathbf{b}$ in all runs presented in this chapter are small compared to the mean-field, $\mathbf{B_0}^2 \sim 100\langle\delta\mathbf{b}^2\rangle$. The reasoning behind using only sub-Alfvénic MHD runs, instead of the stronger levels of magnetic turbulence that we had before, is that the isotropization of test-particle ensembles with a well-defined initial pitch-angle

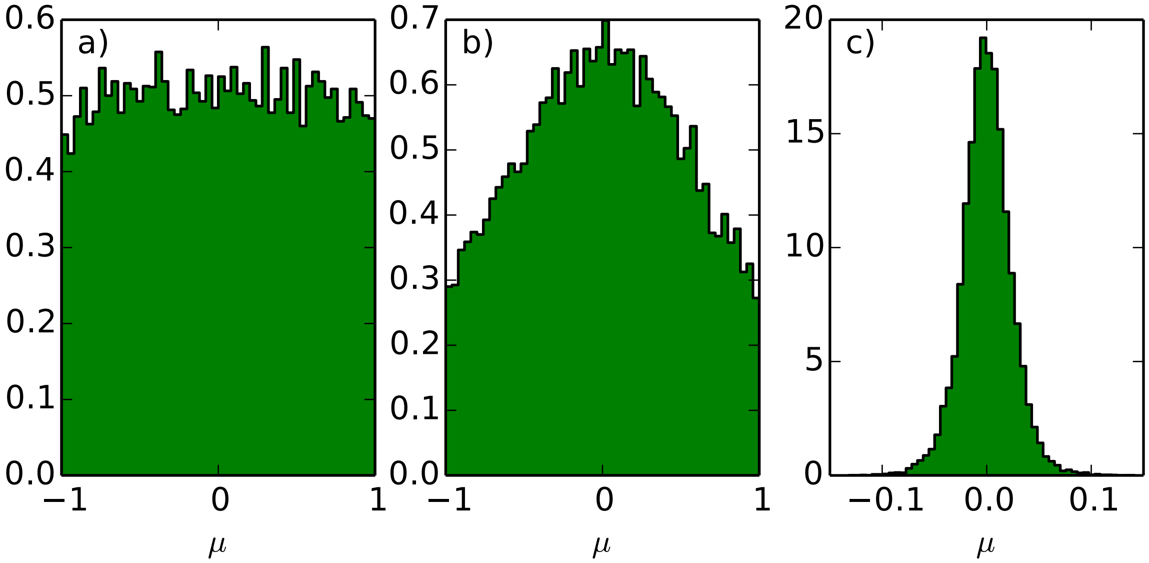

Figure 6.1: Histograms of the pitch-angle distribution ($\mu = \cos v_z/v$) of 20,000 test-particles after one gyroperiod $T = 2\pi/\Omega$, with $\Omega = q/m\langle B^2\rangle^{1/2}$, in (*a*) isotropic MHD turbulence, (*b*) trans-Alfvénic turbulence, (*c*) sub-Alfvénic turbulence with zero cross helicity

with respect to the mean-field direction occurs too quickly in strong turbulence. In figure 6.1, we show histograms of the pitch-angle distribution of test-particle ensembles with a population size of $2 \times 10^4$ in balanced-turbulence runs with various mean-field strengths after one gyroperiod (measured with respect to the averaged magnetic field strength). All particles started with a velocity perpendicular to the $z$-axis and equal to the Alfvén velocity at $t = 0$.

In the isotropic-turbulence setting with $\mathbf{B_0} \equiv 0$, the velocity-distribution has almost completely randomized within a single gyroperiod. Determining the dependency of scattering coefficients on the pitch-angle is next to impossible if the pitch-angle exhibits such a volatile behavior. The isotropization happens at an only marginally smaller speed for trans-Alfénic turbulence (with $\mathbf{B_0}^2 \sim \langle \delta \mathbf{b}^2 \rangle$), shown in figure 6.1b. Since the pitch-angle cosine $\mu = \cos \angle(\mathbf{v}, \mathbf{B_0} + \delta \mathbf{b})$ is limited to the range $(-1, +1)$, the ensemble-averaged mean-square displacement $\langle \Delta\mu^2 \rangle$ is only a meaningful indicator of the scattering rate if the bulk of the test-particle population has not been reflected at these boundaries. At a sub-Alfvénic turbulence strength, however, the histogram shape is a Gaussian curve that is narrow enough, so that a scattering rate for the initial pitch-angle $\mu = 0$ can be reliably determined from $\langle \Delta\mu^2 \rangle$.

In general, however, the exact pitch-angle diffusion coefficient for a particular $\mu$ is difficult to determine even in sub-Alfvénic runs, since an actually diffusive spread of the pitch-angle cosine distribution (in the sense of normal diffusion, such that $\langle \Delta\mu^2 \rangle \propto t$) would require a constant diffusion coefficient. This is not the case, as pointed out by Tautz *et al.* (2013). Instead, the rate at which the pitch-angle cosine changes is a function of the pitch-angle itself. Thus, one can only expect to observe normal diffusion of the pitch-angle if the predicted relative change in $D_{\mu\mu}$ is small, or

$$\left|\Delta\mu\right| \sim \left(D_{\mu\mu}t\right)^{1/2} \ll \left|\frac{D_{\mu\mu}}{\partial_\mu D_{\mu\mu}}\right|$$

over diffusive timescales. This condition poses a strict upper limit on the time $t$ over which numerical investigations of the pitch-angle dependence of $D_{\mu\mu}(\mu)$ are useful, but as we will see shortly, other factors play an even more important role in the limitation of this time.

### 6.2.3 Alfvénic test-particles

Our goal is to investigate the effects of cross helicity on the pitch-angle scattering of particles. As we have shown in figure 3.1, the influence of imbalanced turbulence results in a strongly asymmetric shape of $D_{\mu\mu}(\mu)$. Quasilinear theory predicts that this asymmetry will be strongest if the velocity of the test-particles is comparable to the Alfvén velocity, which can easily be seen from the factor $\gamma = v_A/v$ in equation (3.62). Most of our runs were therefore performed with two values for the norm of the initial test-particle velocity, $v(0) = v_A$ and $v(0) = 3v_A$.

On the other hand, the gyroradius $r_g$ of the test-particles should be adjusted so that the particles interact primarily with turbulent oscillations well inside the inertial range of our simulations. We have already noted in subsection 6.2.1 that a gyroradius in the dissipative range is not convenient to study the influence of the motional electric field. Using a gyroradius significantly larger than the correlation length, on the other hand, would lead to simulation artifacts due to the periodicity of the setup. Moreover, Hauff *et al.* (2010) found that pitch-angle scattering is negligible if the gyroradius is much larger than the correlation length, especially for very small pitch angles. The criterion that $r_g$ lie approximately inside the inertial range determines, together with the particle velocity $v$, the average gyrofrequency $\Omega_0 = \alpha|\mathbf{B_0}| = v/r_g$ and thus the charge-to-mass ratio $\alpha$ we choose for the test-particles. We set $\alpha = 4.0$ for both choices of the velocity, which yields $r_g = 0.12\lambda_\perp$ and $r_g = 0.36\lambda_\perp$, respectively, where $\lambda_\perp = 0.1\lambda_\parallel$ is the perpendicular correlation length (defined for strongly anisotropic turbulence in chapter 4). Unlike in the previous chapter, where even smaller gyroradii yielded interesting results due to the interaction with the small-scale Ohmic field, we will focus entirely on these two choices of gyroradius and velocity in the present chapter.

Figure 6.2 shows distributions of the pitch-angle cosine $\mu$ for test-particles with $v(0) = 3v_A$ (or $r_g(0) = 0.36\lambda_\perp$) after ten gyroperiods, for balanced and strongly imbalanced sub-Alfvénic turbulence. The two ensembles depicted in each case were initialized to propagate either parallel or antiparallel to the direction of the magnetic mean-field. The influence of cross helicity is obvious from the degree of asymmetry in each histogram: In the imbalanced case, co-propagating particles, *i.e.* particles with a positive value of $\mu$, are deflected from their original direction much more quickly by gyroresonant wave-particle interactions than their counterparts in the opposite direc-

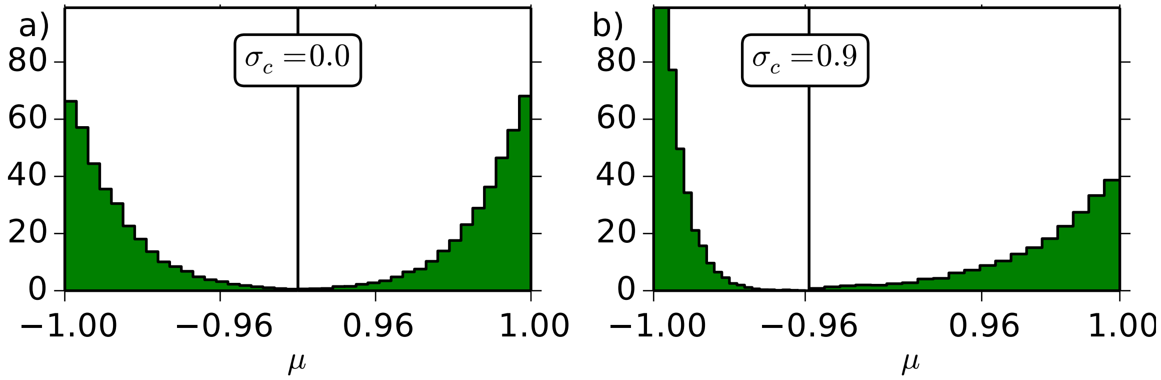

Figure 6.2: Histograms of the distribution of the pitch-angle cosine $\mu$ after ten gyroperiods for particles with initial velocity $v(0) = 3v_A$ directed parallel or antiparallel to the magnetic mean-field direction. (*a*) Balanced turbulence with zero cross helicity and symmetric scattering. (*b*) Strongly imbalanced turbulence with strongly positive cross helicity $\sigma_c = 0.9$ and strongly asymmetric scattering

tion. In the balanced case, the scattering efficiency is completely symmetric for both test-particle ensembles.

### 6.2.4 The pitch-angle scattering rate $\Delta_{\mu\mu}$

We quantify the strength of the wave-particle interaction by half the mean-square displacement of the pitch-angle cosine over one gyroperiod $T_g = 2\pi/\Omega_0$:

$$\Delta_{\mu\mu}((\mu(0)) = \left\langle \frac{1}{2} \frac{\left[\mu(T_g) - \mu(0)\right]^2}{T_g} \right\rangle, \tag{6.1}$$

Here the angular brackets indicate an averaging over each test-particle ensemble. In each turbulence configuration, we determine $\Delta_{\mu\mu}$ separately for 21 ensembles, which only differ in $\mu(0)$: we let the initial pitch-angle cosine vary from -1 to +1 in steps of 0.1 for otherwise identical initial conditions.

We will compare $\Delta_{\mu\mu}(\mu)$ to the quasilinear predictions for the diffusion coefficient $D_{\mu\mu}(\mu)$ as introduced and derived in chapter 3. As a diffusion coefficient in the Fokker-Planck equation (3.42), $D_{\mu\mu}$ corresponds to an infinite-time limit,

$$D_{\mu\mu}(\mu(0)) = \lim_{t\to\infty} \left\langle \frac{1}{2} \frac{[\mu(t) - \mu(0)]^2}{t} \right\rangle, \tag{6.2}$$

provided that it exists and assumes a non-zero value, *i.e.* provided that the long-term evolution of $\mu(t)$ can be modeled as a diffusive random walk. Our choice of measuring $\Delta\mu^2$ after only one gyroperiod may appear conspicuously short, as the test-particles barely have time to sample enough turbulence that the wave-particle interaction could be considered stochastic. Within one gyroperiod, the distance traveled by test-particles with $v = 3v_A$ is only slightly greater than one perpendicular correlation length $\lambda_\perp$, so the random walk performed by $\mu(t)$ has not necessarily reached the regime of normal diffusion yet. However, as noted in subsection 6.2.2, normal diffusion is impossible to observe if the pitch-angle scattering is too fast, since the rate of change of $\mu$ depends on $\mu$ itself. For particle-ensembles traveling almost parallel or antiparallel to the mean-field direction, as in figure 6.2, boundary effects at $\mu = \pm 1$ further complicate the determination of a long-term diffusion coefficient (see Tautz *et al.* , 2013).

Moreover, our approach of comparing $\Delta_{\mu\mu}$ and $D_{\mu\mu}$ is based upon the assumption that the energy of the test-particles remains constant, such that the effect of $D_{\mu p}$ in equation (3.42) can be neglected. This term would lead to adiabatic focusing, *i.e.* an additional change of the pitch-angle due to gradients in the energy distribution (*e.g.* Schlickeiser & Shalchi, 2008). In the presence of an electric field, the conservation of energy will never hold exactly, but on short timescales it is fulfilled to a great degree, as we will show.

Most importantly, the approximate conservation of the magnetic moment $M_{\text{mag}} = mv_\perp^2/(2B)$ does not affect the pitch-angle evolution in any meaningful way over one single gyroperiod, as opposed to longer durations. At least in slowly changing magnetic fields, or weak magnetic turbulence, $M_{\text{mag}}$ is an adiabatic invariant and remains constant (Northrop, 1963; Freidberg, 2008). The relative turbulence amplitude $\delta B/B_0$ that is used in these runs is small enough that, although $M_{\text{mag}}$ is not perfectly conserved, the evolution of $\mu(t)$ is severely constricted after several gyroperiods for some parameters. For weak turbulence we can assume that, on average, the velocity along the local magnetic field direction $v_\parallel$ is approximately equal to the $z$-component of the velocity, $v_z = \mu v$. Since $\mu$, $M_{\text{mag}}$, and the particle energy $E = v^2/2$ (if we set $m$ to unity) are then linked via

$$E \approx \frac{v_\perp^2 + v_z^2}{2} = B\, M_{\text{mag}} + \frac{E}{2}\,\mu^2, \tag{6.3}$$

any long-term change in the pitch-angle cosine will affect the magnetic moment or the energy as well. Thus unlimited pitch-angle diffusion requires that either the particle energy or the magnetic moment be not conserved. This does not pose any problem if both the gyroradius and the turbulence amplitude are chosen extremely small (like, for example, in the studies of Qin *et al.* (2002), Tautz *et al.* (2013), where $\delta B/B_0 < 0.05$, see also Dalena *et al.* (2012)), presumably because the timescales of gyromotion and pitch-angle diffusion are sufficiently separated. Although such a choice of parameters is feasible in simulations with an analytically computed spectrum, we are limited by the constraints on the gyroradius and particle velocity given in the previous subsection, mainly due to the resolution of our three-dimensional MHD simulations.

The upshot of all these caveats is that $\Delta_{\mu\mu}$ (measured after one gyroperiod) is not necessarily identical with the pitch-angle diffusion coefficient $D_{\mu\mu}$ (formally defined as an infinite-time limit, which is inaccessible to our numerical approach). However, we will see that the scaling of $\Delta_{\mu\mu}$ with $\mu$ is in excellent agreement with quasilinear predictions, especially in the dynamic cases.

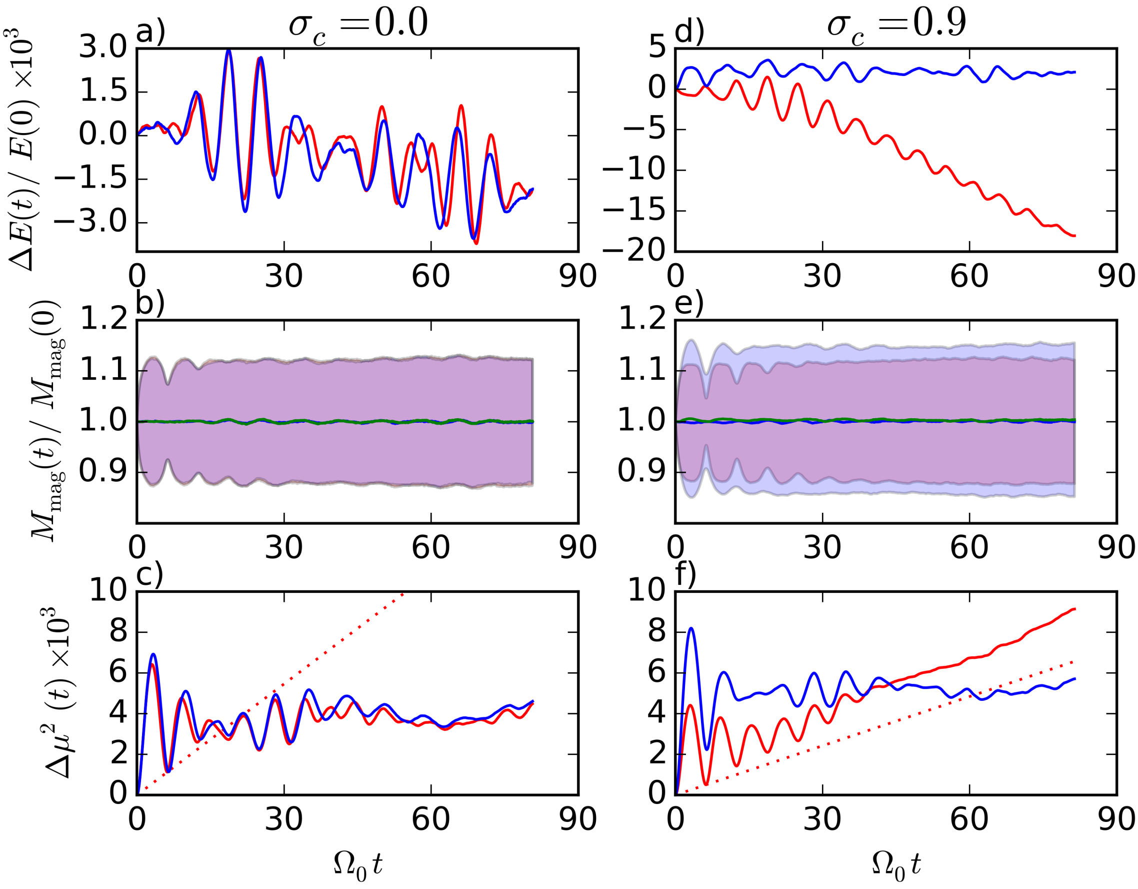

Figure 6.3: Evolution in fully electrodynamic turbulence of test-particle ensembles with $v(0) = 3v_A$ and $\mu(0) = +0.6$ (blue lines) or $\mu(0) = -0.6$ (red lines) in turbulence with $\sigma_c = 0.0$ (left) and $\sigma_c = 0.9$ (right). (*a*,*d*) Relative change of the kinetic energy. (*b*,*e*) Relative change of the mean magnetic moment $M_{\rm mag}$, with the $1\sigma$-variation shaded in blue/red. (*c*,*f*) Mean-square variation of the pitch-angle cosine, with $\Delta_{\mu\mu}$ as extrapolated after one gyroperiod drawn as a dotted line

## 6.3 Dynamic turbulence

### 6.3.1 The magnetic moment in electrodynamic MHD

Figure 6.3 contains the practical implications which follow from the previous considerations. The evolution of the mean kinetic energy $E$, the magnetic moment $M_{\rm mag}$, and the mean-square displacement of the pitch-angle cosine $\mu$ are plotted there, for slightly super-Alfvénic test-particles with $v(0) = 3v_A$ and $\mu(0) = +0.6$ (blue) and $\mu(0) = -0.6$ (red) in balanced and strongly imbalanced turbulence. In these ‘fully electrodynamic’ runs, we consider both the time evolution of the turbulence and the motional electric field. Therefore these fiducial runs constitute fully realistic simulations of charged-particle propagation in MHD turbulence.

The first conclusion we can draw from the results of the balanced case, in the left-hand column, is that all depicted variables evolve almost identically for $\mu(0) = +0.6$ and $\mu(0) = -0.6$ if $\sigma_c = 0.0$. The ensemble energy oscillates and slowly decreases after a few gyroperiods in figure 6.3a. Negligible oscillations in the mean magnetic moment are visible in figure 6.3b, while the mean-square deviation of $M_{\mathrm{mag}}$ averaged over the particle population converges to 12 % of the initial value. Over the first couple of gyroperiods, $\Delta\mu^2(t)$ oscillates strongly, but the minima that $\Delta\mu^2$ reaches after every gyroperiod increase in value for the first two oscillations. Afterwards, $\Delta\mu^2$ becomes almost constant, possibly showing a minute increase on long timescales.

In the imbalanced case ($\sigma_c = +0.9$, right-hand column), this symmetry between test-particles co- and counter-propagating with respect to the mean-field direction is broken. Whereas the mean energy of the co-propagating particles with $\mu(0) = +0.6$ (blue line) remains approximately constant, the mean energy of particles with $\mu(0) = -0.6$ (red line) decreases. The counter-propagating particle ensemble is closer to resonance with the dominating Alfvén wave population, which travels opposite to the magnetic mean field in positive-cross-helicity turbulence (see chapter 2). Meanwhile, the magnetic moment stays approximately constant in both cases. Most importantly, the pitch-angle cosine of the co-propagating particles cannot continue spreading around its initial value at the same rate after one or two gyroperiods, because both $E$ and $M_{\mathrm{mag}}$ change too slowly. Thus the behavior of $\Delta\mu^2(t)$ for particles with $\mu(0) = +0.6$ ceases to even remotely resemble normal diffusion after only a few gyroperiods, instead settling on an approximately constant value, at least on the timescales for which trajectory simulations have been performed. During the first couple of gyroperiods, the scattering is faster than for the particles with $\mu(0) = -0.6$. Those particles, however, continue their pitch-angle scattering for significantly longer because they are affected more strongly by resonant Alfvén waves traveling in the same direction, undergoing an interaction similar to Landau damping (see chapter 3) – in this case, inverse Landau damping, as $E$ decreases. As noted in chapter 3, the Landau resonance primarily affects the energy of propagating particles and is generally assumed to only have a secondary impact on the pitch-angle.

And yet, as a consequence of this prolonged scattering period, $\Delta\mu^2$ is able to reach greater values for $\mu(0) = -0.6$ than for the oppositely directed co-propagating particles with $\mu(0) = +0.6$, even though for the latter ensemble the initial spread of $\mu$ is larger, as measured after only one gyroperiod. The quantity $\Delta_{\mu\mu}$, derived from this initial spread and included in figure 6.3 for the $\mu(0) = 0.6$-ensembles, only measures the scattering of the pitch-angle over one gyroperiod. We found agreement with the analytic form of $D_{\mu\mu}(\mu)$ to be convincing only on these short timescales, but then surprisingly good (see below). In the derivation of QLT, we lost track of processes on timescales comparable to the gyroperiod when we neglected deviations from a gyrotropic distribution in equation 3.26, assuming the gyroperiod to be much smaller than typical scattering times.

### 6.3.2 Results for fully electrodynamic turbulence

Provided that the assumptions of quasilinear theory hold, and that the energy gain of particles due to the electric fields is negligible, the evolution of the pitch-angle cosine $\mu$ should be accurately described by the diffusion coefficient $D_{\mu\mu}$ of equation (3.62) (originally derived by Schlickeiser (1989)):

$$D_{\mu\mu}(\mu) = \frac{\pi}{4}\,(1-\mu^2)\sum_{\beta=\pm 1}\Omega_0^{2-s^\beta}\,\frac{(1+\beta\sigma_c)\,\delta B^2}{B_0^2}\,(s^\beta-1)\,k_{\mathrm{min}}^{s^\beta-1}\,v^{s^\beta-1}\,(1+\beta\mu\gamma)^2\,|\mu+\beta\gamma|^{s^\beta-1}. \tag{6.4}$$

In order to compare this quasilinear result for $D_{\mu\mu}$ with our numerical measurements of $\Delta_{\mu\mu}$, we fit the former to the latter by varying the four parameters[1] $\delta B$, $\sigma_c$, $s^+$, and $s^-$ for four different values of the cross helicity. For the wavenumber $k_{\mathrm{min}} = 2\pi/\lambda_\parallel$ of the parallel correlation length, the mean gyrofrequency $\Omega_0$, and the ratio $\gamma = v_A/v(0)$, we insert the actual values which we use in each run. In other words,

---

[1] We use $\delta B$ in this chapter to denote the root-mean-square value of the magnetic-field perturbations, $\delta B = \langle \delta\mathbf{b}^2\rangle^{\frac{1}{2}}$.

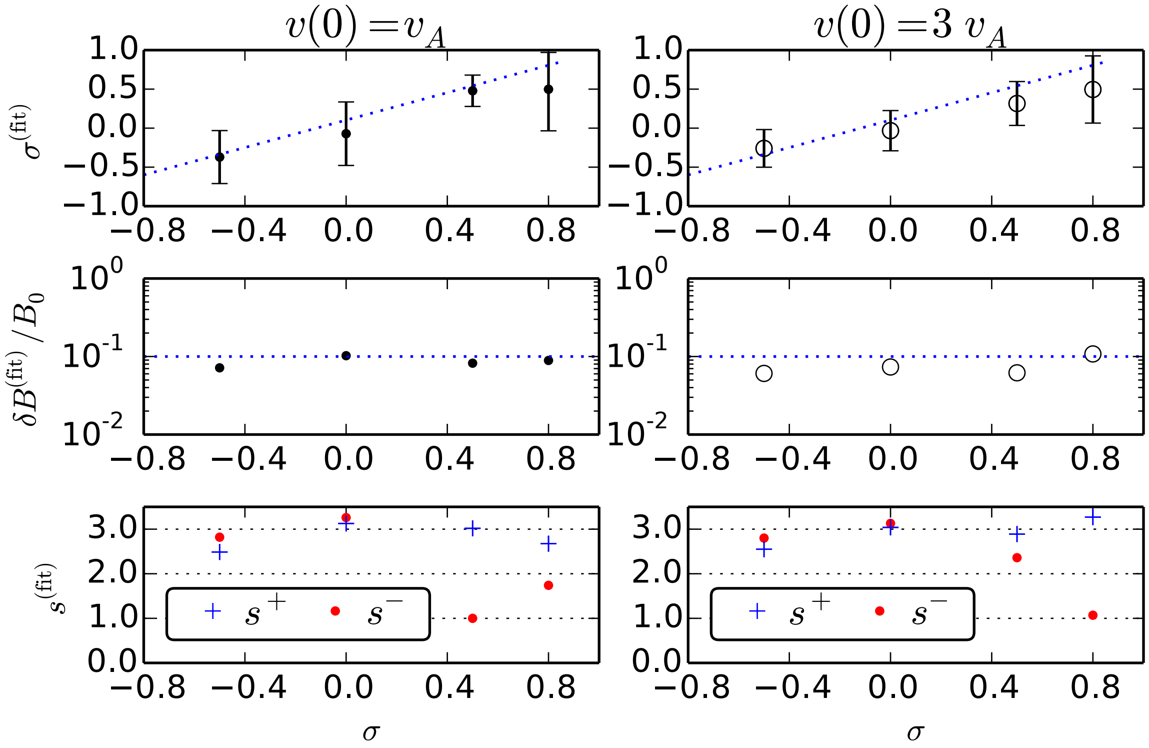

Figure 6.4: Electrodynamic case: best-fit values for the normalized cross helicity $\sigma^{(\mathrm{fit})}$, the normalized amplitude of the magnetic turbulence $\delta B^{(\mathrm{fit})}/B_0$, and the spectral indices $s^+$ and $s^-$, for test-particle ensembles with initial velocity $v(0) = v_A$ (left) and $v(0) = 3v_A$ (right), for four different levels of the cross-helicity injection $\sigma$

we compare the results on the fit-parameters which a direct analysis of the turbulent field configurations yields with the results obtained in an analysis of the test-particle scattering rate $\Delta_{\mu\mu}$. If the quasilinear ansatz were an ideal description of the scattering over one gyroperiod, both parameter sets would coincide.

The best-fit parameters are given in figure 6.4. The fit-values of $\sigma^{(\mathrm{fit})}$ show good agreement with the level of cross-helicity injection (shown on the abscissa in figure 6.4). The deviation is strongest in the strongly cross-helical case with $\sigma = 0.8$, since the quality of the fit decreases drastically as one of the Elsasser energies (in this case $\mathcal{E}^-$) becomes insignificantly small. The relative turbulence amplitude $\delta B/B_0$ is even predicted to be marginally greater than the actual value of 0.1 for test-particles with $v(0) = 3v_A$ and $\sigma = 0.8$. In most cases the best-fit values lie below this value, which can be explained by the pitch-angle scattering being mainly caused by the slab component of the turbulence. Naturally, the amplitude of that component is smaller than the total turbulence amplitude. With the exception of two outliers ($s^- \approx 1.0$) for the strongly subdominant Alfén-wave population, the spectral exponents yielded by the fit procedure are almost always larger than the theoretical inertial-range values of 5/3 or 3/2. These slightly larger results are likely more realistic than the ideal exponents would be, however, due to the steepening of the power spectra of real turbulence at the transition to the dissipative range, which is also exhibited by the spectra in our simulations (see chapter 4). Figure 6.5 compares $\Delta_{\mu\mu}$ for the four cross-helicity levels with the shape of the quasilinear $D_{\mu\mu}(\mu)$ for these parameter sets. The agreement between both graphs is impressive in all cases, even considering these are best-fit curves. While the balanced case is perfectly symmetric with respect to the sign of the initial $\mu(0)$, turbulence in the positively cross-helical cases scatters positive pitch-angles much more effectively over a gyroperiod than particles traveling opposite to the mean magnetic field, while the negative-cross-helicity case scatters negative-pitch-angle particles more effectively.

As explained in chapter 3, particles in perfect coherence with a traveling wave (or $n = 0$ in the resonance condition $\omega_{\mathbf{k}} - k_\parallel v_z - n\Omega_0$) are, within the approximations of QLT, affected only by the electric field parallel to the magnetic mean-field. For ideal shear-Alfvén waves this electric field is negligible, hence we neglected the Landau resonance (with $n = 0$) in subsection 3.3.1. This is the reason why $D_{\mu\mu}$ is smaller for particles in resonance with the dominant Alfvén-wave population, and at least for small timescales, our simulations confirm this quasilinear prediction. The gyroresonant interactions (with $n \neq 0$) scatter Alfvén-speed particles co-propagating with the weaker Alfvén-wave population much more strongly in accordance with the assumptions we have made in chapter 3, resulting in the asymmetric shape of $\Delta_{\mu\mu}(\mu)$.

To show whether the agreement with QLT exists not only on the level of the averaged scattering rate $\Delta_{\mu\mu}$, but extends even to the evolution of the pitch-angle distribution of each individual ensemble, figure 6.6 compares the histograms of the latter with solutions of the Fokker-Planck equation

$$\frac{\partial}{\partial t} f(\mu, t) = \frac{\partial}{\partial \mu}\left[D_{\mu\mu}(\mu)\frac{\partial}{\partial \mu} f(\mu, t)\right]. \tag{6.5}$$

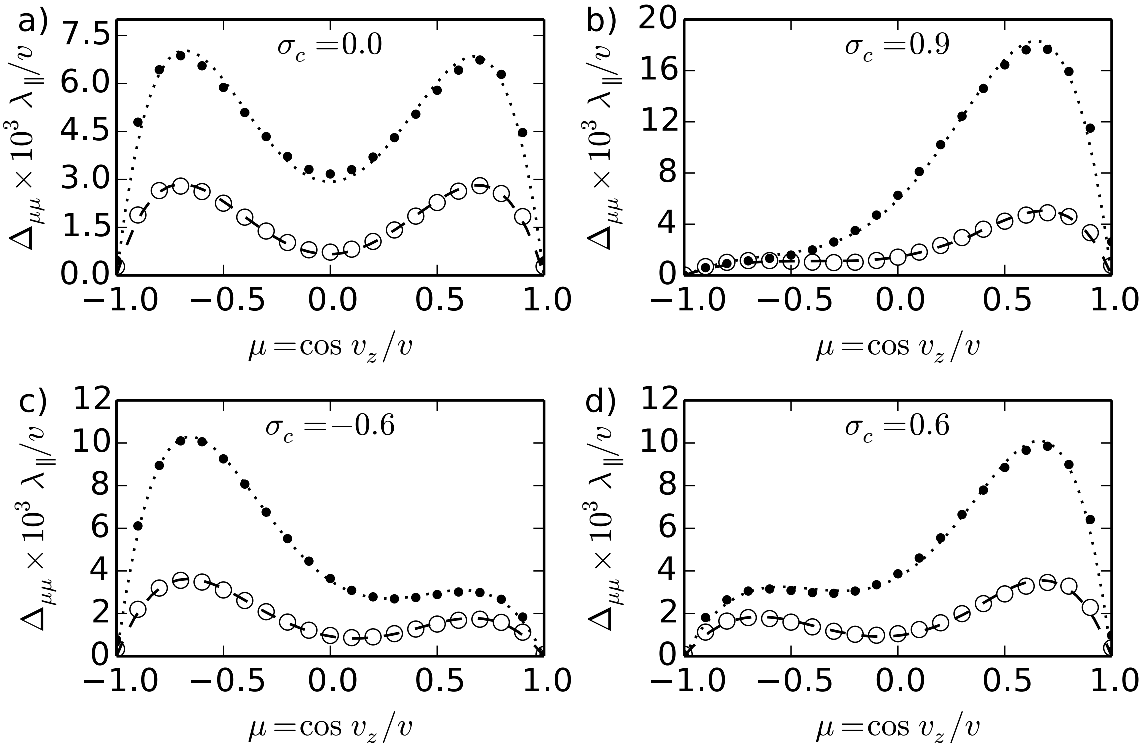

Figure 6.5: Electrodynamic case: Pitch-angle scattering rate $\Delta_{\mu\mu}(\mu)$ for particles with $v = v_A$ and gyroradius $r_0 = v/(\beta B_0) = 0.12\lambda_\perp$ determined numerically (solid dots) and best-fit solution to equation (6.4) (solid line), and for particles with $v = 3v_A$ and gyroradius $r_0 = 0.36\lambda_\perp$ (hollow dots and dashed line). (*a*) Balanced turbulence with $\sigma_c = 0.0$. (*b*) Strongly cross-helical turbulence with $\sigma_c = 0.9$. (*c*) Cross-helical turbulence with $\sigma_c = -0.6$. (*d*) Cross-helical turbulence with $\sigma_c = 0.6$

This equation results from the diffusion equation (3.42), where we first introduced $D_{\mu\mu}$, if the diffusion in the norm of the momentum $p$ is neglected (so that $D_{\mu p} = D_{pp} = 0$) because stochastic heating is negligible – a valid approximation after one gyroperiod, as figure 6.3 shows. The initial condition which we use in each case is a Dirac functional, $f(\mu, t = 0) = \delta[\mu - \mu(0)]$. We show histograms for an ensemble with $v(0) = v_A$ in balanced turbulence, and another ensemble with $v(0) = 3v_A$ in strongly imbalanced turbulence, the latter for the pitch-angle with the largest scattering rate, $\mu = 0.5$. The spectra which we use for both Alfvén-wave types to compute $D_{\mu\mu}(\mu)$ are based on the fit-results obtained above. The almost perfect agreement with the actual $\mu$-distribution after one gyroperiod proves that the Fokker-Planck equation with the quasilinear $D_{\mu\mu}$ describes the pitch-angle scattering accurately on such small timescales.

We can summarize this subsection by stating that cross helicity clearly affects the rate at which the pitch-angles of charged particles are scattered in electrodynamic MHD turbulence. Moreover, quasilinear diffusion theory describes the shape of $\Delta_{\mu\mu}(\mu)$, especially its increasing asymmetry in imbalanced turbulence, very accurately even on small timescales, comparable to a gyroperiod. On longer timescales, however, the ap-

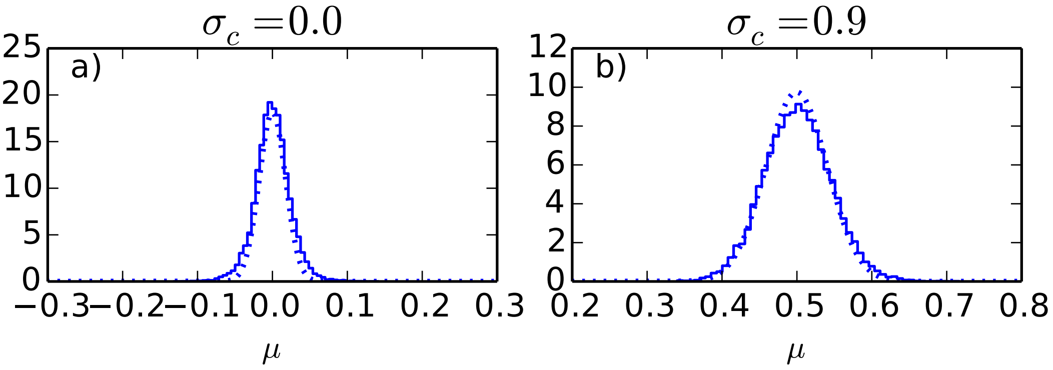

Figure 6.6: Histograms of the pitch-angle cosine distribution in fully electrodynamic turbulence with a strong magnetic mean-field. (*a*) Test-particles with $v(0) = v_A$ and $\mu(0) = 0.0$ after one gyroperiod in balanced turbulence. (*b*) Test-particles with $v = 3v_A$ and $\mu(0) = 0.5$ after one gyroperiod in strongly imbalanced turbulence with $\sigma_c = 0.9$. The dotted lines mark the solution of the pitch-angle diffusion equation (6.5) at the respective times

proximate conservation of the magnetic moment limits the applicability of quasilinear predictions with regard to realistic particle scattering, unless the particle energy changes because of the influence of electric fields.

### 6.3.3 Results for magnetodynamic turbulence

There are two possible mechanisms which might cause the asymmetry of the scattering graphs in imbalanced turbulence: the coherent interaction with traveling Alfvén waves, which is differently strong for co- and counter-propagating particles in imbalanced turbulence, or the structure of the turbulent fields itself. In order to be able to distinguish both contributions to the asymmetry, we will repeat the simulations with either of these effects switched off and study how the shape of $\Delta_{\mu\mu}(\mu)$ in imbalanced turbulence is affected.

In our next series of test-particle runs, we keep the dynamic evolution of the magnetic turbulence as in the previous subsection, but do not include the effect of the electric field on the particles. Although this setup does not correspond to any physical situation, it gives valuable insight into the role of the electric field. The particle acceleration is computed as

$$\dot{\mathbf{v}}_i = \alpha \mathbf{v}_i \times \mathbf{b}(\mathbf{x}_i, t). \tag{6.6}$$

In this 'magnetodynamic' model, energy is perfectly conserved since the acceleration acting on each particle is always perpendicular to its velocity. Figures 6.7a and b confirm this by showing that the energy of test-particle ensembles with the same parameters as in figure 6.3 remains unchanged for the entire run. This constancy has little effect on the evolution of the magnetic moment in the balanced cases and for test-particles with $v(0) = 3v_A$ and $\mu(0) = +0.6$, which proceeds very similarly to the electrodynamic cases in figure 6.3. However, the counter-propagating particles in strongly imbalanced turbulence, which underwent significant heating by electric fields in the previous subsection, now exhibit a continuous increase of $M_{\mathrm{mag}}$ and accordingly a broadening of the magnetic-moment distribution (red shaded region in figure 6.7d).

The evolution of $\Delta\mu^2(t)$ is the same as in the electrodynamic runs for all test-particles, however: The counter-propagating particles in the strongly imbalanced case keep being scattered in pitch-angle for about ten gyroperiods, since this ensemble experiences a coherent magnetic field in the form of Alfvén waves traveling in the same direction, while the value of $\Delta\mu^2$ for $\mu(0) = +0.6$ ceases to increase after about three gyrations. In balanced turbulence, switching off the electric heating appears to have little to no effect on the pitch-angle scattering, as indicated by the extreme similarity of the graphs 6.3c and 6.7c.

To perform a comparison with the quasilinear theory again, we fit the values of $\Delta_{\mu\mu}(\mu)$ defined in (6.1) to the expression for $D_{\mu\mu}(\mu)$ in equation 3.73. Inserting the simple slab-turbulence ansatz given by the spectrum 3.60, we obtain

$$D_{\mu\mu}(\mu)^{(\mathrm{md})} = \sum_{\beta=\pm 1} \frac{\pi\Omega_0^2}{4k_{\mathrm{min}}}(1-\mu^2)\frac{1+\beta\sigma}{|\mu v + \beta v_A|}\left(\frac{k_{\mathrm{min}}\,|\mu v + \beta v_A|}{\Omega_0}\right)^{s^\beta}\frac{\delta B^2}{B_0^2}. \tag{6.7}$$

Fitting this equation to the numerical results for $\Delta_{\mu\mu}(\mu)$ (see figure 6.8) yields the best-fit parameters shown in figure 6.9. For test-particle ensembles with $v(0) = v_A$, the results are highly inaccurate: The cross-helicity levels $\sigma^{(\mathrm{fit})}$ appear to be almost independent of the actual degree of imbalance, the total turbulence amplitude $\delta B^{(\mathrm{fit})}$ is constantly overestimated in comparison to the real value of 0.1, and the spectral exponents $s^{\pm}$ reach values of up to 3.9. It seems that the influence of the magnetic field alone is too weak to imprint the pitch-angle distribution with sufficient information to derive the cross helicity from the shape of $\Delta_{\mu\mu}(\mu)$. Therefore, the electric field must play the dominant part in creating the asymmetry.

For faster particles, with $v(0) = 3v_A$, the scaling of $\sigma^{(\mathrm{fit})}$ is still noticeably weaker than in the electrodynamic case, although it does follow the correct trend. Both the turbulent amplitudes and the spectral exponents obtained in the fitting procedure are comparable to the results of the fully electrodynamic fits. Again, there is an outlier of $s^- = 2.2$ in the strongly imbalanced case, similar to the corresponding run with the electric field included.

The curves of $D_{\mu\mu}(\mu)$ using these best-fit parameters are compared to the test-particle results for $\Delta_{\mu\mu}(\mu)$ in figure 6.8. The asymmetry of both analytic and measured scattering in cross-helical runs is visibly much weaker than in the electrodynamic case, further validating our previous observation that the different scattering properties of balanced and imbalanced turbulence are mainly due to the electric fields.

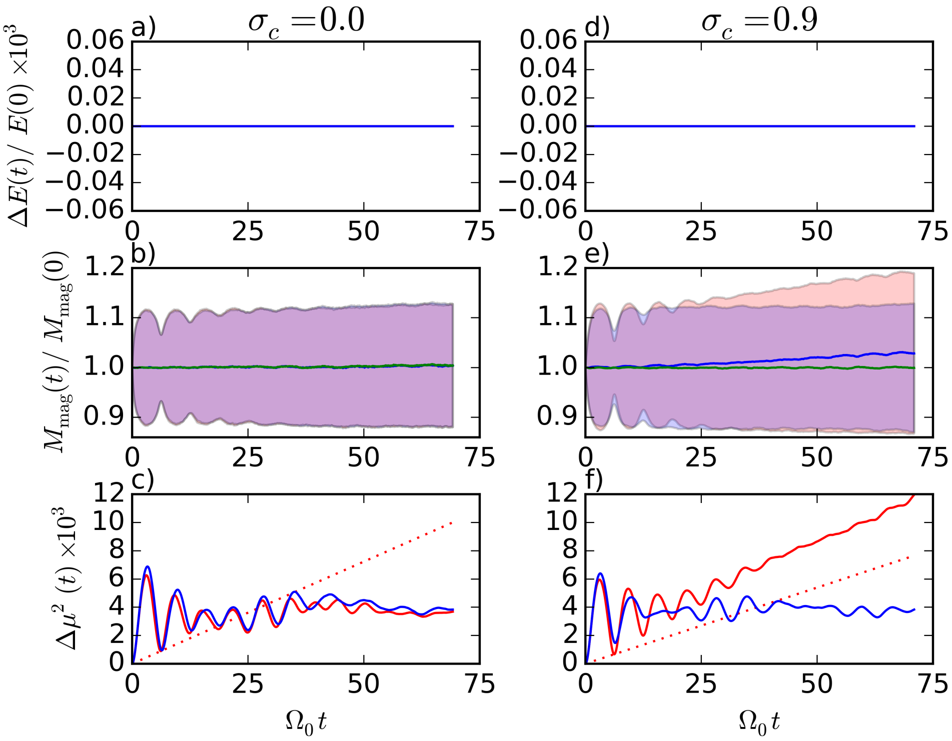

Figure 6.7: As figure 6.3, but for magnetodynamic turbulence (subsection 6.3.3)

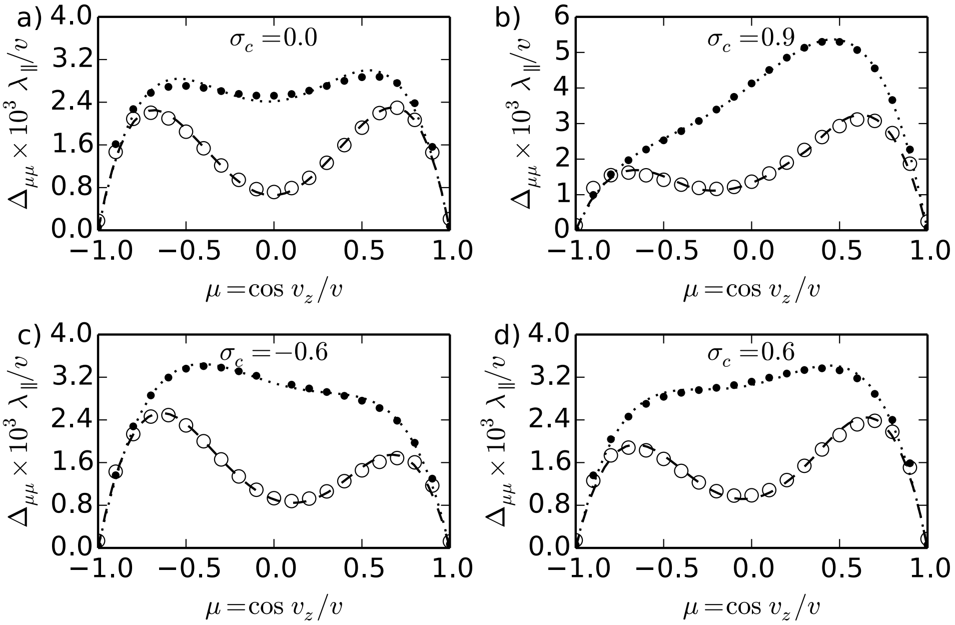

Figure 6.8: As figure 6.5, but for magnetodynamic turbulence (subsection 6.3.3)

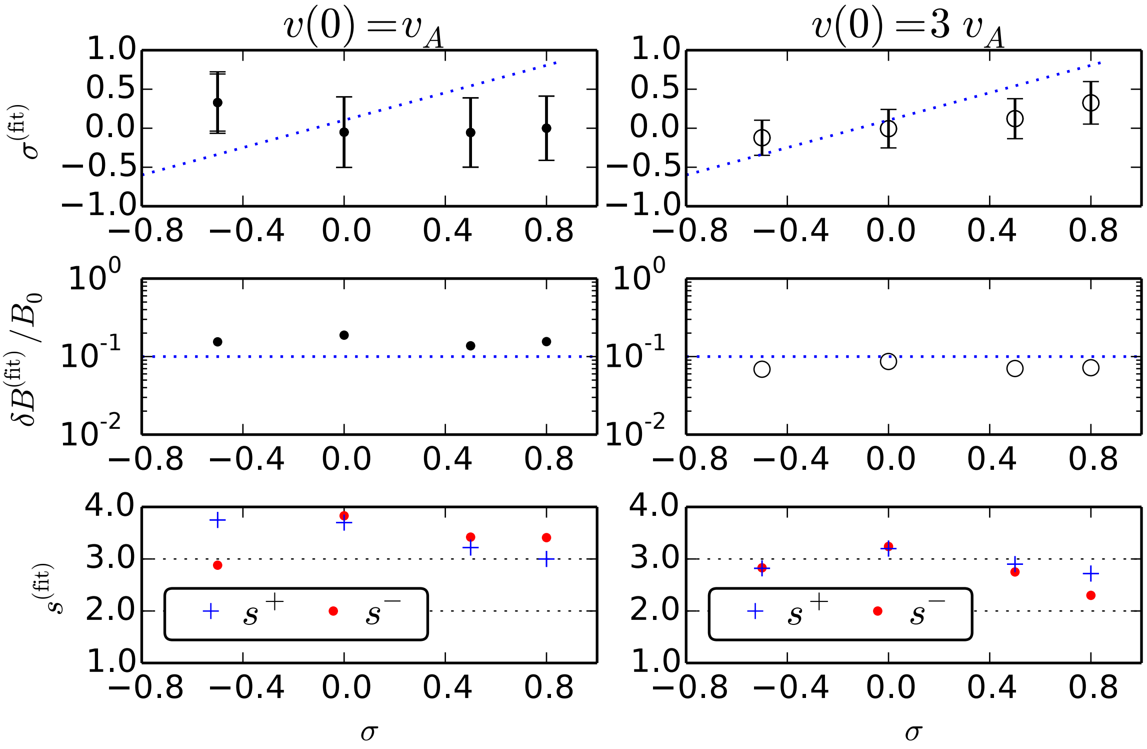

Figure 6.9: Magnetodynamic case: best-fit values for the normalized cross helicity $\sigma^{(\mathrm{fit})}$, the normalized amplitude of the magnetic turbulence $\delta B^{(\mathrm{fit})}/B_0$, and the spectral indices $s^+$ and $s^-$, for test-particle ensembles with initial velocity $v(0) = v_A$ (left) and $v(0) = 3v_A$ (right), for four different levels of the cross-helicity injection $\sigma$

## 6.4 Static turbulence

### 6.4.1 Magnetostatic turbulence

As before, we ignore the electric acceleration of the test-particles, but in the runs presented in this subsection, the fields are not evolved in parallel. The test-particle trajectories were computed in static snapshots of the MHD fields, thus Alfvén waves are 'frozen' in space.

Physically, this corresponds to particles with sufficiently high energy that acceleration due to the electric fields can be neglected. In addition, the particles are fast enough to be unaffected by resonances with propagating Alfvén waves (*i.e.* $v \gg v_A$). This simplification is commonly applied for simulating the propagation of high-energy cosmic-ray particles (*e.g.* Qin *et al.* , 2002; Tautz *et al.* , 2013), with a velocity close to the speed of light, through interstellar turbulence, since the fields of the interstellar medium do not change significantly on the timescales of the cosmic-ray propagation.

The energy of the test-particles remains constant, as in the previous subsection, due to the absence of electric fields. Figure 6.10, which contains the evolution of $E$, $M_{\mathrm{mag}}$, and $\Delta\mu^2$, is similar to the magnetodynamic case (figure 6.7) in almost every

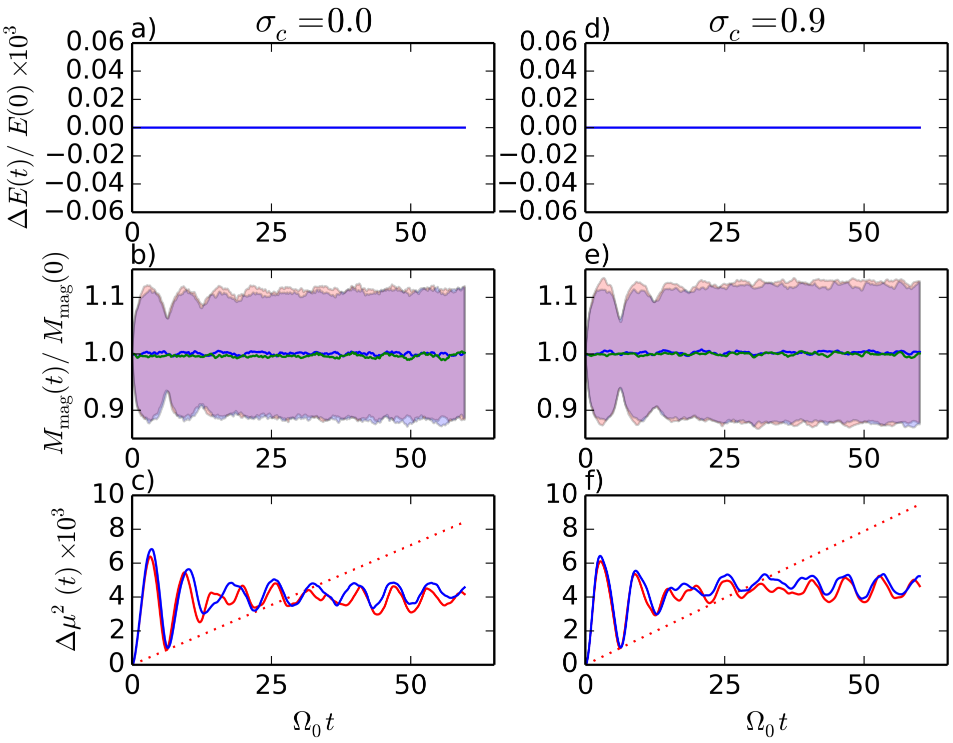

Figure 6.10: As figure 6.3, but for magnetostatic turbulence (subsection 6.4.1)

other aspect, as well, with one notable exception: The counter-propagating particles in the strongly imbalanced case do not show the same increase of the averaged magnetic moment as before. In static-turbulence fields, the (formerly) counter-propagating perturbations of the magnetic field are no longer able to scatter the test-particles with $\mu(0) = -0.6$ coherently. Since the kinetic energy is conserved exactly and the magnetic moment is conserved to a good approximation, none of the depicted test-particle ensembles continues being scattered at the same rate as in the first two gyroperiods, like the counter-propagating particles did in the dynamic runs.

Without a distinction between co- and counter-propagating Alfvén waves, we expect the numerical scattering rates $\Delta_{\mu\mu}(\mu)$ to be symmetric in $\mu$ independent of the level of cross helicity. Indeed, all graphs in figure 6.11 exhibit this symmetry to a certain degree: While the curves for the fast test-particles with $v(0) = 3v_A$ are extremely symmetric for all values of $\sigma_c$, since their greater gyroradius allows them to sample a wider range of fluctuations within one gyroperiod, the test-particles with Alfvén-speed exhibit a fairly large asymmetry ($\Delta_{\mu\mu}(+0.6)/\Delta_{\mu\mu}(-0.6) = 0.2$) in the balanced case.

The asymmetric behavior in the most symmetric turbulence configuration is attributable to statistical noise, which we have found to be generally larger in static simulations than in dynamic simulations. Using ten different snapshots for each cross-helicity value, we found that the results varied by up to $0.1\Delta_{\mu\mu}(\mu)$ for each test-particle ensemble with $2\times10^4$ particles, so we indicate this error in figure 6.11. In the dynamic runs, the results for different starting times lay within only 2 % of each other. Evolving

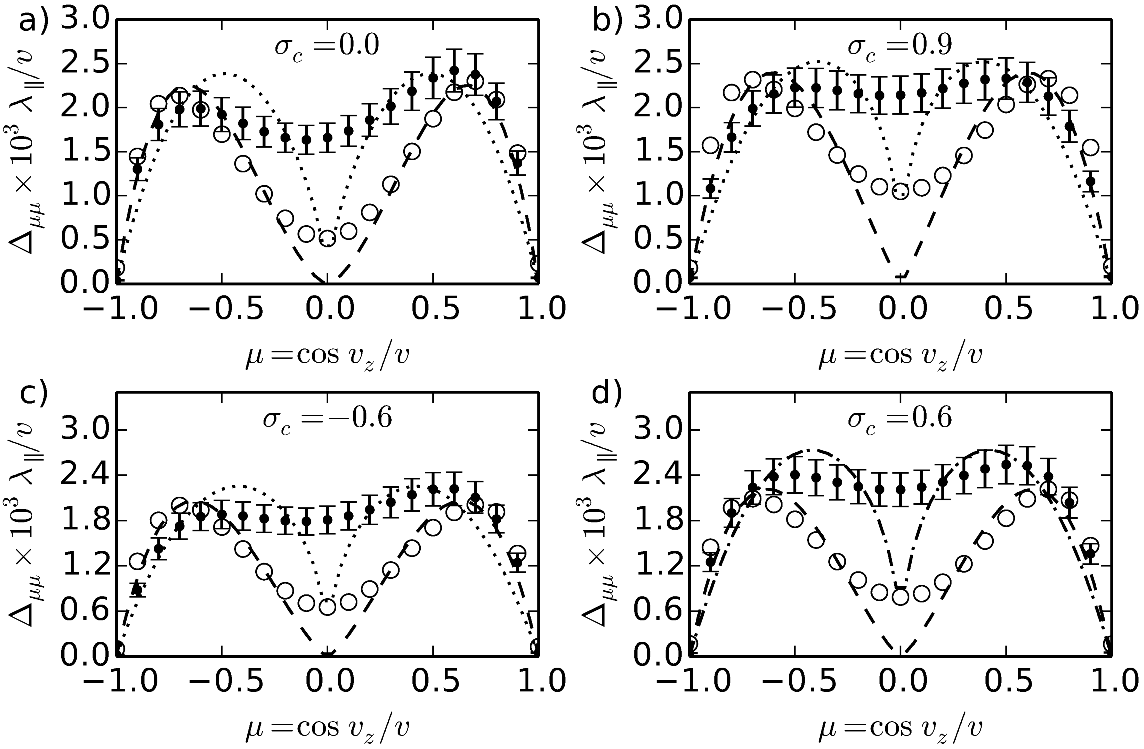

Figure 6.11: As figure 6.5, but for magnetostatic turbulence (subsection 6.4.1)

the trajectories for significantly longer would reduce the noise and is technically possible, since only few of the reasons for the limitation of $\Delta_{\mu\mu}$ to one gyroperiod apply to the magnetostatic case: Energy is fully conserved, and the long-term evolution of the pitch-angle is slow enough that assuming $D_{\mu\mu}$ remains constant would be justified. Since our main goal is to compare the magnetostatic to the fiducial, fully electrodynamic runs, we have chosen the same definition of $\Delta_{\mu\mu}$ for consistency, however.

Figure 6.11 also includes the best-fit curves for the magnetostatic momentum-diffusion coefficient given in equation (3.65), combined with the by-now familiar slab-turbulence ansatz, resulting in

$$D_{\mu\mu}(\mu) = \frac{\pi}{4}\,\Omega_0^{2-s}(1-\mu^2)\,\frac{\delta B^2}{B_0^2}\,|v\mu|^{s-1}(s-1)k_{\min}^{s-1}, \tag{6.8}$$

although the quality of this fit is obviously weak in every case. Apparently the pitch-angle scattering behavior of test-particles after one gyroperiod, as measured by $\Delta_{\mu\mu}$, differs significantly from the predictions which quasilinear theory makes for longer timescales. This discrepancy is particularly obvious at $\mu = 0.0$: Whereas QLT predicts for a slab-turbulence model that no pitch-angle diffusion takes place if a particle propagates at a right angle to the magnetic mean field (due to the factor $|\mu|^{s-1}$), the numerical estimator $\Delta_{\mu\mu}$ only has a local minimum at $\mu = 0.0$, which is particularly pronounced for the faster particles with $v(0) = 3v_A$, but does not reach zero.

In conclusion, particles propagating with initially positive pitch-angle cosine $+\mu$ along the mean magnetic field are scattered approximately as fast as particles traveling in the opposite direction at pitch-angle cosine $-\mu$ in magnetostatic turbulence of any kind, whether balanced or imbalanced. We have already mentioned in chapter 5 the investigations of Beresnyak *et al.* (2011) in static turbulence, who similarly concluded that cross helicity has a negligible effect on the spatial scattering of cosmic-ray particles if the energy of the particles was sufficiently large that the effect of the electric fields could be neglected. As shown in the previous section, however, this statement is only true if the time-dependence of the turbulence can be ignored as well.

## 6.4.2 Static electromagnetic turbulence

We have shown how pitch-angle scattering behaves in the absence of both key components we have identified so far: electric heating and coherent scattering by traveling Alfvénic perturbations. Since the distribution of the $z$-component of the electric field is symmetric in both balanced and imbalanced turbulence (see figure 4.19), one might expect that the electric field cannot cause any asymmetry in the scattering, and that only the time-dependence of the turbulence is crucial for the shape of $\Delta_{\mu\mu}(\mu)$. On the other hand, we have seen that ignoring the influence of the electric fields reduces the level of asymmetry of the graph of $\Delta_{\mu\mu}$.

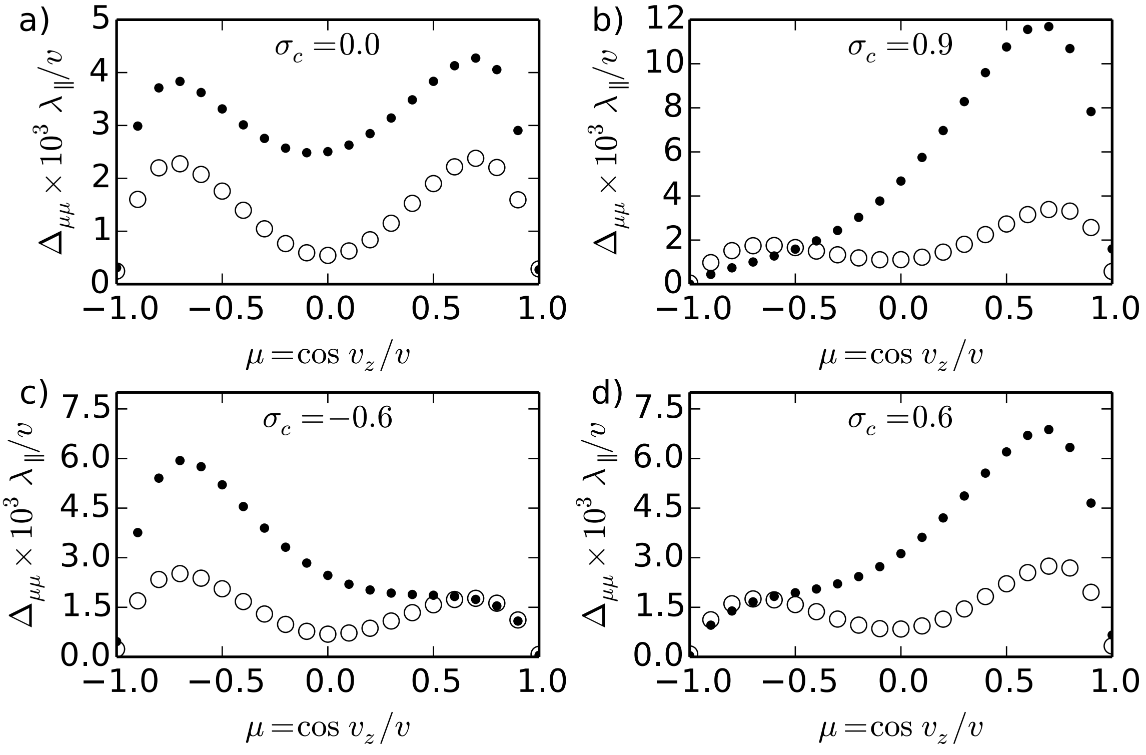

Figure 6.12: As figure 6.5, but for 'frozen-field' turbulence (subsection 6.4.2)

Figure 6.12 shows how electric fields shape the scattering rate in a static turbulence configuration with 'frozen fields'. Unlike in the previous subsection, we include the electric field in addition to the magnetic field. Test-particles propagating in static snapshots of MHD turbulence exhibit the same asymmetric scattering behavior as in evolving turbulence if they interact with both the electric and the magnetic field. Although the numerical values of $\Delta_{\mu\mu}$ in all plots reach only 60 - 70 % of their equivalent values in the fully electrodynamic runs (*cf.* figure 6.5), which implies that the absence of coherence with propagating Alfvén waves reduces the scattering efficiency, the normalized shapes of the $\Delta_{\mu\mu}(\mu)$-curves are almost identical in both figures.

Even though a static superposition of linear shear-Alfvén waves with random phase relations ought to lead to identical scattering properties whether a particle propagates at the same angle in the positive or the negative $z$-direction, the asymmetry in $\mu$ is clearly present. Therefore the scattering asymmetry in imbalanced turbulence must be a result of the spatial structure of the electric field.

---

In this chapter, we have shown that quasilinear predictions for pitch-angle diffusion are valid for Alfvén-speed particles on short timescales: Gyroresonant interactions scatter particles traveling in the direction of the subdominant Alfvén-wave population more effectively than particles in resonance with the dominant wave population.

On longer timescales, test-particles with a gyroradius significantly smaller than the parallel correlation length of the turbulence will show a tendency to maintain their magnetic moment due to adiabatic invariance. This constraint limits the rate at which the pitch-angle distribution can broaden, and the evolution of $\Delta\mu^2(t)$ changes significantly after several gyroperiods. The onset of this transition is delayed for particles in Landau resonance with the stronger Alfvén-wave population, although gyroresonance is weaker for these particles. Thus positive cross helicity in fully electrodynamic turbulence leads, after several gyroperiods, to faster pitch-angle scattering for particles propagating parallel to the mean-field than for oppositely directed particles, in apparent contradiction with the long-term behavior predicted by quasilinear theory.

Furthermore, we found evidence that, even in static turbulence, the spatial configuration of electric fields contributes significantly to the scattering asymmetry in imbalanced turbulence. This effect is likely relevant for strongly super-Alfvénic particles, too, and could have an important effect on the isotropization of cosmic-ray particles upstream of astrophysical shock fronts.

# Chapter 7

# Summary

> *No book can ever be finished. While working on it we learn just enough to find it immature the moment we turn away from it.*
>
> – *The Open Society And Its Enemies* (Karl Popper, 1950)

Whilst certainly some questions about imbalanced turbulence remain left to further investigation, we have uncovered important facets of every aspect that we have investigated:

## 7.1 Cross-helical forcing of incompressible turbulence

We began with an astrophysical example of cross-helical turbulence in the form of supernova remnants in chapter 1, before providing a short primer on the theory of magnetohydrodynamics in chapter 2. The complexity of realistic turbulence models contrasts sharply with the simple slab-spectrum ansatz, which we introduced after deriving quasilinear diffusion coefficients in chapter 3.

In chapter 4 we presented, tested, and successfully applied an algorithm which can be used to inject and maintain a predefined level of cross helicity in a pseudospectral three-dimensional simulation of evolving MHD turbulence. Although this cross-helical forcing only acts directly on modes with wavelengths comparable to the box size, the correlation of velocity and magnetic-field perturbations is transported down to smaller lengthscales by the turbulent cascade.

Importantly, this scheme works not only in the presence of a strong magnetic mean-field, like many other algorithms (we called them Elsasser-forcing schemes in chapter 4) which directly inject Alfvénic perturbations into the simulation. Our algorithm was originally developed only for isotropic turbulence, yet we were able to show that cross helicity can also be driven in strongly anisotropic turbulence, if one deforms the shell in spectral space into which energy is injected.

For any degree of anisotropy, the spectra both parallel and perpendicular to the magnetic mean-field exhibited well-defined inertial ranges in our simulations. The scaling of the spectral Elsasser energies was in good agreement with the power-law predictions of MHD theories by Kraichnan (1965),Goldreich & Sridhar (1995), and Grappin *et al.* (1983), once the turbulence had settled into a steady state.

To show that we not only inject kinetic and magnetic energy in a correlated fashion, but that we are actually able to create imbalanced Alfvénic turbulence by doing so, we performed a spatial and temporal Fourier analysis of strongly anisotropic simulations. As expected, the greatest spectral power was contained in modes fulfilling the dispersion relation of co- and counter-propagating shear-Alfvén waves, with the latter wave population clearly dominating in strongly imbalanced turbulence.

One possible extension of the present work is to apply this forcing algorithm to compressible MHD turbulence, possibly enabling us to study the coupling between shear-Alfvén waves and the fast magnetosonic mode in imbalanced turbulence. The theoretical framework of imbalanced compressible turbulence is still subject of ongoing research, so numerical simulations are crucial to identify promising scaling ansatzes.

## 7.2 Heating mechanisms in cross-helical turbulence

Using trajectories of charged test-particles in evolving MHD-turbulence runs, we have shown in chapter 5 that the heating rates derived from quasilinear theory in chapter 3 are accurate in realistic turbulence. Both the scaling with the gyroradius of the particles and the scaling with the cross helicity of the turbulent fields match quasilinear predictions, provided that the gyroradius exceeds the typical width of current filaments, which is comparable to Kolmogorov's dissipation length in our simulations.

In order to explore energization at such small gyroradii, we allowed for another heating mechanism by including the Ohmic force in the computation of the Lorentz force. We were able to reproduce the two-stage process recently reported by Dalena *et al.* (2014), in which initial Ohmic acceleration parallel to the local magnetic field and subsequent pitch-angle scattering increase the gyroradii of the particles, independently of cross helicity. Eventually, the trajectories are no longer trapped in the current filaments as the particles are able to interact resonantly with Alfvénic fluctuations, and the stochastic heating described by quasilinear theory sets in.

Future work may involve repeating these test-particle simulations in simulations of compressible imbalanced turbulence. Quasilinear theory predicts that stochastic acceleration by the fast magnetosonic mode may be significantly more efficient than by the shear-Alfvén mode in the solar wind (Schlickeiser & Miller, 1998). A numerical verification of this process with a focus on the influence of cross helicity would be possible in compressible runs with our cross-helical forcing scheme.

## 7.3 Pitch-angle scattering in imbalanced and magnetodynamic turbulence

In chapter 6, we showed that the predictions of quasilinear theory for the velocity diffusion of Alfvén-speed charged-particle ensembles accurately describe the mean-square deviation of the pitch-angle after only one gyroperiod. The agreement in evolving electrodynamic turbulence is striking both in balanced and imbalanced field configurations, although the cross-helicity value one needs to insert into the quasilinear expression for $D_{\mu\mu}$ to obtain a good match with test-particle results in strongly imbalanced turbulence is lower than the actual value. The quasilinear prediction for magnetodynamic turbulence has been validated successfully as well.

Test-particle results in static turbulence are subject to greater statistical noise than in evolving turbulence. However, we were able to show that the structure of the electric fields in imbalanced-turbulence configurations leads to different acceleration patterns for particles which are co- or counter-propagating with respect to a magnetic mean-field. Thus the scattering rate $\Delta_{\mu\mu}(\mu)$ after one gyroperiod assumes a shape that is asymmetric in the pitch-angle $\mu$ even if the fields are not evolved, as long as the electric field is included in the computation of the Lorentz force on the particles. If only the static magnetic field is used to advance test-particles, the graph of $\Delta_{\mu\mu}(\mu)$ is almost symmetric.

On longer timescales, however, quasilinear theory loses its predictive value for the parameter regime we have investigated. The approximate conservation of the magnetic moment requires that the spreading of the pitch-angle distribution ceases after a small number of gyrations, unless the mean energy of the particles is variable. This latter case was observed for test-particles interacting coherently with the electric field of the dominant Alfvén-wave population in strongly imbalanced turbulence. The spread of the pitch-angle distribution as predicted by quasilinear theory was generally observed to last for only a few gyroperiods. The implications of this finding, particularly with regard to velocity distributions in the solar wind, are far-reaching and merit extensive further study.

In magnetodynamic simulations, in which only the magnetic part of the Lorentz force affects test-particle trajectories, the energy of the particles remains constant, but the coherent interaction with the magnetic field of Alfvén waves is still able to induce pitch-angle diffusion on longer timescales. The conservation of the magnetic moment $M_{\mathrm{mag}}$ does not hold even approximately anymore in this case, and the mean-square deviation of both $M_{\mathrm{mag}}$ and the pitch-angle cosine increases with time. Since this interaction only affects particles that co-propagate with the dominant Alfvén-wave population, the quasilinear pitch-angle diffusion coefficient suggested by Shalchi *et al.* (2009) is invalid on longer timescales.

## 7.4 Concluding remarks

It is clear from the aforementioned results that cross helicity plays an important effect for the velocity diffusion of charged particles in magnetohydrodynamic turbulence. Since most turbulent systems in the universe are driven anisotropically, shear-Alfvén waves propagating in one direction with respect to the magnetic mean-field often dominate over the oppositely directed wave-population. Therefore cross helicity will affect the transport properties of such media significantly. This applies to both the supernova remnants described in chapter 1 and the solar wind. Future work should address in particular the possible influence on the rate of diffusive shock acceleration of high-energy cosmic-ray particles.

# Appendix A

# The Operator $\hat{P}(\mathbf{k})$

In chapter 3, the evolution equation (3.18) for deviations from an isotropic velocity-space distribution, $\delta f$, involved the differential operator $\hat{P}(\mathbf{k})$. This complicated operator approximates the third term of the Fokker-Planck equation in Fourier space, the term involving the Lorentz force and the velocity derivative, to first-order accuracy. As it may not be immediately transparent how the two expressions for $\hat{P}(\mathbf{k})$ given in equations (3.19) and (3.20) are equivalent, we detail the individual steps involved in arriving at the latter form in this appendix.

After Fourier transforming the Vlasov equation, we obtained an unwieldy integral $\mathcal{I}(\mathbf{k})$ that describes the force term of the Vlasov equation in spectral space. Arguing that the fluctuating fields are produced by the deviations $\delta f$ from isotropy and thus of the same order of magnitude, we neglect the terms in $\mathcal{I}$ involving products of field fluctuations and $\delta f$. Thus we define the operator $\hat{P}(\mathbf{k})$ by leaving out the last two lines of equation (3.5) and simplify it to

$$\mathcal{I}(\mathbf{k}) = -\hat{P}(\mathbf{k}) \cdot \overline{f} + \frac{q}{m} (\mathbf{v} \times \mathbf{B_0}) \cdot \frac{\partial}{\partial v_z} \delta f,$$

where we define $\hat{P}(\mathbf{k})$ as

$$\hat{P}(\mathbf{k}) = -\frac{q}{m} \left[ \tilde{\mathbf{E}}(\mathbf{k}) + \mathbf{v} \times \left( \frac{\mathbf{k}}{\omega_{\mathbf{k}}} \times \tilde{\mathbf{E}}(\mathbf{k}) \right) \right] \cdot \nabla_{\mathbf{v}}, \tag{A.1}$$

where we have applied Faraday's law

$$\nabla \times \mathbf{E} = -\frac{\partial}{\partial t} \mathbf{B} \tag{A.2}$$

in Fourier space to replace the magnetic field by

$$\tilde{\mathbf{B}}(\mathbf{k}) = \frac{\mathbf{k}}{\omega_{\mathbf{k}}} \times \tilde{\mathbf{E}}(\mathbf{k}). \tag{A.3}$$

Written out in explicit form, the individual components of the scalar product with the velocity gradient read

$$\begin{aligned}\hat{P}(\mathbf{k}) \;=\; & -\frac{q}{m}\left[\tilde{E}_x + \frac{v_y(k_x\tilde{E}_y - k_y\tilde{E}_x) - v_z(k_z\tilde{E}_x - k_x\tilde{E}_z)}{\omega_\mathbf{k}}\right]\frac{\partial}{\partial v_x} \\ & -\frac{q}{m}\left[\tilde{E}_y + \frac{v_z(k_y\tilde{E}_z - k_z\tilde{E}_y) - v_x(k_x\tilde{E}_y - k_y\tilde{E}_x)}{\omega_\mathbf{k}}\right]\frac{\partial}{\partial v_y} \\ & -\frac{q}{m}\left[\tilde{E}_z + \frac{v_x(k_z\tilde{E}_x - k_x\tilde{E}_z) - v_y(k_y\tilde{E}_z - k_z\tilde{E}_y)}{\omega_\mathbf{k}}\right]\frac{\partial}{\partial v_z}.\end{aligned}$$

Inverting the Jacobian matrix of the transformation to cylindrical coordinates introduced in definition (3.11),

$$\begin{pmatrix} \partial_{v_\perp} \\ \partial_\phi \\ \partial_{v_\parallel} \end{pmatrix} \cdot \left(v_x; v_y; v_z\right) = \begin{pmatrix} \cos\phi & -v_\perp\sin\phi & 0 \\ \sin\phi & v_\perp\cos\phi & 0 \\ 0 & 0 & 1 \end{pmatrix},$$

it is clear that the perpendicular velocity derivatives in the new coordinate system become

$$\frac{\partial}{\partial v_x} = \cos\phi\,\frac{\partial}{\partial v_\perp} - \frac{\sin\phi}{v_\perp}\frac{\partial}{\partial\phi}$$

and

$$\frac{\partial}{\partial v_y} = \sin\phi\,\frac{\partial}{\partial v_\perp} + \frac{\cos\phi}{v_\perp}\frac{\partial}{\partial\phi}.$$

Thus we can give the polarization tensor in cylindrical coordinates, using definitions (3.10) and (3.11):

$$\begin{aligned}\hat{P}(\mathbf{k}) \;=\; & -\frac{q}{m}\left[\tilde{E}_x + \frac{v_\perp k_\perp \mathrm{s}_\phi(\mathrm{c}_\psi\tilde{E}_y - \mathrm{s}_\psi\tilde{E}_x) - v_\parallel(k_\parallel\tilde{E}_x - k_\perp\mathrm{c}_\psi\tilde{E}_z)}{\omega_\mathbf{k}}\right]\left(\mathrm{c}_\phi\,\partial_{v_\perp} - \frac{\mathrm{s}_\phi\partial_\phi}{v_\perp}\right) \\ & -\frac{q}{m}\left[\tilde{E}_y + \frac{v_\parallel(k_\perp\mathrm{s}_\psi\tilde{E}_z - k_\parallel\tilde{E}_y) - v_\perp k_\perp\mathrm{c}_\phi(\mathrm{c}_\psi\tilde{E}_y - \mathrm{s}_\psi\tilde{E}_x)}{\omega_\mathbf{k}}\right]\left(\mathrm{s}_\phi\,\partial_{v_\perp} + \frac{\mathrm{c}_\phi\partial_\phi}{v_\perp}\right) \\ & -\frac{q}{m}\left[\tilde{E}_z + \frac{v_\perp\mathrm{c}_\phi(k_\parallel\tilde{E}_x - k_\perp\mathrm{c}_\psi\tilde{E}_z) - v_\perp\mathrm{s}_\phi(k_\perp\mathrm{s}_\psi\tilde{E}_z - k_\parallel\tilde{E}_y)}{\omega_\mathbf{k}}\right]\frac{\partial}{\partial v_\parallel},\end{aligned}$$

where we have abbreviated $\sin\phi$ and $\cos\phi$ as $\mathrm{s}_\phi$ and $\mathrm{c}_\phi$, respectively, with similar abbreviations for $\psi$.

With the perpendicular electric field components expressed in terms of the polarized basis $E_L$ and $E_R$ of definition (3.13),

$$\tilde{E}_x = \frac{E_R + E_L}{\sqrt{2}}; \quad \tilde{E}_y = \imath\frac{E_R - E_L}{\sqrt{2}}; \quad \tilde{E}_z = E_\parallel.$$

and the trigonometric functions written as the sum of complex exponentials, this expression becomes slightly cumbersome:

$$
\begin{aligned}
\hat{P}(\mathbf{k}) \;=\; & -\frac{q}{m}\left[\frac{E_R+E_L}{\sqrt{2}}+\frac{v_\perp k_\perp}{\omega_\mathbf{k}}\frac{e^{\imath\phi}-e^{-\imath\phi}}{2\imath}\left(\frac{e^{\imath\psi}+e^{-\imath\psi}}{2}\imath\frac{E_R-E_L}{\sqrt{2}}-\frac{e^{\imath\psi}-e^{-\imath\psi}}{2\imath}\frac{E_R+E_L}{\sqrt{2}}\right)\right.\\
& \left.-\frac{v_\parallel}{\omega_\mathbf{k}}\left(k_\parallel\frac{E_R+E_L}{\sqrt{2}}-k_\perp\frac{e^{\imath\psi}+e^{-\imath\psi}}{2}E_\parallel\right)\right]\left(\frac{e^{\imath\phi}+e^{-\imath\phi}}{2}\,\partial_{v_\perp}-\frac{e^{\imath\phi}-e^{-\imath\phi}}{2\imath\, v_\perp}\partial_\phi\right)\\
& -\frac{q}{m}\left[\imath\frac{E_R-E_L}{\sqrt{2}}+\frac{v_\parallel}{\omega_\mathbf{k}}\left(k_\perp\frac{e^{\imath\psi}-e^{-\imath\psi}}{2\imath}E_\parallel-k_\parallel\imath\frac{E_R-E_L}{\sqrt{2}}\right)\right.\\
& \left.-\frac{v_\perp k_\perp}{\omega_\mathbf{k}}\frac{e^{\imath\phi}+e^{-\imath\phi}}{2}\left(\frac{e^{\imath\psi}+e^{-\imath\psi}}{2}\imath\frac{E_R-E_L}{\sqrt{2}}-\frac{e^{\imath\psi}-e^{-\imath\psi}}{2\imath}\frac{E_R+E_L}{\sqrt{2}}\right)\right]\\
& \times\left(\frac{e^{\imath\phi}-e^{-\imath\phi}}{2\imath}\,\partial_{v_\perp}+\frac{e^{\imath\phi}+e^{-\imath\phi}}{2\, v_\perp}\partial_\phi\right)\\
& -\frac{q}{m}\left[E_\parallel+\frac{v_\perp}{\omega_\mathbf{k}}\frac{e^{\imath\phi}+e^{-\imath\phi}}{2}\left(k_\parallel\frac{E_R+E_L}{\sqrt{2}}-k_\perp\frac{e^{\imath\psi}+e^{-\imath\psi}}{2}E_\parallel\right)\right.\\
& \left.-\frac{v_\perp}{\omega_\mathbf{k}}\frac{e^{\imath\phi}-e^{-\imath\phi}}{2\imath}\left(k_\perp\frac{e^{\imath\psi}-e^{-\imath\psi}}{2\imath}E_\parallel-k_\parallel\imath\frac{E_R-E_L}{\sqrt{2}}\right)\right]\frac{\partial}{\partial v_\parallel},
\end{aligned}
$$

Sorting the terms in this expression by the electric-field component, we obtain:

$$
\begin{aligned}
\frac{\omega_\mathbf{k}\, m}{e}\hat{P}(\mathbf{k}) \;=\; & -E_L\frac{e^{-\imath\phi}}{\sqrt{2}}\left[(\omega_\mathbf{k}-k_\parallel v_\parallel)\left(\frac{\partial}{\partial v_\perp}-\frac{\imath}{v_\perp}\frac{\partial}{\partial\phi}\right)+k_\parallel v_\perp\frac{\partial}{\partial v_\parallel}+\imath k_\perp\frac{e^{\imath\psi}}{\sqrt{2}}\frac{\partial}{\partial\phi}\right]\\
& -E_R\frac{e^{\imath\phi}}{\sqrt{2}}\left[(\omega_\mathbf{k}-k_\parallel v_\parallel)\left(\frac{\partial}{\partial v_\perp}+\frac{\imath}{v_\perp}\frac{\partial}{\partial\phi}\right)+k_\parallel v_\perp\frac{\partial}{\partial v_\parallel}-\imath k_\perp\frac{e^{-\imath\psi}}{\sqrt{2}}\frac{\partial}{\partial\phi}\right]\\
& -E_\parallel\, k_\perp\frac{e^{\imath(\phi-\psi)}}{2}\left(v_\parallel\frac{\partial}{\partial v_\perp}-v_\perp\frac{\partial}{\partial v_\parallel}+\imath\frac{v_\parallel}{v_\perp}\frac{\partial}{\partial\phi}\right)\frac{\partial}{\partial v_\parallel}\\
& -E_\parallel\, k_\perp\frac{e^{-\imath(\phi-\psi)}}{2}\left(v_\parallel\frac{\partial}{\partial v_\perp}-v_\perp\frac{\partial}{\partial v_\parallel}-\imath\frac{v_\parallel}{v_\perp}\frac{\partial}{\partial\phi}\right)\frac{\partial}{\partial v_\parallel}\\
& -E_\parallel\frac{\partial}{\partial v_\parallel}.
\end{aligned}
$$

After introducing the differential operators $\hat{\Lambda}$ and $\hat{H}$ defined in (3.15) and (3.16), which we repeat here for ease of reference:

$$
\begin{aligned}
\hat{\Lambda}(\mathbf{k}) &= \left(1-\frac{k_\parallel v_\parallel}{\omega_\mathbf{k}}\right)\frac{\partial}{\partial v_\perp}+\frac{k_\parallel v_\parallel}{\omega_\mathbf{k}}\frac{\partial}{\partial v_\parallel},\\
\hat{H} &= v_\parallel\frac{\partial}{\partial v_\perp}-v_\perp\frac{\partial}{\partial v_\parallel},
\end{aligned}
$$

we finally obtain

$$
\begin{aligned}
\hat{P} \;=\; & -\frac{q}{m}e^{\imath(\phi-\psi)}\left[\frac{E_R e^{\imath\psi}}{\sqrt{2}}\left(\hat{\Lambda}+\imath\frac{\omega_{\mathbf{k}}-k_{\parallel}v_{\parallel}}{\omega_{\mathbf{k}}v_{\perp}}\partial_{\phi}\right)+\frac{k_{\perp}E_{\parallel}}{2\omega_{\mathbf{k}}}\left(\hat{H}+\imath\frac{v_{\parallel}}{v_{\perp}}\partial_{\phi}\right)\right] \\
& -\frac{q}{m}e^{-\imath(\phi-\psi)}\left[\frac{E_L e^{-\imath\psi}}{\sqrt{2}}\left(\hat{\Lambda}-\imath\frac{\omega_{\mathbf{k}}-k_{\parallel}v_{\parallel}}{\omega_{\mathbf{k}}v_{\perp}}\partial_{\phi}\right)+\frac{k_{\perp}E_{\parallel}}{2\omega_{\mathbf{k}}}\left(\hat{H}-\imath\frac{v_{\parallel}}{v_{\perp}}\partial_{\phi}\right)\right] \\
& -\frac{q}{m}\left[\imath\frac{k_{\perp}}{\omega_{\mathbf{k}}}\left(\frac{E_L e^{-\imath\phi}-E_R e^{\imath\phi}}{\sqrt{2}}\right)\partial_{\phi}+E_{\parallel}\frac{\partial}{\partial v_{\parallel}}\right],
\end{aligned}
$$

which is exactly the form of $\hat{P}(\mathbf{k})$ given in the second line of equation (3.20) in chapter 3.

# Bibliography

Alfvén, H. 1942. Existence of Electromagnetic-Hydrodynamic Waves. *Nature*, **150**, 405–406.

Ambrosiano, J., Matthaeus, W. H., Goldstein, M. L., & Plante, D. 1988. Test particle acceleration in turbulent reconnecting magnetic fields. *Journal of Geophysical Research*, **93**, 14383–14400.

Bell, A. R. 1978. The acceleration of cosmic rays in shock fronts. I. *Monthly Notices of the Royal Academy of Sciences*, **182**, 147–156.

Bell, A. R. 2004. Turbulent amplification of magnetic field and diffusive shock acceleration of cosmic rays. *Monthly Notices of the Royal Academy of Sciences*, **353**, 550–558.

Belmont, G., Grappin, R., Mottez, F., Pantellini, F., & Pelletier, G. 2014. *Collisionless Plasmas in Astrophysics*. Berlin: Wiley-VCH.

Beresnyak, A. 2014. Spectra of Strong Magnetohydrodynamic Turbulence from High-resolution Simulations. *Astrophysical Journal Letters*, **784**, L20.

Beresnyak, A., Yan, H., & Lazarian, A. 2011. Numerical Study of Cosmic Ray Diffusion in Magnetohydrodynamic Turbulence. *Astrophysical Journal*, **728**, 60.

Berezinsky, V. 2013. UHECR: Signatures and models. *Page 1003 of: European Physical Journal Web of Conferences*, vol. 53.

Biskamp, D. 2003. *Magnetohydrodynamic Turbulence*. Cambridge: Cambridge University Press.

Breech, B., Matthaeus, W. H., Milano, L. J., & Smith, C. W. 2003. Probability distributions of the induced electric field of the solar wind. *Journal of Geophysical Research (Space Physics)*, **108**, 1153.

Coleman, Jr., P. J. 1968. Turbulence, Viscosity, and Dissipation in the Solar-Wind Plasma. *Astrophysical Journal*, **153**, 371.

Compton, A. H., & Getting, I. A. 1935. An Apparent Effect of Galactic Rotation on the Intensity of Cosmic Rays. *Physical Review*, **47**, 817–821.

Cramer, N. F. 2001. *The Physics of Alfvén Waves*. Berlin: Wiley-VCH.

Dalena, S., Greco, A., Rappazzo, A. F., Mace, R. L., & Matthaeus, W. H. 2012. Magnetic moment nonconservation in magnetohydrodynamic turbulence models. *Physical Review E*, **86**, 016402.

Dalena, S., Rappazzo, A. F., Dmitruk, P., Greco, A., & Matthaeus, W. H. 2014. Test-particle Acceleration in a Hierarchical Three-dimensional Turbulence Model. *Astrophysical Journal*, **783**, 143.

Davidson, P. A. 2004. *Turbulence : an introduction for scientists and engineers*. Oxford: Oxford University Press.

Dmitruk, P., Matthaeus, W. H., & Seenu, N. 2004. Test Particle Energization by Current Sheets and Nonuniform Fields in Magnetohydrodynamic Turbulence. *Astrophysical Journal*, **617**, 667–679.

Draine, B. T. 2011. *Physics of the Interstellar and Intergalactic Medium*. Princeton: Princeton University Press.

Drury, L. O., & Falle, S. A. E. G. 1986. On the Stability of Shocks Modified by Particle Acceleration. *Monthly Notices of the Royal Academy of Sciences*, **223**, 353.

Dung, R., & Schlickeiser, R. 1990. The influence of the Alfvenic cross and magnetic helicity on the cosmic ray transport equation. I - Isospectral slab turbulence. *Astronomy & Astrophysics*, **240**, 537–540.

Elmegreen, B. G., & Scalo, J. 2004. Interstellar Turbulence I: Observations and Processes. *Annual Review of Astronomy and Astrophysics*, **42**, 211–273.

Elsasser, W. M. 1950. The Hydromagnetic Equations. *Physical Review*, **79**, 183–183.

Fermi, E. 1949. On the Origin of the Cosmic Radiation. *Physical Review*, **75**, 1169–1174.

Freidberg, J. P. 2008. *Plasma Physics and Fusion Energy*. Cambridge: Cambridge University Press.

Freidberg, J. P. 2014. *Ideal MHD*. Cambridge: Cambridge University Press.

Gendrin, R. 1968. Pitch angle diffusion of low energy protons due to gyroresonant interaction with hydromagnetic waves. *Journal of Atmospheric and Terrestrial Physics*, **30**, 1313–1330.

Goedbloed, J. P. H., & Poedts, S. 2004. *Principles of Magnetohydrodynamics*. Cambridge: Cambridge University Press.

Goldreich, P., & Sridhar, S. 1995. Toward a theory of interstellar turbulence. 2: Strong alfvenic turbulence. *Astrophysical Journal*, **438**, 763–775.

Gotoh, Toshiyuki, & Fukayama, Daigen. 2001. Pressure Spectrum in Homogeneous Turbulence. *Phys. Rev. Lett.*, **86**, 3775–3778.

Grant, H. L., Stewart, R. W., & Moilliet, A. 1962. Turbulence spectra from a tidal channel. *Journal of Fluid Mechanics*, **12**, 241–268.

Grappin, R., Leorat, J., & Pouquet, A. 1983. Dependence of MHD turbulence spectra on the velocity field-magnetic field correlation. *Astronomy & Astrophysics*, **126**, 51–58.

Greisen, K. 1966. End to the Cosmic-Ray Spectrum? *Physical Review Letters*, **16**, 748–750.

Hauff, T., Jenko, F., Shalchi, A., & Schlickeiser, R. 2010. Scaling Theory for Cross-Field Transport of Cosmic Rays in Turbulent Fields. *Astrophysical Journal*, **711**, 997–1007.

Heiles, C., & Crutcher, R. 2005. Magnetic Fields in Diffuse HI and Molecular Clouds. *Page 137 of:* Wielebinski, R., & Beck, R. (eds), *Cosmic Magnetic Fields*. Lecture Notes in Physics, Berlin Springer Verlag, vol. 664.

Hess, V. F. 1912. Über Beobachtungen der durchdringenden Strahlung bei sieben Freiballonfahrten. *Physikalische Zeitschrift*, **13**, 1084–1091.

HESS Collaboration, Aharonian, F. A., Akhperjanian, A. G., Aye, K.-M., Bazer-Bachi, A. R., Beilicke, M., & et al. 2004. High-energy particle acceleration in the shell of a supernova remnant. *Nature*, **432**, 75–77.

Hillas, A. M. 1984. The Origin of Ultra-High-Energy Cosmic Rays. *Annual Review of Astronomy and Astrophysics*, **22**, 425–444.

Iroshnikov, P. S. 1964. Turbulence of a Conducting Fluid in a Strong Magnetic Field. *Soviet Astronomy*, **7**, 566.

Jokipii, J. R. 1966. Cosmic-Ray Propagation. I. Charged Particles in a Random Magnetic Field. *Astrophysical Journal*, **146**, 480.

Kafle, P. R., Sharma, S., Lewis, G. F., & Bland-Hawthorn, J. 2012. Kinematics of the Stellar Halo and the Mass Distribution of the Milky Way Using Blue Horizontal Branch Stars. *Astrophysical Journal*, **761**, 98.

Kennel, C. F., & Engelmann, F. 1966. Velocity Space Diffusion from Weak Plasma Turbulence in a Magnetic Field. *Physics of Fluids*, **9**, 2377–2388.

Kolmogorov, A. N. 1991 (originally 1941). The local structure of turbulence in incompressible viscous fluid for very large Reynolds numbers. *Royal Society of London Proceedings Series A*, **434**, 9–13.

Kowal, G., de Gouveia Dal Pino, E. M., & Lazarian, A. 2011. Magnetohydrodynamic Simulations of Reconnection and Particle Acceleration: Three-dimensional Effects. *Astrophysical Journal*, **735**, 102.

Kraichnan, R. H. 1965. Inertial-Range Spectrum of Hydromagnetic Turbulence. *Physics of Fluids*, **8**, 1385–1387.

Krause, O., Tanaka, M., Usuda, T., Hattori, T., Goto, M., Birkmann, S., & Nomoto, K. 2008. Tycho Brahe's 1572 supernova as a standard typeIa as revealed by its light-echo spectrum. *Nature*, **456**, 617–619.

Kulsrud, R., & Pearce, W. P. 1969. The Effect of Wave-Particle Interactions on the Propagation of Cosmic Rays. *Astrophysical Journal*, **156**, 445.

Lagage, P. O., & Cesarsky, C. J. 1983. The maximum energy of cosmic rays accelerated by supernova shocks. *Astronomy & Astrophysics*, **125**, 249–257.

Landau, Lev Davidovich. 1946. On the vibrations of the electronic plasma. *Zh. Eksp. Teor. Fiz.*, **10**, 25.

Lee, M. A. 1982. Coupled hydromagnetic wave excitation and ion acceleration upstream of the earth's bow shock. *Journal of Geophysical Research*, **87**, 5063–5080.

Lehe, R., Parrish, I. J., & Quataert, E. 2009. The Heating of Test Particles in Numerical Simulations of Alfvénic Turbulence. *Astrophysical Journal*, **707**, 404–419.

Lerche, I. 1968. Quasilinear Theory of Resonant Diffusion in a Magneto-Active, Relativistic Plasma. *Physics of Fluids*, **11**, 1720–1727.

Liboff, R. L. 2003. *Kinetic theory : classical, quantum, and relativistic descriptions*. New York: Springer.

Longair, M. S. 2011. *High Energy Astrophysics*. Cambridge: Cambridge University Press.

Lynn, J., Parrish, I. J., & Quataert, E. 2011. Heating and Diffusion of Test Particles in Alfvenic Turbulence. *AGU Fall Meeting Abstracts*, B2036.

Marsch, E., & Tu, C.-Y. 1990. On the radial evolution of MHD turbulence in the inner heliosphere. *Journal of Geophysical Research*, **95**, 8211–8229.

Matthaeus, W. H., Ambrosiano, J. J., & Goldstein, M. L. 1984. Particle-acceleration by turbulent magnetohydrodynamic reconnection. *Physical Review Letters*, **53**, 1449–1452.

Matthaeus, W. H., Pouquet, A., Mininni, P. D., Dmitruk, P., & Breech, B. 2008. Rapid Alignment of Velocity and Magnetic Field in Magnetohydrodynamic Turbulence. *Physical Review Letters*, **100**, 085003.

Morlino, G., & Caprioli, D. 2012. Strong evidence for hadron acceleration in Tycho's supernova remnant. *Astronomy & Astrophysics*, **538**, A81.

Northrop, T. G. 1963. *The Adiabatic Motion of Charged Particles*. Interscience Tracts on Physics and Astronomy, vol. 21. New York: Interscience Publishers.

Onofri, M., Isliker, H., & Vlahos, L. 2006. Stochastic Acceleration in Turbulent Electric Fields Generated by 3D Reconnection. *Physical Review Letters*, **96**, 151102.

Orszag, S. A. 1971. On the Elimination of Aliasing in Finite-Difference Schemes by Filtering High-Wavenumber Components. *Journal of Atmospheric Sciences*, **28**, 1074–1074.

Parker, E. N. 1971. The Generation of Magnetic Fields in Astrophysical Bodies. II. The Galactic Field. *Astrophysical Journal*, **163**, 255.

Perez, J. C., & Boldyrev, S. 2010. Numerical Simulations of Imbalanced Strong Magnetohydrodynamic Turbulence. *Astrophysical Journal Letters*, **710**, L63–L66.

Planck Collaboration, Ade, P. A. R., Aghanim, N., Armitage-Caplan, C., Arnaud, M., Ashdown, M., & et al. 2014. Planck 2013 results. XVI. Cosmological parameters. *Astronomy & Astrophysics*, **571**, A16.

Podesta, J. J., Roberts, D. A., & Goldstein, M. L. 2007. Spectral Exponents of Kinetic and Magnetic Energy Spectra in Solar Wind Turbulence. *Astrophysical Journal*, **664**, 543–548.

Pope, S. B. 2000. *Turbulent Flows*. Cambridge: Cambridge University Press.

Qin, G., & Shalchi, A. 2009. Pitch-Angle Diffusion Coefficients of Charged Particles from Computer Simulations. *Astrophysical Journal*, **707**, 61–66.

Qin, G., Matthaeus, W. H., & Bieber, J. W. 2002. Perpendicular Transport of Charged Particles in Composite Model Turbulence: Recovery of Diffusion. *Astrophysical Journal Letters*, **578**, L117–L120.

Richardson, L. F. 1922. *Weather Prediction by Numerical Process*. Cambridge: Cambridge University Press.

Roberts, D. A., Goldstein, M. L., Matthaeus, W. H., & Ghosh, S. 1992. Velocity shear generation of solar wind turbulence. *Journal of Geophysical Research*, **97**, 17115.

Saddoughi, S. G., & Veeravalli, S. V. 1994. Local isotropy in turbulent boundary layers at high Reynolds number. *Journal of Fluid Mechanics*, **268**, 333–372.

Schlickeiser, R. 1989. Cosmic-ray transport and acceleration. I - Derivation of the kinetic equation and application to cosmic rays in static cold media. II - Cosmic rays in moving cold media with application to diffusive shock wave acceleration. *Astrophysical Journal*, **336**, 243–293.

Schlickeiser, R. 2002. *Cosmic Ray Astrophysics*. Berlin: Springer.

Schlickeiser, R., & Miller, J. A. 1998. Quasi-linear Theory of Cosmic-Ray Transport and Acceleration: The Role of Oblique Magnetohydrodynamic Waves and Transit-Time Damping. *Astrophysical Journal*, **492**, 352–378.

Schlickeiser, R., & Shalchi, A. 2008. Cosmic-Ray Diffusion Approximation with Weak Adiabatic Focusing. *Astrophysical Journal*, **686**, 292–302.

Sedov, L. I. 1958. Examples of Gas Motion and Certain Hypotheses on the Mechanism of Stellar Outbursts. *Reviews of Modern Physics*, **30**, 1077–1079.

Shalchi, A. 2009. *Nonlinear Cosmic Ray Diffusion Theories*. Astrophysics and Space Science Library, vol. 362. Berlin: Springer.

Shalchi, A., Koda, T. Å., Tautz, R. C., & Schlickeiser, R. 2009. Analytical description of nonlinear cosmic ray scattering: isotropic and quasilinear regimes of pitch-angle diffusion. *Astronomy & Astrophysics*, **507**, 589–597.

Skilling, J. 1975. Cosmic ray streaming. I - Effect of Alfven waves on particles. *Monthly Notices of the Royal Academy of Sciences*, **172**, 557–566.

Somov, B. V. 2006. *Plasma Astrophysics, Part I: Fundamentals and Practice*. New York: Springer.

Sreenivasan, K. R. 1995. On the universality of the Kolmogorov constant. *Physics of Fluids*, **7**, 2778–2784.

Sridhar, S., & Goldreich, P. 1994. Toward a theory of interstellar turbulence. 1: Weak Alfvenic turbulence. *Astrophysical Journal*, **432**, 612–621.

Stanev, T. 2011. *High Energy Cosmic Rays*. Springer Praxis Books / Astronomy and Planetary Sciences Series. London: Springer.

Stix, T. H. 1992. *Waves in plasmas*. New York: American Institute of Physics.

Tautz, R. C., Dosch, A., Effenberger, F., Fichtner, H., & Kopp, A. 2013. Pitch-angle scattering in magnetostatic turbulence. I. Test-particle simulations and the validity of analytical results. *Astronomy & Astrophysics*, **558**, A147.

Taylor, G. 1950. The Formation of a Blast Wave by a Very Intense Explosion. I. Theoretical Discussion. *Royal Society of London Proceedings Series A*, **201**, 159–174.

Teaca, B. 2010. *Numerical simulations of transport processes in magnetohydrodynamic turbulence*. Ph.D. thesis, Université Libre de Bruxelles & Universitatea din Craiova.

Teaca, B., Verma, M. K., Knaepen, B., & Carati, D. 2009. Energy transfer in anisotropic magnetohydrodynamic turbulence. *Physical Review E*, **79**, 046312.

Teaca, B., Weidl, M. S., Jenko, F., & Schlickeiser, R. 2014. Acceleration of particles in imbalanced magnetohydrodynamic turbulence. *Physical Review E*, **90**.

Tverskoǐ, B. A. 1967. Contribution to the Theory of Fermi Statistical Acceleration. *Soviet Journal of Experimental and Theoretical Physics*, **25**, 317.

Vallee, J. P. 1991. Reversing the axisymmetric (m = 0) magnetic fields in the Milky Way. *Astrophysical Journal*, **366**, 450–454.

Vallée, J. P. 2008. New Velocimetry and Revised Cartography of the Spiral Arms in the Milky Way – A Consistent Symbiosis. *Astronomical Journal*, **135**, 1301–1310.

Vlasov, AA. 1938. On high-frequency properties of electron gas. *Journal of Experimental and Theoretical Physics*, **8**, 291–318.

Völk, H. J., Berezhko, E. G., & Ksenofontov, L. T. 2005. Magnetic field amplification in Tycho and other shell-type supernova remnants. *Astronomy & Astrophysics*, **433**, 229–240.

Weidl, M. S., Teaca, B., Jenko, F., & Schlickeiser, R. 2014. Charged-particle heating in imbalanced MHD turbulence . *Page 48 of: Proceedings of Science*, vol. PoS(CRISM2014).

Weidl, M. S., Jenko, F., Teaca, B., & Schlickeiser, R. 2015. *Pitch-Angle Scattering in Imbalanced MHD Simulations*. submitted to the Astrophysical Journal.

Zatsepin, G. T., & Kuz'min, V. A. 1966. Upper Limit of the Spectrum of Cosmic Rays. *Soviet Journal of Experimental and Theoretical Physics Letters*, **4**, 78.

# Danksagung

> *"Allen gewidmet, von denen ich lernte."*
>
> –*Beim Häuten der Zwiebel* (Günter Grass, 2006)

My deepest gratitude goes to Professor Frank Jenko, for giving me the opportunities to work on all these fascinating topics, and to Professor Harald Lesch, for being the inspiration that he is to physicists and laypeople alike. I am also thankful to Professor Reinhard Schlickeiser and Bogdan Teaca for many an enlightening discussion, on physics as well as on other subjects.

The folks in Princeton offered their generous hospitality to me, and I am particularly grateful to Damiano for teaching me all about Tycho's SNR, to Anatoly and Jim for their advice, and to everybody else at Peyton Hall for providing the most interesting, illuminating, and inspiring environment I've ever been in. In this context I should also like to thank the DoE, especially the guy with the tie.

All of my colleagues in the TOK group at IPP have been incredibly supportive, but some special mentions are in order. First of all, thank you, Mirjam, for donating a proper coffeemaker to our group. Thanks also go to Michael, who proofread early versions of most chapters in this thesis, and who has wisely learnt to trust my taste in cinema. My officemates, Francis, Konstantin, and Vasil (in chronological order), never complained about the creative chaos on my desk. (On the other hand, the plant on my desk is still alive and well, while they pretty much killed off theirs.) And then there's Tobias, who successfully filled his role as ombudsman and occasional therapist.

Last but certainly not least, the two persons deserving of the greatest portion of gratitude for where I stand in life at this point are, obviously, my parents. Thank You!

# Lebenslauf

Martin Simon Weidl

| | |
|---|---|
| 9. Okt. 1986 | Geboren in Ehingen an der Donau |
| 1996-2006 | Apian-Gymnasium Ingolstadt (Abiturnote 1,0) |
| 2006-2009 | Bachelor-Studium an der LMU München (Abschlussnote 1,1),<br>Mitglied im Max-Weber-Programm Bayern |
| 2009-2011 | Master-Studium an der LMU München (Abschlussnote 1,0) |
| 2012-2015 | Wissenschaftlicher Mitarbeiter am Max-Planck-Institut für Plasmaphysik in Garching,<br>Mitglied in der Helmholtz Graduate School for Plasma Physics,<br>Researcher am Max-Planck/Princeton Center for Plasma Physics |